UNIVERSIDADE FEDERAL DE SANTA CATARINA
CENTRO TECNOLÓGICO
PROGRAMA DE PÓS-GRADUAÇÃO EM ENGENHARIA MECÂNICA

Gabriel de Andrade Janene Gonini

Development of an indirect method for knock prediction in CRFD simulations of internal combustion engines

Florianópolis
2023

Gabriel de Andrade Janene Gonini

Development of an indirect method for knock prediction in CRFD simulations of internal combustion engines

Dissertação do Programa de Pós-Graduação em Engenharia Mecânica do Centro Tecnológico da Universidade Federal de Santa Catarina como requisito para a obtenção do título de Mestre em Engenharia Mecânica

Orientador: Prof. Leonel Rincón Cancino, Dr. Eng.
Coorientador: Prof. Amir Antônio Martins Oliveira Jr., Ph.D.

Florianópolis
2023

Ficha de identificação da obra elaborada pelo autor,
através do Programa de Geração Automática da Biblioteca Universitária da UFSC.

Gonini, Gabriel de Andrade Janene
Development of an indirect method for knock prediction in CRFD simulations of internal combustion engines / Gabriel de Andrade Janene Gonini ; orientador, Leonel Rincón Cancino, coorientador, Amir Antônio Martins Oliveira Jr., 2023.
172 p.

Dissertação (mestrado) - Universidade Federal de Santa Catarina, Centro Tecnológico, Programa de Pós-Graduação em Engenharia Mecânica, Florianópolis, 2023.

Inclui referências.

1. Engenharia Mecânica. 2. Previsão de detonação. 3. Tempo de atraso de ignição (IDT). 4. Motores a combustão interna. 5. Integral de Livengood-Wu. I. Cancino, Leonel Rincón. II. Oliveira Jr., Amir Antônio Martins. III. Universidade Federal de Santa Catarina. Programa de Pós Graduação em Engenharia Mecânica. IV. Título.

Gabriel de Andrade Janene Gonini

Development of an indirect method for knock prediction in CRFD simulations of internal combustion engines

O presente trabalho em nível de mestrado foi avaliado e aprovado por banca examinadora composta pelos seguintes membros:

Prof. Emilio Ernesto Paladino, Dr. Eng.
Universidade Federal de Santa Catarina

Prof. Fernando Luiz Sacomano Filho, Dr.
Universidade de São Paulo

Prof. Stephan Hennings Och, Dr.Eng.
Universidade Federal do Paraná

Certificamos que esta é a versão original e final do trabalho de conclusão que foi julgado adequado para obtenção do título de Mestre em Engenharia Mecânica.

Documento assinado digitalmente
Henrique Simas
Data: 18/04/2023 07:54:58-0300
CPF: ***.194.639-**
Verifique as assinaturas em https://v.ufsc.br

Prof. Henrique Simas, Dr. Eng.
Coordenação do Programa de Pós-Graduação

Documento assinado digitalmente
Leonel Rincon Cancino
Data: 11/04/2023 22:37:50-0300
CPF: ***.643.649-**
Verifique as assinaturas em https://v.ufsc.br

Prof. Leonel Rincón Cancino, Dr. Eng.
Orientador

Florianópolis, 2023.

Este trabalho é dedicado à minha família, amigos e professores.

AGRADECIMENTOS

Aos Profs. Leonel Cancino e Amir de Oliveira pela orientação ao longo do mestrado. Aos amigos e colegas dos Laboratório de Motores de Combustão Interna (LABMCI) e do Laboratório de Combustão e Engenharia de Sistemas Térmicos (LabCET) pelo apoio nos estudos e na pesquisa. À Coordenação de Aperfeiçoamento de Pessoal de Nível Superior (CAPES) pela bolsa de mestrado Processo 88887.658279/2021-00. Ao programa AVL AST University Partnership Program (UPP) pelo uso e suporte das ferramentas AVL-AST™ .

"Knock, knock.
Who's there?"

RESUMO

A detonação é uma combustão indesejada que pode danificar o motor. A fluidodinâmica reativa computacional (CRFD) auxilia no desenvolvimento de motores, embora a previsão de detonação seja um desafio devido à sua natureza localizada. O objetivo desta pesquisa é desenvolver um método de previsão numérica indireta de detonação para ser usado em simulações de CRFD de motores de combustão interna, aplicando a integral de Livengood-Wu baseada em uma correlação de tempo de atraso de ignição (IDT) obtida por uma abordagem automatizada e multivariada, com os valores locais de pressão, temperatura e composição da mistura. A correlação é uma expressão de Ahrrenius modificada, obtida após sucessivas regressões lineares múltiplas (MLR), em função de temperatura, índice anti-detonação (AKI), pressão e razão de equivalência, em uma região fora do coeficiente negativo de temperatura (NTC). A base de dados reúne dados experimentais publicados de IDT. A cada iteração, removem-se pontos com alto erro e as MLRs são recalculadas até atingir um limite de erro. Os resultados são validados para uma base de dados restrita (álcoois de cadeia normal de um a quatro carbonos), antes de implementar na maior. A simulação CRFD de referência é um motor a centelha com injeção direta, cujos principais modelos são: chama coerente estendida de 3 zonas (ECFM-3Z) para combustão; $k-\zeta-f$ para turbulência; TABKIN FGM e Knock Shell para detonação. Dados de escoamento e mistura são extraídos de 16 esferas igualmente espaçadas no ponto morto superior, em uma análise a posteriori. Esses valores são usados para avaliar a integral L-W com diferentes métodos de IDT, obtidos de simulações de cinética química de Cantera ou a partir de correlações de IDT. O início da detonação estimado através das integrais L-W é comparado ao ângulo de virabrequim apontado por dois valores de referência, quando as esferas atingem 1000 K e $\Omega_{1\%}$ (quando há ao menos 1% de probabilidade de detonação). Entre os resultados, para as correlações de IDT, destacam-se um erro absoluto médio próximo de 10% e R^2 de 0.991 para álcoois e 0.987 para a base completa. Para a análise a posteriori, os métodos baseados em mecanismos estão mais próximos das referências em 500 e 1000 RPM. No entanto, a correlação deste trabalho tem uma previsão conservadora em 14 das 16 esferas a 2000 RPM comparada a $\Omega_{1\%}$ e dista, em média, 0.6 ângulos de virabrequim da referência de 1000 K. Para 4000 RPM, no entanto, há uma previsão tardia generalizada.

Palavras-chave: Previsão de detonação. Tempo de atraso de ignição (IDT). Motores de combustão interna de ignição por faísca de injeção direta (DI-SI ICE). Integral de Livengood-Wu. Regressão linear múltipla (MLR).

ABSTRACT

Knock is an undesired combustion event that can damage the engine. Computational reactive fluid dynamics (CRFD) assists in engine development, although knock prediction is challenging due to its localized nature. The objective of this research is to develop an indirect method for knock prediction to be used in CRFD simulations of internal combustion engines, applying the Livengood-Wu integral based on an ignition delay time (IDT) correlation obtained by a multivariate and automatized approach, with local values of pressure, temperature and mixture composition. The correlation is a modified Ahrrenius expression, obtained after successive multiple linear regressions (MLR), as a function of temperature, anti-knock index (AKI), pressure and equivalence ratio, in a region outside the negative temperature coefficient (NTC). The database gathers published IDT experimental data. At each iteration, points with high error are removed and the MLRs are recalculated until an error threshold is reached. The results are validated for a restricted database (normal chain alcohols of one to four carbons), before implementing in the larger one. The reference CRFD simulation is a direct-injection spark engine, whose main models are: 3-zone extended coherent flame (ECFM-3Z) for combustion; $k-\zeta-f$ for turbulence; TABKIN FGM and Knock Shell for detonation. Flow and mixture data are extracted from 16 spheres equally spaced at top dead center in an a posteriori analysis. These values are used to evaluate the L-W integral with different IDT methods, obtained from Cantera chemical kinetics simulations or from IDT correlations. The knock onset estimated through the L-W integrals is compared to the crank angle pointed by two reference values, when the spheres reach 1000 K and $\Omega_{1\%}$ (when there is at least 1% probability of knock). Among the results, for the IDT correlations, it is worth mentioning an average absolute error close to 10% and R^2 of 0.991 for alcohols and 0.987 for the complete database. For the a posteriori analysis, the mechanism-based methods are closer to the references at 500 and 1000 RPM. However, this work's correlation conservatively predicted the knock onset on 14 of the 16 spheres at 2000 RPM compared to $\Omega_{1\%}$ and is, on average, 0.6 crank angle degrees away from the 1000 K reference. At 4000 RPM, however, there is a generalized late prediction.

Keywords: Knock prediction. Ignition delay time (IDT). Direct-injection spark-ignition internal combustion engines (DI-SI ICE). Livengood-Wu integral. Multiple linear regression (MLR).

RESUMO EXPANDIDO

Introdução

A injeção direta de combustível (DI) nebuliza combustível diretamente a altas pressões no cilindro, promovendo um efeito de resfriamento, maior compressão do motor e consequente aumento de eficiência. No entanto, esse efeito de resfriamento é normalmente usado para aumentar a taxa de compressão com a mesma sensibilidade de detonação. A combustão irregular compreende processos não iniciados pela ignição por centelha, mas sim por autoignição. A detonação é uma autoignição que ocorre após o tempo de ignição. No caso de combustão por detonação, a frente de chama não se propaga com rapidez suficiente pela câmara de combustão e a autoignição da mistura não queimada ocorre antes da chegada da chama. A mistura fresca nessa área pode queimar abruptamente, gerando ondas de pressão que refletem nas paredes, com amplitudes que podem ser grandes o suficiente para causar danos mecânicos. Existem muitos fatores que aumentam a probabilidade e o poder de detonação da combustão, como alta taxa de compressão, baixa rotação do motor, combustíveis com baixo índice de octanas e resfriamento insuficiente da parede. Durante os testes de bancada, deve-se identificar eventos de combustão irregulares usando sensores que identificam a detonação. No entanto, durante as simulações numéricas, a identificação depende da correta modelagem e resolução, por se tratar de um fenômeno local. Os modelos de combustão são responsáveis por simular a depleção e formação de espécies, ignição e combustão de misturas ar/combustível e seus gases de exaustão. Além disso, as taxas médias de reação química são geralmente funções não lineares dependentes dos valores locais de temperatura e concentrações de espécies e, portanto, são difíceis de determinar. Modelos de combustão como os Coherent Flame Models (CFM) contribuem para a descrição desse problema. A família CFM assume que as escalas de tempo químicas são muito menores do que as turbulentas. Assim, é possível aplicar uma abordagem de elemento de chama (flamelet) laminar, em que a velocidade e a espessura da chama são valores médios integrados ao longo da frente de chama, dependentes apenas da pressão, temperatura e estequiometria dos gases não queimados. Como tal, ela permite desacoplar química e turbulência; no entanto, espera-se que a variação no modelo de turbulência influencie em algumas mudanças nos campos de escoamento e espécies químicas e, em última análise, a taxa de liberação de calor. O objetivo desta pesquisa é desenvolver um método de previsão numérica indireta de detonação para ser usado em simulações de motores de combustão interna usando fluidodinâmica computacional reativa (CRFD), aplicando uma correlação de tempo de atraso de ignição (IDT) obtida por meio de uma abordagem multivariada e automatizada. Para objetivos específicos, busca-se desenvolver uma abordagem multivariada e automatizada para obter uma correlação do tempo de atraso de ignição em função da pressão, temperatura, razão de equivalência e índice anti-detonação e aplicá-la a bancos de dados de experimentos publicados de álcoois primários C_1 a C_4 e combustíveis relevantes para a indústria de transporte; e busca-se propor uma análise a posteriori que extraia os valores locais de pressão, temperatura e concentrações de espécies em regiões de interesse de um motor de ignição por centelha com injeção direta de gasolina para aplicar à integral Livengood-Wu com base em cinética química e correlações de IDT.

Revisão de literatura

Basicamente, existem atualmente apenas duas principais tecnologias de ignição comercial, por centelha e compressão (SI e CI, respectivamente). Uma terceira estratégia em escala de pesquisa é a ignição por compressão homogênea de carga (HCCI). Com relação à injeção de combustível, ela pode ser interna ou externa à câmara de combustão. Para a preparação externa, há o

carburador, a injeção do corpo do acelerador (TBI), e os injetores para cada cilindro, conhecido como injeção no corpo de admissão (PFI). Para preparação interna, ela pode ocorrer de forma indireta (pré-câmara) ou diretamente. Com o foco em aplicações de escala automotiva de ignição por centelha, DI e PFI são os sistemas mais comuns. Dadas as razões citadas anteriormente, a predição de detonação tem maior interesse em aplicações DI. A predição de detonação pode ser feita por três grandes grupos de modelos: por correlações empíricas, cinética química e por fluidodinâmica computacional. Além disso, a modelagem de motores pode ser de uma zona 0D, multizona, quase-1D e multidimensional. A literatura mostra que o nível de detalhamento físico e químico do processo de detonação define a qualidade da caracterização da detonação. Para os modelos de detonação baseados em correlação, grande parte se baseia em tempo de atraso de ignição (IDT) e, dentro desse grupo, uma representação muito comum é via a integral de Livengood-Wu (L-W). Juntando esses fatores, tem-se grande flexibilidade, ao poder considerar expressões de Ahrrenius modificadas, para incluir mais efeitos além de temperatura no IDT. Entre os recentes avanços no campo de modelagem de detonação, destaca-se a aplicação de mais de uma integral de L-W por volume de controle em simulações, o uso de tabulação em pré-processamento, aplicação de funções de densidade de probabilidade assumidas (PDF), bem como diversos critérios de detecção do início da detonação. Além disso, modelos também propuseram o acoplamento de equações de transporte da combustão com equações de transporte da L-W como um escalar passivo. Com relação à forma de avaliação da detonação, há propostas de usar regiões localizadas na câmara de combustão e também quanto ao número de ciclos para considerar variações ciclo a ciclo, por se tratar de um fenômeno não estacionário e local. No contexto de correlações de IDT, por meio de experimentos e mecanismos cinéticos publicados, a revisão trouxe uma extensa lista para duas bases de dados, uma de álcoois primários de um a quatro carbonos e uma de combustíveis e substitutos relevantes à indústria de transporte (índice anti-detonação acima de 80), sendo a primeira utilizada para testar e validar a rotina automatizada a ser aplicada na segunda.

Materiais e Métodos

A correlação de IDT proposta envolve a linearização de uma expressão de Ahrrenius modificada, com dependências de pressão, temperatura, estequiometria e AKI. A partir de uma abordagem de regressão linear múltipla (MLR) via método de quadrados mínimos ordinário (OLS), uma base de dados de experimentos de IDTs publicados é submetida sucessivamente à rotina, removendo pontos com desvios acima de um limite a cada iteração. Esse limite é ajustado levemente a cada iteração, o qual se baseia no erro logarítmico. A forma de avaliação se dá não somente pelas sobrepredição e subpredição máximas, o erro absoluto médio e o coeficiente de determinação (R^2) mas também por uma comparação dos expoentes com os de correlações já publicadas. Para as simulações de IDT e velocidade de chama laminar, utiliza-se Cantera, via as abordagens de reator perfeitamente misturado a volume constante (CV-PSR) e chama laminar de propagação livre, respectivamente. Para o modelo de CRFD, que simula uma câmara de combustão de um motor DI a gasolina, a fundamentação mostra os modelos de combustão (modelo de chama coerente estendido de 3 zonas), turbulência ($k-\zeta-f$ e $k-\varepsilon$), de nebulização e injeção de combustível (modelo de gotículas discretas), de detonação (modelo Shell mais modelo TABKIN FGM aplicado à detonação) e demais modelos. Com relação aos ciclos simulados, eles se dividem em ciclos de validação com dados numéricos e ciclos de aplicação (usados para a análise a posteriori de detonação). Na validação com dados numéricos, dada a falta de dados experimentais para comparação ou de mais condições de operação conhecidas, as variações de RPM são pequenas o suficiente para não descaracterizar as condições de contorno originais mas grandes o suficiente para causar diferenças nos regimes de turbulência e avaliar

os efeitos na combustão. E, para os ciclos de aplicação, as condições são bem mais severas, para gerar o aparecimento de detonação em situações bem diferentes e maior abrangência do modelo. A respeito do modelo de predição de detonação, ele segue uma discretização numérica da integral de L-W, aplicada a 16 regiões esféricas de interesse, localizadas no plano do ponto morto superior, para a consequente extração de quantidades de interesse do CRFD para pós-processamento externo. A partir dessas quantidades, aplica-se à integral de L-W uma série de métodos, variando de mecanismos cinéticos a correlações de IDT propostas na literatura, para comparar com a correlação proposta por este projeto de pesquisa.

Resultados e Discussão

Os resultados podem ser divididos em diferentes fases para a construção do método de predição de início de detonação. Primeiramente, a rotina multivariada e automatizada proposta para obter a correlação IDT é validada usando o banco de dados de álcoois primários. Observou-se um desempenho estatístico muito forte, com sobrepredição e subpredição máximas de cerca de +25% e -20%, desvio absoluto médio de cerca de 10% e R^2 de 0.991. Os parâmetros físicos e químicos se mantiveram em forte concordância com a literatura, à exceção do expoente de AKI, que, por ser negativo, é considerado contraintuitivo (esperava-se que um maior AKI gerasse um maior IDT, logo, um expoente positivo). Para aprofundar o entendimento nesse resultado, a mesma base de dados foi aplicada a simulações de IDT em Cantera para dois mecanismos cinéticos detalhados diferentes, os quais geraram valores diferentes do expoente de AKI também. Por essa razão, é possível de dizer que esse é um resultado numérico resumido em uma única expressão mas que representa diversos combustíveis (e, consequentemente, diversos caminhos cinéticos), sob diferentes condições de operação. Por essa razão, e dado o forte desempenho nos demais quesitos avaliados, o expoente contraintuitivo pode ser fruto também de um número restrito de AKIs considerados (apenas 4). Em seguida, a rotina é aplicada ao banco de dados mais amplo, para combustíveis SI-ICE relevantes para o transporte. Para esse caso, o forte desempenho estatístico também se repete, com índices muito próximos, e R^2 em 0.987. Dessa vez, possivelmente por conta de haver mais AKIs diferentes, todos os expoentes analisados estão em forte concordância com a literatura. Na sequência, o modelo CRFD é validado, mostrando a influência dos modelos de turbulência na combustão, através de parâmetros tangíveis do motor e indicadores de combustão. Em resumo, o modelo de turbulência $k-\zeta-f$ foi capaz de capturar uma detonação numérica leve para a faixa de menor rotação, mostrando-se mais adequada que o modelo $k-\varepsilon$ para esta pesquisa. Em seguida, o modelo CRFD é aplicado a condições de motor mais severas, para extrair as grandezas de interesse, a serem aplicadas à rotina de pós-processamento externo para previsão de detonação. Finalmente, esses dados são usados para avaliar o IDT ao longo do ciclo por vários métodos. Em linhas gerais, nota-se que os IDTs previstos pelos mecanismos cinéticos são próximos entre si, e que uma das correlações anda muito próxima a eles, mas com uma péssima adesão após a ignição por centelha. Em seguida, quando calculadas as integrais de L-W para cada método de IDT, observa-se que mecanismos que sofrem com quedas bruscas na predição de IDT antes da ignição geram saltos fortes nas integrais, antecipando em muito a predição de início de detonação. Além disso, essa correlação que se desvincula das tendências dos mecanismos aponta um início de detonação muito antecipado para os ciclos mais intensos. Para as outras correlações, incluindo a proposta neste trabalho, nota-se que as integrais de L-W começam a subir mais tardiamente, mas dado o ritmo mais acelerado, produzem resultados similares aos mecanismos. Comparando essas predições com valores de referência para detonação, a saber, 1000 K e $\Omega_{1\%}$ (quantidade do modelo TABKIN FGM escolhida neste caso), nota-se que a 500 RPM a grande maioria dos resultados é muito antecipado pelas integrais de L-W. A 1000 RPM, essa diferença diminui, mas, dessa

vez, as duas melhores correlações já melhoram em muito seu desempenho. A 2000 RPM, há uma melhoria generalizada, tanto dos mecanismos quanto das correlações. A 4000 RPM, ainda existe uma certa predição dentro de margens boas, mas, dessa vez, com uma predição mais para o lado tardio e menos conservador.

Conclusão

Para a correlação de álcoois primários, os resultados tiveram boa adesão à literatura, exceto para o expoente contraintuitivo de AKI, que pode ser devido a uma combinação de fatores. Uma correlação IDT, independentemente do número de variáveis independentes, é uma equação matemática única e mais simples do que todas as informações fornecidas por um mecanismo detalhado. É uma representação muito conveniente, mas deve ser considerada juntamente com os intervalos de validade de cada variável e os tipos de combustível. Como ambos os mecanismos forneceram correlações consistentes, o expoente AKI pode ser devido ao número limitado de AKIs. Uma vez que o objetivo é incluir apenas biocombustíveis puros relevantes para o transporte, uma opção para aprofundar este trabalho é realizar simulações numéricas unidimensionais em ciclos de motores. Para os combustíveis SI-ICE e substitutos de combustível, há boa concordância com a literatura, pois, dessa vez, o expoente AKI foi positivo. Com relação à validação numérica do modelo CRFD, a influência do modelo de turbulência na ocorrência de detonação foi observada principalmente para a menor RPM. Os modelos de chama coerentes calculam a densidade da superfície da chama, que é afetada pela turbulência. Além disso, uma maior densidade da superfície da chama aumenta a velocidade turbulenta da chama, reduzindo o intervalo de queima. Os resultados sugeriram que $k-\varepsilon$ produziu menor intensidade de turbulência e, portanto, uma densidade de superfície de chama reduzida entre a ignição e o ponto morto superior. Assim, a mistura não queimada a menores níveis de pressão e temperatura teve um maior tempo de atraso de ignição. Por outro lado, $k-\zeta-f$ teve resultados opostos que levaram a uma leve detecção numérica de detonação. Por isso, o modelo final considerou $k-\zeta-f$ e ECFM-3Z (CFM estendido com 3 zonas). Além disso, para avaliar a detonação localmente, o modelo de detonação TABKIN FGM teve que ser adicionado junto ao modelo Knock Shell. Para os IDTs pós-processados obtidos das 16 esferas no plano TDC, os mecanismos apresentaram algumas flutuações na previsão do IDT. No entanto, essas flutuações afetam significativamente a integral L-W somente se forem mergulhos (quedas abruptas do IDT) nos momentos anteriores, geralmente em torno do tempo de ignição. Quando comparado com o critério de 1000 K como valor de referência de detonação, a 500 RPM, os métodos anteciparam muito o início da detonação. A 1000 RPM as margens são reduzidas e as correlações têm um melhor desempenho. A 2000 RPM, as correlações previram muito bem o início da detonação. A 4000 RPM, há uma previsão tardia generalizada, mas com margens consideravelmente menores do que a previsão inicial a 500 RPM. Especialmente a 2000 RPM, a correlação proposta previu a detonação conservativamente em 14 das 16 esferas.

Palavras-chave: Previsão de detonação. Tempo de atraso de ignição (IDT). Motores de combustão interna de ignição por faísca de injeção direta (DI-SI ICE). Integral de Livengood-Wu. Regressão linear múltipla (MLR).

LIST OF SYMBOLS

ACRONYMS

0D	Zero dimensional
1D	One dimensional
3D	Three dimensional
AAE	Average Absolute Error, %
AKI	Anti-Knock Index
ATcT	Active Thermochemical Tables
BSFC	Brake-Specific Fuel Consumption, g/kWh
CA	Crank-angle
CAD	Crank-angle degree; Computer Aided Design
CBD	Combustion Duration, CAD
CCRC	Clean Combustion Research Center
CCV	Cycle-to-Cycle Variation
CDS	Center Differentiation Scheme
CFD	Computational Fluid Dynamics
CFDM	Computational Fluid Dynamics Models
CFM	Coherent Flame Model
CI	Compression Ignition
CKM	Chemical Kinetics Models
CRECK	Chemical Reaction Engineering and Chemical Kinetics Lab
CRFD	Computational Reactive Fluid Dynamics
CV	Constant Volume
DDM	Discrete Droplet Model
DI	Direct Injection

DOI	Duration Of Injection, CAD
DRG	Directed Relation Graph
DRGEP	Directed Relation Graph with Error Propagation
DS	Differentiation Scheme
ECFM	Extended Coherent Flame Model
ECFM-3Z	Extended Coherent Flame Model 3 Zones
ECM	Empirical Correlation Models
EGR	Exhasut Gas Recirculation
EOI	End Of Injection, CAD
EVC	Exhaust Valve Closing, CAD
EVO	Exhaust Valve Opening, CAD
FEP	FAME Engine Plus
FGM	Flamelet Generated Manifold
FIT	Fuel Ignition Tester
FQ	Intermediate Species Q Mass Fraction, -
GDI	Gasoline Direct Injection
GGPR	Generalized Gas Phase Reactions
HCCI	Homogeneous Charge Compression Ignition
HPST	High Pressure Shock Tube
HTM	Hybrid Turbulence Model
ICE	Internal Combustion Engine
IDT	Ignition Delay Time, μs
IMEP	Indicated Mean Effective Pressure, bar
IQT	Ignition Quality Tester
IVC	Intake Valve Closing, CAD
IVO	Intake Valve Opening, CAD

KAUST	King Abdullah University of Science and Technology
KPI	Key Performance Indicator
KPV	Knock Progress Variable, -
KPV-PROB	Ignition probability, %
KSM	Knock Shell Model
LE	Logarithmic Error, -
LES	Large Eddy Simulation
LFS	Laminar Flame Speed, m/s
LPST	Low Pressure Shock Tube
L-W	Livengood-Wu
MFB	Mass Fraction Burnt, -
MLR	Multiple Linear Regression
MON	Motor Octane Number
NTC	Negative Temperature Coefficient
OLS	Ordinary Least Squares
ON	Octane Number
PCCI	Premixed Charge Compression Ignition
PDF	Presumed Distribution Function
PFI	Port Fuel Injection
PM	Particulate Matter
POLIMI	Politecnico di Milano
PRF	Primary Reference Fuel
PSR	Perfect Stirred Reactor
PV	Progress Variable, -
RANS	Reynolds-Averaged Navier-Stokes
RCCI	Reactivity Charge Compression Ignition

RCM	Rapid Compression Machine
RNG	Renormalization Group
ROHR	Rate Of Heat Release, J/CAD
RON	Research Octane Number
RPM	Rotation Per Minute
RSM	Reynolds-Stress Model
RVP	Reid Vapour Pressure
SI	Spark Ignition
SKM	Soot Kinetic Model
SOI	Start Of Injection, CAD
ST	Shock Tube
TBI	Throttle Body Injection
TDC	Top Dead Center
TPRF	Toluene Primary Reference Fuel
UHC	Unburnt hydrocarbon

VARIABLES

A	Pre-exponential factor
a	Pre-exponential factor converted to exponent in base 10
b	Exponent
C_m	Piston mean velocity, m/s
c	Exponent
$\tilde{c}$	Reaction Progress Variable, -
c_p	Specific heat at constant pressure, kJ/(kg.K)
c_k	Knock Progress Variable, -
d	Exponent

D	Generic Diffusion Coefficient, m^2/s
E	Mixing model source term
E_a	Global apparent activation energy, kJ/mol
F	Empirical function
f	Reversible function; elliptical relaxation function
G	Production/destruction term of k by body forces
h	Reversible function
I_P	Ignition probability, %
J	Diffusive flux, $kg/(m.s^2)$
k	Turbulent kinetic energy, m^2/s^2
L	Length scale, m
m_{I_P}	Total mass in regions where I_P is greater than the ε threshold, kg
N	Size of the database
p	Pressure, bar
P	Production term of k by mean-flow deformation
P_k	Turbulent kinetic energy production term
R	Universal gas constant, kJ/(mol.K)
Re	Reynolds Number, -
R^2	Coefficient of determination, -
S	Strain tensor; source term
Sc	Schmidt Number, -
T	Temperature, K; turbulent time scale, s
t	Time, s
u	Velocity, m/s
$\overline{v^2}$	Wall-normal velocity scale, m^2/s^2
V	Diffusive flux velocity, m/s

V_{I_P}	Total volume of regions where I_P is greater than the ε threshold, m^3
W	Molecular weight, kg/mol
x	Ignition carrier amplitude or concentration, -; x-coordinate, m
X	Molar Fraction, -
y	Height normal to the wall, m; y-coordinate, m
y^+	Non-dimensional wall distance, -
Y	Mass Fraction, -
z	z-coordinate, m
Z	Mixture Fraction, -

GREEK ALPHABET VARIABLES

ϕ	Fuel/Air equivalence ratio/Stoichiometry, -
ε	Turbulent kinetic energy dissipation m^2/s^3; threshold
λ	Thermal conductivity, W/(m.K)
τ	Ignition delay time, μs
ζ	Normalized wall-normal velocity scale, -
ν_t	Eddy viscosity, m^2/s
ρ	Density, kg/m^3
ω	Source term
Ω_{I_P}	Region where I_P is greater than the ε threshold

SUBSCRIPTS AND SUPERSCRIPTS

A	Unmixed air
actual	Actual experimental value
b	Burnt
c	Critical value
F	Unmixed fuel

Fu	Fuel
predict	Mathematically predicted value
M	Mixed air and fuel
m	Multicomponent
t	Turbulent
u	Unburnt
w	Wall
$\tilde{A}''^2$	Variance

LIST OF FIGURES

LIST OF TABLES

CONTENTS

1 INTRODUCTION

Fuel direct injection (DI) is not a new technology, but its importance has been increasing in recent developments of spark ignition (SI) internal combustion engines (ICE). The fuel is directly sprayed at high pressures in the cylinder, promoting a cooling effect, a higher engine compression, and a consequent efficiency increase (Bosch (49)). In essence, with the same compression ratio as in manifold or port fuel injection (PFI), the compression temperature and resultantly the knocking sensitivity would be reduced; however, this cooling effect is normally used to increase the compression ratio with the same knocking sensitivity (Merker; Schwarz; Teichmann (83)). In the automotive industry, the development of this and other ICE technologies is better assisted with computational reactive fluid dynamics (CRFD) simulations.

Irregular combustion comprises combustion processes in the SI engine that are not (or not exclusively) initiated by the spark ignition but rather by autoignition (Merker; Schwarz; Teichmann (83)). Knocking occurs after the regular ignition time, promoted by a secondary flame front initiated by mixture autoignition. The flame front initiated by the spark increases the pressure and temperature in the entire combustion chamber, including the unburnt mixture. In the case of knocking combustion, the flame front does not propagate quickly enough through the combustion chamber and autoignition of the unburnt mixture occurs before it arrives. The fresh mixture between the two flame fronts (the first one from the spark plug, and the second one from the mixture autoignition) can burn abruptly, generating pressure waves at high velocities (inherent of detonation combustion process) that reflect against the combustion chamber walls. These reflections lead to an acoustic resonance, which is the characteristic noise of knocking. But more importantly, these pressure amplitudes may be large enough to cause mechanical damage.

There are many factors that increase the likelihood and power of knocking combustion, such as high compression ratio, low engine speed, low octane number fuels and insufficient wall cooling. During bench tests, the engineers must identify irregular combustion events by using sensors which enable the localization of irregular ignition origins (Merker; Schwarz; Teichmann (83)). However, during numerical simulations, the identification is dependent upon the correct modeling and geometrical resolution, as it is a local phenomenon.

Combustion models are responsible for simulating species depletion and formation, ignition and combustion of fuel/air mixtures and their exhaust gases. Besides, the mean chemical reaction rates are usually non-linear functions dependent upon the local values of temperature and species concentrations and, therefore, are hard to determine. Detailed chemical kinetics mechanisms are currently computationally expensive due to the number of species and the consequent number of transport equations. On the other hand, a single-step irreversible reaction is too simple to represent the chemical kinetics related to hydrocarbon's combustion. Combustion models such as the Coherent Flame Models (CFM) balance much better this problem, with a

combination of more complex oxidation schemes, composed of some reaction steps and some equilibrium reactions (AVL (45)).

The CFM family assumes that the chemical time scales are much smaller than the turbulent ones, a plausible assumption for reciprocating ICEs. Thus, it is possible to apply a laminar flamelet approach, in which flame velocity and thickness are average values integrated along the flame front, only dependent on pressure, temperature, and stoichiometry of the unburnt gases (AVL (45)). As such, it decouples chemistry and turbulence; however, the variation on the turbulence model is expected to promote some changes in flow and chemical species fields, which influence the flamelet prediction and, therefore, the rate of heat release.

Regarding numerical simulations, the most complete representation of the combustion process in an ICE is represented by a 3D CRFD simulation of a cylinder, comprising not only the combustion chamber but also the gas exchange through the valves openings, the fuel injection, the spark occurrence and the cyclical movement of the piston. For spark ignition engines, the type of engine where knock becomes more relevant in transportation applications is the direct injection type, due to the reasons mentioned beforehand. Therefore, there is particular interest in predicting the knock onset numerically for DI-SI engines, which will be the focus of this research.

1.1 OBJECTIVES

The objective of the present research is to develop an indirect numerical knock prediction method to be used in internal combustion engine simulations using computational reactive fluid dynamics (CRFD), by applying an ignition delay time correlation obtained through a multivariate and automatized approach.

The specific objectives are as follows:

- Develop a multivariate and automatized approach to obtain an ignition delay time correlation as a function of pressure, temperature, equivalence ratio and anti-knock index and apply it to databases of published experiments of C_1 to C_4 primary alcohols and transportation relevant fuels;
- Propose a post-processing routine that extracts the local values of pressure, temperature and species concentrations on regions of interest of a gasoline direct injection spark ignition engine to apply to the Livengood-Wu integral based on chemical kinetics and IDT correlations.

1.2 DISSERTATION OUTLINE

This dissertation divides the research in three branches: the statistical model to obtain an ignition delay time correlation to be used in the computational reactive fluid dynamics (CRFD) model, the CRFD model itself, and the chemical kinetics simulations that complements the

investigations of the two other branches. The sections of the document are briefly described in sequence, to outline the main topics covered in each one.

In Section 2 (literature review), some background is given for internal combustion engines, in terms of ignition and fuel injection technologies. In the context of knocking combustion, there is first a brief definition of combustion events that may occur in spark ignition engines, prior to entering in a review of numerical knock models and knock prediction. There is particular interest in works that use the so-called Livengood-Wu integral. In sequence, there is a collection of data regarding ignition delay time (IDT) and laminar flame speed experiments, and chemical kinetics mechanisms for primary alcohols from one to four carbons and for relevant spark-ignition transportation fuels.

In Section 3 (materials and methods), the in-house Python routine developed to apply iteratively multiple linear regressions is described, for linearized modified Ahrrenius expressions to predict the ignition delay time. The chemical kinetics simulations held in Cantera are presented, showing the assumptions taken for both ignition delay time and laminar flame speed simulations. The CRFD model is then detailed, in terms of the physical modeling, the preprocessing setup, ranging from geometry, meshing, boundary conditions, solver setup. The proposed knock onset method to be used for post-processing is also described, with the regions within the computational domain from where flow and species quantities are extracted and how they are applied to Cantera and correlations to obtain the Livengood-Wu integral.

In Section 4 (results and discussion), the validation of the multivariate and automatized routine is shown towards the primary alcohols IDT database. After validating the results and comparing to other published correlations, the routine is applied to a broader database, of fuels relevant to the transportation industry and fuel surrogates. The correlation is discussed with other literature findings. In sequence, the CRFD model is validated, comparing the influence of different turbulence models on the combustion characterization for different engine speeds of a gasoline direct-injection simulation in AVL FIRE. After that, the model is simulated for more intense conditions to extract the flow quantities at the regions of interest, to be post-processed with different methods applied to the Livengood-Wu integrals. At last, the results are compared to a reference criterion and also to a knock-related quantity taken as a reference for the knock model.

In Section 5 (conclusion), the whole path to the development of the indirect knock prediction method is summarized, with the key findings of each section, ranging from the in-house Python routine and the proposed correlations, the CRFD model and the consequent post-processing approach that gathered the correlation, the CRFD model, and chemical kinetics simulations, with suggestions of possible future studies.

2 LITERATURE REVIEW

Prior to advancing to the CRFD simulation of the SI-DI engine, some background is given for ICE types and technologies. In the context of numerical simulations, there is some background to cover, ranging from zero-dimensional (0D) combustion simulations to three-dimensional computational reactive fluid dynamics (CFRD) simulations. This is relevant as each level of detail and formulation has its own limitations and applications in the industry, and how they influence on the knock study. The types of combustion events are described as well, to give room to the numerical knock modeling available in the literature.

The development of an ignition delay time (IDT) correlation is dependent upon experimental data. Since the scope of this research is not to perform IDT experiments, a database is constructed through a literature review on published experiments. Moreover, other IDT correlations are also listed to be compared with the one obtained in this work. Similarly, it is also not in the scope the realization of laminar flame speed experiments or the elaboration of detailed chemical kinetics mechanism. Thus, they are gathered from the literature as well. As it will be mentioned in Section 2.4, the development of an multivariate and automatized approach for obtaining an IDT correlation was first validated for a more restricted sample of fuel, namely C_1-C_4 primary alcohols (methanol, ethanol, *n*-propanol, and *n*-butanol). After this validation, the broader range of fuels concerns SI-ICE transportation fuels, surrogates and biofuels.

2.1 INTERNAL COMBUSTION ENGINES

Internal combustion engines can be categorized by several ways, such as the mechanism to produce rotation, the ignition type, the injection type, and the thermodynamic cycle. To restrict the scope of the description, in order to be relevant to the automotive industry, only reciprocating applications are listed (Wankel, gas turbines, rocket motor excluded), and there is no distinction on the number of strokes or thermodynamic cycle. Thus, only ignition and injection technologies for reciprocating engines are mentioned, always with a focus on spark ignition engines.

2.1.1 Ignition technologies

In essence, there are currently only two main commercial-wise ignition technologies, spark and compression ignition (SI and CI, respectively) ICEs. A third strategy that is under research since 1989 is the homogeneous charge compression ignition (HCCI). Similarly, researches on premixed and reactivity CCI (PCCI and RCCI) started on 2010 onwards, but all still lacking large scale production (Paykani et al. (94)). Table 1 brings a summary of the three main technologies, while Fig. 1 depicts the ignition in three schematic combustion chambers.

Table 1 – Comparison of SI, CI, HCCI engine characteristics. Adapted from Paykani et al. (94).

	SI	CI	HCCI
Ignition type	Spark ignited	Compression ignited	
Fuel type	High octane	High cetane	Blend of every liquid or gaseous fuel
Power output control	Airflow control, with near stoichiometric air–fuel ratio	Fuel flow control, with lean air–fuel ratio	Fuel flow control, typically with lean air–fuel ratio or charge dilution
Mechanism controlling fuel burning rate	Flame propagation speed	Time for fuel vaporization and mixing	Chemical kinetics
Emission characteristics	Cleaner with three-way catalyst and higher CO_2	Higher PM and NO_x (without after-treatment) and lower CO_2	Higher UHC and CO and lower NO_x

SI: spark ignited; CI: compression ignition; HCCI: homogeneous charge compression ignition.
PM: particulate matter; UHC: unburned hydrocarbon.

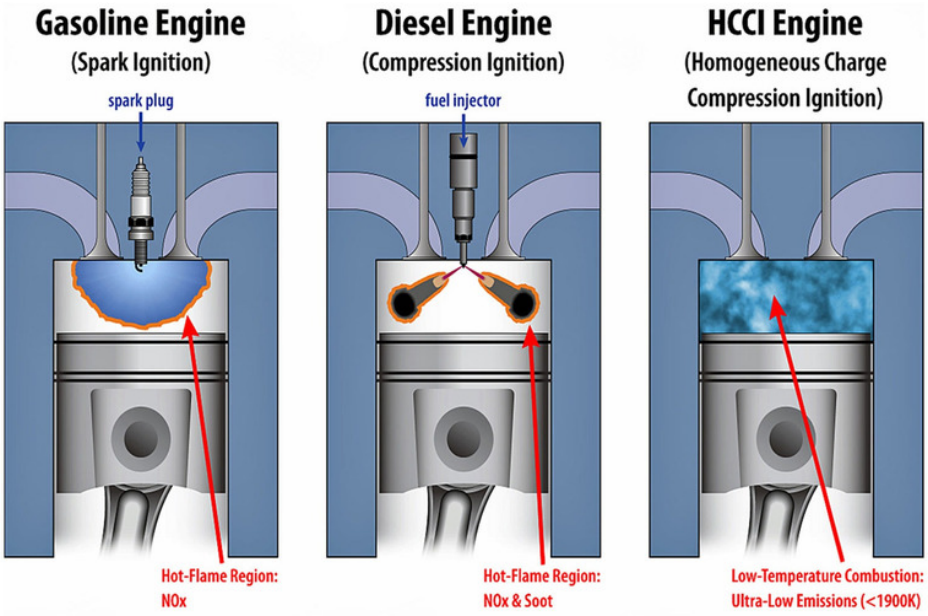

Figure 1 – Schematics representation of the ignition in SI, CI, HCCI engines (Pitz; Westbrook (99)).

2.1.2 Fuel injection technologies

The fuel injection system is responsible for mixture formation. It can happen inside or before the combustion chamber. Regarding external mixture preparation, the carburettor is an older technology, already in disuse for passenger cars. In short, it follows the Bernoulli principle, through a venturi pipe where the air flows at a higher speed and draws a certain amount of fuel due to the lower static pressure of the mainstream, and a throttle valve regulates the flow rate to the intake. The manifold injection may use a fuel injector for all cylinders, known as throttle body injection (TBI), or injectors for each cylinder, known as port-fuel injection (PFI) (M. Sharma (115)). Figure 2 shows the schematic views of a carburettor's cross-section and of a PFI engine.

For internal mixture preparation, it can happen indirectly (in a swirl/prechamber), where fuel injector and spark plug are placed on a smaller chamber, or directly, the so-called direct injection (DI). On top of that, DI can be via common rail feeders and unit injectors. Figure 2 shows the schematic views of a prechamber, swirl-chamber and direct injection (DI).

Since the focus is on SI-ICE automotive scale applications, DI and PFI are the most common systems. For DI, the fuel is directly sprayed at high pressures in the cylinder, promoting a cooling effect, a higher engine compression, and a consequent efficiency and torque increase, with less consumption (Bosch (49)). In essence, with the same compression ratio as in PFI, the compression temperature and resultantly the knocking sensitivity would be reduced; however, this cooling effect is normally used to increase the compression ratio with the same knocking sensitivity (Merker; Schwarz; Teichmann (83)). Also, both systems can be combined, as PFI has lower friction losses in partial-load cycles, and has a good mixture homogenization, with

less particle emission.

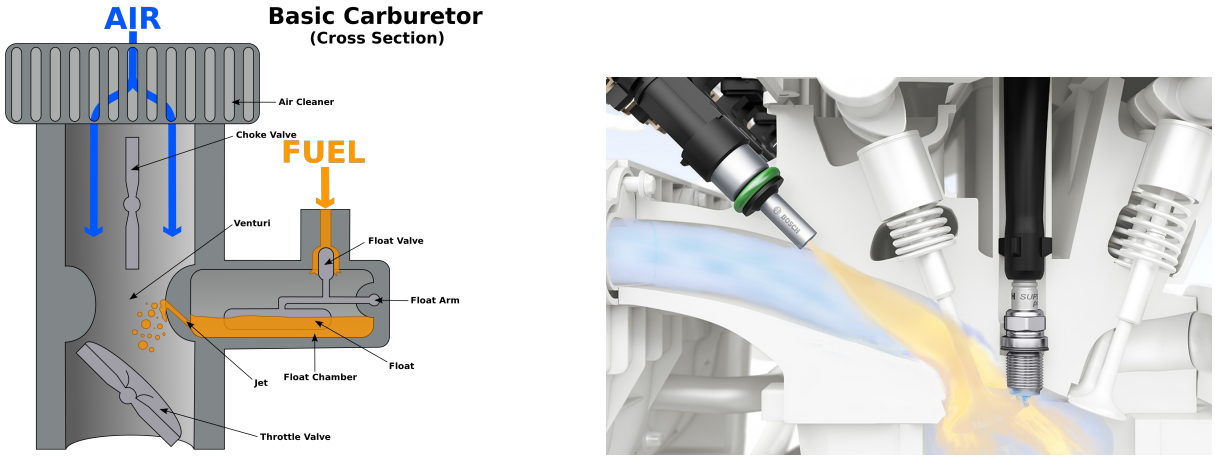

(a) Carburetor (18). (b) Port-fuel injection (PFI) (50).

Figure 2 – External mixture preparation technologies.

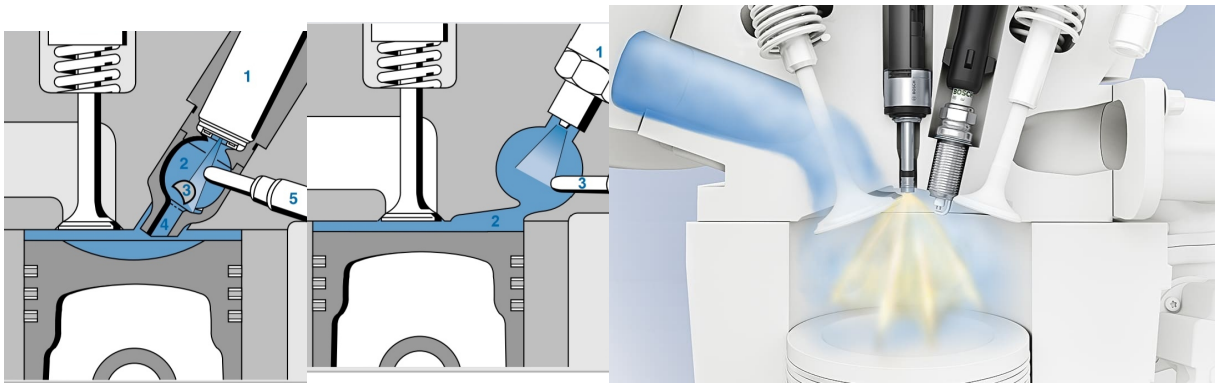

(a) Prechamber (128). (b) Swirl chamber (128). (c) Direct injection (DI) (49).

Figure 3 – Internal mixture preparation technologies.

2.2 IRREGULAR SI COMBUSTION EVENTS

Irregular combustion in a SI engine are not (or not exclusively) initiated by the spark but rather by autoignition (Merker; Schwarz; Teichmann (83)). Knocking is an autoignition combustion that occurs after the regular ignition time. Combustion is fast but not instantaneous. The flame front initiated by the spark increases the pressure and temperature in the entire combustion chamber, including the unburned mixture. In the case of knocking combustion, the flame front does not propagate quickly enough through the combustion chamber and autoignition of the unburned mixture occurs before it arrives. The fresh mixture in this area can burn abruptly, generating pressure waves that reflect against the combustion chamber walls. These reflections lead to an acoustic resonance, which is the characteristic noise of knocking. But more importantly, these pressure amplitudes may be large enough to cause mechanical damage.

Knocking might be aggravated by high compression ratio, low speed, high load, poor octane rating fuel, miss-designed chambers, and hot spots. This abnormal event limits the spark advance, which ultimately restricts efficiency, power density, durability, driveability and acoustic comfort (Merker; Schwarz; Teichmann (83)).

Other irregular combustion phenomena, which instead occur before the regular ignition time, are preignition and glow ignition. While preignition is more sporadic and vanishes after some cycles, glow ignition gets self-reinforced through cycles. They can be caused by remaining carbonaceous deposits detached due to pressure or hot spots (Merker; Schwarz; Teichmann (83)).

2.3 NUMERICAL KNOCK MODELING AND KNOCK PREDICTION

2.3.1 Knock and engine models classification

N. Sharma (116) divides the knock prediction methods into three categories: empirical correlation models (ECMs), chemical kinetics models (CKMs), and computational fluid dynamics models (CFDMs). The ECMs use empirical correlations obtained by tuning experimental data. As such, they can be tuned for any engine, as long as they are independent of the geometry. Besides, these correlations can either use chemical kinetics fundamentals, thermodynamic and physical parameters or pure mathematics and curve fitting. The CKMs use chemical mechanisms to evaluate the reactants and products compositions. The CFDMs solve the governing equations and add the combustion modeling to this representation, in order to capture the knock quantities of interest.

Moses; Yarin; Bar-Yoseph (89) divide the spark ignition engine models into four categories: single-zone 0D, multizone, quasi-1D and multidimensional. 0D (or thermodynamic) models consider temperature, pressure and species concentrations disregarding the flow field. Merker; Schwarz; Teichmann (83) add that they normally require empirical combustion models, and treat every point in time as ideally mixed. Multizone models divide the combustion chamber into burnt and unburnt regions with different temperature and composition, but within each region the flow field is disregarded, to be treated as 0D. The quasi-1D (or phenomenological) models add the flow field influence, but without transversal variation. Finally, the multidimensional (CFD/CRFD) models consider the flow and turbulence, with correspondent governing equations and more complete models.

In their literature review, Moses; Yarin; Bar-Yoseph (89) show that single-zone 0D SI engine models can have good results in knock prediction when coupled with detailed chemical kinetics. On the other hand, for multidimensional models, there might be still some dependency upon (semi)-empirical terms to close the problem with respect to turbulence. Also, these terms are usually determined for non-reactive flows, and do not account for the interaction between turbulence and flame propagation or heat release. Therefore, the good knock models are more tightly related to their definitions, rather than to the complexity of the SI engine models.

2.3.2 Livengood-Wu integral

Regarding empirical correlation models (ECMs), most methods predict knock onset based on the ignition delay time (IDT) (N. Sharma (116)). Within this group, a common representation is via the Livengood-Wu integral, proposed in Livengood; Wu (78), as known as the knock integral method. In essence, the Livengood-Wu (L-W) integral is a knock onset parameter which points to the occurrence of the phenomenon and not its severity/intensity.

Livengood; Wu (78) details the whole deduction of the method, but their integral essentially describes the advancement of a specific mixture towards ignition, as the cumulative contribution of the instantaneous ignition delay time (IDT) along time

$$\frac{x(t)}{x(\tau)} = \int_{t=0}^{t} F\left(\frac{t}{\tau}\right) \mathrm{d}t \tag{1}$$

where x represents the concentration (or the amplitude) of an ignition carrier (a variable or quantity which increases in concentration or amplitude during ignition, e.g. CO mass fraction or heat release), t is the time, τ is the IDT, and F is an empirical function.

Khaled; Badra; Farooq (67) facilitates the interpretation of this mathematical operator. Their deduction is presented in sequence. The physical interpretation of the L-W integral is that the amplitude of ignition carriers (x) can only increase towards its critical value (x_c) at ignition, where x could be heat release or CO mass fraction, for instance. Thus

$$\frac{x}{x_c} = f\left(\frac{t}{\tau}\right) \tag{2}$$

where f increases, bounded by $f(0) = 0$, $f(1) = 1$. This way, it is a reversible function, and this expression can be rewritten as

$$h\left(\frac{x}{x_c}\right) = \frac{t}{\tau} \tag{3}$$

where h is also increasing and bounded by the same values.

The IDT is not primarily time-dependent but it is rather a function of pressure and temperature, which in turn are function of time. Assuming that they are constant from t to $t + \mathrm{d}t$, the IDT is also constant in this range, so the time derivation of the expression above results in

$$\frac{\mathrm{d}}{\mathrm{d}t}\left[h\left(\frac{x}{x_c}\right)\right] = \frac{1}{\tau} \tag{4}$$

where its integration leads to

$$h\left(\frac{x(t)}{x_c(\tau)}\right) = \int_0^t \frac{1}{\tau}\,\mathrm{d}t \tag{5}$$

Finally, for $t = \tau$, $x = x_c$, and $h(x/x_c) = h(1) = 1$, which leads to the final form of the L-W integral, showing the cumulative contribution that the instantaneous IDT has towards autoignition (usually defined when the integral reaches unity)

$$L - W = \int_0^t \frac{1}{\tau} \mathrm{d}t \tag{6}$$

By following this condensed deduction described in more details in Khaled; Badra; Farooq (67), the order of kinetics did not have to be assumed. By the original deduction, Livengood; Wu (78) had to assume a zeroth order such that F becomes constant. Even prior to this generalization demonstration, it should be noted that the L-W was already successful in combustion, when most reactions generally have non-zeroth order.

For DI engines, due the high pressures during fuel injection, the knock is already a concern from the start of ignition (SOI), as the fuel might autoignite, thus $t_0 = t_{SOI}$. For PFI engines, this moment can be either the spark occurrence or the start of compression, for more conservative estimates. In addition, in most cases the knock onset is defined by when the L-W integral reaches a critical unity value, except when some calibration is performed.

According to Kozarac et al. (69), the L-W integral also has the flexibility to regard one or more Ahrrenius-like expressions, accounting for temperature, pressure, equivalence ratio, exhaust gas recirculation (EGR) and other variables. In addition, look-up tables based on detailed mechanisms can speed up the calculation, by running prior to the 0D simulation, which makes this operator widely used.

2.3.3 Recent progress in knock onset models and applications

As proposed by Kozarac et al. (69), the knock model should include flame propagation and detailed chemical kinetics in the unburned cells, and it should allow cycle-to-cycle variation (CCV). However, this makes the model too computationally demanding, and simplifications must be done, in order to make it affordable, such as reduced mechanisms (e.g. the Knock Shell Model, Halstead; Kirsch; Quinn (52)). In their model, Kozarac et al. (69) used two detailed mechanisms to evaluate both low and high temperature regimes for constant volume reactor IDT simulations, leading to two L-W integrals. They were considered critical at 0.95 due to calibration with the mechanisms. The model also accounted for CCV for temperature stratification by subdividing the unburnt region in zones with the same mass. Four different engines and 15 engines conditions were modeled in 3D CRFD (AVL FIRE, RANS, $k-\varepsilon$ turbulence, ECFM-3Z combustion, with up to 1.2 million cells, approximately) and led to a presumed probability distribution function (PDF). For this part of the work, cells with the progress variable above 0.1 were taken as burnt due to the temperature increase, which matches the threshold used by Moses; Yarin; Bar-Yoseph (89).

Kalghatgi; Babiker; Badra (63) use the L-W integral as well. Their correlation is tailored for a TPRF with a specific RON/MON of a commercial gasoline. It had good results, missing the knock onset by roughly ± 1.5 CAD, when compared to experiments. Overall, for engine applications, it proved to be adequate above 1000 RPM cycles, as it ignored low pressure and temperature chemistry.

Besides, for engine applications, Tao; Han; P. Zhao (119) argue that the engine speed constraints the residence time allowed for both combustion and autoignition, and it is valuable to assess the L-W integral performance under different rotations.

Commercially, in AVL BOOST, an 1D engine simulation software, the knock model is based on the L-W integral, with the IDT predicted by the correlation of Douaud; Eyzat (27), as shown in Section 2.6.1. However, the model is stated as currently valid only for external mixture preparation gasoline engines (AVL (42)).

Regarding correlations and other IDT calculation methods applied to the L-W integral, N. Sharma (116) presented an extensive work. The models based on the Ahrrenius function tend to estimate lower IDT compared to chemical kinetics models. However, the models from both the categories had weak agreement with the experiments and yielded knock in no knocking situations.

Yue; Som (130) proposed a transported L-W integral for CRFD. In essence, as a passive progress variable, there is no feedback to the flow field, and the temperature increases locally due to flame propagation and not autoignition. It captures autoignition in the unburnt region and is coupled with the G-equation (a scalar field equation which describes the instantaneous flame position), which captures the turbulent premixed combustion. The model has been validated in homogeneous charge compression ignition (HCCI) simulations, and applied in sequence for direct-injection spark-ignition (DI-SI) CRFD simulations. Besides, the source term is calculated beforehand in an 0D solver and translated into a look-up table, also considering sub-grid fluctuations of temperature and equivalence ratio. Overall, the method was found to be ten times more efficient than methods based on pressure oscillation and detailed kinetics (Yue et al. (131)). Furthermore, the end-gas temperature is taken as the mean among 16 points located along the cylinder liner and 1 mm below the cylinder head. By doing so, they observed that this average end-gas temperature is lower than the mean in-cylinder temperature, especially at higher loads and longer injections. Thus, there is some thermal stratification due to spray wall impingement and heat loss. Also concerning fluctuations, it was found that CCV required eight cycles to reduce the fluctuations (plus one for initialization). However, they are less intense than in experiments due to the nature of the RANS formulation (closed by $k-\varepsilon$ RNG) and the mesh resolution (2 mm, 1 mm within cylinder, 0.5 mm near walls, and 0.25 mm near the spark plug, with up to 1.2 million cells), and primarily attributed to near-spark-plug variations at spark. Also, the use of end-gas temperature allows to analyze the thermodynamic state beyond spark discharge, which is an experimental limitation.

Later on, in Yue et al. (131), they extended the L-W integral transport equation from single-stage ignition to two-stage ignition processes to broaden the range of valid fuels.

And more recently, Cho et al. (20) presented a novel technique for knock onset, where a 0D model was improved via supervised machine learning.

2.4 C_1-C_4 PRIMARY ALCOHOLS (NARROW DATABASE)

The choice for this restricted sample has also the current appeal for biofuels. Even though electrification is increasing its share in the automotive industry, the use of internal combustion engines (ICEs) still receives a lot of attention to become cleaner, more efficient and more powerful. Biofuels are interesting alternatives as fuels or fuel additives due to the high energy density and lower associated fuelling and distribution infrastructure costs compared to hydrogen and electrification (Vancoillie et al. (123)).

Alcohols have high knock resistance and octane rating. As such, they reduce the ignition likelihood and enable spark ignition (SI) ICEs to operate at higher compression ratios and produce higher power output without knocking (Gautam; Martin; Carder (40)). While the lower alcohols (methanol and ethanol) provide the octane improvement, the higher alcohols (propanol, butanol and pentanol) provide water tolerance, volatility control and lower Reid vapor pressure (RVP) (Gautam; Martin; Carder (40)). Alcohols with five or more carbons have octane ratings lower than that of gasoline and, therefore, would reduce the knock resistance of SI engine fuels. On the other hand, a decreased octane number correlates with an increased cetane number (i.e. greater propensity for ignition), which makes them suitable for compression ignition (CI) engine applications (S. M. Sarathy et al. (108)).

Methanol can be employed in flex-fuel and dedicated engines to increase efficiency and reduce NO_x and CO_2 emissions. As a lower alcohol, the elevated knock resistance can be partly understood due to the considerable cooling effect. Besides, this opens opportunities for increased power and efficiency by applying higher compression ratios, optimal spark timing and aggressive downsizing. Additionally, methanol is less hazardous than gasoline in terms of fire safety and, therefore, it is used in some SI racing engines in the USA (Vancoillie et al. (123)).

Ethanol is probably the most researched and most used biofuel in the world. Its potential as an ICE fuel has been recognized for more than a century. Brazil is one of the largest ethanol producers and it is where the first mass-production car (in the modern automotive era) capable of running on neat ethanol was launched in 1979 and where the first flex-fuelled (ethanol/gasoline) car was launched in 2003 (Pearson; Turner (95)).

Propanol (*n*-propanol and *i*-propanol) is more expensive to produce than gasoline and its energy density is not much higher than that of ethanol and is much lower compared to butanol. However, it is suitable to use in alcohol mixtures (Scully; Orlygsson (111)); it is less toxic and less volatile than methanol, convenient properties for a fuel (Minteer (86)).

Butanol (*n*-butanol, 2-butanol, *t*-butanol and *i*-butanol) has a higher energy density and lower vapor pressure than ethanol, which makes it more attractive as fuel or blending agent (Van Ree et al. (121)). Frequently, it can replace gasoline with no modifications. In several tests, the consumption is similar to that of gasoline, and when blended with gasoline, it provides better performance and corrosion resistance than that of ethanol or E85 (Bhatia (9)). However, it is relatively costly to product (Ayas (4)).

Table 2 shows the motor octane number (MON), the research octane number (RON), and the anti-knock index (AKI, defined as the mean between MON and RON), for $C_1 - C_4$ primary alcohols.

Table 2 – Octane ratings for primary alcohols

Fuel	MON	RON	AKI	Ref.
Methanol	93	122	107.5	(70)
Ethanol	90	109	99.5	(60)
n-Propanol	89	104	96.5	(103)
n-Butanol	85	98	91.5	(103)

2.5 SI-ICE RELEVANT FUELS FOR THE TRANSPORTATION INDUSTRY (BROAD DATABASE)

To be considered relevant for the transportation industry, in this research, the fuel has to be liquid, economically affordable, with large availability, and an octane rating compatible with spark ignition engines. Or they can be fuel surrogates with the same characteristics. As a minimum, the fuels are restricted to an anti-knock index (AKI) above 80, although all off them are above 83.4, apart from primary reference fuel 80 (PRF 80). Due to the reasons above, fuels and blends with methanol, propanol and butanol isomers are all disregarded. Table 3 shows the fuels, their octane numbers, and the reference from where these values are taken. Naser; S. M. Sarathy; Chung (90) bring a vast collection of data and was the go-to reference to get an AKI/RON/MON reference when papers did not bring this information.

2.6 IGNITION DELAY TIME CORRELATIONS

Concerning knock, the ignition delay time (IDT) is arguably the main quantity of interest. The IDT is the time required for autoignition to happen once the fuel/air mixture is raised to a given pressure and temperature and held at that condition in a rapid compression machine (RCM) or a high pressure shock tube (HPST) (Herzler et al. (57)). Davidson; Hanson (26) argue that the IDT measurement uses many markers, such as pressure rise, CH* and OH*, and very too much in terms of the thermodynamic and mixture conditions. Therefore, it is not surprising to miss IDT by an order of magnitude. However, correlations can still give a fair approximation even outside its validity range. The study is also necessary as it is more affordable to embed correlations in reactive flow software than chemical kinetics mechanisms. Besides, they guide the choice of the experimental conditions to characterize a particular fuel, and can compare different findings as well.

Table 3 – Octane ratings SI relavant fuels and surrogates

Fuel	MON	RON	AKI	Ref.
BR1	89.5	101.5	95.5	(17)
Coryton	86.6	97.5	92.05	(72)
E85	89	104	96.5	(23)
Ethanol	90	109	99.5	(60)
Ethanol/isoctane (25/75% vol.)	101	109	105	(15)
FACE A	83.6	83.5	83.55	(109)
FACE C	83.6	84.7	84.15	(109)
FACE F	88.8	94.4	91.6	(64)
FGF-KAUST	88.9	93.6	91.5	(19)
FGF-LLNL	89.5	93.8	91.6	(19)
Gasoline surrogate	84.7	90.3	87.5	(23)
Haltermann	83.4	91	87.2	(72)
KM9096	88	97.9	92.95	(38)
LLNL surrogate	83	91	87	(71)
PR6918	87.9	98	92.95	(38)
PRF 80	80	80	80	-
PRF 84	84	84	84	-
PRF 90	90	90	90	-
PRF 91	91	91	91	-
PRF 91.5	91.5	91.5	91.5	-
PRF 95	95	95	95	-
PRF 100	100	100	100	-
Quinary mixture[1]	86.7	95.1	90.9	(15)
RD387	-	-	87	(41)
RON95E10	85.2	96.5	90.85	(13)
Stanford surrogate A	84	89	86.5	(71)
Surrogate A	-	-	98.75	(14)
Surrogate A TPRF	83.32	87.18	85.25	(41)
Surrogate B TPRF	82.78	85.57	84.18	(41)
Toluene	102.2	116.3	109.25	
TPRF 87[2]	-	-	87	-
TPRF F	89.1	94.4	91.8	(64)
TPRF toluene/isoctane (10/90% vol.)	98.52	100.59	99.56	(54)

[1] Isoctane/toluene/*n*-heptane/di-iso-butylene/ethanol (30/25/22/13/10% volume)

[2] 56% isoctane, 17% *n*-heptane, 27% toluene in mole

In this context, the Arrhenius expression is the simplest mathematical equation used to predict the IDT

$$IDT = A \exp\left(\frac{-E_a}{RT}\right) \tag{7}$$

where A is the pre-exponential factor, E_a the global apparent activation energy, R the universal gas constant and T the temperature.

Since it only establishes a dependency with temperature, the so-called modified Arrhenius

expressions are more complete relations as they might include the effects of pressure, equivalence ratio, anti-knock index, molar concentrations. For instance, the modified Arrhenius expression including the first three variables of this enumeration, which will be the focus of this research, is

$$IDT = A \exp\left(\frac{-E_a}{RT}\right) AKI^b \, p^c \, \phi^d \tag{8}$$

where AKI is the anti-knock index, p the pressure, ϕ the equivalence ratio and b, c, d their dependency exponents, respectively. Note that throughout the present paper, IDT is represented in μs, E_a in kJ/mol, pressure in bar and R in kJ/(mol.K). Besides, the pre-exponent factor A is represented as 10^a, following the format of some papers L. Cancino et al. (17, 15, 16).

Note that the additional parameters can be measured on the test gigs and by knowing the fuel composition. In order to obtain more easily a mathematical correlation, this multi-exponential form of Eq. 8 can be linearized by applying the natural logarithm on both sides

$$\ln IDT = \ln A - \left(\frac{E_a}{RT}\right) + b \ln AKI + c \ln p + d \ln \phi \tag{9}$$

This way, a multiple linear regression (MLR) can be applied to this linearized form. Sundberg (118) proved this linearization to be preferred to non-linear methods. This strategy was also reported by L. Cancino et al. (17) to predict the IDT of an ethanol-containing gasoline surrogate

$$IDT = 10^{-4.92 \pm 0.47} \exp\left(\frac{109 \pm 1.32}{RT}\right) AKI^{1.11 \pm 0.24} \tag{10}$$

reaching a coefficient of determination $R^2 \approx 0.99$, from 915 K to 1225 K, AKI from 83.5 to 95.5, scaling the data to 30 bar and stoichiometry.

L. R. Cancino et al. (15) obtained two correlations in their work. The first one for a binary mixture of ethanol and *i*-octane (25%/75% in liquid volume with RON/MON of 109/101 - or an AKI of 105)

$$IDT = 10^{-3.7 \pm 1.2} \exp\left(\frac{124.8 \pm 23.7}{RT}\right) \tag{11}$$

valid from 980 to 1200 K and at 30 bar, and another for a quinary mixture of *i*-octane, toluene, *n*-heptane, di-*i*-butylene and ethanol (30%/25%/22%/13%/10% in liquid volume with RON/MON of 95.1/86.7 - or an AKI of 90.9), for the same temperature range

$$IDT = 10^{-1.1 \pm 0.81} \exp\left(\frac{101 \pm 14.3}{RT}\right) p^{-1.05 \pm 0.3} \tag{12}$$

L. R. Cancino et al. (16) obtained a regression for ethanol

$$IDT = 10^{-3.21 \pm 0.46} \exp\left(\frac{139.3 \pm 9.2}{RT}\right) p^{-0.88 \pm 0.1} \tag{13}$$

for a temperature range from 990 K to 1200 K. The authors evaluated E_a from the CH* emissions. In comparison, they cite that Dunphy; Simmie (33) obtained 122.8, 129.2, and 141.0 kJ/mol derived from the OH*, CO2*, and pressure methods, respectively, for pressures from

1.0 to 4.6 bar and temperatures from 1300 to 1700 K. The authors also highlight that E_a shifts to approximately 75 kJ/mol at approximately 950 K, in accordance with other experiments with different fuels. In the end, at 10 bar and below 1000 K, their model over-predicts the ignition delay times. However, their model shows good agreement with the experimental results in terms of E_a (an 8% deviation was obtained). Besides this experimental fit, they also proposed a numerical model

$$IDT = 10^{-3.79\pm0.06} \exp\left(\frac{151.6 \pm 1.1}{RT}\right) p^{-0.89\pm0.1} \tag{14}$$

for a temperature range from 990 K to 1200 K.

Du et al. (28) obtained two correlations for E92 ethanol/gasoline mixture dependent upon equivalence ratio

$$IDT = 10^{-2.09} \exp\left(\frac{124}{RT}\right) \phi^{1.56} \tag{15}$$

this one valid for 2.8 bar, from 1100 K to 1800 K and

$$IDT = 10^{-3.62} \exp\left(\frac{145}{RT}\right) \phi^{1.60} \tag{16}$$

valid for 5.6 bar, from 1100 K to 1800 K. In addition, their third correlation fitted the data to stoichiometry to show a dependency upon pressure

$$IDT = 10^{-3.30} \exp\left(\frac{124}{RT}\right) p^{-1.76} \tag{17}$$

Ma et al. (79) published a follow-up study of Du et al. (28) and reports Equation 15 once again for E92 (in this case, rounding the pressure to 3 bar) and the following one for neat ethanol

$$IDT = 10^{-2.73} \exp\left(\frac{137}{RT}\right) \phi^{1.49} \tag{18}$$

for 3 bar, from 1100 K to 1800 K.

Cooper et al. (23) published a correlation for gasoline surrogate and its blends with oxygenated fuels (up to E85). In order to represent it in the same way as the previous ones, with the pre-exponential factor converted to 10^a and E_a to kJ/mol (converting $R = 1.987 \times 10^{-3}$ kcal/(mol.K), used by the referred author, to $R = 8.314 \times 10^{-3}$ kJ/(mol.K), used in this research), their correlation becomes

$$IDT = 10^{-2.09} \exp\left(\frac{124.23}{RT}\right) p^{-0.880} \phi^{-0.283} \tag{19}$$

and yielded a R^2 of 0.96, for temperature from 968 K to 1361 K, pressure from 4 to 50 bar and equivalence ratio from 0.5 to 1.0. Also, the R^2 increases to 0.99 for fits for each pressure condition, indicating the repeatability of the experiments. Furthermore, the authors developed another correlation for their compilation of experiments

$$IDT = 10^{-1.38} \exp\left(\frac{110.9}{RT}\right) p^{-0.989} \phi^{-0.577} \tag{20}$$

that yielded a R^2 of 0.91, for AKI above 84, for data within the linear regime on the plot, which excluded most RCM data and values above 2000 μs. In addition, low-pressure data were excluded due to their contribution to the error. The resulting data set includes 573 experiments ranging from 859 K to 1386 K, up to approximately 120 bar and equivalence ratios from 0.3 to 2.1.

Shariatmadar; Pakdehi; Zarei (114) brings a literature review which gathered around twenty IDT correlations, but out of the scope here, since they mostly deal with exponents for number of carbons and fuel and oxidizer mole fractions, and for methane, butane, *n*-heptane, *n*-decane, kerosene, Jet-A and ethylene.

It is also worth mentioning that more sophisticated approaches can yield an IDT correlation. Khaled; Farooq (68) proposed a high-temperature universal IDT correlation, which comes from an harmonic mean of the IDTs of individual components in a multicomponent surrogate, based on the Livengood-Wu integral, following composition and thermodynamic constraints. On top of that, the ϕ exponent is dependent upon $1/T$ too.

2.6.1 Correlations used in commercial software

Concerning 3D computational fluid dynamics (CFD) and 1D engine simulation software, there are some examples of commercial packages that have built-in knock models. ANSYS Fluent 2021R1 (3) knock model in SI engines has two options. The first one is the vastly tested correlation developed by Douaud; Eyzat (27)

$$IDT = 0.01768 \left(\frac{ON}{100}\right)^{3.402} p^{-1.7} \exp\left(\frac{3800}{T}\right) \tag{21}$$

where, in this case, IDT is expressed here in seconds, ON is the octane number of the fuel, p is the absolute pressure in atmospheres and T is the temperature in Kelvin.

Note that this correlation is also used in AVL BOOST 2021R1 (42) and in AVL CRUISE M 2021R1 (43), 1D engine simulation tools, applied via the Livengood-Wu integral criterion, as previously mentioned. Furthermore, the octane number can be isolated in the equation to calculate the minimum ON for a knock free operation in external mixture preparation gasoline engines. In short, this is done by limiting the L-W integral from the start of combustion to the time when 85% of the mass fraction is burnt. BOOST and CRUISE M also allow the user to change the constants/exponents accordingly, but recommend tuning the model by changing the pre-exponential factor (A).

In addition, this correlation is also used in AVL FIRE, the 3D CRFD tool from AVL AST, under the name of AnB knock model, referring to the the constants/exponents of the model (pre-exponential factor, pressure exponent and activation temperature). However, in this case, ON is pointed as the research octane number (RON).

The second expression available in ANSYS Fluent is a generalized expression, which can

reproduce many existing Arrhenius correlations, and has the following form

$$IDT = A\left(\frac{ON}{100}\right)^{a} p^{b} T^{c} RPM^{d} \phi^{e} \exp\left(\frac{-E_a}{RT}\right) \tag{22}$$

where A is the pre-exponential factor with units in seconds and RPM is the engine speed in cycles per minute.

2.7 PUBLISHED COMBUSTION EXPERIMENTS

2.7.1 Ignition delay time

The data gathered in this review involves experiments done in high/low pressure shock tube (HPST/LPST), rapid compression machine (RCM), ignition quality tester (IQT) and fuel ignition tester (FIT). However, the IQT and FIT points will be disregarded for the database composition as they cannot isolate the kinetics effects from the thermo-fluid-dynamic effects (atomization, vaporization, mixing), masking the contribution of the autoignition stage.

2.7.1.1 Primary alcohols

Table 4 shows the papers from where the experimental points were extracted. All papers Nativel et al. (91), Zhang et al. (132), Mathieu et al. (82), Noorani; Akih-Kumgeh; Bergthorson (92), Pinzón et al. (98), L. R. Cancino et al. (16), U. Burke et al. (12), Stranic et al. (117), Pelucchi et al. (96) e Xu et al. (129) present neat alcohol experiments, except one (AlRamadan et al. (2)), that presents a 68.8% 2-butanol/ 31.2% *t*-butanol volumetric mixture.

Table 4 – Previously published experimental data for ignition delay time of $C_1 - C_4$ alcohols gathered in this research

Fuel	T [K]	p [bar]	ϕ	Device	Ref.
Ethanol	800-1250	20	1	HPST	(91)
Ethanol	650-1250	20-40	0.5-2.0	HPST, RCM	(132)
Ethanol	944-1589	1.3-53[1]	0.5-2.0	HPST	(82)
Methanol, ethanol, *n*-propanol, *n*-butanol	1070-1760	2-12[1]	0.5-2.0	HPST	(92)
Methanol	940-1540	1-14.9[1]	0.5-2.0	HPST	(98)
Ethanol	650-1220	10-50	0.3-1.0	HPST	(16)
Methanol	820-1650	2-50[1]	0.5-2.0	L/HPST, RCM	(12)
n-butanol, 2-butanol, *t*-butanol, *i*-butanol	800-1600	1-43[1]	0.5-1.0	LPST, HPST	(117)
Ethanol, *n*-propanol, *n*-butanol	704-935	10-30	1.0	RCM	(96)
2-butanol/*t*-butanol mixture	800-1200	20-40	1.0	HPST	(2)
n-butanol	812	24	0.1	FIT	(129)

[1] atm

2.7.1.2 SI-ICE transportation fuels

Table 5 shows the published IDT experiments for relevant SI-ICE applications/research.

Table 5 – Previously published experimental data for ignition delay time of relevant SI-ICE transportation fuels gathered in this research

Fuel	T [K]	p [bar]	ϕ	Device	Ref.
BR1	910-1212	9.1-32.1	0.35-1.3	HPST	(17)
Coryton, Haltermann	923-1386	8.7-42.4	0.45-1.8	HPST	(72)
E85, gasoline surrogate	968-1361	3.4-59.9	0.5-1.0	HPST	(23)
Ethanol	1100-1623	1.8-13.5	0.5-2.0	HPST	(92)
Ethanol	912-1234	9.0-53.0	0.3-1.0	HPST	(16)
Ethanol	918-1318	18.0-21.6	1.0	HPST	(91)
Ethanol	931-1172	17.6-45.3	0.5-2.0	HPST	(132)
Ethanol	944-1589	1.1-54.2	0.5-2.0	HPST	(82)
Ethanol	960-1150	23.1-24.7	1.0	HPST	(105)
Ethanol/isoctane (25/75 volume), quinary mixture [1]	928-1243	9.3-31.9	1.0	HPST	(15)
FACE F, FGF-KAUST, FGF-LLNL, TPRF F, PRF 91.5	689-995	20.0-40.0	1.0	RCM	(64)
FGF-KAUST/FGF-LLNL + 0/10/20/30% ethanol	697-1005	10.0-110.0	0.3-1.0	RCM	(19)
KM9096, PR6918	690-964	15.0	15.0	RCM	(38)
LLNL surrogate, Stanford surrogate A	666-950	20.0-40.0	0.3-0.5	RCM	(71)
PRF 80, PRF 90, PRF 100	917-1191	40.0	1.0	HPST	(36)
PRF 80, PRF 91, PRF 95	912-1319	7.9-42.3	0.5-1.08	HPST	(1)
PRF 84, FACE A, FACE C	910-1423	9.1-43.5	0.5-1.0	HPST, LPST	(109)
PRF 100	643-991	15.0-30.0	0.4-1.0	RCM	(35)
PRF 100	739-1098	3.0-30.0	0.25-1.0	RCM	(81)
PRF 100	943-1027	5.2-23.4	0.25-1.0	RCM	(55)
PRF 100, E25, E50, E75, ethanol	883-974	10.0	0.92-1.06	IQT	(6)
PRF 100	1250-1665	1.7-4.9	1.0	ST	(126)
PRF 100	914-1185	25.3-62.1	0.84-1.07	HPST	(113)
PRF 100, toluene	927-1269	13.2-56.4	0.5-1.0	HPST	(25)
RD387, surrogate A TPRF, surrogate B TPRF	914-1280	14.4-61.7	0.5-2.1	HPST	(41)
RON95E10	696-918	20.0-30.0	0.77-1.18	RCM	(13)
Surrogate A	930-1201	9.8-51.0	1.0	HPST	(14)
Toluene, PRF100, TPRF toluene/isoctane (10/90 vol%)	910-1199	36.5-44.0	0.5-1.0	HPST	(54)
TPRF 87 [3]	1085-1421	10.0-20.0	0.5-2.0	HPST	(73)

[a] atm

[b] Isoctane/toluene/*n*-heptane/di-iso-butylene/ethanol (30/25/22/13/10% volume)

[c] 56% isoctane, 17% *n*-heptane, 27% toluene in mole

2.7.2 Laminar flame speed

Although laminar flame speed is not the main quantity of interest in knock study, it is tightly related to the flame propagation. Thus, it is a complementary way of assessing mechanisms.

2.7.2.1 Primary alcohols

Table 6 shows the conditions of each laminar flame speed (LFS) experiment for primary alcohols. Note that all of them used a twin counterflow configuration. They were performed by Veloo et al. (125) e Veloo; Egolfopoulos (124).

Table 6 – Previously published experimental data for laminar flame speed of $C_1 - C_4$ alcohols gathered in this research

Fuel	T [K]	p [atm]	ϕ	Device	Ref.
Methanol	343	1	0.7-1.5	Twin counterflow flame	(125)
Ethanol	343	1	0.7-1.5	Twin counterflow flame	(125)
n-propanol	343	1	0.75-1.5	Twin counterflow flame	(124)
n-butanol	343	1	0.7-1.5	Twin counterflow flame	(125)

2.7.2.2 SI fuels and surrogates

Table 7 shows the conditions of each laminar flame speed (LFS) experiment for SI-ICE fuel surrogates. For simplicity, only PRFs are simulated.

Table 7 – Previously published experimental data for laminar flame speed of PRF gathered in this research

Fuel	T [K]	p [bar]	ϕ	Device	Ref.
PRF 0, 85, 90, 95, 100	298	1[1]	0.7-1.4	Twin counterflow flame	(59)
PRF 87	373	10, 15, 20, 25	0.7-1.2	Constant volume bomb	(61)

[1] atm

2.8 DETAILED CHEMICAL KINETICS MECHANISMS

The primary alcohols database targets the model validation. Thus, the results yielded by the regressions must be compared to strong baselines, in other words, the experiments themselves and to detailed chemical kinetics simulations. Since these mechanisms are not targeted for CRFD, they can be detailed for alcohols.

2.8.1 Primary alcohols

POLIMI's CRECK Modelling Group developed a detailed kinetics mechanism that was lastly updated by Bagheri et al. (5) (referred as CRECK for simplicity). This mechanism is composed by the following sub-mechanisms and thermodynamic properties, plus several reactions that were updated for the sake of performance improvement: H_2/O_2 and $C_1 - C_2$ (Metcalfe et al. (84)); C_3 (S. M. Burke et al. (11)); heavier species (Ranzi et al. (100) e Ranzi et al. (102)); acetaldehyde (Pelucchi et al. (97)); rate rule for H-abstraction reactions (Ranzi et al. (101)); thermochemical properties of hydrogen and syngas cores from Active Thermochemical Tables (ATcT) (Ruscic et al. (104)); and from other important species (Burcat; Ruscic (10) e Ranzi et al. (100)).

S. M. Sarathy et al. (108) followed a manual generation method to develop their mechanism, although it should not be considered new. Essentially, it is an hierarchical assembly of data on reaction mechanisms, rate coefficients, and species thermodynamic and transport properties available in the literature. The sub-mechanisms are: $C_0 - C_2$ hydrocarbon oxidation (AramcoMech 1.3 by Metcalfe et al. (84), which bases its $H_2/CO/O_2$ sub-mechanism on Kéromnès et al. (66)); C_4 and C_5 alkane and alkene (Healy et al. (56)); methanol (Metcalfe et al. (84)); ethanol (Mittal et al. (87)); *n* and *i*-propanol (Johnson et al. (62)), with modifications by Man et al. (80), plus several important low temperature reaction pathways; butanol isomers (S. M. Sarathy et al. (107)); *n*-pentanol (Heufer et al. (58)); *i*-pentanol (M. Sarathy et al. (106)). Table 8 shows the mechanisms in terms of number of elements, species and reactions. Note also that (108) has a high-temperature sub-mechanism, described in parenthesis. Since the laminar flame speed data in this study do not lie in this region, only the complete mechanism is considered. For the rest of this work, this mechanism is referred as CCRC (Clean Combustion Research Center, King Abdullah University of Science and Technology - KAUST).

Table 8 – Detailed kinetics models used assessing $C_1 - C_4$ alcohols in this work. Numbers within parentheses are relative to the high-temperature sub-mechanism

	CRECK	CCRC
Elements	6	6 (6)
Species	339	687 (354)
Reactions	9781	3674 (2625)
Reference	(5)	(108)

2.8.2 SI fuels and surrogates

As will be mentioned later, the post-processing in Cantera based on the data extracted from the CRFD simulations would take longer than the CRFD processing if detailed chemical kinetics mechanisms were considered. Therefore, Tab. 9 shows the three reduced mechanisms for PRF regarded in this work.

Table 9 – Chemical kinetics models used assessing PRF surrogates in this work.

	(75)	(77)	(120)
Elements	7	5	4
Species	61	56	33
Reactions	279	190	48

3 MATERIALS AND METHODS

This section covers the materials methods used in the many instances of this work, namely the development of the multivariate and automatized approach for ignition delay time correlations, the 0D and 1D chemical kinetics simulations for ignition delay time and laminar flame speed, the 3D computational reactive fluid dynamics model and the post-processing approach that ties all the other branches together to evaluate knock.

3.1 THE IN-HOUSE PYTHON ROUTINE FOR IDT CORRELATIONS

As previously shown, the modified Arrhenius expression involving T, AKI, p, ϕ has been linearized in Equation 9. The in-house Python routine uses a statistical open-source library (Seabold, Skipper; Perktold (112)) to perform the multiple linear regression (MLR), following the ordinary least squares (OLS) scheme. This choice is due to the combination of log-transformed data with OLS being preferred to non-linear methods (Sundberg (118)). The regression is dependent upon the input data; after removing outliers, the metrics of the regression are likely to improve but the regression itself might change as well. Therefore, a new MLR should be run after the outliers are removed. To avoid removing many data points per run, a threshold criterion is gently tightened every run. The threshold is the so-called logarithmic error, taken as the difference between the natural logarithm of the predicted value and the natural logarithm of the actual value. More precisely, unity is added to both logarithms to avoid operations with zero

$$LE = \ln(1 + IDT_{predict}) - \ln(1 + IDT_{actual}) \tag{23}$$

where LE is the logarithmic error and the subscripts $predict$ and $actual$ represent the mathematical prediction and the experimental value, respectively.

The metrics associated with the linear regression are the R^2, the average absolute error and the global apparent activation energy (E_a). While the first two are statistical features, the last one is related to chemical kinetics. This way, the combination of them should provide a statistically significant result and in agreement with the fuel characteristics. The R^2 is the coefficient of determination and it measures the strength of the relationship between the model and the dependent variable on a 0 to 100% scale, where 100% represents a model that explains all the variation in the response variable around its mean (Frost (37)). The average absolute error (AAE) is the absolute (i.e. disregarding the sign) percentage difference of the predicted value relative to the actual value, as follows

$$AAE = \frac{1}{N} \sum \left| \frac{IDT_{predict} - IDT_{actual}}{IDT_{actual}} \right| \times 100\% \tag{24}$$

where N is the size of the database.

In addition to the linear regression dependent on T, AKI, p, ϕ, another three regressions are derived too, for the validation database (primary alcohols). One as a function of T, AKI, P and scaling the data to stoichiometry, another one as a function of T, AKI, ϕ and scaling to 30 bar (considered as an intermediate pressure for HPST and RCM tests) and the third one as a function of T, AKI, scaling to stoichiometry and 30 bar. The outliers are removed based on the logarithmic error considering the most complete regression, the focus of this research. Therefore, it is likely that the metrics improve more and faster for the complete case than the others. Besides, all regressions use the same database to enable a fair comparison.

Figure 4 summarizes the steps described above that compose the in-house Python routine.

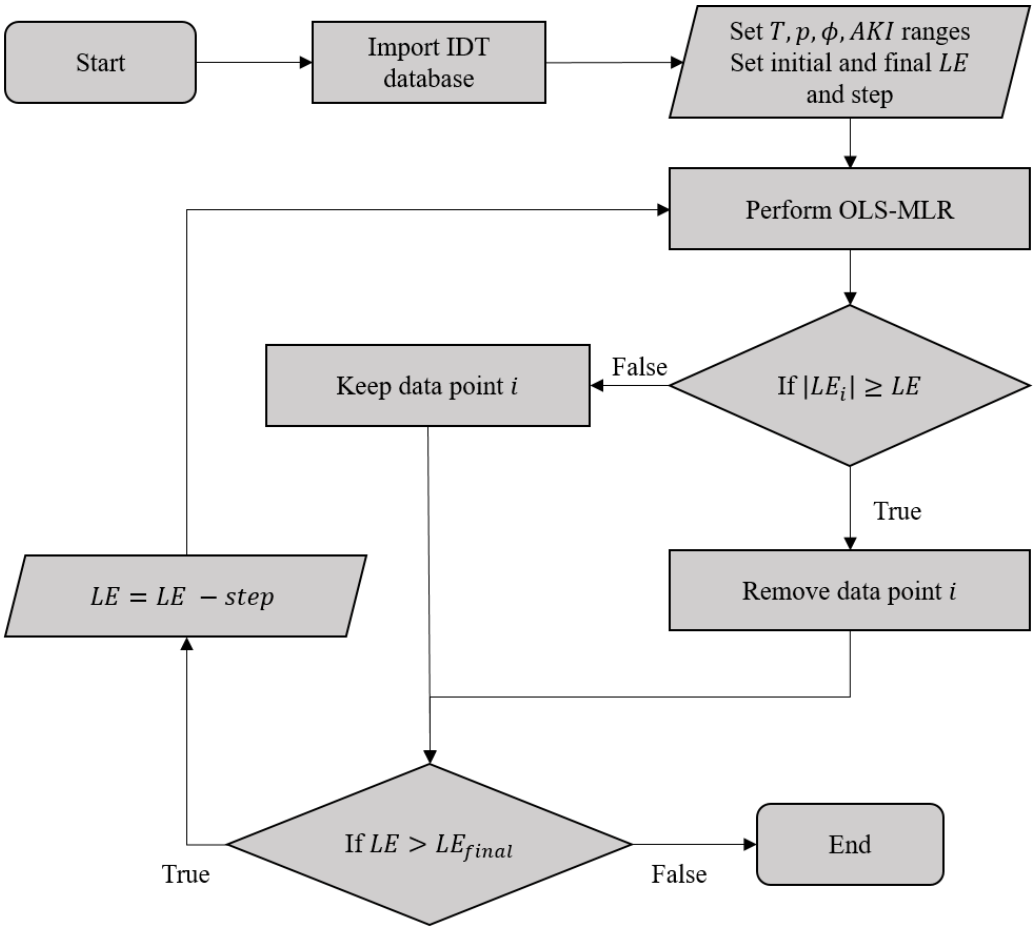

Figure 4 – Flowchart representing the in-house Python routine for IDT correlations.

3.2 THE CANTERA SUITE TOOLS

In this work, Cantera 2.5.1 and 2.6.0 versions are used. Cantera is an open-source suite of tools for problems involving chemical kinetics, thermodynamics, and transport processes developed by Goodwin et al. (51). Its functions can automate the chemical kinetics simulation process. Cantera provides classes of objects representing phases of matter, interfaces, reaction managers, reactor networks, and reacting flows. Additional information about Cantera can

be found at the Cantera website. In this work, two kinds of simulations of reactive systems are performed: ignition delay time simulations on homogeneous adiabatic constant volume reactors and laminar freely propagating flame speed.

3.2.1 Ignition delay time simulation

The ignition delay time is obtained by modeling a homogeneous 0D reactor. In this case, more specifically, as a constant volume (CV) perfectly stirred reactor (PSR) (Fig. 5). Also, the IDT criterion is associated with the peak OH mass fraction.

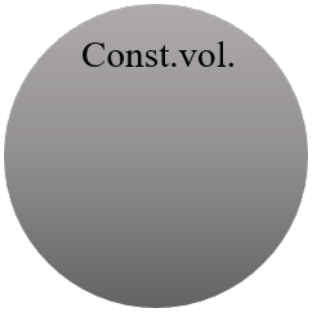

Figure 5 – Constant volume perfectly stirred reactor (CV-PSR).

3.2.2 Freely propagating flame simulation

In order to model premixed laminar flames, the formulation of mass transport laws must take into account different chemical species, with different individual properties. In addition, large temperature gradients, typical of flames, produce a second mass diffusion potential alongside that generated by concentration gradients. This temperature gradient driven mass diffusion, named thermal diffusion or Soret effect, results in the diffusion of light molecules from low to high-temperature regions and of heavy molecules from high to low-temperature regions. Besides the Soret effect, hydrocarbon flames are also characterized by their emission of visible radiation. When burning with excess air, the fast reacting zone appears blue, a color that results from the spontaneous emission of radiation by the excited CH radicals in the high-temperature region. This way, it is also possible to turn on the effects of radiation in the energy equation.

In essence, single gas-phase species can be either modeled via mixture-averaged or multicomponent transport models. Note that the inclusion of the Soret effect is only possible in Cantera via the multicomponent transport model. In this transport formulation, the diffusive flux (J) is assumed proportional to all species gradients, thus, each specie contributes to it. For a one-dimensional approach, for a generic specie k

$$J_k = \rho V_k \tag{25}$$

where V is the diffusive flux velocity, which is composed by two terms

$$V_k = V_{km} + V_{kT} \tag{26}$$

where the first is the multicomponent diffusion velocity and the second is due to thermal gradients.

The first is one is defined by

$$V_{km} = \frac{1}{X_k \overline{W}} \sum_{j=1}^{k} W_j D_{kj} \frac{\mathrm{d}X_j}{\mathrm{d}x} \tag{27}$$

where X is the molar fraction, W the molecular weight, and D the diffusion coefficient.

While the second one is defined by

$$V_{kT} = -\frac{D_k^T}{\rho Y_k} \frac{1}{T} \frac{\mathrm{d}T}{\mathrm{d}x} \tag{28}$$

where Y is the mass fraction.

Based on this, the solver transport algorithm automates the grid refinement in a coarse-to-fine approach with adequate mesh placement given an initial width, to enhance the convergence.

As previously shown in Tab. 6, all of the primary alcohols' LFS experiments used a twin counterflow configuration (Fig. 33a). In Cantera, the correspondent function requires mass flux boundary conditions, that are not described in Veloo et al. (125) e Veloo; Egolfopoulos (124), and the authors no longer keep this information (Egolfopoulos, personal communication). Due to the limited dimensions of the experimental domain, with burners of up to 20 mm in diameter and separated by up to 20 mm, it is possible to neglect curvature effects and assume a flat flame (Fig. 33a). This way, Cantera no longer needs the unavailable mass flux boundary conditions. In addition, Veloo et al. (125) and Veloo; Egolfopoulos (124) simulated their flames with PREMIX (Kee et al. (65)), as a freely propagating flame. Also, they accounted for thermal radiation of CH_4, CO, CO_2, H_2O and the Soret effects in their simulations. Even though they used a mixture-averaged transport formulation, it is only possible to turn the Soret effect in Cantera using a multicomponent formulation. Therefore, to assess the differences between mechanisms and between turning on or off these effects, each experimental point is simulated as a freely-propagating flame (laminar flat flame) under the following set-ups: without radiation and Soret effects, with Soret and with both effects, for both mechanisms, all of them following the multicomponent transport formulation.

3.3 CRFD MODEL

The CRFD model comprises many phases, from pre, post and processing, each of them divided into many steps. Especially for the combustion simulation of an engine, there are several modules to be set within the preprocessing, which also yield several output quantities. For this reason, the following subsections take care of describing the steps taken during the simulation workflow, resembling the outline presented by Galpin (39).

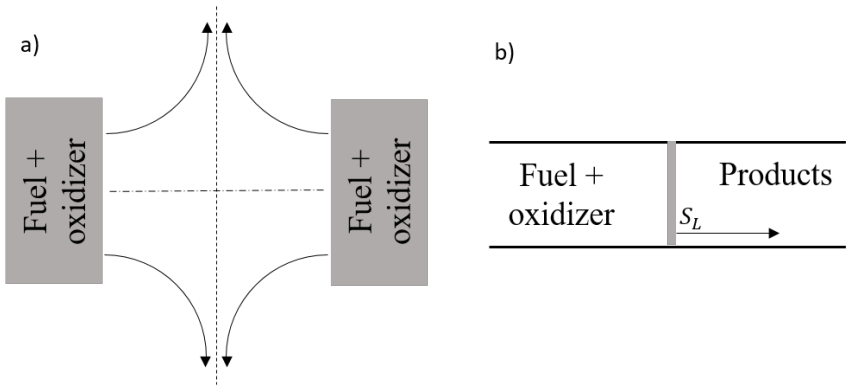

Figure 6 – a) Twin counterflow flame; b) Freely propagating (laminar flat) flame.

3.3.1 Physics modeling

In AVL FIRE, the cell-centered finite volume CRFD software used in this research (which has a partnership program with the research laboratory), most engine-related physical models come as modules, which need to be activated prior to the setup. Therefore, the following details are basically separated by module, but there are also considerations on how they affect each other.

3.3.1.1 Combustion modeling

The Coherent Flame Model (CFM) family assumes that the chemical time scales are much smaller than the turbulent ones, a plausible assumption for reciprocating ICEs (AVL (45)). Thus, it is possible to apply a laminar flamelet approach, in which flame velocity and thickness are averaged values integrated along the flame front, only dependent on pressure, temperature, and stoichiometry of the unburned gases (AVL (45)). As such, it decouples chemistry and turbulence; however, the variation on the turbulence model is expected to promote some changes in flow and chemical species fields, which influence the rate of heat release.

The Extended CFM (ECFM) has been mainly developed for DI-SI engines. While port fuel injection (PFI) SI engines run under homogeneous conditions, DI-SI may run under very stratified conditions (Colin; Benkenida; Angelberger (22)). The large scale stratification is described by local values of unburnt equivalence ratio, burnt and unburnt gases composition and temperature. Additionally, the small scale stratification is included via a variance/scalar dissipation model in combination with a presumed probability density function (PDF) for the fuel stratification (Colin; Benkenida; Angelberger (22)).

The ECFM differs from CFM because the CFM developed by Duclos; Bruneaux; Baritaud (29) does not consider exhaust-gas recirculation (EGR) within the fresh gases composition. This way, the fresh gases temperature is estimated using a polytropic compression law. To cope with stratification, Duclos; Zolver (30) introduced the fuel and oxygen tracers which allow to compute locally the fresh gases composition even in the presence of EGR. Conversely, their

fresh gases enthalpy equation computes precisely the fresh gases temperature (Colin; Benkenida; Angelberger (22)).

Since the fresh gases state is more accurately predicted, the local laminar flame speed (LFS) is better predicted as well. Furthermore, for the models like the CFMs, the reaction rate is proportional to LFS. Hence, the ECFM is expected to describe better the fresh gases and better account for large scale stratification effect on combustion (Colin; Benkenida; Angelberger (22)). With respect to small scale stratification, the average equivalence ratio used to calculate the LFS may lead to deviations. In short, this problem is solved by applying a PDF for the fuel mass fraction and then substituted in the LFS integration (or interpolation, for faster calculation) to yield a statistical average LFS.

To summarize, the ECFM couples combustion with spray modeling to allow stratified combustion, EGR and NO modeling (AVL (45)). On top of that, the 3-Zones Extended Coherent Flame Model (ECFM-3Z) is a combustion model that works with all combustion modes (autoignition, propagation flame and diffusion flame) without knowing which one might take place beforehand (Colin; Benkenida (21)). This is particularly important as autoignition may occur in SI ICEs as the undesirable knock. In fact, some knock considerations were already present in the ECFM formulation of Colin; Benkenida (21), as they argue that the fresh gases state has to be defined accurately to yield a correct estimation of the laminar flame characteristics and of the autoignition delay time for a correct prediction of knock and detail this modeling.

The state of the gas mixture is described by a 2D space of mixture fraction and reaction progress (Z and $\tilde{c}$, respectively). Regarding the probability density function (PDF), it is described by Z, and each computational cell is divided into three mixing zones: the unmixed fuel zone, the mixed zone containing fuel, air and EGR, and the unmixed air plus EGR zone. Regarding $\tilde{c}$ (where the tilde stands for the Favre-filtered value), it is null for unburnt gases and unity for completely burnt gases (Colin; Benkenida (21)). In essence, this combustion model is based on a flame surface density transport equation and a mixing model that describes the three combustion modes (AVL (45)). In-deep detail about the equations and the model can be checked in Colin; Benkenida (21) and AVL (45).

Figure 7 shows the ECFM-3Z zones for a schematic cell with a flame front.

In this model, the species are transported using Favre-averaged mass fractions ($\tilde{Y}$). For a generic specie X, the transport is stated as

$$\frac{\partial \bar{\rho}\tilde{Y}_X}{\partial t} + \frac{\partial \bar{\rho}\tilde{u}_i\tilde{Y}_X}{\partial x_i} - \frac{\partial}{\partial x_i}\left(\left(\frac{\mu}{Sc} + \frac{\mu_t}{Sc_t}\right)\frac{\partial \tilde{Y}_X}{\partial x_i}\right) = \bar{\dot{\omega}}_X \tag{29}$$

where $\bar{\dot{\omega}}_X$ is the combustion source term, and Sc the Schmidt number.

This way, for the unburnt fuel mass fraction, the transport is given by

$$\frac{\partial \bar{\rho}\tilde{Y}^u_{Fu}}{\partial t} + \frac{\partial \bar{\rho}\tilde{u}_i\tilde{Y}^u_{Fu}}{\partial x_i} - \frac{\partial}{\partial x_i}\left(\left(\frac{\mu}{Sc} + \frac{\mu_t}{Sc_t}\right)\frac{\partial \tilde{Y}^u_{Fu}}{\partial x_i}\right) = \bar{\rho}\tilde{\dot{S}}^u_{Fu} + \bar{\dot{\omega}}^u_{Fu} \tag{30}$$

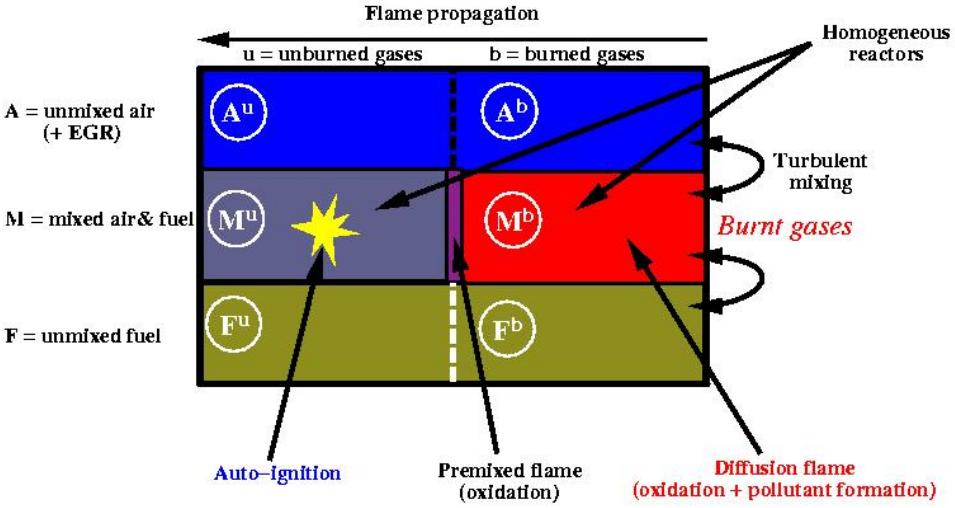

Figure 7 – Zones in ECFM-3Z (AVL (45)) for a control volume. Flame propagates from right to left. Curved arrows indicate the mixing between the zones of unmixed air, mixed zone and unmixed fuel.

where $\bar{\dot{S}}^{u}_{Fu}$ is the source term relative to the fuel evaporation in the unburnt gases, and $\bar{\dot{\omega}}^{u}_{Fu}$ is the source term taking into account the oxidation of the unburnt fuel.

Conversely, the equation for the burnt fuel mass fraction transport is analogous, only changing the superscript u to b.

In order to describe the mixing, there are transport equations for the unmixed fuel ($\tilde{Y}^{F}_{Fu}$) and the unmixed oxidizer ($\tilde{Y}^{A}_{O_2}$). For $\tilde{Y}^{F}_{Fu}$, it is

$$\frac{\partial \bar{\rho}\tilde{Y}^{F}_{Fu}}{\partial t} + \frac{\partial \bar{\rho}\tilde{u}_i\tilde{Y}^{F}_{Fu}}{\partial x_i} - \frac{\partial}{\partial x_i}\left(\frac{\mu}{Sc}\frac{\partial \tilde{Y}^{F}_{Fu}}{\partial x_i}\right) = \bar{\rho}\tilde{\dot{S}}^{F}_{Fu} + \bar{\rho}\bar{\dot{E}}^{F\rightarrow M}_{Fu} \tag{31}$$

Conversely, for $\tilde{Y}^{A}_{O_2}$,

$$\frac{\partial \bar{\rho}\tilde{Y}^{A}_{O_2}}{\partial t} + \frac{\partial \bar{\rho}\tilde{u}_i\tilde{Y}^{A}_{O_2}}{\partial x_i} - \frac{\partial}{\partial x_i}\left(\frac{\mu}{Sc}\frac{\partial \tilde{Y}^{A}_{O_2}}{\partial x_i}\right) = \bar{\rho}\bar{\dot{E}}^{A\rightarrow M}_{O_2} \tag{32}$$

where the source terms $\bar{\dot{E}}^{F\rightarrow M}_{Fu}$ and $\bar{\dot{E}}^{A\rightarrow M}_{O_2}$ describe the mixing model, described in more details by Colin; Benkenida (21).

Based on these unmixed quantities, it is possible to construct the mixed quantities, essentially by applying the conservation of mass for each specie in the control volume, and also taking into consideration the consumption given by the progress variable. For example, the unburnt and burnt fuel mass fractions in the mixing zone can be described by

$$\bar{\rho}^{u,M}_{Fu} = \bar{\rho}^{u}_{Fu} - (1-\tilde{c})\,\bar{\rho}^{F}_{Fu} \tag{33}$$

$$\bar{\rho}^{b,M}_{Fu} = \bar{\rho}^{b}_{Fu} - \tilde{c}\bar{\rho}^{F}_{Fu} \tag{34}$$

where $\bar{\rho}_X$ is given by

$$\bar{\rho}_X = \bar{\rho}\tilde{Y}_X \tag{35}$$

3.3.1.2 Turbulence modeling

A near-wall turbulent flow can be divided into a inner region that scales on a viscous length and an outer region that scales on a flow length. The wall-bounded turbulent shear flow ought to be correctly modelled to capture turbulent quantities in this inner region. The kinematic blocking caused by a wall is governed by an elliptical partial differential equation, hence, non-local effects in non-homogeneous turbulent flows should consider an elliptical model. Moreover, the damping factors (correction functions) are artificial manoeuvres to represent the kinematic constraints caused by blocking (Durbin (34)).

The $\overline{v^2} - f$ model proposed by Durbin (34) (not implemented in AVL FIRE but described here for context) eliminates empirical damping functions and accounts for some near-wall anisotropic turbulent effects, modelled through the elliptic relaxation function f, which is analogous to a redistribution term ("Models with Tensor Variables" (88)). This way, it is a better option than $k-\varepsilon$ and similar models that only considers isotropic turbulence and use damping terms. Yet, it is still inferior to second-moment and advanced non-linear eddy viscosity models when used in three-dimensional flows, with strong secondary recirculation, rotation and swirl, like ICE CRFD simulations.

The main computational inefficiency of the $\overline{v^2} - f$ model is its f wall boundary condition (f_w) sensitiveness, proportional to y^{-4} ($f_w = \lim_{y\to 0} -20\overline{v^2}\nu^2/(\varepsilon y^4)$). Due to this exponent, it suffers with small y^+, contrary to most near-wall models. This concern would be reduced by solving both equations simultaneously, but most numerical solvers use segregated schemes. The $k-\zeta-f$ model proposed by Hanjalić; Popovac; Hadžiabdić (53) is an upgrade of the previous model and overcomes this problem by solving a transport equation for ζ instead of $\overline{v^2}$. $\overline{v^2}$ is a wall-normal velocity scale, also understood as a velocity fluctuation normal to the streamlines. ζ is a normalization of this variable, but also regarded as the ratio of the two time scales: scalar k/ε (isotropic), and lateral $\overline{v^2}/\varepsilon$ (anisotropic) (CFD Online (93)). Moreover, the model formulates a better f_w boundary condition, this time proportional to y^{-2} ($f_w = \lim_{y\to 0} -2\nu\zeta/y^2$). The main improvement is that ε no longer appears on the $\overline{v^2}$ equation and its role is reproduced by the turbulent kinetic energy production (P_k) in the ζ equation. Essentially, the problem switches from a calculation of a variable (ε) that is dependent upon near-wall treatment to a variable (P_k) that is dependent upon the local turbulent stress and the mean velocity gradient capture, the goal of turbulence closure models (Hanjalić; Popovac; Hadžiabdić (53)).

In AVL FIRE (44), the $k-\zeta-f$ model is composed by the following equations. The eddy-viscosity (ν_t) is obtained from

$$\nu_t = C_\mu \zeta \frac{k^2}{\varepsilon} \tag{36}$$

While the rest of the transport equations of turbulence kinetic energy (k), turbulence kinetic energy dissipation (ε), and ζ are, respectively

$$\rho \frac{\mathrm{D}k}{\mathrm{D}t} = \rho (P_k - \varepsilon) + \frac{\partial}{\partial x_j} \left[\left(\mu + \frac{\mu_t}{\sigma_k} \right) \frac{\partial k}{\partial x_j} \right] \tag{37}$$

$$\rho \frac{\mathrm{D}\varepsilon}{\mathrm{D}t} = \rho \frac{C^*_{\varepsilon 1} P_k - C_{\varepsilon 2} \varepsilon}{T} + \frac{\partial}{\partial x_j} \left[\left(\mu + \frac{\mu_t}{\sigma_\varepsilon} \right) \frac{\partial \varepsilon}{\partial x_j} \right] \tag{38}$$

$$\rho \frac{\mathrm{D}\zeta}{\mathrm{D}t} = \rho f - \rho \frac{\zeta}{k} P_k + \frac{\partial}{\partial x_j} \left[\left(\mu + \frac{\mu_t}{\sigma_\zeta} \right) \frac{\partial \zeta}{\partial x_j} \right] \tag{39}$$

where f has the following elliptical differential equation

$$f - L^2 \frac{\partial^2 f}{\partial x_j \partial x_j} = \left(C_1 + C_2 \frac{P_k}{\varepsilon} \right) \frac{(2/3 - \zeta)}{T} \tag{40}$$

where the turbulent time scale (T) and the length scales (L) are given by the two equations below, which represent the Kolmogorov time and length scale as the lower bounds, plus realizability constraints (Hanjalić; Popovac; Hadžiabdić (53))

$$T = \max \left(\min \left(\frac{k}{\varepsilon}, \frac{a}{\sqrt{6} C_\mu |S| \zeta} \right), C_T \left(\frac{\nu}{\varepsilon} \right)^{1/2} \right) \tag{41}$$

$$L = C_L \max \left(\min \left(\frac{k^{3/2}}{\varepsilon}, \frac{k^{1/2}}{\sqrt{6} C_\mu |S| \zeta} \right), C_\eta \frac{\nu^{3/4}}{\varepsilon^{1/4}} \right) \tag{42}$$

where a is no greater than unity and S is the strain tensor.

Note also that, in this formulation, there is an additional modification to the ε equation, in which the constant $C_{\varepsilon 1}$ is dampened close to the wall, in the form of

$$C^*_{\varepsilon 1} = C_{\varepsilon 1} \left(1 + 0.045 \sqrt{1/\zeta} \right) \tag{43}$$

Where the constants can be summarized in Tab. 10 (Hanjalić; Popovac; Hadžiabdić (53)).

Table 10 – $k - \zeta - f$ coefficients

C_μ	$C_{\varepsilon 1}$	$C_{\varepsilon 2}$	C_1	C_2	σ_k	σ_ε	σ_ζ	C_T	C_L	C_η
0.22	$1.4(1 + 0.012/\zeta)$	1.9	0.4	0.65	1	1.3	1.2	6.0	0.36	85

Overall, this is set of equations is computationally more robust than the original model $\overline{v^2} - f$. As part of the numerical validation process, as shown in Section 4.3, turbulence interacts with combustion, and vice-versa. Since the ECFM-3Z is the most complete combustion model available in AVL, this model is fixed for all simulations. On the other hand, the turbulence

model can be changed to evaluate each one helps identifying knock better. Thus, the other turbulence model considered is the $k-\varepsilon$ (standard formulation, with hybrid wall treatment, just like $k-\zeta-f$).

The $k-\varepsilon$ model is the most widely used turbulence model, particularly for industrial computations and has been implemented into most CRFD codes. It is numerically robust and has been tested in a broad variety of flows, including heat transfer, combustion, free surface and two-phase flows. Despite numerous shortcomings, which have been discovered over the past three decades of use and validation, it is generally accepted that the $k-\varepsilon$ model usually yields reasonably realistic predictions of major mean-flow features in most situations (AVL (44)). It is particularly recommended for a quick preliminary estimation of the flow field, or in situations where modelling other physical phenomena, such as chemical reactions, combustion, radiation, multi-phase interactions, brings in uncertainties that outweigh those inherent in the $k-\varepsilon$ turbulence model.

Unlike earlier turbulence models, it focuses on the mechanisms that affect the turbulent kinetic energy. The mixing length model lacks this kind of generality (Versteeg; Malalasekera (127)). The underlying assumption is that the turbulent viscosity is isotropic, that is, the ratio between Reynolds stress and mean rate of deformations is the same in all directions. The complete standard, high-Re-number $k-\varepsilon$ model, in AVL FIRE (44) has the following k equation

$$\rho\frac{\mathrm{D}k}{\mathrm{D}t}=P+G-\varepsilon+\frac{\partial}{\partial x_j}\left(\mu+\frac{\mu_t}{\sigma_k}\frac{\partial k}{\partial x_j}\right) \tag{44}$$

where P is the production of k by mean-flow deformation (work of turbulent stresses associated with the mean flow deformation, or transfer of the energy from the mean motion to the turbulent fluctuations by the action of Reynolds stresses); G is the production/destruction of k by body forces; ε is the dissipation of k. And for ε

$$\rho\frac{\mathrm{D}\varepsilon}{\mathrm{D}t}=\left(C_{\varepsilon 1}P+C_{\varepsilon 3}G+C_{\varepsilon 4}k\frac{\partial U_k}{\partial x_k}-C_{\varepsilon 2}\varepsilon\right)\frac{\varepsilon}{k}+\frac{\partial}{\partial x_j}\left(\frac{\mu_t}{\sigma_\varepsilon}\frac{\partial \varepsilon}{\partial x_j}\right) \tag{45}$$

where P is

$$P=2\mu_t S\cdot S-(2/3)\left[\mu_t\left(\mathrm{tr}S\right)+k\right]\left(\mathrm{tr}S\right) \tag{46}$$

with S being the strain tensor and tr$S$ its trace. For G

$$G=-\frac{\mu_t}{\rho\sigma_\rho}\nabla\rho \tag{47}$$

And the turbulent viscosity is

$$\mu_t=C_\mu\rho\frac{k^2}{\varepsilon} \tag{48}$$

with the coefficients all set to their standard values, as shown in Tab. 11

Table 11 – $k-\varepsilon$ standard coefficients

C_μ	$C_{\varepsilon 1}$	$C_{\varepsilon 2}$	$C_{\varepsilon 3}$	$C_{\varepsilon 4}$	σ_k	σ_ε	σ_ρ
0.09	1.44	1.92	0.8	-0.373	1	1.3	0.9

3.3.1.3 Spray modeling

The spray is modeled in a Lagrangian multiphase approach. More precisely, the Discrete Droplet Model (DDM) treats the Lagrangian particles and the Eulerian flow in a two-way coupling manner with simultaneous and non-iterative calculations (J. K. Dukowicz (32)). Essentially, each droplet is treated using Newton's Second Law (and this is the basis of a more detailed formulation given by AVL (48), where the relevant forces are considered and modeled).

The discrete phase is modeled statistically and not deterministically. This way, as a Lagrangian phase, the particles avoid suffering from numerical diffusion and allow individual attributes to be statistically assigned for each particle. Since the spray is limited to a small part of the domain's mesh and the accuracy is reached with a moderate number of particles, the computational cost is affordable. Also, as part of the statistical treatment, identical non-interactive droplets are grouped as parcels (AVL (48)). Nevertheless, the standard DDM treats the parcels as point sources for mass, momentum and enthalpy in the frame of the Eulerian gas flow field.

In this research, the spray is injected at 293.15 K and taken as a single-component gasoline-equivalent fluid (that is, not a hydrocarbon mixture but a single specie representing the fuel). The coupling affects momentum, mass and energy transport equations. The atomization also considers drag (arguably the most important force that influences droplet flow), turbulence dispersion, evaporation and breakup. Most of these submodels are additions to DDM's original formulation proposed by J. K. Dukowicz (32). For the current work, the drag law is from Schiller; Naumann (110), the evaporation model from J. Dukowicz (31) and the WAVE breakup model.

The investigation of spray is not the focus of this research. However, it plays important roles in turbulence and combustion too. In relation to turbulence-spray interaction, the individual turbulent eddies influence particle motion and, conversely, the particles inertia affect the eddies (AVL (48)). Due to the large number of time and length scales, this interaction is accounted stochastically through the so-called turbulent dispersion submodel. In relation to combustion-spray interaction, the flame promotes evaporation, while spray leads to proper mixture formation. In addition, there are competing effects of cooling due to spray evaporation and flame propagation (Zhou et al. (134)).

3.3.1.4 Knock modeling

The Knock Shell Model, proposed by Halstead; Kirsch; Quinn (52), has a mechanism composed by eight reactions, whose reactants and products are general chemical compound groups with similar characteristics, instead of specific species. Table 12 describes the Knock

Shell Model (KSM) reactions, for a generic hydrocarbon RH (C_xH_y). The groups are divided into R· radicals, P products, B lumped branching agents, Q intermediate species (resembling Curran's notation for C_nH_{2n} species or structures, in Curran et al. (24)), and NR non-reactive compounds. Note that the description of the kinetic constants is out of the scope here, and can be checked in Halstead; Kirsch; Quinn (52).

Table 12 – Knock Shell Model mechanism. Adapted from Halstead; Kirsch; Quinn (52)

Number	Reaction	Description
(R1)	$RH + O_2 \xrightarrow{K_q} 2R\cdot$	Initiation
(R2)	$R\cdot \xrightarrow{K_p} R\cdot + P + \text{heat}$	Propagation cycle
(R3)	$R\cdot \xrightarrow{f_1 K_p} R\cdot + B$	Propagation forming B
(R4)	$R\cdot + Q \xrightarrow{f_2 K_p} R\cdot + B$	Propagation forming B
(R5)	$R\cdot \xrightarrow{f_3 K_p} NR$	Linear termination
(R6)	$R\cdot \xrightarrow{f_4 K_p} R\cdot + Q$	Propagation forming Q
(R7)	$2R\cdot \xrightarrow{K_t} NR$	Quadratic termination
(R8)	$B \xrightarrow{K_b} 2R\cdot$	Degenerate branching

However, this model alone is not suitable for this research. In AVL FIRE, it divides the cross-section into regions in the final third of the section (i.e. from 2/3 of the chamber radius to the wall), and considers a knock probability based on the Q mass fraction (or FQ) normalized by its maximum occurring value within the segments. The clock-like structure does not allow localized knock evaluation, as shown in Fig. 8 (top view of the cross-section at the top dead center).

To model knock with local resolution, the TABKIN FGM knock model needs to be activated on top of the Knock Shell Model. It is based on the work of Linse; Kleemann; Hasse (76), and extends the TABKIN FGM (flamelet generated manifold) model in a way to estimate the knock probability. The combustion model is still the ECFM-3Z but the knock approach gathers the coupling probability methods of Linse; Kleemann; Hasse (76) with TABKIN FGM, via the introduction of a knock progress variable (KPV) and its variance. This way, the model considers the influence of both the detailed chemical kinetics and the variances of mixture fraction and temperature in order to provide information on the ignition probability (AVL (45)).

The knock progress variable (c_k or KPV) describes the state of the autoignition process in the unburnt gas

$$c_k = \frac{Y_k}{Y_{k,max}} \tag{49}$$

where Y_k is the mass fraction of the characteristic species k and $Y_{k,max}$ is its maximum value at the time of autoignition (i.e., where $c_k = 1$). Besides, it is presumed that the KPV is zero in the burnt gas, thus c_k can be equated as

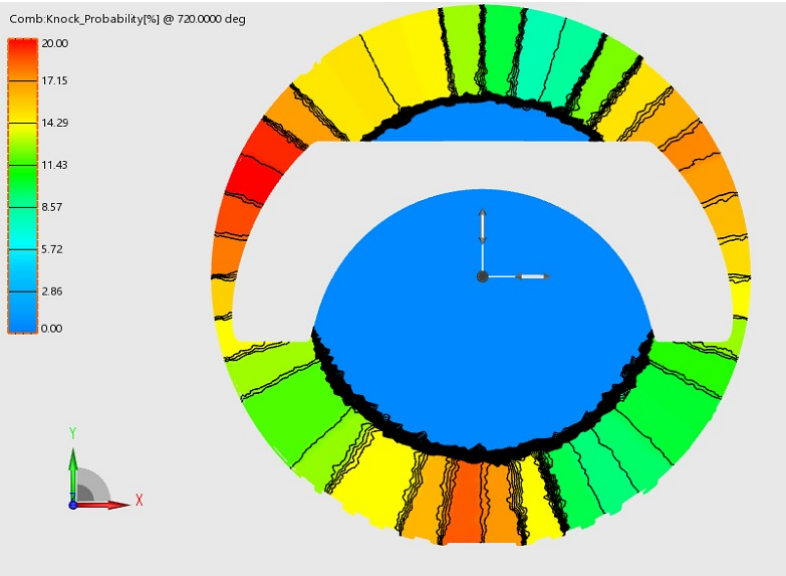

Figure 8 – Knock probability in AVL FIRE when the Knock Shell Model is activated alone. Top view of the cross-section at the top dead center (TDC, 720 CAD). Note that the piston head is not flat.

$$c_k = (1-c)\cdot c_k|_{c=0} \tag{50}$$

where c is the reactive progress variable and $c_k|_{c=0}$ is the KPV in the unburnt mixture.

With these definitions in mind, the KPV transport equation is

$$\frac{\partial}{\partial t}(\overline{\rho}\tilde{c_k}) + \frac{\partial}{\partial x_i}(\overline{\rho}\tilde{u_i}\tilde{c_k}) = \frac{\partial}{\partial x_i}\left(\overline{\rho}\,(D+D_T)\,\frac{\partial \tilde{c_k}}{\partial x_i}\right) + \overline{\rho}\,\tilde{\omega}_{c_k} \tag{51}$$

where D is the diffusion coefficient of the KPV.

Conversely, for the KPV variance

$$\frac{\partial}{\partial t}\left(\overline{\rho}\widetilde{c_k''^2}\right) + \frac{\partial}{\partial x_i}\left(\overline{\rho}\tilde{u_i}\widetilde{c_k''^2}\right) = \frac{\partial}{\partial x_i}\left(\overline{\rho}\,(D+D_T)\,\frac{\partial \widetilde{c_k''^2}}{\partial x_i}\right) + 2\overline{\rho}D_T\left(\frac{\partial \widetilde{c_k''^2}}{\partial x_i}\right)^2 - 2\overline{\rho}\frac{\tilde{\varepsilon}}{\tilde{\kappa}}\widetilde{c_k''^2} + 2\overline{\rho}\widetilde{c_k''\omega_{c_k}} \tag{52}$$

Note that both equations need a chemical source term closures, given by

$$\tilde{\omega}_{c_k} = (1-\tilde{c})\,\widetilde{\tau^{-1}}|_{c=0} - \tilde{c_k}|_{c=0}\tilde{\omega}_c \tag{53}$$

where the first group represents the formation of the KPV, while the second one accounts for the chemical conversion of the KPV due to combustion (Linse; Kleemann; Hasse (76)).

And

$$\widetilde{c_k''\omega_{c_k}} = \tilde{c_k}\widetilde{\tau^{-1}}|_{c=0} - \tilde{c_k}\tilde{c_k}|_{c=0}\tilde{\omega}_c - \tilde{c_k}\cdot\tilde{\omega}_{c_k} \tag{54}$$

However, Eqs. 53 and 54 which are the mean ignition delay $\tilde{\tau^{-1}}|_{c=0}$ and the mean KPV in the unburnt gas ($\tilde{c_k}|_{c=0}$). The second one can be written as

$$\tilde{c_k}|_{c=0} = \frac{\tilde{c_k}}{1-\tilde{c}} \tag{55}$$

Regarding tabulation, the source term $\tilde{\omega}_c$ is a function of pressure, fresh gas temperature, mixture fraction, mixture fraction variance, progress variable, progress variable variance and EGR

$$\tilde{\omega}_c = f(\bar{p}, \tilde{T}|_{c=0}, \tilde{Z}, \tilde{Z''^2}, \tilde{c}, \tilde{c''^2}, \tilde{Y}_{EGR}) \tag{56}$$

The mean ignition delay $\tilde{\tau^{-1}}|_{c=0}$ carries the detailed chemistry influence and its tabulation is a function of pressure, fresh gas temperature, mixture fraction, mixture fraction variance, residual gas mass fraction and fresh gas temperature variance

$$\tilde{\tau^{-1}}|_{c=0} = f\left(\overline{p}, \tilde{T}|_{c=0}, \tilde{Z}, \tilde{Z''^2}, \tilde{Y}_{EGR}, \tilde{T''^2}|_{c=0}\right) \tag{57}$$

Where the temperature variance has its correspondent transport equation

$$\frac{\partial}{\partial t}\left(\overline{\rho}\tilde{T''^2}\right) + \frac{\partial}{\partial x_i}\left(\overline{\rho}\tilde{u}_i\tilde{T''^2}\right) = \frac{\partial}{\partial x_i}\left(\left(\frac{\lambda}{c_p} + \frac{\lambda_T}{c_p}\right)\frac{\partial \tilde{T''^2}}{\partial x_i}\right) + 2\frac{\lambda_T}{c_p}\left(\frac{\partial \tilde{T''^2}}{\partial x_i}\right)^2 - 2\overline{\rho}\frac{\tilde{\varepsilon}}{\tilde{\kappa}}\tilde{T''^2} \tag{58}$$

Given that the KPV and its variance are clearly stated, the way of translating their meaning into simulations and knock prediction can be understood by the ignition probability (I_p or KPV-PROB, as written in AVL's colorbar legends). It can be estimated anywhere in the computational domain by a clipped Gaussian probability density function (PDF) (Linse; Kleemann; Hasse (76)). Both Linse; Kleemann; Hasse (76) and AVL FIRE clip the range for a KPV between 0.95 and unity (i.e. autoignition)

$$I_p(\vec{x}, t) = \int_{0.95}^{1.0} PDF\left(\tilde{c}_k, \tilde{c''^2_k}, \vec{x}, t\right) dc_k \tag{59}$$

where the PDF is shown in Fig 9, and is determined by its first two moments, the mean and the variance (c_k, c_k'').

In possession of this variable, it is possible to identify a region where I_p is greater than a threshold (ε)

$$\Omega_{I_p} = \{(x,y,z) \in \mathbb{R}^3 \,|\, I_p(x,y,z) \geq \varepsilon\} \tag{60}$$

According to both Linse; Kleemann; Hasse (76), ε can be taken as 1% to identify possible knocking cells. Besides, in order to get the total volume of Ω_{I_p} regions, they can be summed up in a variable called V_{I_p}. Conversely, the mass contained in this total volume is (m_{I_p}).

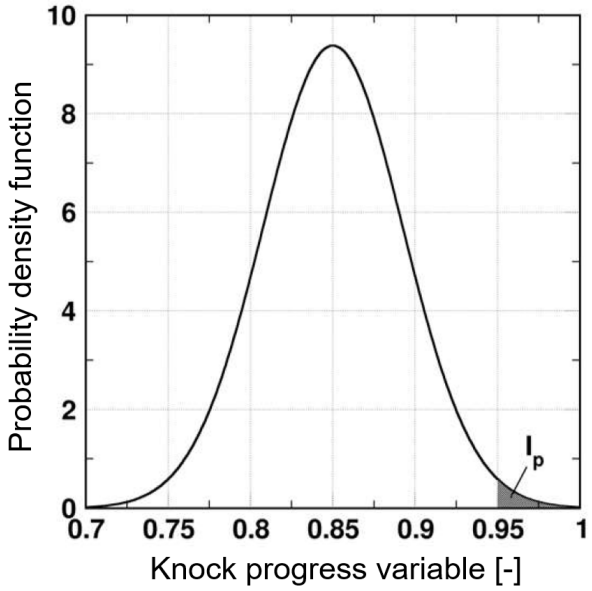

Figure 9 – Ignition probability based on KPV PDF. (AVL (45)).

In this context, the TABKIN FGM knock model is set as standard, which means that it has 5 active scalars (c, Z, EGR, KPV and KPV variance) and 38 passive scalars ($V_{I_p}, m_{I_p}, \Omega_{I_p}$, for the following thresholds: $\varepsilon = \{0.1\%, 0.4\%, 0.7\%, 1\%, 3\%, 6\%, 10\%, 40\%, 95\%\}$; as well as ϕ, and segregation and source-related scalars).

3.3.1.5 Additional models

There are other models involved in the setup, which are briefly described here for the sake of completeness of the physics and chemistry description. Also, as a reactive flow following the Reynolds Averaged Navier Stokes (RANS) formulation, the governing equations of mass, momentum, energy and species are also necessary (and can be referred in more detail in AVL (44)).

The emission module treats the major emission products formulation, NO and soot, following AVL FIRE's recommendations for engine applications. NO is usually formed from the following mechanisms: thermal NO, due to the dissociation N_2 contained in air; prompt NO (or Fenimore NO), due to the attack of hydrocarbon fragments on N_2 contained in air; NO formed from nitrogen-containing fuels (AVL (46)).In ICE applications, the second path usually contributes to less than 5% of the total NO formation and can be neglected, and the third one can be neglected due to the type of fuel. NO will be formed in both the flame front and post-flame gases. This way, the recommended NO model is the NO extended Zeldovich formulation

$$N_2 + O \underset{k_{1b}}{\overset{k_{1f}}{\leftrightarrow}} NO + N \tag{61}$$

$$N + O_2 \underset{k_{2b}}{\overset{k_{2f}}{\leftrightarrow}} NO + O \tag{62}$$

$$\mathrm{N} + \mathrm{OH} \underset{k_{3b}}{\overset{k_{3f}}{\leftrightarrow}} \mathrm{NO} + \mathrm{H} \tag{63}$$

This is an adequate choice because chemical mechanisms are applicable only for simple flame computations, with complex interactions with turbulence, radiation, heat transfer for ICE simulations. Therefore, the overall NO concentration (c_{NO}) change along time becomes

$$\frac{\partial c_{NO}}{dt} = k_{1f} c_O c_{N_2} + k_{2f} c_N c_{O_2} + k_{3f} c_N c_{OH} - k_{1b} c_{NO} c_N - k_{2b} c_{NO} c_O - k_{3b} c_{NO} c_H \tag{64}$$

For soot emission, the Kinetic Soot Model is the recommended model. It gathers several mechanisms ranging from polyaromatic hydrocarbons, polyynes, soot precursor formation, soot particle growth. However, it treats them in a reduced manner, where reaction constants and best parameters are set automatically and also as a function of the local equivalence ratio.

Regarding wall film, it is a separate single phase, different from the gas phase. It is not a two-phase model but a two single-phased model attached at the film surface. As a rather detailed formulation due to the several submodels, it is set as default, in which it solves wall shear, momentum, energy, turbulence, evaporation, entrainment, balancing, splashing. The coupling is via vapor mass and energy sources. In terms of submodels, it gathers: combined evaporation, Schadel-Hanratty's entrainment, Kataoka's entrained droplet sizing, Kuhnke's spray-wall splashing.

For spark modeling, the spherical model develops a flame kernel from the spark coordinate, with a certain ignition time, radius, duration, and flame density. This density is constant for the cells within the kernel for the duration of the spark. At end of ignition, the combustion propagates if the flame surface density remains self-sustaining.

3.3.2 Preprocessing

The following sections describe the main aspects of the preprocessing workflow, ranging from geometry, mesh, boundary conditions, solver and models, and operating conditions. Additional information can be checked in AVL FIRE Installation Example 990 - Gasoline Direct Injection Engine (AVL (47)), from where the main setup is derived.

3.3.2.1 Geometry and computational domain

The computational domain consist of a single cylinder of a gasoline direct injection (GDI) engine, alongside the intake and the exhaust ports (Fig. 10). The cylinder is divided into chamber and liner, while each port is divided into valve seat, valve stem and upper port regions. The cylinder has a bore of 81.97 mm, a stroke of 86 mm and the connecting rod is 144 mm long. The simulation lasts for a complete four-stroke cycle (i.e., 720 crank angle degrees), from 172.0 CA to 892.0 CA, for a single cycle.

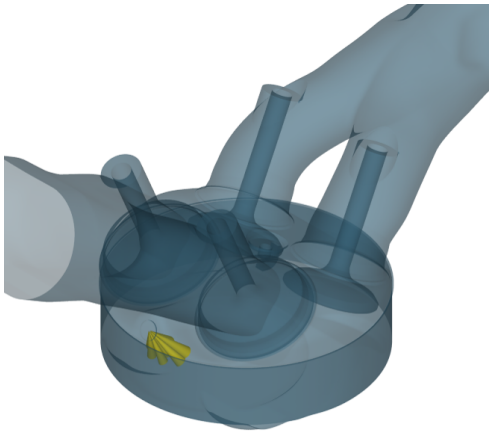

Figure 10 – Representation of the computational domain, with cylinder, ports, valves and spark. Injection spray in yellow to better localize the injector.

There are two intake and two exhaust valves, which lift curves are shown in Fig. 11. Table 13 aids the comprehension, summarizing important positions, that may be signalized in some results plots. Note that the simulation starts exactly at exhaust valve opening (EVO). For meshing purposes, the valves are considered closed at 0.2 mm of valve lift, to avoid skewed elements between valve and valve seat.

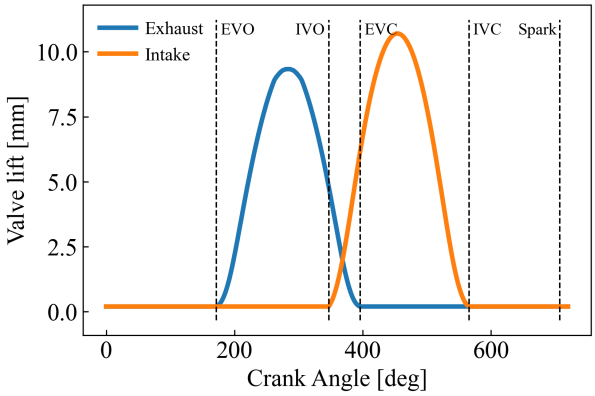

Figure 11 – Valve lift curves.

3.3.2.2 Meshing

The 3D four-stroke ICE is inherently a transient simulation. Also, it is a moving mesh simulation, with the crankshaft driving the piston up and down. The domain is constantly changing its volume and, therefore, it needs a moving mesh. The mesh quality must be appropriate on every moment of the simulation. This way, the meshing considers the worst case surface, which is at the top dead center (TDC).

Table 13 – Valve lift details

Position	CA [deg]
Exhaust valve opening (EVO) at 0.2 mm	172.0
Exhaust valve closing (EVC) at 0.2 mm	396.0
Intake valve opening (IVO) at 0.2 mm	347.0
Intake valve closing (IVC) at 0.2 mm	566.0
Max. exhaust lift	280.0
Max. intake lift	454.0

AVL FIRE FAME is the meshing tool that handles this process. The Engine Selection option automatically creates walls to close valve gaps and cuts unnecessary parts while using a single surface. For instance, the both ports can be suppressed at the compression and expansion phases to reduce the mesh file size and save computational resources. The engine settings are then informed, together with some meshing parameters. The volumetric mesh cell size is 1.4 mm (finer than used by (Yue; Som (130))), with a boundary layer of 0.4 mm made of two layers of cells. In sequence, the FAME Engine Plus (FEP) mesh environment must be set. The geometry must be cleaned and the moving parts labeled as moving, fixed or buffer (transition regions between moving and fixed parts). For the whole cycle, a single surface cannot be prescribed, nevertheless. Due to valve lift, and in this case valve overlap, there must be crank-angle intervals within different surfaces are valid, summarized in Tab 14.

Table 14 – Surface mesh interval of validity. Four surface meshes are used for the analyzed cycle.

Position	CA [deg]
EVO to IVO	172.0-347.0
IVO to EVC (overlap)	347.0-396.0
EVC to IVC	396.0-566.0
IVC to EVO	566.0-892.0

Even though there are only four surface validity intervals, it is not possible to create four meshes for the entire cycle. The generated meshes are valid up to a 20 crank-angle degrees span, created by the FEP mesher. There are also mesh refinements, which include a spherical region near the spark plug during ignition and early combustion stages, near the injector during fuel injection and near valve seats during valve lift. The resultant meshes are polyhedrical. Figure 12 shows the mesh refinements near the valves, the injector nozzle and the spark plug.

Overall, the mesh varies from roughly 260 thousand cells at the top dead center to 3.2 million at the bottom dead center. Regarding y^+, for the case with the highest piston velocity (4000 RPM), the average y^+ along the cycle is about 4 at the ports and valves, and about 15 for liner, piston and spark. Also, the peaks identified for ports and valves are related to valves closing (where the gap below 0.2 mm is replaced by a wall) and scale up to $y^+ = 20$. For liner, piston and spark, the peak is very brief and intense during the spark discharge, scaling up to $y^+ = 90$, very shortly.

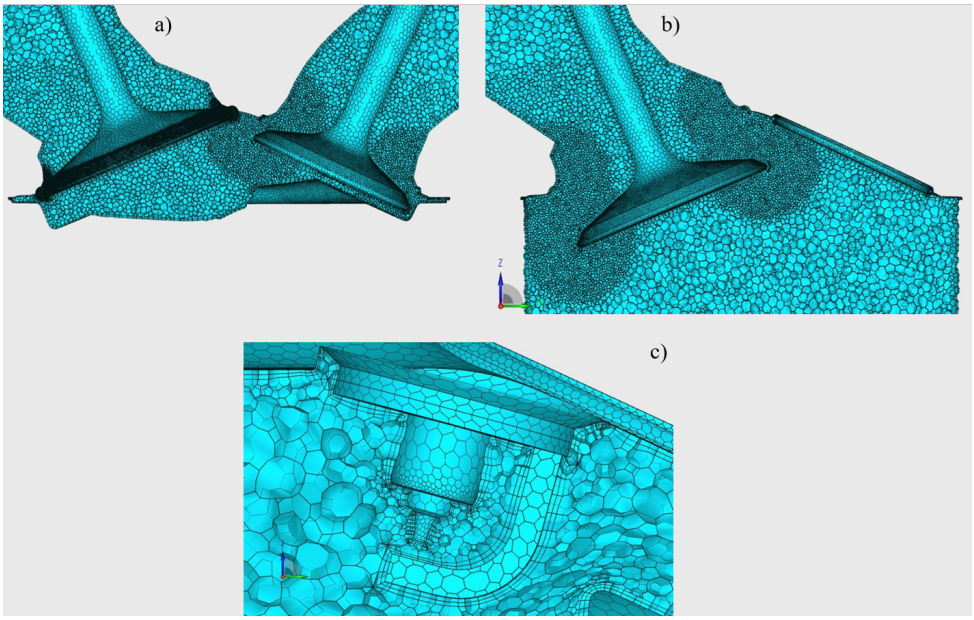

Figure 12 – Mesh refinement examples: a) Exhaust valve, $x = -0.02$ m at 359.5 CAD; b) Intake valve and injector nozzle, $x = -0.02$ m at 432 CAD; c)Spark plug, $x = 0$ m at 708 CAD.

3.3.2.3 Boundary conditions

The inlet boundary conditions are only activated when intake valve is open, i.e., between IVO and IVC. Conversely, the outlet boundary conditions are only turned on between EVO and EVC. Moreover, due to the valve overlap (all valves are open), there is a moment in which the domain is influenced by all boundary conditions, between IVO and EVC. Figure 13 shows the locations of inlet/outlet, in comparison to intake/exhaust valve for better understanding. Note that, ideally, the ports would need to be longer, to capture the pressure wave from the plenum and to avoid recirculation. However, since the focus is on the development of the method to predict knock, the geometry provided by AVL is kept unchanged. Figure 14 shows the details of each boundary condition along the cycle. Note that null values of temperature and total pressure do not mean 0 K or 0 bar; instead, they represent when the conditions cease. Besides these transient boundary conditions, Tab. 15 brings wall thermal conditions.

The fluid in its initial state is taken as air at 1 bar at 1457 K, with a density of 1.19 kg/m^3. The turbulent kinetic energy and the turbulent length scale are set to 1 m^2/s^2 and 0.001 m, respectively. Table 16 shows the initial conditions.

Regarding the physics, the modules and models are summarized in Tab. 17.

The spherical spark is set with an initial flame density of 1000 1/m, unity stretch and consumption factors, flame kernel size of 0.003 m, timed at 707 CAD and lasting for 0.0003 s, seeded at (0, 0.0065, 0.0034) m.

Although the actual gasoline is a mixture of molecules, it is numerically treated as a single-compound equivalent molecule (C_8-H_{17}). The fuel spray is at 293.15 K, injected from seven

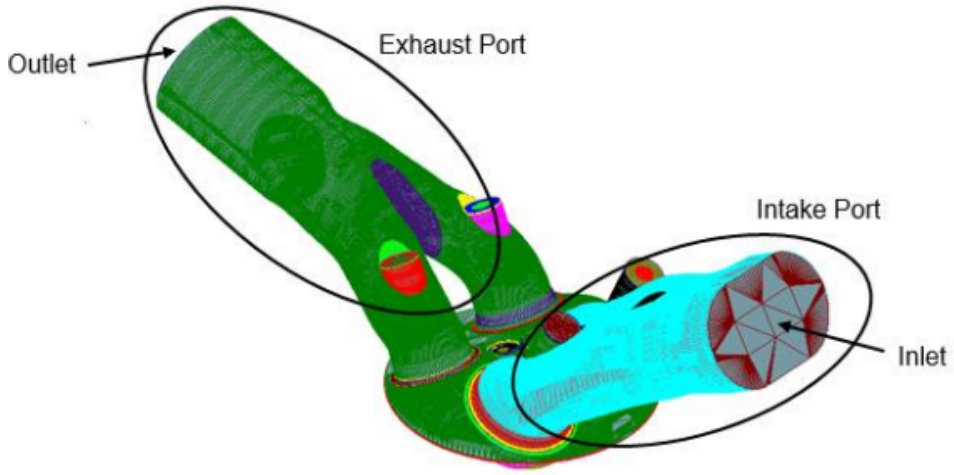

Figure 13 – Inlet/outlet boundary locations, in comparison to port locations. Adapted from AVL (45).

Table 15 – Thermal boundary conditions [K].

Intake port	310
Exhaust port	510
Piston	510
Head	510
Liner	510
Spark	550
Gasket	450
Intake valve lower	500
Intake valve upper	370
Exhaust valve lower	620
Exhaust valve upper	530
Intake seat	330
Exhaust seat	530
Injector	510
Exhaust valve wall lower	620
Intake valve wall lower	500

nozzles emerging from the injector. The Annex A shows the GDI spray and injection spreadsheet provided by AVL for FIRE simulations, for the baseline setup (4000 RPM). Table 18 shows the parameters that change for spray and fuel injection for each simulation.

3.3.2.4 Solver control

The solver control gathers discretization schemes, equation control, under-relaxation factors, differencing schemes, linear solver types, convergence criteria, among others. Among the details, it is worth mentioning that the pressure-velocity scheme is SIMPLE/PISO (a combination of both SIMPLE and PISO, for a transient simulation) the differentiation schemes (DS) are MINMOD-bounded for momentum, central (CDS) for continuity, and upwind (UDS) for

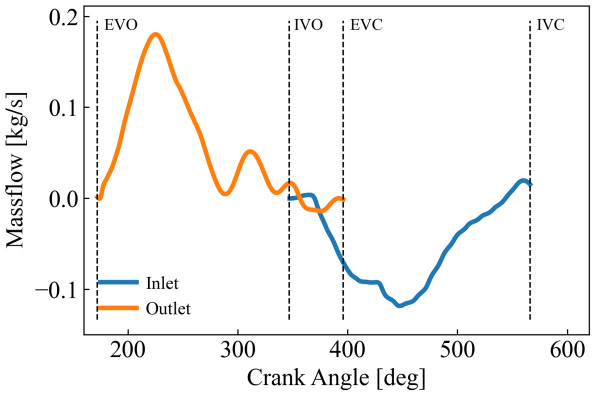

(a) Mass flow rate.

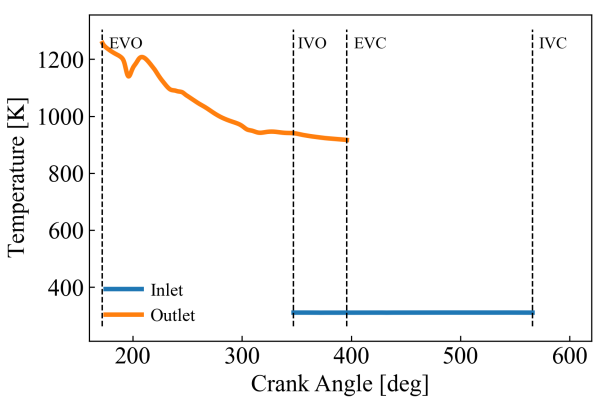

(b) Temperature.

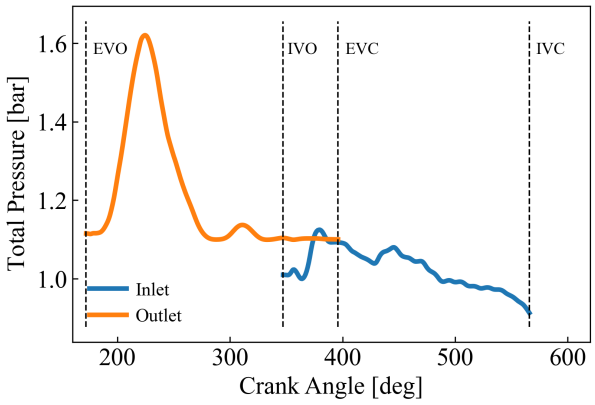

(c) Total pressure.

Figure 14 – Inlet and outlet boundary conditions.

Table 16 – Initial conditions

Region	Pressure [bar]	T [K]	k [m^2/s^2]	Turb. length scale [m]	ε [m^2/s^3]	EGR mass fraction [-]	ϕ [-]
Cylinder	4.75175	1502	10	0.001	-	1	0
Intake port	0.93489	330	8.4	0.005	-	0	0
Reinit. at 347.2 CA	1.01	330	1	-	168	0	0
Exhaust port	1.12520	1261	10	0.001	-	1	0
Intake valve gap	0.969775	332	8.4	0.000978	-	1	0
Reinit. at 347.2 CA	0.85422	326	0.8	-	1000	0	0
Exhaust valve gap	2.93847	1382	10	0.001	-	0	0

turbulence, energy and scalars, and the solution is considered converged when it reaches a 1e-4 normalized residual criteria for all equations, or the limit of 50 iterations per timestep (except at start, with 80, but always at least 10). In addition, the solution considers effects of compressibility, viscous heating, and pressure work.

Table 17 – Physics models selection

Physics	Models
Fuel	Gasoline (single component C_8H_{17})
Species	Standard species transport
Turbulence	$k-\zeta-f$
Combustion model	ECFM-3Z
Autoignition	Knock Shell Model (KSM) + TABKIN FGM knock model
Spark	Spherical model
Laminar flame speed	Metghalchi; Keck (85)
Spray	Discrete Droplet Model (DDM)
NO	Extended Zeldovich model
Soot	Soot Kinetic Model (SKM)

Table 18 – Spray and fuel injection parameters for each simulation.

Paramater | [RPM]	4750	4000	3250	2000	1000	500
Fuel mass [mg]	32.20	32.20	32.20	56.35	128.80	193.20
Fuel mass [% of baseline]	100	100	100	175	400	600
Start of injetion (SOI)			430.0			
Duration of injection (DOI)	60.4	51.1	41.8	44.9	51.1	38.7
End of injection (EOI)	490.4	481.1	471.8	474.9	481.1	468.7

3.3.2.5 Operating conditions

Since the goal is to develop a numerical indirect knock method, the construction of the whole CRFD setup is important but not the focus here. Therefore, the base setup is derived from one of AVL FIRE's 2021R1 database, with modifications. Due to the lack of experimental data to validate the numerical setup, the baseline simulation is first compared with slight setup modifications to evaluate how they influence the knock prediction. Due to the immense number of modules used for this setup, only the turbulence model is varied, to evaluate its influence on the combustion process (the so-called turbulence-chemistry or turbulence combustion interaction - TCI). Furthermore, the lack of more operating points or boundary conditions (inlet/outlet mass flow rate, temperature and pressure, wall temperature, and engine speed) is tackled by slightly changing the RPM. The change is not too large to avoid changing too much the equivalence ratio and also to avoid going too far from the actual boundary conditions for the new RPMs. However, it is not to small, in order to provide different ranges of turbulence timescales to interact with the chemical timescales, and see the influence of these interactions with the turbulence model and the knock onset.

The baseline simulation uses the $k-\zeta-f$ turbulence model, at 4000 RPM. The variations involve changing the turbulence model to $k-\varepsilon$ (both keeping the hybrid wall treatment, a generalized treatment that ensures a gradual change between viscous sub-layer and the wall functions, where the integration of the equations occur for small values of y^+ and the standard wall function takes place for the large values of y^+ (AVL (44))) and/or the rotation to 3250

and 4750 RPM. Concerning the boundary conditions, inlet and outlet mass flow rates, total temperature and pressure were kept the same, only varying the spray module according to the rotation speed. This way, different speeds yield different equivalence ratios. Figure 14 shows the boundary conditions. Note that they only affect the simulation between valve openings, and none of them happen from 566 to 892 CA.

For the knock evaluation, however, these cycles have high RPMs and are not severe enough to have relevant knock occurrence. Thus, the chosen configuration is replicated for the following pairs of RPM and fuel: 4000 RPM, 100% of fuel injected (here 100% means in relation to the baseline), 2000 RPM and 175% of fuel, 1000 RPM and 400% of fuel, and 500 RPM and 600% of fuel. As mentioned above, all cycles have their spray module adjusted to the RPM and fuel quantity.

The fluid in its initial state is taken as ideal-gas air at 1 bar and 1457 K, with a density of 1.19 kg/m^3. The cylinder starts at 1502 K and roughly 4.75 bar. The remaining models involved in the set-up are the laminar flame speed model from (Metghalchi; Keck (85)), knock shell model, spherical spark ignition model, NO extended Zeldovich model, and soot kinetics models. Each simulation ran for roughly 120 hours on a Dell Precision T7500 workstation, which has 48 GB of DDR3 RAM, and a six-core Intel Xeon X5675 @ 3.07 GHz, running AVL FIRE 2021R1 on Windows 7/10. Alternatively, they ran for roughly 100 hours on a Dell OptiPlex 5070 workstation, which has 64 GB of DDR4 RAM, and a six-core Intel CORE i5-9500 @ 3.00 GHz on Windows 10.

3.4 THE PROPOSED KNOCK ONSET METHOD

The knock onset method has to predict the timing when knocking combustion occurs. Note that it regards timing and not severity or intensity. To be considered a good method, it needs to consistently predict the timing in different scenarios, preferably on the safe side, that is, ideally matching the timing given by a reference model/quantity or predicting it before. Otherwise, this could lead to unsafe situations. The completeness of the description involves the proposed method itself, how it is calculated, which quantities it needs, where it is calculated, how it performs towards some reference values and to which simulation it is tested.

3.4.1 The Livengood-Wu integral in discrete numerical terms

For CRFD the simulations held in this research, the time-step advancement can be derived from the crank-angle degree of each output, based on the engine rotation speed. Thus, the Livengood-Wu (L-W) integral is approximated by the cumulative sum between time intervals. In case the critical value is reached between outputs, the crank-angle degree (or time) is linearly interpolated. Knock starts when the integral reaches unity, and the integral starts to be computed after the start of injection (SOI at 430.0 CAD) and stops at 800.0 CAD. This cut-off is applied because the likelihood of knock so far from the top dead center is too small to justify the

extra computational effort beyond this point. Thus, in mathematical terms, the L-W integral calculated from the discrete numerical outputs of the CRFD simulation is approximated as

$$L-W=\int_0^t \frac{1}{\tau}\mathrm{d}t \approx \sum_{i=\mathrm{SOI}}^{n} \frac{1}{\tau(t_i)}\Delta t_i \tag{65}$$

where i and n are relative to the time instants from the SOI (430.0 CAD) to the cut-off value (800.0 CAD), respectively, τ the IDT, and Δt the interval between the current CRFD output and the previous one. Note that the outputs are 0.1-1.0 CAD apart, usually 0.2 CAD.

3.4.2 Regions of interest

As previously mentioned, knock is a local phenomenon. Besides, the DI-SI is known for its stratification, also influenced by the tumbling and swirling promoted by the design of the chamber and the piston head. A vertical stratification can also happen while the piston moves up and down. A radial stratification can happen due to the position of the regions relative to the spark (which is not perfectly centered), the injection nozzle, and the valves. Therefore, the proposed model must be well-balanced to be applicable to other engines and scenarios as well.

On top of that, in order to develop a model to estimate the knock onset there is an inherent duality: large regions where knock is estimated suffer from averaging/diluting effects, while, in tiny regions, knock prediction can be missed by a few millimeters to the side. The locations can be planes, spheres, ring cylinders (a toroid with rectangular cross-section) created in AVL FIRE during pre-processing. A cross-section plane loses precision since it accounts for both near-wall and near-center regions, that are both farther from and closer to the flame front, in very different conditions. Take as an example the lack of resolution given by the Knock Shell Model applied alone (Fig. 8 showing the cross-section plane at TDC). This large spread can be reduced by the ring cylinder regions, closer to the walls, or even better, by equally spaced small spheres on the same plane.

To balance all these factors, the proposed model considers sixteen equally spaced spherical regions on the top dead center (TDC) plane ($z = 0$), near the rim. Centering them at 1 mm from the rim, with a radius of 1 mm is enough to account for near wall heat spots, vertical stratification ($-1 \leq z \leq 1$ mm) and gives quite enough space resolution. In other words, the mesh targeted 1.4 mm control volume cells, and the 2 mm diameter allows to capture at least more than one cell (note that the spheres account for cells within the region, not needing to be entirely within it). In addition, the initial idea contained eight spheres, but as will be shown in Section 4, sixteen spheres give more resolution, although it takes twice as much post-processing effort. As a reminder, Yue; Som (130) used 16 locations as well. Figure 15 shows schematically the axes, which guide the spheres nomenclature (0° onwards).

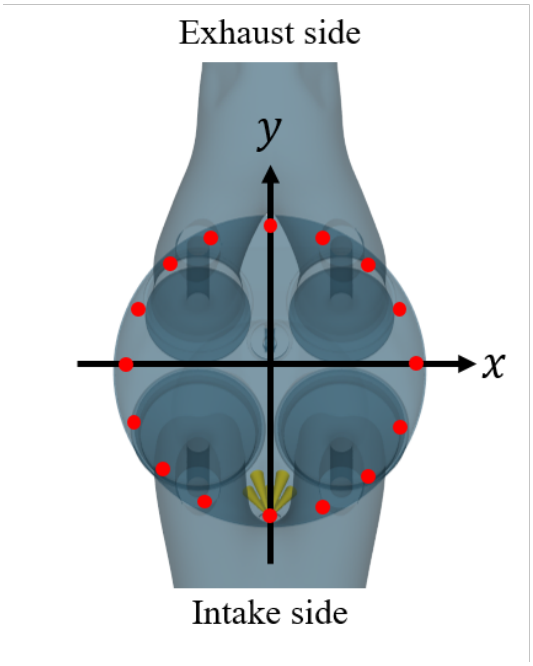

Figure 15 – GDI top view schematically representing the axes that guide the spheres nomenclature. Spheres out of scale for representation purposes.

3.4.3 Quantities of interest and data extraction

The quantities of interest for this post-processing are extracted as mean values based on the cells that belong to these spheres. They include pressure, temperature, species mass fractions, and other flow and knock-related quantities. These local quantities need to be written in C++-like formulas prior to the simulation. The quantities relative to the TABKIN FGM knock module, however, could not be extracted in this way. They are considered as advanced support (AVL FIRE Support Team, Personal Communication) and have to be manually extracted after the simulation, using AVL IMPRESS M (via the so-called Picking and Sampling workflow).

Apart from the quantities necessary for the methods applied to the L-W integral, there must be reference quantities for comparison, which may indicate the flame arrival to the region, an IDT criterion or a knock-related quantity. The references are maximum peaks in pressure, temperature, CO mass fraction, OH mass fraction, 5% of OH peak, temperature equals to 1000 K, reaction progress variable equals to 10% and 85%, knock progress variable, ignition probability, $\Omega_{1\%}$ and $\Omega_{95\%}$. Note that all values are extracted from the same regions, so they are spatially static. In other words, all references are 0D. None of the them consider the spatial displacement or evolution of the flame or other quantities, due to the already mentioned limitations in creating C++ formulas for 2D results.

3.4.4 IDT methods for the Livengood-Wu integral

Regarding the methods for IDT calculation, the post-processed quantities from FIRE can be applied to Cantera using any mechanism or evaluated by any IDT correlation. The chosen methods are three reduced mechanisms to be run in Cantera (Y. Li et al. (75), Liu et al. (77) e Tsurushima (120)) as sequential constant volume perfect stirred reactors (CV-PSR), the same approach used by (Kozarac et al. (69)), and three IDT correlations, namely the one proposed in this work (Eq. 67), the six-compound surrogate model proposed by L. Cancino et al. (17) (Eq. 10) and the vastly employed correlation developed by Douaud; Eyzat (27) (Eq. 21).

It can be argued that detailed chemical kinetics mechanisms could be a better alternative than reduced mechanisms but, as will be seen in sequence, each of the four simulations has sixteen locations where the input data for Cantera is extracted, which extends for more than 1000 timesteps. Even restricting to a range of CAD of interest (SOI to 800 CAD), as Cantera originally supports single-core processes, the time taken to evaluate all IDTs of a single CRFD run is larger than the one of the CRFD processing time itself.

Regarding Cantera simulations, some ECFM-3Z species do not belong to the regarded mechanisms. To be consistent among all mechanisms, N, NO, which have very low concentrations are added to the N_2 mass fraction. Furthermore, the CRFD simulations consider C_8H_{17} as a gasoline-equivalent molecule, so, Cantera first converts this specie to isoctane (C_8H_{18}) as it is the specie with the closest molecular mass to it, and then redistributes it to isoctane and *n*-heptane to form PRF 87. It should be noted, however, that the knock models used in AVL FIRE are not AKI/ON dependent (AVL FIRE Support Team, personal communication), which are in fact solely based on the chemical composition and the thermodynamic state.

3.4.5 Proposed method flowchart

To better illustrate how the information flows from the CRFD simulation to the calculations in Python, Fig. 16 summarizes the major steps in the process. In short, this process is repeated for each CRFD simulation, for each IDT method for the L-W integrals and the results are then compared to each reference quantity. As a final comment, since there are 16 spheres and 6 IDT methods to obtain the L-W, it is clear that applying this routine to all control volumes instead of the spheres would be computationally expensive.

3.5 FAILED OR INVIABLE ATTEMPTS

Regarding turbulence models, more demanding models were tested and diverged, as they would require finer meshes. These models are the AVL hybrid turbulence models (HTM 1 and HTM 2), which are a hybrid between $k-\varepsilon$ and RSM (Basara; Jakirlic (7)), the RSM model itself, and a low-Reynolds model, represented by $k-\varepsilon$ with the near-wall approach as the wall treatment. Similarly, the large eddy simulation (LES) would also require finer meshes,

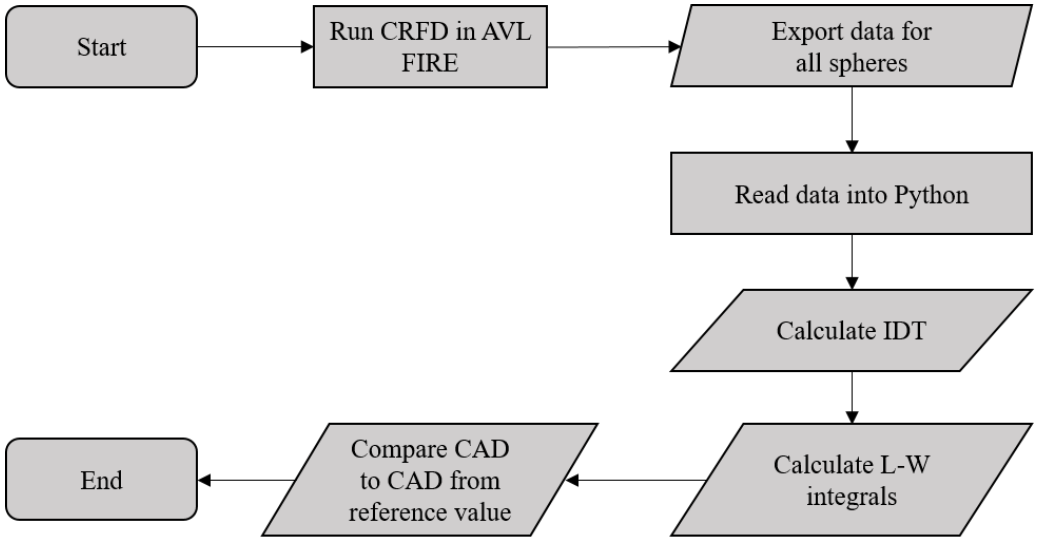

Figure 16 – Flowchart showing the proposed knock onset method.

although it introduces an interesting advantage towards RANS in terms of the local prediction that is targeted in the proposed knock method.

Since CFM are combustion models, there are inherent simplifications and limitations in their formulations. In order to overcome them, extensive work has been done trying to simulate AVL FIRE using the so-called general gas phase reactions (GGPR) species transport, which changes the modeled combustion to a mechanism-based approach, with the correspondent species, transport and thermodynamic files provided by the user. In this context, no simulation managed to reproduce the baseline (ECFM-3Z at 4000 RPM) either by the lack of ignition, or by divergence, or unmatched boundary conditions (AVL FIRE Support Team, Personal Communication). The mechanisms considered were the ones from Y. Li et al. (75), Liu et al. (77) e Tsurushima (120), as they are reduced and more compatible with the computational resources available, worth mentioning that the first one was especially developed to be less stiff in CRFD environments. In addition, there were unsuccessful attempts trying to reduce detailed mechanism via Directed Relation Graph with and without Error Propagation (DRGEP and DRG), based on IDT or IDT and LFS experimental data.

Regarding the lack of ignition, many tests included varying the spark timing, duration, model, intensity and kernel size, none of them capable of even changing the last digit of fuel/oxidizer mass fractions. In addition, attempts in converting those mechanisms into tabulated kinetics via a flamelet generated manifold approach (AVL TABKIN FGM) were not successful as well (GGPR+FGM).

4 RESULTS AND DISCUSSION

The results can be divided into different phases towards the construction of the indirect numerical knock onset method. First, the proposed multivariate and automatized routine to obtain the IDT correlation is validated using the primary alcohols database. Then, it is applied to the broader database, for transportation relevant SI-ICE fuels. In sequence, the CRFD model is validated, showing the influence of the turbulence models in the combustion, through tangible engine parameters and combustion indicators. After that, the CRFD model is applied to more demanding engine conditions, to extract the quantities of interest, to be applied to the external post-processing routine for knock prediction. Finally, these data are used to assess the IDT along the cycle by many methods, each of them applied to the L-W integral, which is then compared to some knock reference quantities.

4.1 IDT CORRELATION FOR C_1-C_4 PRIMARY ALCOHOLS

Initially, the database gathered previously published experimental data regarding low and pressure shock tubes (LPST/HPST), rapid compression machines (RCM) and ignition quality testers (IQT) for alcohols from one to four carbons. The IQT experimental points were discarded as they cannot isolate the kinetics effects from the thermo-fluid-dynamic effects (atomization, vaporization, mixing), masking the contribution of the autoignition stage. It also should be noted that branched-chain isomers were discarded as they dropped the global apparent activation energy far below the values obtained by experiments and other regressions (L. R. Cancino et al. (16), Dunphy; Simmie (33) e Noorani; Akih-Kumgeh; Bergthorson (92)). Besides, points that stated a range of values instead of a precise number were discarded too (e.g.: $\phi = 0.2 - 0.3$).

The points were limited to $1000/T$ from 0.6 to 1.2 (1666.67 K to 833.33 K). This large range was possible due to the absence of a negative temperature coefficient (NTC) in this region for alcohols. This way, there were 833 experimental points following these criteria, shown in Fig. 17 (note that the IDT plot is logarithmic and usually in relation to $1000/T$). Electing an initial logarithmic error of 2.500 and a final one of 0.222 (that gives a maximum overshoot of about 25% and a maximum undershoot of -20%), with a step of 0.001, the data-set was reduced to 275 points, shown in Fig. 18. Despite being reduced to roughly one-third of the original size, none of the literature experiments (Nativel et al. (91), Zhang et al. (132), Mathieu et al. (82), Noorani; Akih-Kumgeh; Bergthorson (92), Pinzón et al. (98), L. R. Cancino et al. (16), U. Burke et al. (12), Stranic et al. (117) e Pelucchi et al. (96)) was completely removed in the process.

Comparing both figures, in the initial database, the RCM data exclusively occurs after $1000/T > 1.0$, where it yielded higher IDT than shock tube experiments. RCM experiments take longer to happen and lead to higher heat loss. In addition, the higher IDT may lead to a

higher slope of the curve, leading to a higher global apparent activation energy. This way, after the iterations, only three RCM experimental points remained in the final database, a trend that was similarly reported by (Cooper et al. (23)), when they cleaned their database.

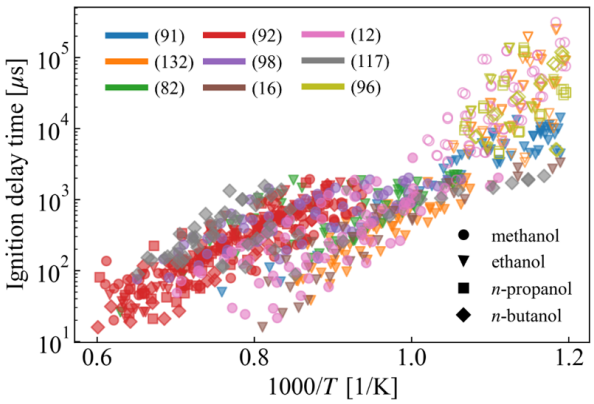

Figure 17 – Initial database ignition delay time. Filled markers represent ST data and open markers represent RCM data

Overall, the parameters of the final database ranged in the following way: pressure ranged from 0.9 to 50 bar, equivalence ratio from 0.3 to 2.0, AKI from 91.5 (*n*-butanol) to 107.5 (methanol) and IDT from 21 to 14140 μs. Methanol and ethanol correspond to the majority of the data, with ethanol being the only fuel represented above $1000/T = 1.1$ (i.e. below 909.09 K). The *n*-propanol and *n*-butanol points lay predominantly between $1000/T$ of 0.6 and 0.9 (1111.11 K to 1666.67 K), with some *n*-butanol points going up to 1.1.

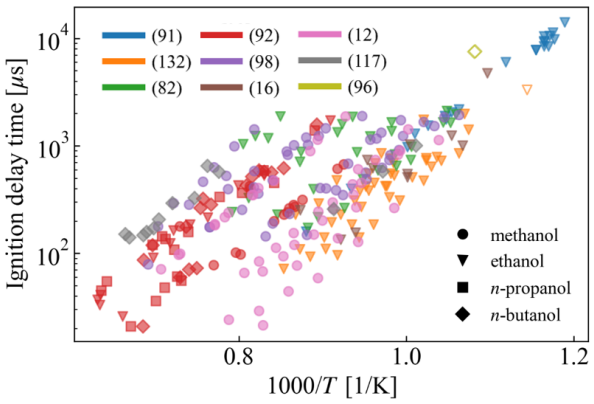

Figure 18 – Final database ignition delay time, based on the automatized and multivariate routine regarding the complete regression (T, AKI, p, ϕ). Filled markers represent ST data and open markers represent RCM data

Figure 19 shows the evolution of R^2 throughout the iterations for the four regressions. Note that the goal here is to perform the data removal based on the most complete correlation and compare the results with the three less complete correlations (removing pressure and/or equivalence ratio exponents). In the beginning, the R^2 of the complete regression is similar to the

one of the regression scaled to stoichiometry, both slightly below 0.88. The other two regressions (one scaled to 30 bar and the other scaled to 30 bar and stoichiometry) are very much alike, both slightly above 0.92. Therefore, for the initial set, the pressure scaling increases R^2. After roughly 1000 iterations, when the database has about 800 points, the R^2 of the first two regressions intensify their slope, especially for the complete regression after 1800 iterations, where it becomes evident that the routine is dedicated to improving this correlation. Eventually, it reaches a R^2 of 0.991 and the database finishes with 275 points.

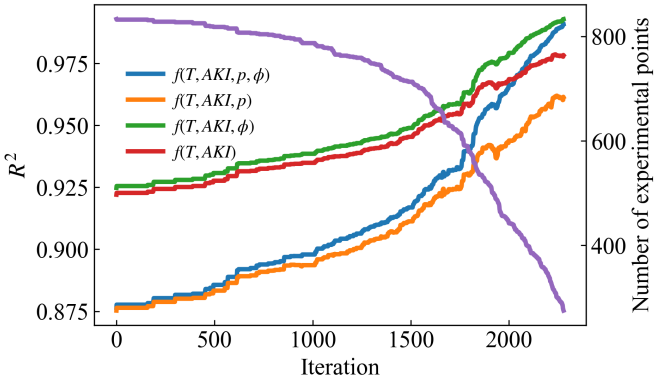

Figure 19 – Coefficient of determination (R^2) and size of database along iterations (in purple), for the complete correlation and for the correlations scaled to a common pressure (30 bar) and/or to stoichiometry.

Figure 20 shows the global apparent activation energy. It has a major downward tendency along with the iterations but with some positive fluctuations in the end. The green and the red curves are pretty much overlapped since these regressions are scaled to the same pressure. The final value of E_a is in good agreement with the literature. In fact, taking the experimental values obtained by Noorani; Akih-Kumgeh; Bergthorson (92) (converted to kJ/mol: $105.8 \pm 2.1, 134.3 \pm 2.9, 129.3 \pm 5.0, 139.3 \pm 5.4$, for methanol, ethanol, *n*-propanol, and *n*-butanol, respectively), and weighting by the number of points per fuel, the weighted average is 123.3 kJ/mol, which means that the predictions are not far from it. As a reference, L. R. Cancino et al. (16), in their regression for ethanol (Eq. 13), observed a 8% deviation in respect to experiments.

Figure 21 shows the average absolute error after each iteration. The overall error for the complete regression drops to nearly 10%, while it is roughly 60% for both regressions scaled to pressure. As a reminder, the final logarithmic error of 0.222 led to an overshoot of up to 25% and an undershoot of up to -20%. And, to visualize better these metrics, Figure 22 compares the predicted values to the experimental ones, where the dashed black line represent perfect parity and the two grey-dashed lines represents the region within plus/minus the average absolute error.

Table 21 summarizes the coefficients and their standard errors for each regression, alongside the metrics commented above. As a reminder, the regressions are represented by the following

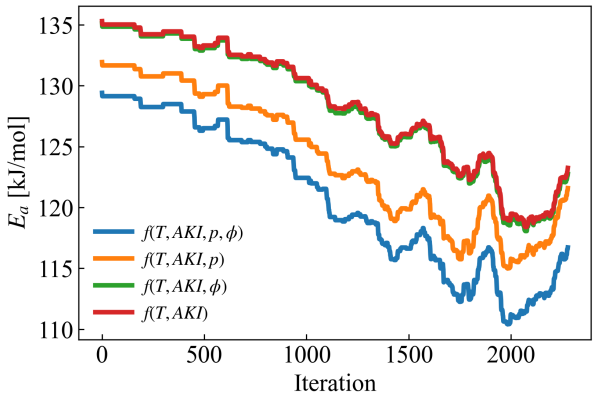

Figure 20 – Global apparent activation energy (E_a) along iterations

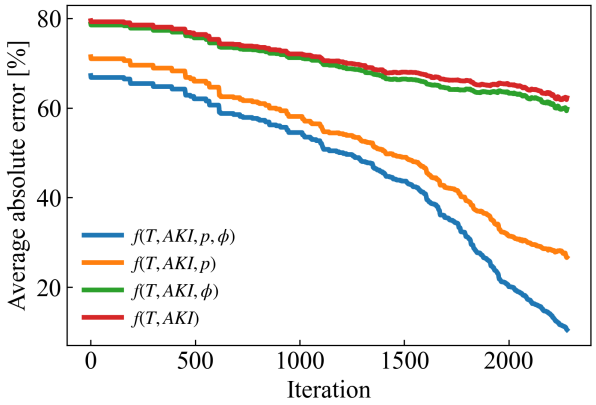

Figure 21 – Average absolute error along iterations

shape, to be comparable with the regressions shown in Section 2.6 from other works

$$IDT = 10^{a} \exp\left(\frac{E_a}{RT}\right) AKI^{b}\, p^{c}\, \phi^{d} \tag{66}$$

where 10^{a} represents the pre-exponential factor A.

Overall, the regressions presented high R^2. Even though the regression scaled to 30 bar is slightly better in terms of R^2, it is much worse in relation to the complete regression in terms of average absolute error and over/undershooting. In particular, overshooting is more important than undershooting as the goal is to be on the safe side preventing knock on real spark ignition engine applications. Therefore, R^2 should not be used alone. In terms of standard errors, they increase when the dependency upon equivalence ratio is removed (lines two and four of the table). In terms of pre-exponential factor, they decrease when the dependency upon pressure is removed (lines three and four of the table). This is basically a mathematical compensation since the pressure exponent no longer exists.

Even though some regressions shown in Section 1 represent oxygenated gasoline surrogates instead of pure alcohol fuels, some comparisons can be done. Still, there was no correlation found in the extent of the literature review that brings all coefficients. The pressure exponent

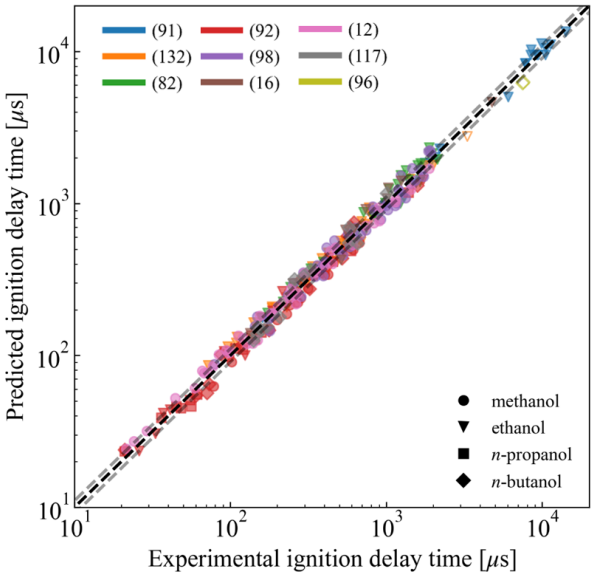

Figure 22 – Experimental versus predicted ignition delay times. Filled markers represent ST data and open markers represent RCM data. The Dashed black line represents perfect match and the two grey dashed lines represent the average absolute error

is the only exponent that remains negative for all correlations. It ranges from -0.88 to -1.76, as shown in Section 2.6. Therefore, the higher the pressure, the lower the IDT. The equivalence exponent ranges from -0.283 to 1.56. The closest value to the two shown in Tab. 21 (-0.49 and -0.55) is -0.577 from Eq. 20. This is an interesting result because Cooper et al. (23) derived this correlation from a compilation of previously published experiments too.

The AKI exponent appears only on the correlation of L. Cancino et al. (17) as 1.11. It seems reasonable as a higher AKI means a higher knock resistance, thus, leading to higher IDTs. According to Tab. 21, however, the AKI exponent is always negative and varies little from regression to regression. This result might seem counter-intuitive, but the whole process showed that the statistical metrics are very good and the other exponents are in good agreement with the literature. Therefore, this topic is further investigated, and this is the goal of the next sections.

Table 19 – Summary results for all correlations

Regression	a	E_a	b	c	d	R^2	AAE	Oversh.	Undersh.
T, AKI, p, ϕ	0.82 ± 0.28	116.7 ± 0.7	-1.39 ± 0.14	-0.89 ± 0.01	-0.49 ± 0.02	0.991	10.5%	24.4%	-20.0%
T, AKI, p[1]	0.70 ± 0.62	121.6 ± 1.5	-1.40 ± 0.31	-0.97 ± 0.02	-	0.961	26.6%	101.1%	-44.0%
T, AKI, ϕ[2]	-1.06 ± 0.35	122.8 ± 0.6	-1.28 ± 0.18	-	-0.55 ± 0.02	0.993	59.8%	67.8%	-96.8%
T, AKI[3]	-0.90 ± 0.62	123.2 ± 1.1	-1.37 ± 0.31	-	-	0.978	62.3 %	112.0%	-97.3%

[1] Scaled to stoichiometry.
[2] Scaled to 30 bar.
[3] Scaled to stoichiometry and 30 bar.

4.1.1 Correlations from Cantera IDT simulations

To better understand the negative AKI exponent, the following sections try to isolate the influences of each fuel and also of the different test benches by treating first the correlations with respect to each fuel and also using Cantera IDT results obtained from the experimental input data. Similarly, to give a better base of comparison between the 0D IDT simulations, two different detailed chemical kinetics mechanisms are considered, and also their assessment towards 1D laminar flame speed (LFS) simulations.

4.1.1.1 Regressions for each fuel treated separately

To avoid overwhelming plots when comparing experiments to Cantera simulations, Fig. 23 shows the IDT per fuel. The best line is displayed for simulations instead of individual points. It is clearer to read but it considers multiple conditions at once. Note that when handling one single fuel, the AKI is always the same and this exponent is zero. Overall, the scattering that occurs in RCM experiments is severely reduced, since the simulations do not account for the extended heat loss, when compared to shock tube experiments. For this reason, the simulations of RCM points mostly underpredict the IDT (although most shock tube points also lie on the underpredicted side too). In addition, the absence of heat loss effects seems to reduce the slope of the plots, which represents the global apparent activation energy. Nevertheless, as discussed previously, this visual inspection might be tricky, as the data presents wide ranges concerning different dependencies (T, p, AKI, ϕ).

For this reason, Tab. 20 shows multiple linear regressions (MLR) for each fuel regarding the four variables. Concerning pressure, stoichiometry and IDT, the regressions are valid for the following ranges: methanol for $1.0 \leq p \leq 50.0$ bar, $0.5 \leq \phi \leq 2.0$, $20 \leq$ IDT ≤ 312100 μs; ethanol for $1.0 \leq p \leq 54.0$ bar, $0.3 \leq \phi \leq 2.0$, $16 \leq$ IDT ≤ 249500 μs; *n*-propanol for $2.0 \leq p \leq 30.0$ bar, $0.5 \leq \phi \leq 2.0$, $21 \leq$ IDT ≤ 136400 μs; *n*-butanol for $0.9 \leq p \leq 45.7$ bar, $0.5 \leq \phi \leq 2.0$, $16 \leq$ IDT ≤ 118200 μs.

Noorani; Akih-Kumgeh; Bergthorson (92) regressions based on experiments had the following E_a values for methanol, ethanol, *n*-propanol, and *n*-butanol, respectively: $105.8 \pm 2.1, 134.3 \pm 2.9, 129.3 \pm 5.0, 139.3 \pm 5.4$ kJ/mol, when converted $R = 1.987 \times 10^{-3}$ kcal/(mol.K), used by the referred author, to $R = 8.314 \times 10^{-3}$ kJ/(mol.K). When based in their simulations, the values change to $126.8 \pm 0.4, 150.2 \pm 1.7, 149.8 \pm 1.3, 160.3 \pm 1.7$ kJ/mol, respectively. Note that their regressions are dependent upon *T, p*, ϕ, and *D*, which is the ratio of argon to oxygen mole fraction. Therefore, while simulations from Noorani; Akih-Kumgeh; Bergthorson (92) always overpredict E_a, CRECK and CCRC yielded much better agreement with this respect. In addition, they reported that methanol had the lowest E_a compared to the other fuels. However, Tab. 20 shows that methanol, ethanol and *n*-propanol have comparable E_a and that *n*-butanol has the lowest one, for both experiments and simulations.

By visual inspection, it seems that for $1000/T > 1.1$ there might be a negative temperature

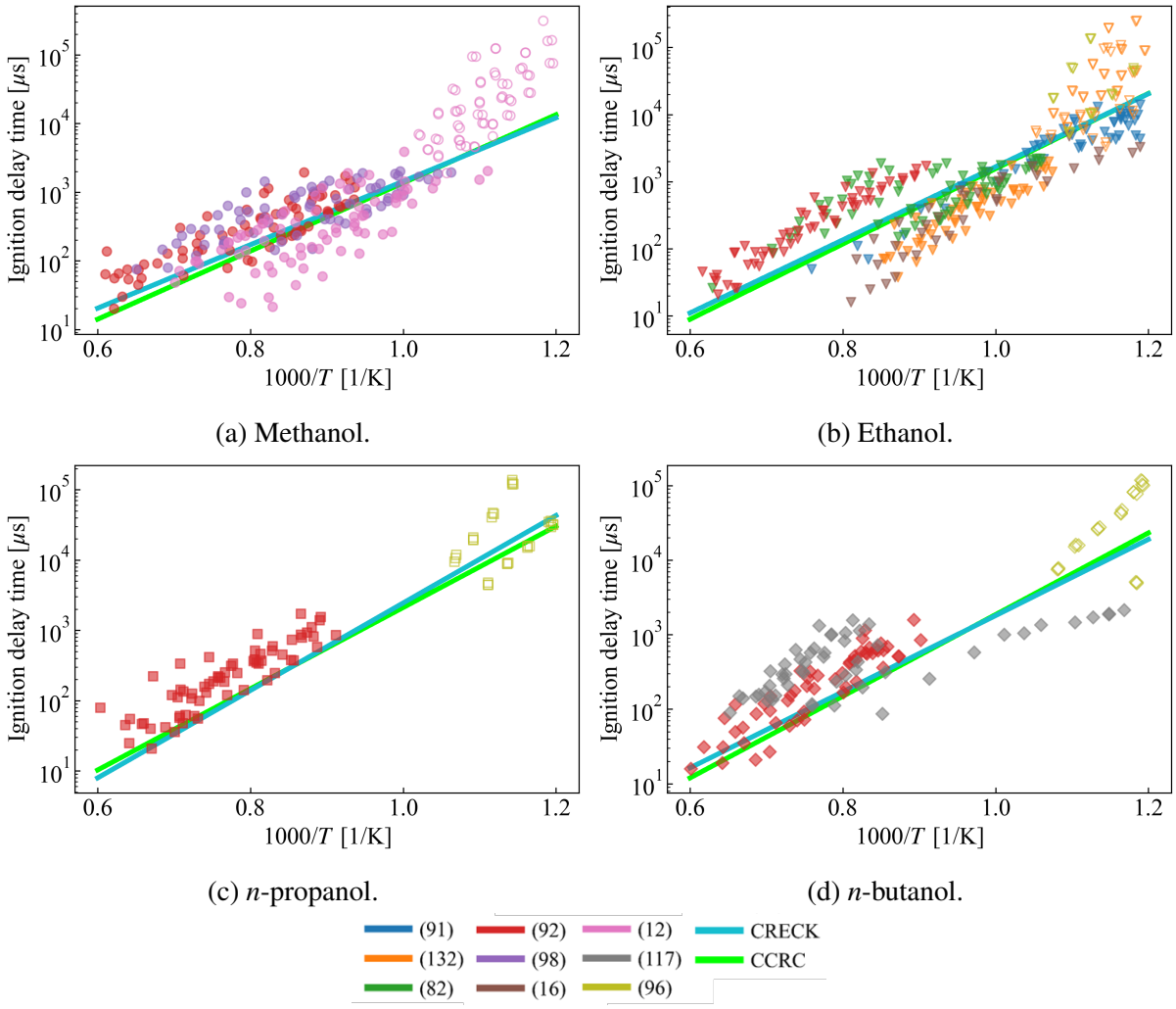

Figure 23 – Ignition delay time results comparing Cantera CVR simulations to published experiments. Filled markers represent ST data and open markers represent RCM data.

Table 20 – IDT correlations for each fuel correlation considering *T, AKI, p, ϕ*

Fuel	Regression	a	E_a	b	c	d	R^2
Methanol	Experiments	-3.04 ± 0.14	142.8 ± 3.6	-	-0.80 ± 0.05	-0.57 ± 0.09	0.876
	CRECK	-3.03 ± 0.02	140.1 ± 0.5	-	-0.94 ± 0.01	-0.52 ± 0.01	0.997
	CCRC	-2.67 ± 0.01	133.8 ± 0.3	-	-0.95 ± 0.01	-0.53 ± 0.01	0.999
Ethanol	Experiments	-2.72 ± 0.12	136.7 ± 2.9	-	-0.99 ± 0.05	-0.62 ± 0.09	0.880
	CRECK	-3.13 ± 0.01	140.9 ± 0.1	-	-0.87 ± 0.01	-0.60 ± 0.01	0.999
	CCRC	-2.91 ± 0.01	136.3 ± 0.3	-	-0.83 ± 0.01	-0.56 ± 0.01	0.999
n-propanol	Experiments	-2.32 ± 0.12	130.2 ± 3.7	-	-0.84 ± 0.10	-0.89 ± 0.18	0.958
	CRECK	-2.84 ± 0.05	136.2 ± 1.4	-	-0.91 ± 0.04	-0.52 ± 0.07	0.994
	CCRC	-3.17 ± 0.04	142.3 ± 1.3	-	-0.83 ± 0.03	-0.42 ± 0.06	0.996
n-butanol	Experiments	-1.68 ± 0.13	112.3 ± 3.5	-	-0.73 ± 0.07	-0.47 ± 0.20	0.901
	CRECK	-2.73 ± 0.05	129.2 ± 1.2	-	-0.78 ± 0.02	-0.28 ± 0.07	0.990
	CCRC	-2.29 ± 0.08	118.4 ± 2.0	-	-0.66 ± 0.04	-0.07 ± 0.11	0.970

coefficient (NTC) for *n*-butanol, which can justify the reduction in E_a. One possible reason is that it is the largest molecule studied in this work. Concerning other works, Ma et al. (79) found 137 kJ/mol for their ethanol experiments and L. R. Cancino et al. (16) found 139.3 kJ/mol for ethanol experiments, and 151.6 kJ/mol for their simulations. Therefore, both CRECK and CCRC mechanisms have much better agreement than L. R. Cancino et al. (16) simulations, with respect to E_a. At last, the mechanism that is closer agreement in terms of E_a is always closer in terms of the pre-exponential factor (CRECK being better for methanol and *n*-propanol and CCRC for ethanol and *n*-butanol).

Concerning pressure, the mechanisms perform similarly and in good agreement with the experiments. In fact, the pressure exponent is close to the ones from L. R. Cancino et al. (16), as they obtained -0.88 and -0.89 for their regressions based on experiments and simulations, respectively. This is expected to happen since IDT mechanisms have some pressure-dependent-Ahrrenius reactions with rate constants that exhibit more regular behavior in comparison with temperature-dependent reactions. Other dependencies such as temperature, on the other hand, are more complex, leading to different regions, like NTC.

In relation to stoichiometry, the mechanisms reproduce well this dependency for methanol and ethanol. Note that, for *n*-butanol the uncertainty regarding this exponent is larger than its own value for CCRC. The points mostly have ϕ of 0.5, 1.0, 2.0, and sometimes 0.3. These are very few and very different conditions and may lead to some uncertainties. However, it is better to represent ϕ as it is than to scale the data to a common equivalence ratio by a scalar factor (e.g.: ϕ_{old}/ϕ_{new}). In general, the scaling might not be linear between very distant conditions as the kinetics change a lot with ϕ (check LFS results, for instance).

Looking at the metrics, R^2 seems to be low for methanol and ethanol regressions based on experiments, while this is not the case for the other two fuels. This is expected to happen because the first two alcohols have more RCM data, which leads to increased scattering. When compared to regressions based on simulations, R^2 is extremely high, probably because the scattering caused by heat loss is not considered in simulations. Furthermore, the simulations do not account for differences caused by test facilities.

The average absolute error (i.e. relative error to the experiments, without sign), and the over/undershoot might seem alarming; however, a proper IDT study is composed of many points on multiple conditions, and, in the case of the present work, the conditions are very vast and for multiple variables. Furthermore, most studies compare the trends regarding each set of experiments. When analyzing the plots in a more holistic view, the simulations are in good agreement with the experiments.

4.1.1.2 Regressions for all fuels treated together

To add the AKI exponent to this comparison, it is not simple to gather the four fuels into a single regression. If done in this way, the errors above might be even larger. Therefore, the correlations shown in Tab. 21 are from regressions that underwent the automatized approach,

to drop data that leads to large individual errors to the regression. The first row was already presented in the past sections. Previously, different correlations starting from the same initial database and arrived at the same final database to describe the method. In this section, however, the each correlation has its own final database, since the goal here is to analyze the differences among experiments and mechanisms.

The final databases (Fig. 24) have 275, 209, and 175 points for experiments, CRECK and CCRC, respectively. The pressure and equivalence ratio exponent are in excellent agreement, as well as the statistical metrics. The mechanisms predicted similar but higher E_a. Nevertheless, this value is close to the ones described in Tab. 20, where each fuel was individually regarded. Finally, the largest difference is with respect to AKI. This time, CRECK yielded a negative but close to zero value and CCRC yielded a positive value. Similarly to ϕ, there are limited AKI bins, which may lead to uncertainties regarding this exponent. In addition, different AKIs mean different fuels and different reaction pathways. Therefore, it is even harder to reduce uncertainties. This validation phase could have considered more alcohols but they might not be relevant to the transportation industry. The conclusion is that, even counter-intuitive, this exponent is acceptable as an IDT regression is a simpler representation of detailed mechanisms, for broad conditions regarding multiple fuels.

Table 21 – Summary results for all correlations considering *T, AKI, p*, ϕ

Regression	a	E_a	b	c	d	R^2	AAE	Oversh.	Undersh.
Experiments	0.82 ± 0.28	116.7 ± 0.7	-1.39 ± 0.14	-0.89 ± 0.01	-0.49 ± 0.02	0.991	10.5%	24.4%	-20.0%
CRECK	-2.90 ± 0.38	139.1 ± 0.8	-0.04 ± 0.18	-0.93 ± 0.01	-0.55 ± 0.02	0.994	10.6%	28.9%	-20.8%
CCRC	-4.40 ± 0.37	140.4 ± 0.8	0.73 ± 0.18	-0.94 ± 0.01	-0.49 ± 0.02	0.995	9.8%	25.1%	-20.5%

4.1.1.3 Laminar flame speed simulations

Figure 32f shows the results for all LFS simulations in comparison with the experiments from Veloo et al. (125) and Veloo; Egolfopoulos (124). Overall, there is a better agreement with the data for lean and stoichiometric conditions. This is similarly reported by Veloo et al. (125), Veloo; Egolfopoulos (124), Vancoillie et al. (122). Nevertheless, only ethanol over-predicts the LFS on the lean side of the plots, while all alcohols over-predict the results on the rich side.

For all alcohols, the experiments yielded peak LFSs at $\phi = 1.1$. The simulations confirmed this trend except for methanol, which LFS peak occurred at $\phi = 1.2$. This difference was also reported by Veloo et al. (125) when they used the model from Z. Zhao et al. (133). Similarly, Vancoillie et al. (122) reported this event in their simulation at 298 K, using the mechanism proposed by J. Li et al. (74), following a multicomponent formulation considering only the Soret effect in CHEM1D. Unfortunately, they highlighted that it was not possible to perform the experiment at $\phi = 1.2$.

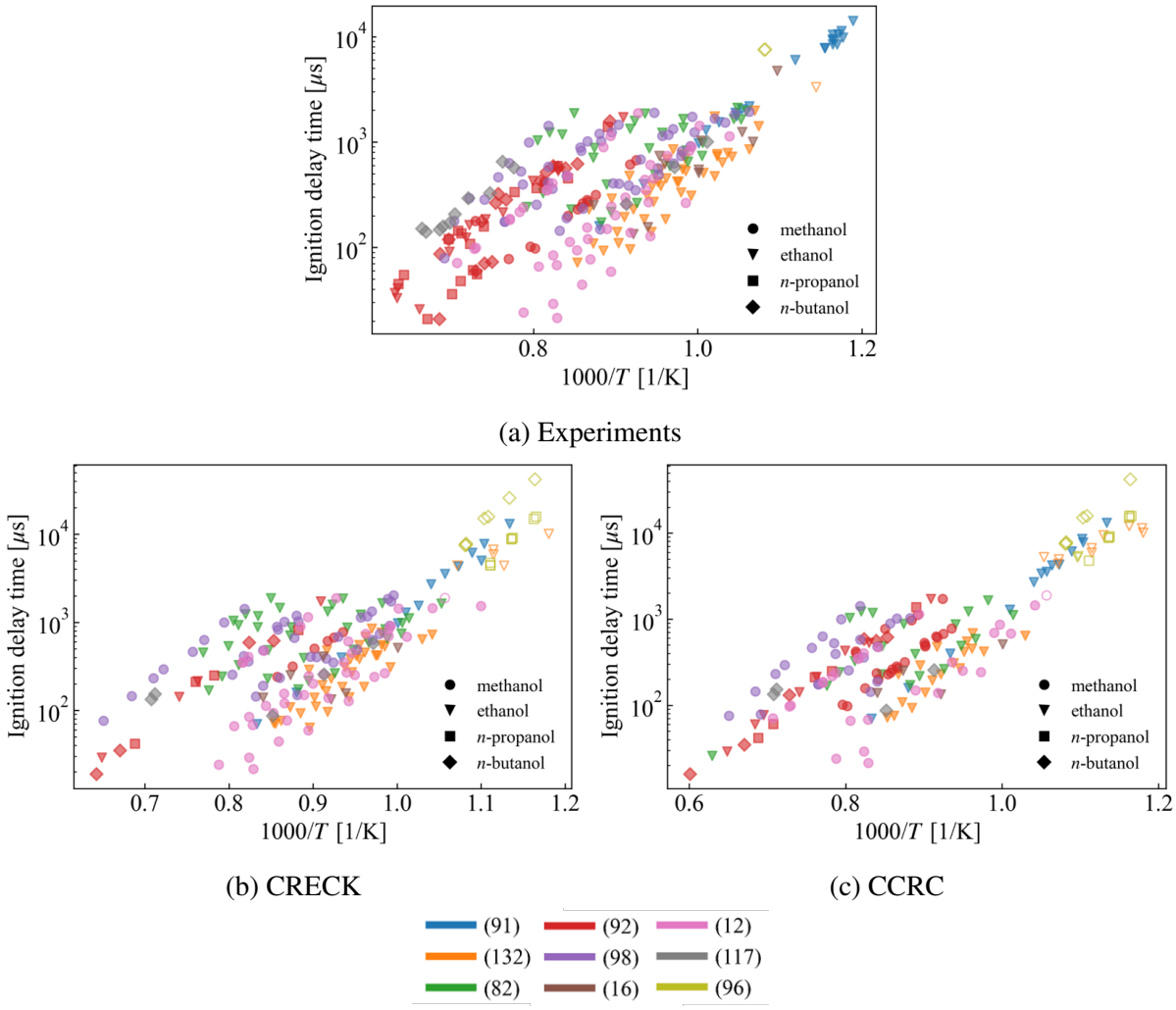

Figure 24 – Final database shape after automatized multivariate routine, targeting three different improvements (based on predictions of experiments, and simulations using CRECK and CCRC). Filled markers represent ST data and open markers represent RCM data.

Methanol showed velocities higher than the three much similar results for the other alcohols, which was also reported by Veloo et al. (125). Concerning the LFS peak magnitude, the experiments show similar peaks LFS magnitudes for ethanol, *n*-propanol and *n*-butanol, 51.0, 51.0, and 50.0 cm/s, respectively, while methanol has a peak LFS of 57.1 cm/s. The simulations ranged from 55.2 to 57.2 cm/s for ethanol, from 50.8 to 52.6 cm/s for *n*-propanol, from 50.4 to 53.3 cm/s for *n*-butanol, and from 57.8 to 62.2 cm/s for methanol. Therefore, the parity among ethanol, *n*-propanol and *n*-butanol was preserved only for the latter two.

Table 22 shows the average absolute error among simulations and experiments. Overall, simulations without both the Soret and radiation effects perform worst. The simulations with Soret are comparable between them but the one with both effects is better in 7 out of 8 times. In addition, CRECK produces always the best results on average, except for *n*-butanol.

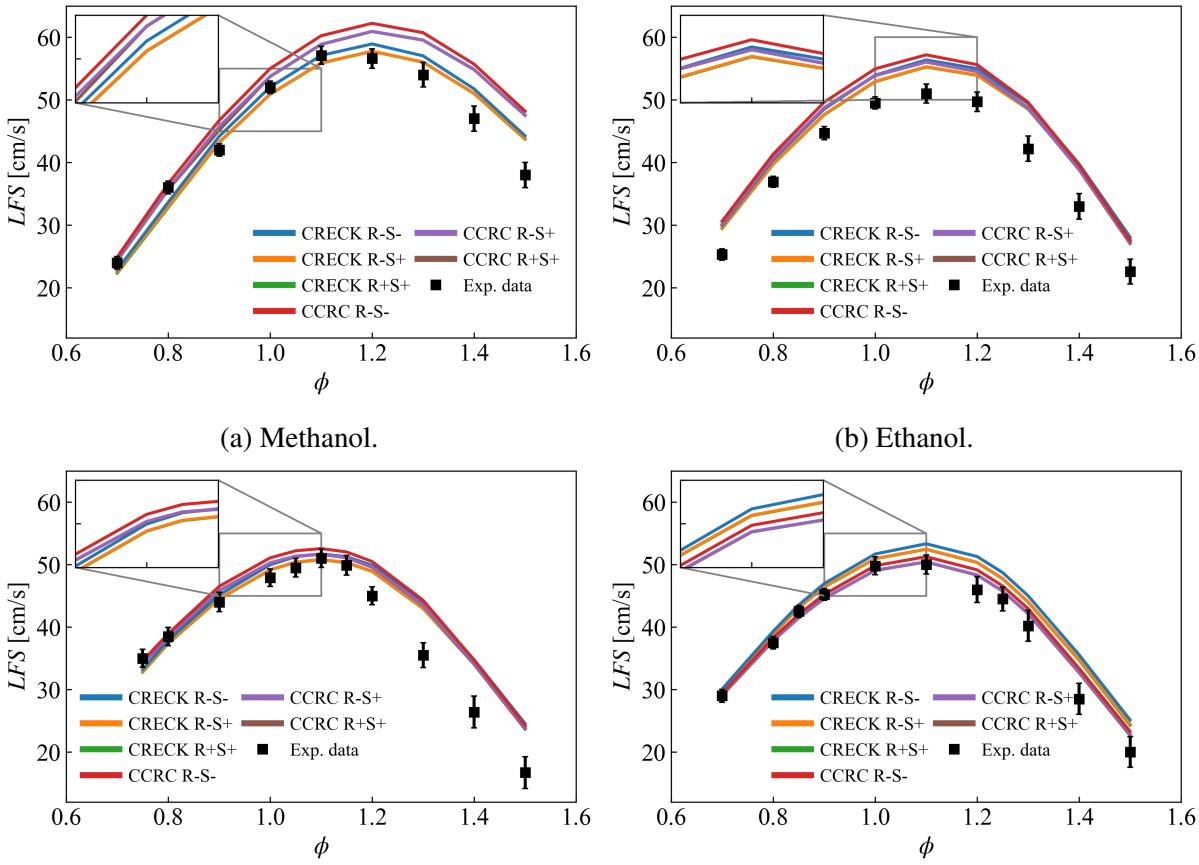

(a) Methanol.

(b) Ethanol.

(c) *n*-propanol.

(d) *n*-butanol.

Figure 25 – Laminar flame speed results comparing Cantera laminar flat flame simulations to twin counterflow experiments Veloo et al. (125) and Veloo; Egolfopoulos (124), at 1 atm and 343 K. R and S stand for radiation and Soret effect, respectively. + and - stand for turning these effects on or off.

Table 22 – Average absolute error per simulation [%]. R and S stand for radiation and Soret effect, respectively. + and - stand for turning these effects on or off

Fuel	CRECK			CCRC		
	R-S-	R-S+	R+S+	R-S-	R-S+	R+S+
Methanol	5.9	5.7	5.8	10.6	8.7	8.4
Ethanol	14.3	12.4	12.2	15.4	13.5	13.2
n-propanol	12.2	10.9	10.7	12.8	11.3	11.1
n-butanol	9.9	8.2	8.0	5.4	4.6	4.4

4.2 IDT CORRELATION FOR SI-ICE TRANSPORTATION FUELS AND SURROGATES

Based on the results of the validation phase, where practically all RCM were removed for the final database and on the observations of Cooper et al. (23), the broader database does not consider them for starters. So, the experiments from Barraza-Botet et al. (6) (IQT) and Cai et al. (13), Cheng et al. (19), Fang et al. (35), Gail et al. (38), He et al. (55), Kang et al. (64), Kukkadapu et al. (71) e Mansfield et al. (81) are not considered.

In addition, the temperature range for this database is $0.6 \leq 1000/T \leq 1.1$ (909.09 to 1666.67 K), as this can provide a large application range, and capture a slight negative temperature coefficient (NTC) region but not large enough to spoil the linear-like behavior.

The logarithmic error's threshold also starts from ± 2.500 and finishes at ± 0.222, with a step of 0.001, the same way as the validation run. The difference here is that it was observed a stall in the points removal, with several of the first iterations in which no points were removed. Since the current database is larger than the previous one, the regressions have to deal with larger arrays and, consequently, the routine takes longer to run. As an improvement, the routine previously calculates the maximum error at the first iteration and recalibrates the initial ± 2.5 threshold to this number. In practice, this reduced by 31.3% the number of iterations taken.

The points were limited to $1000/T$ from 0.6 to 1.1 (1666.67 K to 909.09 K). This way, there were 1097 experimental points following these criteria, shown in Fig. 26. The data-set was reduced to 550 points (approximately half of the original size), shown in Fig. 27. Overall, the parameters of the final database ranged in the following way: pressure ranged from 2.0 to 60.0 bar, equivalence ratio from 0.35 to 2.0, AKI from 80.0 (PRF 80) to 109.25 (toluene), and IDT from 21 to 9655 μs.

This time, however, four out of the initial twenty papers had their data completely removed from the database, (L. R. Cancino et al. (15, 16), H. Li et al. (73) e Zhang et al. (132)). They include HPST experiments for ethanol, ethanol/isoctane (25/75 volume), iso-octane/toluene/n-heptane/di-iso-butylene/ethanol (30/25/22/13/10) and TPRF 87 (56% isoctane, 17% *n*-heptane, 27% toluene in mole). It should be noted that all points from L. R. Cancino et al. (15, 16) e Zhang et al. (132) were cleaned by overprediction and all from H. Li et al. (73) were underpredicted. However, it is not possible to determine if this is bench-related. L. R. Cancino et al. (15, 16) performed their experiments at the IVG-UDE (Duisburg-Essen University, Germany) but L. R. Cancino et al. (14, 17) performed as well. Zhang et al. (132) performed their experiments at UB and at NUIG (Galway, Ireland). No other experiments have been performed at UB but Lee et al. (72) e L. Cancino et al. (17) performed there too. At last, H. Li et al. (73) was the only one to perform at SJTU (Shanghai Jiao Tong University, China).

Figure 28 shows the evolution of R^2 along iterations. This time, as the database is more diverse and larger, it started from a lower value (0.818) than the validation database but finished at 0.987, in an always upward trend. Figure 29 shows E_a along iterations. Differently than the validation case, where it had a downward trend with a slight increase in the end, it had now a very moderate increase during the first half, followed by an increase in the end. Figure 30 shows the AAE along iterations. It follows the same downward trend as in the validation case, but this time started with a much smaller AAE (36.6% versus roughly 70%). Figure 31 shows the parity plot, comparing the experimental IDT to the predicted IDT based on the obtained correlation.

Thus, overall the IDT correlation has the following shape, with a R^2 of 0.987, an average

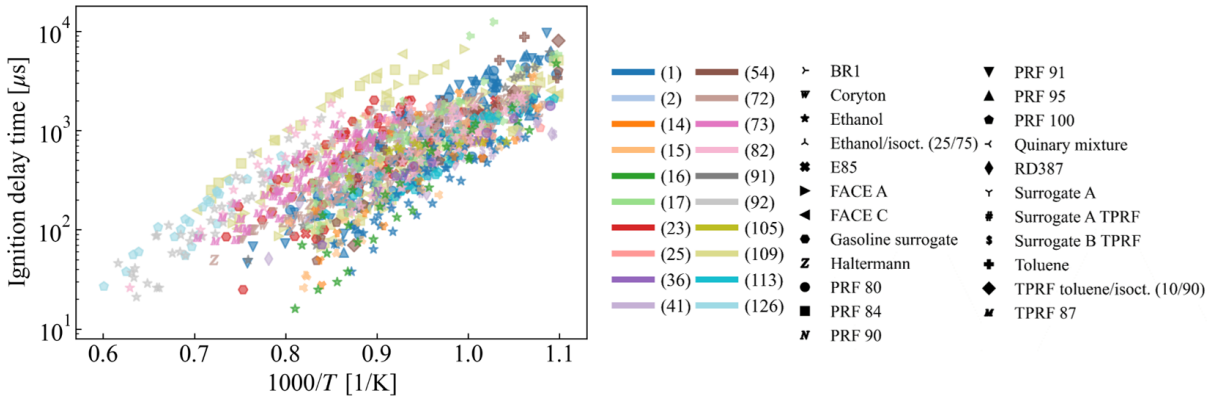

Figure 26 – Initial database ignition delay time for SI-ICE transportation fuels.

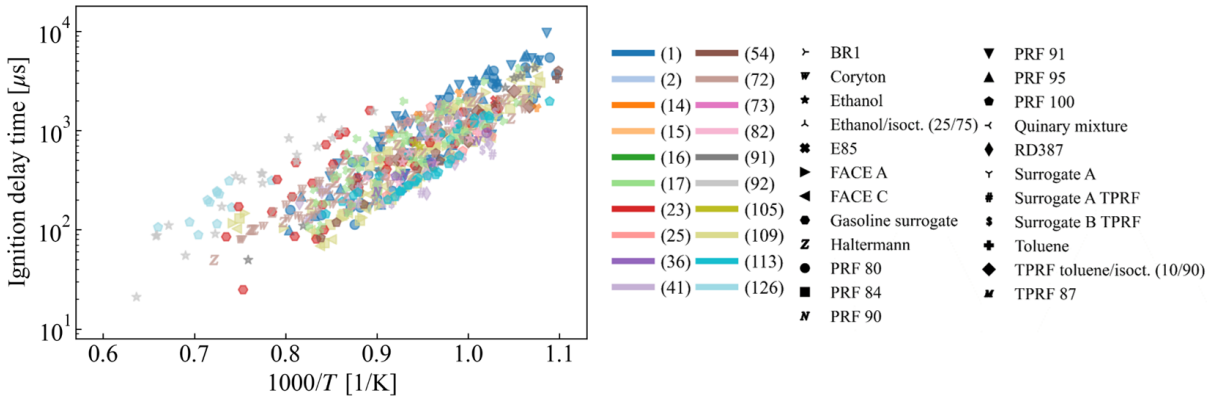

Figure 27 – Final database ignition delay time for SI-ICE transportation fuels.

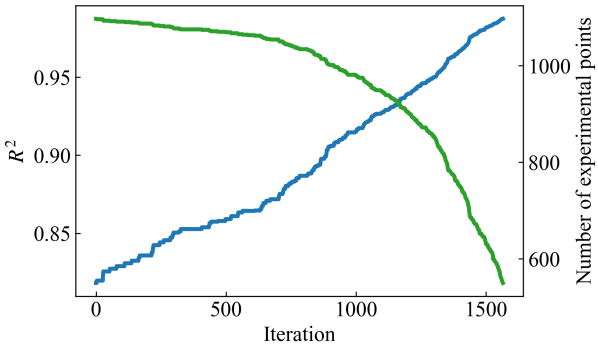

Figure 28 – Coefficient of determination (R^2) and size of database along iterations for SI-ICE transportation fuels.

absolute error of 9.7%, and an over/undershoot of 24.9% and -19.9%, respectively.

$$IDT = 10^{-3.34\pm0.15} \exp\left(\frac{111.5 \pm 0.5}{RT}\right) AKI^{0.90\pm0.07}\, p^{-0.85\pm0.01}\, \phi^{-0.46\pm0.01} \tag{67}$$

This correlation draws some comparisons with other published correlations, especially from L. Cancino et al. (17) (Eq. 10). The E_a is very alike, 111.5 kJ/mol versus 109, overlapped if con-

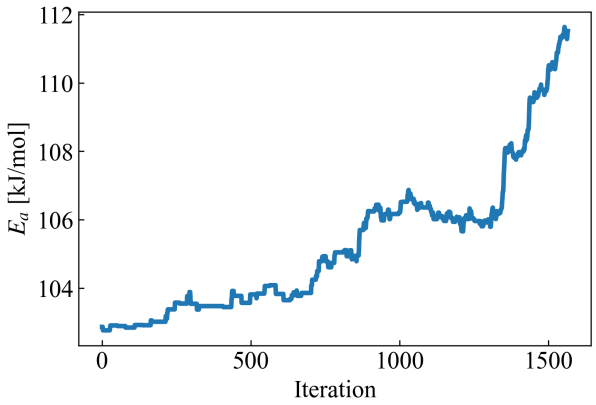

Figure 29 – Global apparent activation energy (E_a) along iterations for SI-ICE transportation fuels.

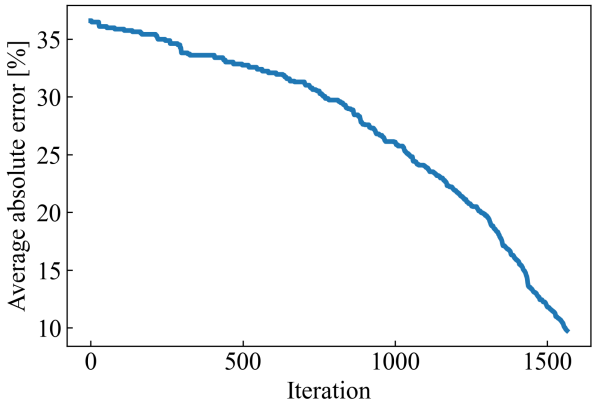

Figure 30 – Average absolute error along iterations for SI-ICE transportation fuels.

sidered the standard errors. The value is very similar to 110.9 (Eq. 20), obtained by Cooper et al. (23), worth mentioning that their research was also based on a gathered base of experiments. Furthermore, it is also close to 124.8±23.7 (ethanol/isoctane 25/75% in liquid volume, Eq. 11), 101±14.3 (*i*-octane, toluene, *n*-heptane, di-*i*-butylene and ethanol (30%/25%/22%/13%/10% in liquid volume, Eq. 12) from L. R. Cancino et al. (15) due to the larger standard error for these ones, Similarly, for AKI, the 0.90±0.07 compared to 1.11±0.24 overlaps in the same way. Note that, this time, it is positive and is not counter-intuitive.

Regarding the pressure exponent, similarly to what was pointed in the validation phase, it is very consistent with the findings of L. R. Cancino et al. (16), for both their experimental-based and simulation-based correlations (although they are both ethanol), the experimental-based correlation from Cooper et al. (23) and in slight agreement with L. R. Cancino et al. (15) for their quinary mixture (overlaps if the standard errors are considered). For the equivalence ratio exponent, it is closer to the exponent obtained from the database of Cooper et al. (23).

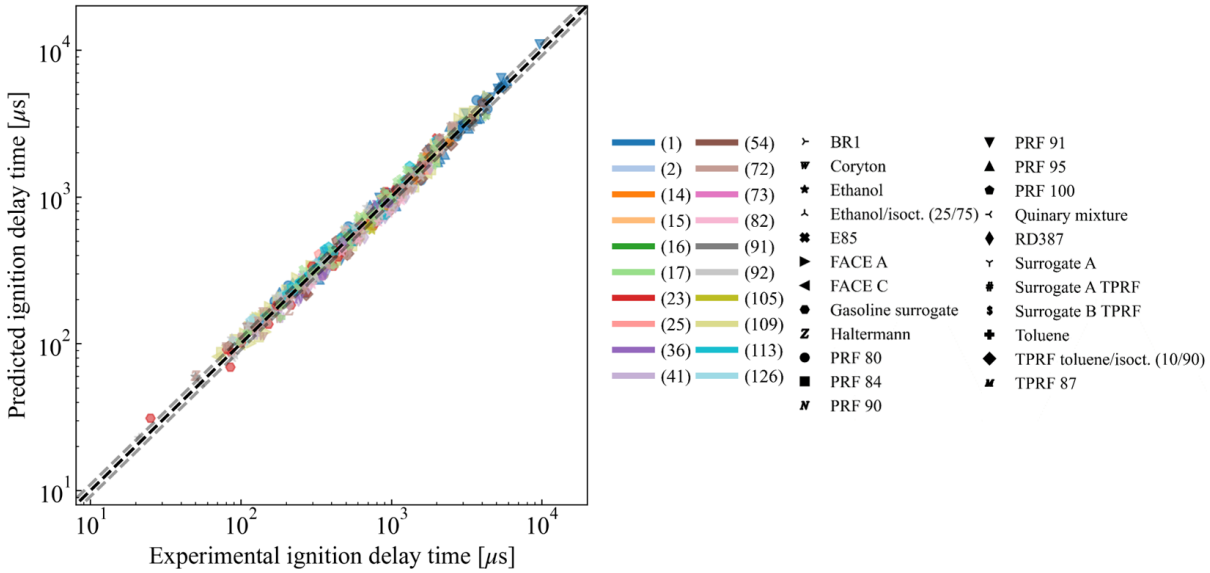

Figure 31 – Experimental versus predicted ignition delay times for SI-ICE transportation fuels. The Dashed black line represents perfect match and the two grey dashed lines represent the average absolute error

4.3 CRFD MODEL NUMERICAL VALIDATION

First of all, the inlet and outlet boundary conditions of mass flow, pressure and temperature were kept constant for all simulations, due to the lack of more operating conditions. Since the engine speed influences the time interval when the valves are open, the quantity of air varies. Thus, the change in rotational speed implies a change in equivalence ratio, as a lower speed yields a leaner mixture and a higher speed yields a richer mixture. More precisely, the maximum equivalence ratio (ϕ) for the 3250, 4000, 4750 RPM simulations are 0.87, 1.03, and 1.18, respectively. In addition, by keeping the same spark timing, it is possible that the spark advancement changes its optimum with different speeds. Therefore, the cases should be analyzed within each speed condition for a fairer comparison. Furthermore, the lack of experimental/reference values limits the analysis to a numerical comparison, not being possible to say which model is in better agreement with bench tests.

Table 27 shows the key performance indicators (KPI) for each simulation. There are two parameters to characterize the combustion and four others that are more tangible indicators. MFB stands for mass fraction burnt (in percentage), CBD is the combustion duration/interval between MFBs, IMEP is the indicated mean effective pressure, and BSFC is the brake-specific fuel consumption. The difference column refers to the relative difference (percentage) comparing $k-\varepsilon$ results to $k-\zeta-f$ results. Note that MFB is an instant in time and CBD is a time interval. For this reason, it makes more sense to describe the MFB difference as crank-angle degrees instead of percentage. To aid these comparisons, Tab. 24 shows the mean in-cylinder values of temperature, pressure, heat release and laminar flame speed (LFS), with their correspondent

peak magnitudes, when they occurred, and the average value along the four-stroke cycle.

Table 23 – Key performance indicators (KPI) calculated for a single four-stroke cycle.

KPI	3250 RPM			4000 RPM			4750 RPM		
	$k-\zeta-f$	$k-\varepsilon$	Diff.	$k-\zeta-f$	$k-\varepsilon$	Diff.	$k-\zeta-f$	$k-\varepsilon$	Diff.
MFB_2 [CA]	719.0	720.9	+1.9	720.6	719.7	-0.9	719.6	719.3	-0.3
MFB_{10} [CA]	724.0	727.2	+3.2	725.8	725.3	-0.5	725.2	724.8	-0.4
MFB_{50} [CA]	731.2	737.0	+5.8	733.4	734.0	+0.6	733.8	734.2	+0.4
MFB_{90} [CA]	739.9	746.8	+6.9	742.8	743.7	+0.9	744.4	745.6	+1.2
CBD_{2-90} [CA]	20.9	25.9	+23.9%	22.2	23.9	+7.9%	24.8	26.3	+6.0%
CBD_{10-50} [CA]	7.1	9.8	+37.3%	7.6	8.7	+15.0%	8.7	9.3	+7.8%
CBD_{10-90} [CA]	15.9	19.6	+23.0%	17.0	18.4	+8.0%	19.2	20.8	+8.1%
IMEP [bar]	12.9	12.5	-3.1%	11.1	11.2	+0.9%	10.1	10.0	-1.0%
Torque [Nm]	47.2	45.8	-3.0%	40.6	41.0	+1.0%	37.1	36.6	-1.3%
Power [kW]	16.1	15.6	-3.1%	17.0	17.2	+1.2%	18.4	18.2	-1.1%
BSFC [g/kWh]	195.4	201.6	+3.2%	227.3	225.0	-1.0%	248.7	252.0	+1.3%

Table 24 – In-cylinder mean quantities.

KPI	3250 RPM			4000 RPM			4750 RPM		
	$k-\zeta-f$	$k-\varepsilon$	Diff.	$k-\zeta-f$	$k-\varepsilon$	Diff.	$k-\zeta-f$	$k-\varepsilon$	Diff.
Peak T [K]	2376.2	2329.7	-2.0%	2347.7	2359.6	+0.5%	2400.6	2360.9	-1.7%
When [CA]	741.5	749.0	+7.5	745.0	746.0	+1.0	746.0	747.5	+1.5
Avg. T [K]	927.3	919.6	-0.8%	928.2	929.4	+0.1%	941.2	932.9	-0.9%
Peak p [bar]	72.9	59.0	-19.2%	58.3	56.9	-2.5%	52.3	50.1	-4.1%
When [CA]	736.0	742.0	+6.0	738.4	739.2	+0.8	738.8	739.2	+0.4
Avg. p [bar]	7.3	7.0	-4.6%	6.3	6.3	+0.4	5.8	5.7	-0.6%
Peak ROHR [J/deg]	101.2	75.4	-25.5%	74.8	66.4	-11.2%	63.1	54.8	-13.1%
When [CA]	731.2	738.0	+6.8	731.6	732.4	+0.8	731.8	731.0	-0.8
Accum. HR [J]	1373.8	1381.6	+0.6%	1225.7	1242.3	+1.4%	1118.2	1112.7	-0.5%
Peak LFS [cm/s]	69.6	69.4	-0.3%	77.4	78.8	1.8%	87.1	85.1	-2.3%
When [CA]	750.0	751.0	1.0	748.5	748.0	-0.5	745.5	746.0	0.5
Avg. LFS [cm/s]	21.6	21.8	+0.8%	23.0	23.5	+2.2%	25.4	24.9	-2.1%

Overall, the higher CBDs in $k-\varepsilon$ simulations show that the combustion takes longer to happen with this model. In particular, the 3250 RPM cases have the largest differences (up to 37.3% in CBD_{10-50}). However, this speed condition should be treated carefully, as the Q mass fraction (Curran's C_nH_{2n} species or structures), an intermediate reaction variable that monitors knock, increased for the $k-\zeta-f$ case by approximately two orders of magnitude (Fig. 32a). This increase is not sufficient to produce oscillations in pressure (Fig. 32b), but it caused a notable peak (roughly 14 bar more than $k-\varepsilon$ for the same speed). Therefore, this slight knock occurrence might be the reason for the earlier MFBs and shorter CDBs in this case, possibly due to the increased time for turbulence scales to affect the combustion.

Moreover, the lengthier combustions influence the peak rate of heat release (ROHR), reducing the peak magnitude. Yet, the large changes in peak rate [J/deg] did not reflect much in the accumulated heat release [J]. Figures 32c and 32d show the ROHR and the accumulated heat release along the cycle. Since ROHR resembles a time derivative of heat release, and accumulated heat release is the integration along the cycle, it is possible to see the early increase in accumulated heat release for the 3250 RPM $k-\zeta-f$ case and a later catch-up of $k-\varepsilon$. Similarly, this is also reflected in temperature (Fig. 32e), with an earlier increase for 3250 RPM $k-\zeta-f$ and a delayed increase for $k-\varepsilon$.

As previously mentioned, the ECFM-3Z is a more robust method to predict laminar flame speeds (LFS) than the other CFM models, as it accounts for EGR (Colin; Benkenida; Angelberger (22)). Besides, as a laminar flamelet method, it decouples combustion and chemistry in this respect. Figure 32f shows that there are no major differences in LFS between the turbulence models. Moreover, Tab. 24 shows only slight changes and that, the richer the mixture, the higher the LFS.

Figure 32g shows a normalized turbulence variable that enables a fairer comparison among different engine speeds, and it is the preferred quantity for displaying turbulence intensity (AVL (44)). It is the average local velocity component due to turbulent fluctuations ($u' = \sqrt{2k/3}$) (Merker; Schwarz; Teichmann (83)), normalized by mean piston velocity (u'/C_m). Notable differences between the turbulence models start after IVO, when the domain is subjected to inflow, but it seems especially affected by the spray, as fuel injection occurs from 430 CA onwards. The $k-\varepsilon$ seems to overpredict the normalized turbulence intensity within that range, with a peak almost matching the one presented nearly to the spark occurrence. Regarding spray and turbulence, this difference might be due to multiphase turbulent mixing, associated to interfacial momentum interaction (Battistoni; Grimaldi (8)), and to the inherent two-way interaction of the DDM formulation (J. K. Dukowicz (32)). But note that this is not the focus here, and only the default spray model is considered.

The coherent flame models calculate the flame surface density, which is affected by the turbulence. Besides, a higher flame surface density increases the turbulent flame speed, reducing the burning interval. The results from Tab. 27 suggest that $k-\varepsilon$ produces less turbulence intensity, and therefore, a reduced flame surface density. Note that, even though u'/C_m is higher for $k-\varepsilon$ for most of the cycle, it becomes lower after the ignition (Figs. 32g and 32h).

This is also related to the IMEP, because the reduced flame surface density leads to a slower turbulent flame speed, which alters the pressure peak in location relative to the top dead center (TDC). Note that the differences in the peak location are higher for the lowest RPM (Fig. 32b).

The same rationale may explain the slight knock at 3250 RPM for $k-\zeta-f$. Since the normalized turbulence is higher, the turbulent flame speed is expected to be higher, which leads to a higher compression of the unburnt mixture prior to the TDC. For the lowest RPM, there is more time for this to happen, leading to ignition. For $k-\varepsilon$, the opposite happens, and associated with lower temperature and pressure, the ignition delay time (IDT) is longer and the ignition

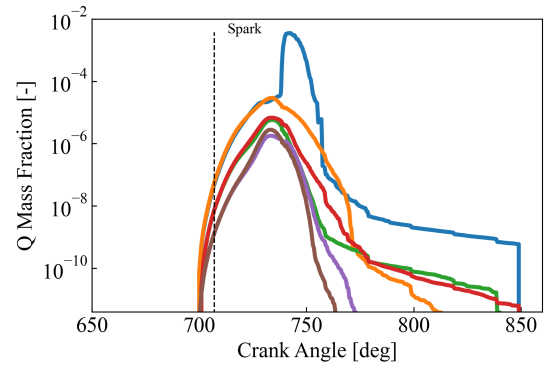

(a) Curran's C_nH_{2n} species or structures. Plot in log-scale.

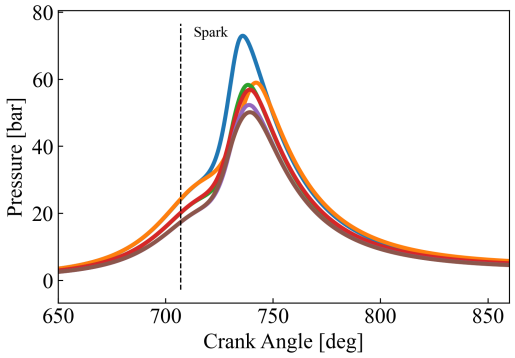

(b) Pressure.

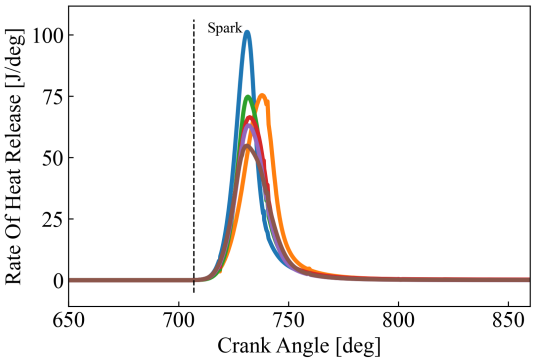

(c) Rate of heat release.

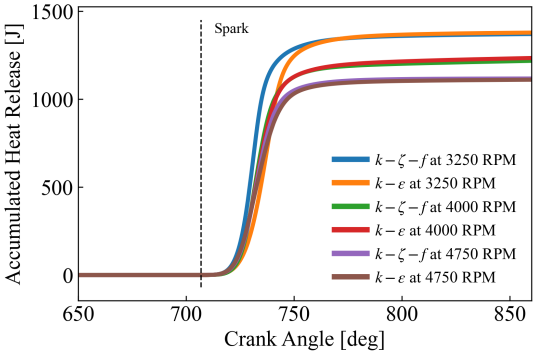

(d) Accumulated heat release.

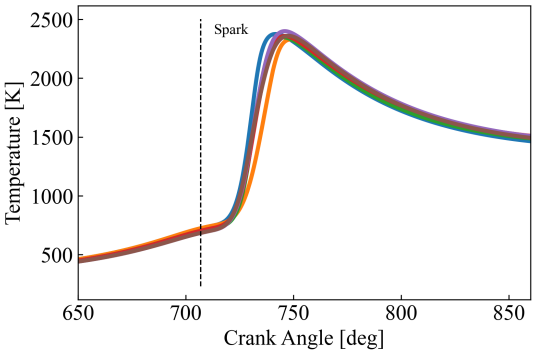

(e) Temperature.

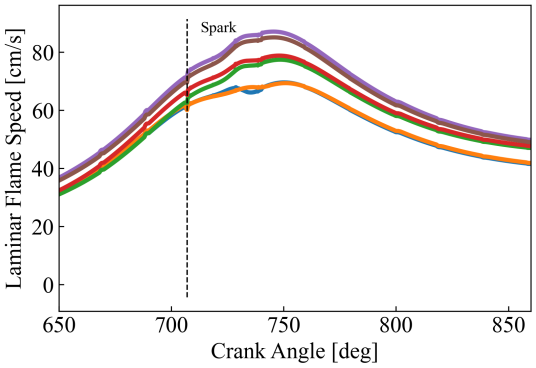

(f) Laminar flame speed.

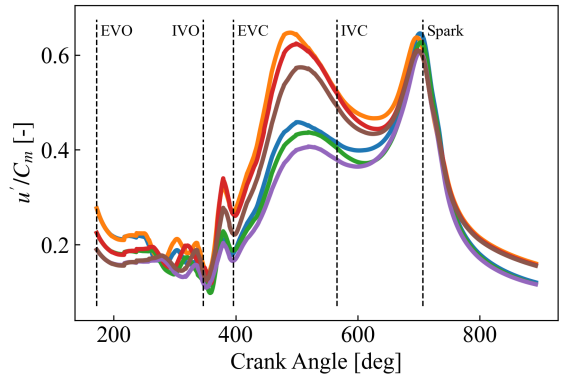

(g) Normalized turbulence: u' divided by piston velocity (C_m).

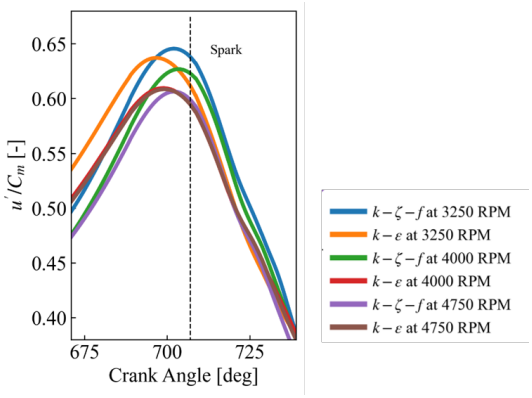

(h) u'/C_m zoom near spark occurrence.

Figure 32 – Mean in-cylinder quantities along crank angle.

that leads to knock does not occur. Conversely, for higher RPMs, there is less time for knock onset.

At last, Fig. 33 shows the top view of MFB_{50} isosurfaces, representing the flame front. Note that it represents different crank-angles but equivalent flame situations (same MFB) and qualitatively depicts the flame front advancement numerically, for visualization purposes. However, there are no experimental flame contours to see which model represents best the flame front propagation.

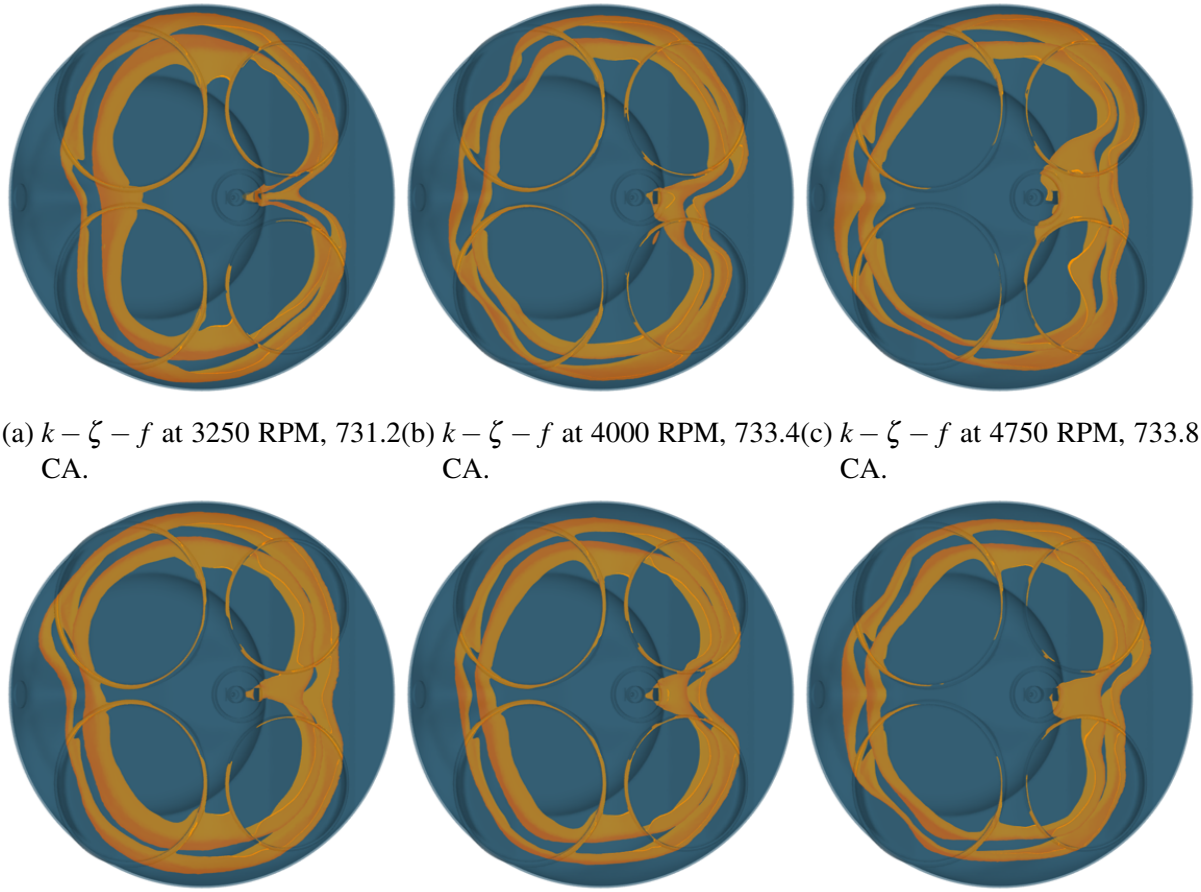

(a) $k-\zeta-f$ at 3250 RPM, 731.2 CA. (b) $k-\zeta-f$ at 4000 RPM, 733.4 CA. (c) $k-\zeta-f$ at 4750 RPM, 733.8 CA.

(d) $k-\varepsilon$ at 3250 RPM, 737.0 CA. (e) $k-\varepsilon$ at 4000 RPM, 734.0 CA. (f) $k-\varepsilon$ at 4750 RPM, 734.2 CA.

Figure 33 – Top view of MFB_{50} isosurfaces representing the flame front.

4.4 FINAL CYCLES CONSIDERED

As previously mentioned, the CRFD validation cases varied the turbulence model to assess how they influence on the combustion process. After the combustion and flow characterization, it was determined that the $k-\zeta-f$ managed to capture a slight numerical knock situation where $k-\varepsilon$ could not. The rotation speed was not varied much to avoid moving too far from the engine operation condition given, that is, there was only one set of boundary conditions provided and no experimental data to validate the results. For this part now, the cycles are more severe, since the goal here is to capture and analyze conditions more susceptible to knock.

Appendix shows the KPIs and the characterization of the combustion, but the flame is presented in Fig. 34 to give some background on how it is propagating for different conditions. Note that it approaches the walls in different timings and may lead to the differences in knock results further observed.

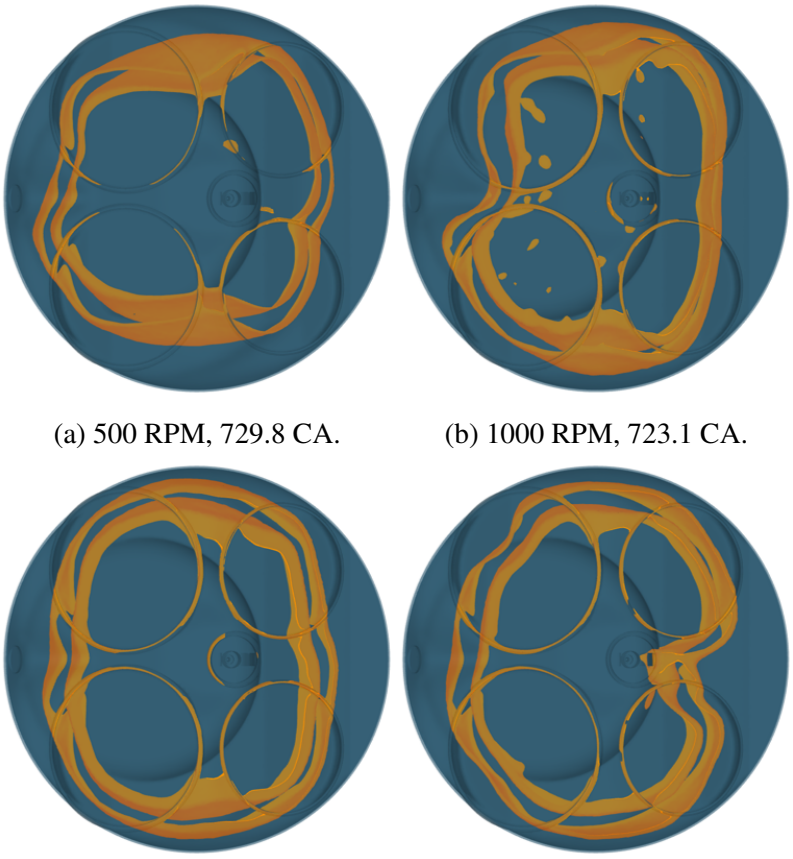

(a) 500 RPM, 729.8 CA. (b) 1000 RPM, 723.1 CA.

(c) 2000 RPM, 724.9 CA. (d) 4000 RPM, 733.4 CA.

Figure 34 – Top view of MFB_{50} isosurfaces representing the flame front.

4.5 KNOCK PREDICTION

4.5.1 Reference quantity for comparison

As previously mentioned, to give a reference for comparison between the knock onset models, some quantities are considered. They may indicate an IDT criterion, a knock-related quantity or the flame arrival. Regarding the quantities belonging to the TABKIN FGM knock model, Moses; Yarin; Bar-Yoseph (89) considers the region to be burnt after the reaction progress variable ($\tilde{c}$ or PV) reaches 10%, while AVL BOOST (42) considers 85% to estimate the minimum octane rating for knock-free operation. Other alternatives are to consider the peak PV, the peak KPV, the peak KPV probability (I_p), and Ω_{I_p}, such as 1% Halstead; Kirsch; Quinn (52) or 95%.

The peak PV and KPV are not adequate as they are progress variables that cumulative increase towards the end of the simulation. The I_p peak varies from simulation to simulation and from region to region. Considering different peaks means considering different knock criteria. Therefore, it is more adequate to choose a fixed Ω_{I_p}. Since $\Omega_{95\%}$ could not be reached for 4000 and 2000 RPM, it should not be the reference for consistency, leaving $\Omega_{1\%}$ as a reference, the same one suggested by Halstead; Kirsch; Quinn (52).

According to Moses; Yarin; Bar-Yoseph (89), pressure is usually considered uniform in the combustion chamber because the characteristic time of sound waves propagation over its length is much smaller than the characteristic time of combustion. Therefore, pressure peak is not a good reference too, as it gives almost the same CAD for all spheres.

Regarding OH and 5% of maximum OH mass fraction, they are references for IDT. These and the other candidates for knock reference are shown in Appendix D, where the crank-angle degree when each one is detected is presented in a table, alongside the same information for each Livengood-Wu integral considered.

The instant when temperature reaches 1000 K seems to be an adequate reference since it is thermo-fluid-dynamic and easily applicable to other studies as well. In other words, it can be used in CRFD, 1D and 0D simulations as it is an elementary quantity for fluid flows. Besides, it can be compared to other model-dependent quantities. Thus, in a first step, both the L-W integrals and the TABKIN FGM knock $\Omega_{1\%}$ are compared to the 1000 K criterion, and then compared among them as well.

4.5.2 Ignition delay times and L-W integrals per method

4.5.2.1 Chemical kinetics mechanisms assessment

To give a better understanding of the chemical kinetics mechanisms to be applied to obtain the L-W integrals, they are assessed in terms of IDT (via CV-PSR Cantera simulations) and LFS (via laminar flat flame Cantera simulations). The results are available in Appendix B, for the IDT conditions of some PRF (0, 60, 70, 80, 84, 91, 95, 100), and LFS given in Tab. 7.

For IDT, Y. Li et al. (75) usually predicts a negative temperature coefficient (NTC) region slightly to the right of the other two, that is, for lower temperatures, especially for PRF 60 and 70. Also, it usually predicts lower IDTs and a less pronounced slope for the high temperature range, especially for higher AKIs. The other two mechanisms are more alike, but for PRF 91 onwards, Tsurushima (120) loses the linear trend for higher temperatures, predicting higher IDTs than the other mechanisms.

For LFS, it should be noted, however, that Tsurushima (120) does not have a transport file and the one obtained by merging other files yielded poor results for LFS. More specifically, they not only were far from the others but also were unable to converge when regarding radiation effects together with the Soret effect. The only cases where it managed to give appropriate results for LFS were the conditions given by Jerzembeck et al. (61) (Tab. 25). Y. Li et al. (75) perfor-

med better for the simulations of Huang; Sung; Eng (59). It better predicted the whole range of equivalence ratios, with slight overpredictions on the lean side and slight underpredictions on the rich side. However, it performed worse than Liu et al. (77) for Jerzembeck et al. (61), which have higher temperature and pressure levels. It had a good agreement on the lean side but the underprediction on the rich side was more intense. In contrast, Liu et al. (77) overpredicted almost the whole range of Huang; Sung; Eng (59) and shifted the peak LFS more to the rich side.

Table 25 – Average absolute error per simulation [%]. Simulations consider the Soret effect.

Fuel	(75)	(77)	(120)
PRF 0	3.9	13.2	-
PRF 85	8.9	15.6	-
PRF 87 at 10 bar	7.0	8.9	23.0
PRF 87 at 15 bar	9.4	8.2	18.4
PRF 87 at 20 bar	8.1	5.7	9.0
PRF 87 at 25 bar	14.3	7.8	6.5
PRF 90	8.2	16.4	-
PRF 95	8.8	16.9	-
PRF 100	10.1	19.2	-

4.5.2.2 L-W integrals per method

As previously mentioned, there are six IDT calculation methods considered, three via Cantera CV-PSR IDT simulations and three via IDT correlations. The three chemical kinetics mechanisms are reduced, from Y. Li et al. (75), Liu et al. (77) e Tsurushima (120), while the three correlations are the ones from Douaud; Eyzat (27) (Eq. 21) and L. Cancino et al. (17) (Eq. 10) and the one proposed in this work (Eq. 67).

Appendix E shows all IDT curves along the cycle. Although the considered interval for the L-W calculation is from 430 CAD (SOI) to 800 CAD, the vast majority of the Cantera simulations detected ignition only after 680 CAD, approximately. Besides, there were some points where the mechanisms fluctuated in their IDT predictions. In general terms, Tsurushima (120) suffers the least from these points. For the correlations, they can be considered more robust towards the variations in pressure, temperature and composition as they are simplistic representations that disregard individual reactions and reaction rates.

The IDT predicted by the correlation of Douaud; Eyzat (27) is closer to the ones simulated by mechanisms in the portion before the spark. After it, it has the worst agreement and overpredicts the IDT by usually at least one order of magnitude. And before the point where mechanisms detect the first IDTs (≈680 CAD), this correlation predicts the IDT much lower than the other correlations. However, in few cases, like at 500 RPM, for spheres from 67.5° to 112.5°, this correlation predicts the lowest IDTs in the post-ignition region.

The L-W integrals are presented in Appendix F. Due to some fluctuations in IDT mentioned above, the L-W integrals based on the Y. Li et al. (75) mechanism get large contributions from these points and quickly reaches unity, while this is not observed for the other mechanisms. By looking at the IDTs, it is likely that the dips in IDT for this mechanism in instants near the spark (earlier or later) affect the L-W integral more intensely. Liu et al. (77) suffers from this as well, but the dips occur much later, when the L-W has already reached unity. For the earlier moments, however, the fluctuations occur but are more upward, contrary to the IDT dips for Y. Li et al. (75). Apart from these spikes, the three mechanisms generally build up the L-W value in similar manners.

At 4000 RPM, the L-W based on the correlation from Douaud; Eyzat (27) is in tight agreement with the ones from the mechanisms, but for all the other more intense cycles this correlation yields unity much earlier than the mechanisms.

Overall, the mechanism-based L-W integrals increase earlier than the ones based on the correlations from L. Cancino et al. (17) and this work's. These two start their increase about 20 CAD later, as a rule of thumb, and their slopes are way more intense, and build from 0 to unity and narrower intervals. For some spheres at 1000 RPM and for most spheres at 500 RPM, the tight agreement between L. Cancino et al. (17) and this work's proposed correlation is lost, with the first one losing the very intense slope and yielding unity later on.

4.5.3 L-W integrals compared to knock references

Since there are 16 spheres, 4 operating conditions and 6 L-W integral methods to be compared with the other knock reference quantities (totalling 384 scenarios for each quantity), the information is summarized in polar heatmaps, in order to facilitate the comprehension. Each polar heatmap has four or six rings (four speed engine speeds or six L-W methods, respectively) and 16 division (16 spheres). In addition, the precise numbers are available in Appendix G, in the form of tables, also with the absolute mean (i.e. disregarding the sign) and with the standard deviation (regarding the sign).

The integrals are first compared to the 1000 K criterion. Then the $\Omega_{1\%}$ (a quantity from the chosen AVL FIRE knock model, the TABKIN FGM knock model) is compared to the same reference. Only then the integrals are compared to this knock model quantity. The plots are presented by method and by engine speed, on different plots. Although the same information is presented twice, these aids the comprehension in both senses. Note also that the color scales are in log scale, and a positive value means that the integral predicted knock later than the reference, considered a non-conservative situation.

Figure 35 shows the L-W integrals compared to the 1000 K criterion. Note that blank cells mean that the criterion was not reached. Based on this criterion, at 500 RPM, all L-W integrals perform badly, anticipating too much the knock onset. The exception is made for L. Cancino et al. (17), where four spheres are within a 1 CAD range. In addition, note that for spheres from 67.5° to 112.5° the temperature rises extremely late or not even reaches 1000 K.

At 1000 RPM, the mechanisms still predict the knock onset earlier, but not exaggeratedly as for 500 RPM. The worst performance is for Douaud; Eyzat (27). L. Cancino et al. (17) performs extremely well, within roughly a 1 CAD margin. However, this is almost always on the positive side of the range, meaning that it predicts the knock onset later than the reference, which is not a conservative situation. This work's correlation also performs well. Although within a larger margin, it is predominantly on the safe side (negative, i.e. predicts knock earlier).

At 2000 RPM, the mechanisms and Douaud; Eyzat (27) reduce the margin a lot, but still miss by 3.7 CAD, on average. L. Cancino et al. (17) performs well, again on the non-conservative side, and misses by 1.4 CAD. This time, this work's correlation performs on the non-conservative side by 0.6 CAD from the 1000 K reference.

At 4000 RPM, all values are on the non-conservative side, but the mechanisms, this time, are the closest ones to the 1000 K reference, while L. Cancino et al. (17) and this work's correlations are not far behind and very similar to each other.

Figure 36 shows the comparison between $\Omega_{1\%}$ and the 1000 K criterion. Overall, the best agreement is at 2000 RPM, where $\Omega_{1\%}$ misses by roughly 3 CAD on average. However, as noted for the L-W integrals, 500 RPM has the farthest predictions in relation to the 1000 K criterion. What can be understood from this preliminary comparison is that the TABKIN FGM knock model is dependent upon several variables for both the pre-tabulation and the calculation phases (see the list of coordinates/variables and active progress variables), not only temperature.

Figure 37 shows the comparison between the L-W integrals and $\Omega_{1\%}$. At 500 RPM, the mechanism-based L-W integrals perform better the correlations. At 1000 RPM, the result is similar for the mechanisms, but L. Cancino et al. (17) and this work's correlation improve their performance. At 2000 RPM, the trend for the mechanisms is still the same, while the two correlations now predict on the safe side with even smaller margins. It is worth mentioning that, for this condition, 14 out of the 16 spheres lie on the conservative side. At 4000 RPM all methods predict on the non-conservative side and miss by quite a few CAD.

Figures 38 and 39 show the results gathered by method, only to give an overall impression for all methods side by side. In general terms, the two correlations from L. Cancino et al. (17) and from this work have quite good results, and are able to predict the knock onset well for intermediate conditions (1000 and 2000 RPM cycles).

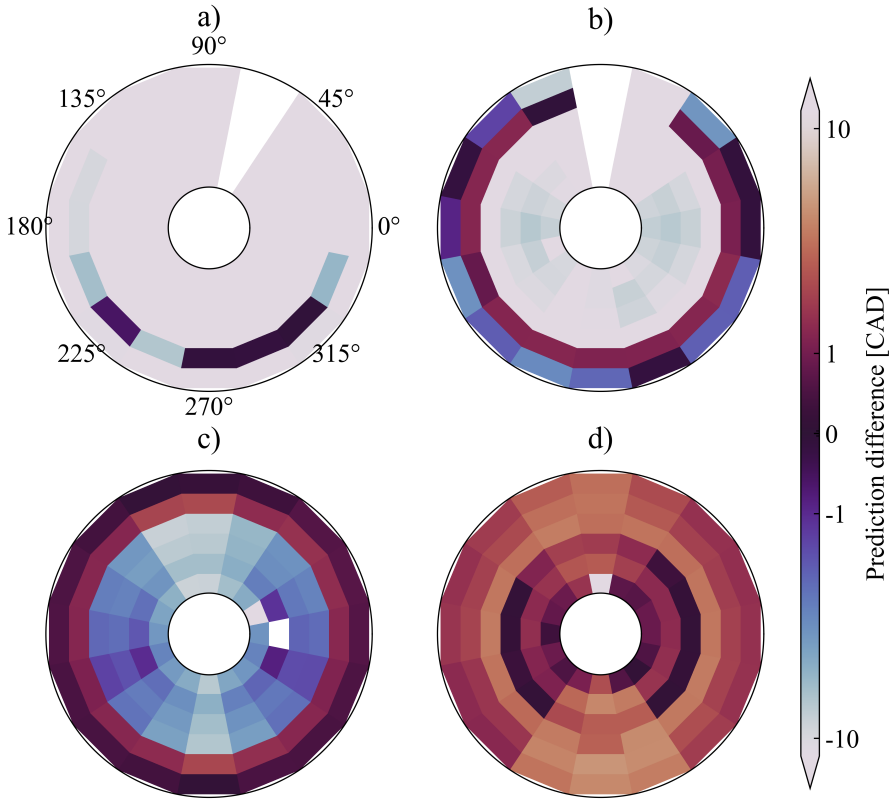

Figure 35 – Livengood-Wu integrals knock onset prediction compared to 1000 K criterion, shown by sphere. Blank means the criterion is not reached. Color scale in log scale. From inner to outer layer: Y. Li et al. (75) mechanism; Liu et al. (77) mechanism; Tsurushima (120) mechanism; Douaud; Eyzat (27) correlation; L. Cancino et al. (17); This work's correlation. a) 500 RPM; b) 1000 RPM; c) 2000 RPM; d) 4000 RPM.

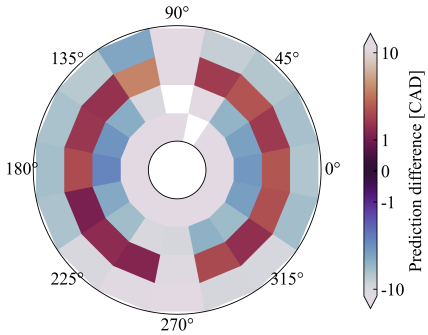

Figure 36 – $\Omega_{1\%}$ scalar compared to 1000 K criterion, shown by sphere. Color scale in log scale. From inner to outer layer: 500, 1000, 2000 and 4000 RPM. Blank means the criterion is not reached.

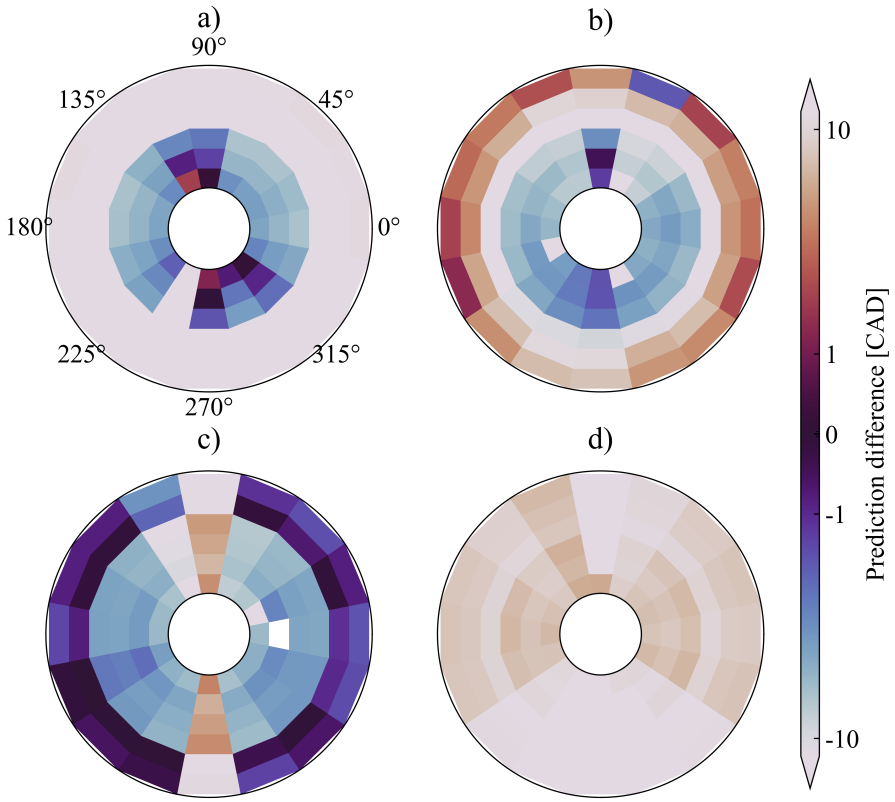

Figure 37 – Livengood-Wu integrals knock onset prediction compared to $\Omega_{1\%}$ criterion, shown by sphere. Blank means the criterion is not reached. Color scale in log scale. From inner to outer layer: Y. Li et al. (75) mechanism; Liu et al. (77) mechanism; Tsurushima (120) mechanism; Douaud; Eyzat (27) correlation; L. Cancino et al. (17); This work's correlation. a) 500 RPM; b) 1000 RPM; c) 2000 RPM; d) 4000 RPM.

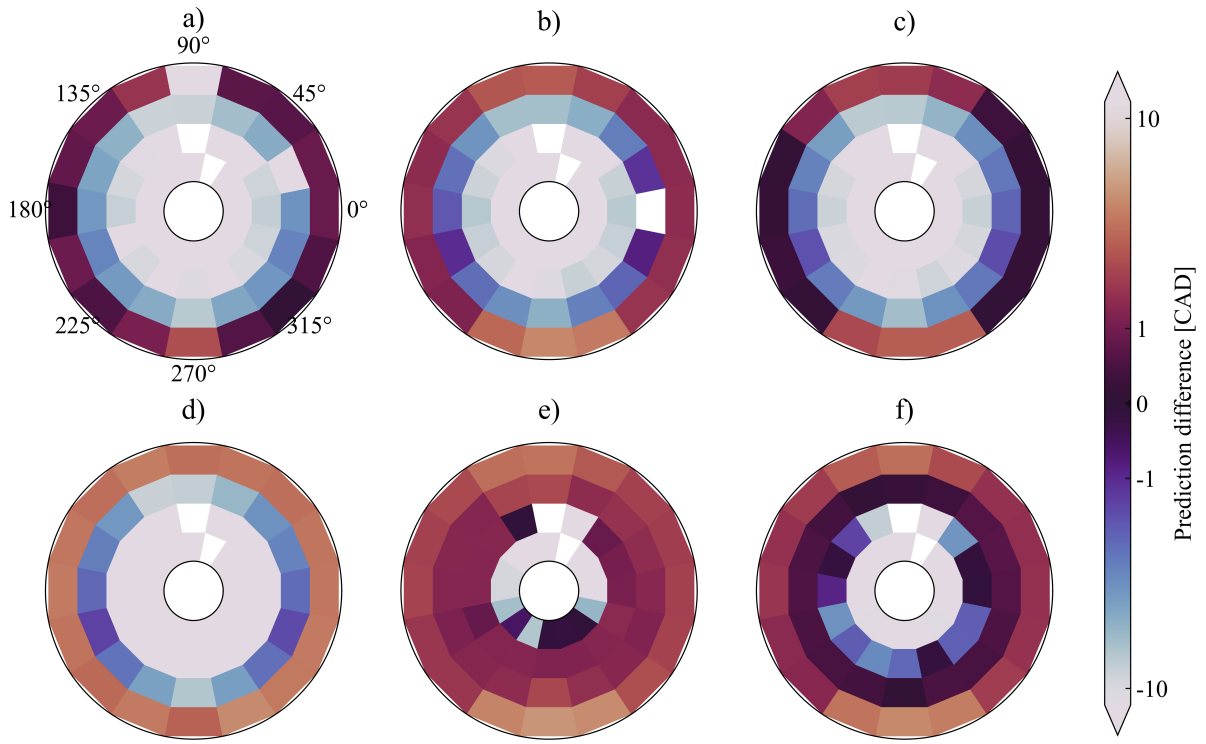

Figure 38 – Livengood-Wu integrals knock onset prediction compared to 1000 K criterion, shown by sphere. From inner to outer layer: 500, 1000, 2000 and 4000 RPM. Blank means the criterion is not reached. Color scale in log scale. a) Y. Li et al. (75) mechanism; b)Liu et al. (77) mechanism; c) Tsurushima (120) mechanism; d)Douaud; Eyzat (27) correlation; e) L. Cancino et al. (17); f) This work's correlation.

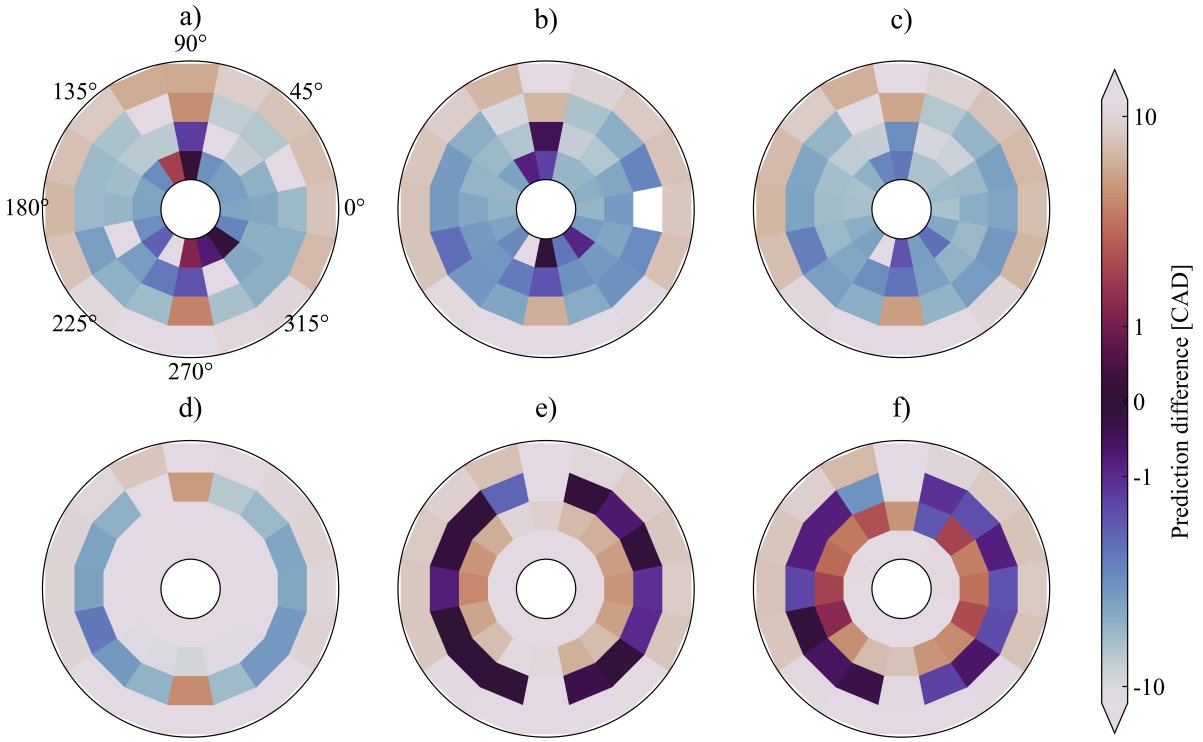

Figure 39 – Livengood-Wu integrals knock onset prediction compared to $\Omega_{1\%}$ criterion, shown by sphere. From inner to outer layer: 500, 1000, 2000 and 4000 RPM. Blank means the criterion is not reached. Color scale in log scale. a) Y. Li et al. (75) mechanism; b)Liu et al. (77) mechanism; c) Tsurushima (120) mechanism; d)Douaud; Eyzat (27) correlation; e) L. Cancino et al. (17); f) This work's correlation.

5 CONCLUSION

This research presented an automatized way to iteratively clean a database of ignition delay time (IDT) experiments that were already published in the literature to obtain modified Arrhenius expressions via multiple linear regression (MLR), as a function of pressure, temperature, equivalence ration and anti-knock index (AKI). It was first validated towards a database of pure fuels made of normal-chain alcohols from one to four carbons ($C_1 - C_4$), i.e, methanol, ethanol, *n*-propanol and *n*-butanol, then applied to the final database of relevant transportation fuels and fuel surrogates for spark-ignition engines.

In the context of computational reactive fluid dynamics (CRFD), a gasoline direct injection spark ignition engine simulation was first validated by investigating the influence on the turbulence model in the combustion. More demanding cycles were simulated to evaluate an numerical indirect knock method, based on the IDT correlation obtained by the MLR routine, applied to sixteen spheres located on the top dead center plane, via the Livengood-Wu integral (L-W). This method was compared to other L-W integrals based on three reduced mechanisms, and two correlations, namely, Y. Li et al. (75), Liu et al. (77), Tsurushima (120), Douaud; Eyzat (27) e L. Cancino et al. (17).

For the primary alcohols correlation, the results are valid for $1000/T$ from 0.6 (1666.66 K) to 1.2 (833.33 K), pressure from 0.9 to 50 bar, equivalence ratio from 0.3 to 2.0, AKI from 91.5 (*n*-butanol) to 107.5 (methanol) and IDT from 21 to 14140 μs. Concerning the metrics, the R^2 alone is not sufficient to evaluate the correlations. The regressions predict the IDT and it is a way of avoiding knock, so it cannot be highly overshot. In addition, while the over/undershoot provides information about the extreme values, the average absolute error (AAE) provides an overall metric to complement the analysis. Besides, the global apparent activation energy showed that the mathematical regressions are in good agreement with the literature. The final result produced a R^2 of 0.991, an AAE of 10.5% and a maximum overshoot of 24.4%.

In addition, they were in good agreement concerning the global apparent activation energy (E_a) and pressure. Even for different fuels, the pressure exponent is consistent. This might be due to a more regular behavior of pressure-dependent-Ahrrenius reactions and their rate constants in comparison with other factors such as temperature. Regarding the equivalence ratio exponent, it is good but suffers a bit due to the limited number of bins ($\phi = 0.3, 0.5, 1.0, 2.0$), and it is better represented this way than suppressing the exponent and rescaling the data to a common condition. The counter-intuitive anti-knock index (AKI) exponent might be due to a combination of factors. An IDT correlation, regardless of the number of independent variables, is a single mathematical equation and it is simpler than all the information given by a detailed mechanism. It is a very convenient representation but should be considered alongside the ranges of validity of each variable and the types of fuel. Since both mechanisms delivered similar

correlations with respect to E_a, p, ϕ and strong statistical metrics, the AKI exponent might be due to the limited number of bins (only four fuels). Since the goal is to include only relevant neat transportation biofuels, an option to further investigate this work is to perform one-dimensional numerical simulations on engine cycles.

For the SI-ICE fuels and fuel surrogates, the points were limited to $1000/T$ from 0.6 to 1.1 (1666.67 K to 909.09 K). Overall, the parameters of the final database ranged in the following way: pressure ranged from 2.0 to 60.0 bar, equivalence ratio from 0.35 to 2.0, AKI from 80.0 (PRF 80) to 109.25 (toluene), and IDT from 21 to 9655 μs. The global apparent activation energy and the pressure exponent were in good agreement with the literature. This time, the AKI exponent was positive was matched the one from L. Cancino et al. (17) when considering the uncertainty given by the standard errors.

Concerning the CRFD model numerical validation, the relation between turbulence and combustion was observed especially for the lowest RPM. The coherent flame models calculate the flame surface density, which is affected by the turbulence. Besides, a higher flame surface density increases the turbulent flame speed, reducing the burning interval. The results suggested that $k-\varepsilon$ produced less turbulence intensity, and therefore, a reduced flame surface density between the ignition and the top dead center. The unburnt mixture became less compressed and, associated with reduced pressure and temperature led to a longer ignition delay time. On the other hand, $k-\zeta-f$ had opposite results which led to a slight numerical knock detection. For this reason, the final model considered $k-\zeta-f$ and ECFM-3Z (extended CFM with 3 zones). Also, in order to evaluate knock locally, the Knock Shell Model had to be coupled to the TABKIN FGM knock model as well.

For the post-processed IDTs obtained from the 16 spheres at the TDC plane, the mechanisms presented some fluctuations in IDT prediction. However, these fluctuations significantly affect the L-W integral only if they are dips (abrupt IDT falls) at the earlier moments, usually around the spark timing. Y. Li et al. (75) is the only one affected by these dips. Besides, the correlation from Douaud; Eyzat (27) shows good agreement with the mechanism up to the instants before the spark and later on suffer from quite large deviations.

When compared to the 1000 K criterion as a knock reference value, at 500 RPM, the methods anticipated knock too much. At 1000 RPM the margins are reduced and the correlations performed better. At 2000 RPM, the correlations from L. Cancino et al. (17) and from this work predicted knock very well. At 4000 RPM, there is a generalized late prediction but on margins considerably smaller than the early prediction at 500 RPM.

Regarding the $\Omega_{1\%}$, it was the TABKIN FGM knock model reference quantity. With respect to 1000 K, there is good agreement for the intermediate conditions. Due to the other ones, it seems that $\Omega_{1\%}$ is influenced by other variables, as shows its model formulation. When comparing the L-W integrals to $\Omega_{1\%}$, the differences are reduced. Especially at 2000 RPM, the proposed correlation predicted knock on the safe side on 14 out of the 16 spheres.

For future works, the correlation can be implemented in 1D simulation codes, like AVL BO-

OST or even Cantera to evaluate knock compared to the available models. Besides, as lighter simulations, the so-called cycle-to-cycle variation (CCV) could be evaluated too. Besides, in the context of CCV, influence of boundary conditions and oscillations, the 0D/1D simulations could be coupled to the 3D model at the inlet and the outlet, the number of cycles could be extended and also the ports could be longer as well. Due to the lack of more boundary conditions or experimental data, future 3D CRFD simulations can regard other compression ratios or engines, as this can capture the influence of temperature stratification and swirl and tumble effects. Conversely, lower exhaust gas recirculation (EGR) ratios at the inlet boundary condition could be simulated, to reduce the end-gas time to autoignition due to higher temperatures. Furthermore, more complex 3D CRFD models can be implemented, such as the general gas phase reactions (GGPR), which embeds a chemical kinetics mechanism to rule the combustion, not to mention turbulence models such as Reynolds stress models (RSM) and large eddy simulations (LES).

REFERENCES

1 ALABBAD, Mohammed et al. Ignition Delay Time Measurements of Primary Reference Fuel Blends. **Combustion and Flame**, v. 178, p. 205–216, abr. 2017. ISSN 0010-2180. DOI: 10.1016/j.combustflame.2016.12.027.

2 ALRAMADAN, Abdullah S. et al. Mixed Butanols Addition to Gasoline Surrogates: Shock Tube Ignition Delay Time Measurements and Chemical Kinetic Modeling. **Combustion and Flame**, v. 162, n. 10, p. 3971–3979, out. 2015. ISSN 0010-2180. DOI: 10.1016/j.combustflame.2015.07.035.

3 ANSYS, Inc. **ANSYS Fluent User's Guide 2021R1**. [S.l.: s.n.], 2021.

4 AYAS, Nezihe. 2.13 Solvent Materials. In: DINCER, Ibrahim (Ed.). **Comprehensive Energy Systems**. Oxford: Elsevier, jan. 2018. P. 368–395. ISBN 978-0-12-814925-6. DOI: 10.1016/B978-0-12-809597-3.00226-1.

5 BAGHERI, Ghobad et al. Comprehensive Kinetic Study of Combustion Technologies for Low Environmental Impact: MILD and OXY-fuel Combustion of Methane. **Combustion and Flame**, v. 212, p. 142–155, fev. 2020. ISSN 00102180. DOI: 10.1016/j.combustflame.2019.10.014.

6 BARRAZA-BOTET, Cesar L. et al. The Impact of Physicochemical Property Interactions of Iso-Octane/Ethanol Blends on Ignition Timescales. **Fuel**, v. 224, p. 401–411, jul. 2018. ISSN 0016-2361. DOI: 10.1016/j.fuel.2018.03.105.

7 BASARA, B.; JAKIRLIC, S. A New Hybrid Turbulence Modelling Strategy for Industrial CFD. **International Journal for Numerical Methods in Fluids**, v. 42, n. 1, p. 89–116, 2003. ISSN 1097-0363. DOI: 10.1002/fld.492.

8 BATTISTONI, Michele; GRIMALDI, Carlo Nazareno. Numerical Analysis of Injector Flow and Spray Characteristics from Diesel Injectors Using Fossil and Biodiesel Fuels. **Applied Energy**, v. 97, p. 656–666, set. 2012. ISSN 0306-2619. DOI: 10.1016/j.apenergy.2011.11.080.

9 BHATIA, S. C. 24 - Algae Fuel for Future. In _____. **Advanced Renewable Energy Systems**. Edição: S. C. Bhatia. [S.l.]: Woodhead Publishing India, jan. 2014. P. 645–678. ISBN 978-1-78242-269-3. DOI: 10.1016/B978-1-78242-269-3.50024-3.

10 BURCAT, A.; RUSCIC, B. **Third Millenium Ideal Gas and Condensed Phase Thermochemical Database for Combustion (with Update from Active Thermochemical Tables).** [S.l.], jul. 2005. DOI: 10.2172/925269.

11 BURKE, Sinéad M. et al. An Experimental and Modeling Study of Propene Oxidation. Part 2: Ignition Delay Time and Flame Speed Measurements. **Combustion and Flame**, v. 162, n. 2, p. 296–314, fev. 2015. ISSN 0010-2180. DOI: 10.1016/j.combustflame.2014.07.032.

12 BURKE, Ultan et al. A Detailed Chemical Kinetic Modeling, Ignition Delay Time and Jet-Stirred Reactor Study of Methanol Oxidation. **Combustion and Flame**, v. 165, p. 125–136, mar. 2016. ISSN 0010-2180. DOI: 10.1016/j.combustflame.2015.11.004.

13 CAI, Liming et al. Impact of Exhaust Gas Recirculation on Ignition Delay Times of Gasoline Fuel: An Experimental and Modeling Study. **Proceedings of the Combustion Institute**, v. 37, n. 1, p. 639–647, jan. 2019. ISSN 1540-7489. DOI: 10.1016/j.proci.2018.05.032.

14 CANCINO, L. R. et al. Autoignition of Gasoline Surrogate Mixtures at Intermediate Temperatures and High Pressures: Experimental and Numerical Approaches. **Proceedings of the Combustion Institute**, v. 32, n. 1, p. 501–508, jan. 2009. ISSN 1540-7489. DOI: 10.1016/j.proci.2008.06.180.

15 _____. Ignition Delay Times of Ethanol-Containing Multi-Component Gasoline Surrogates: Shock-tube Experiments and Detailed Modeling. **Fuel**, v. 90, n. 3, p. 1238–1244, mar. 2011. ISSN 0016-2361. DOI: 10.1016/j.fuel.2010.11.003.

16 _____. Measurement and Chemical Kinetics Modeling of Shock Induced Ignition of Ethanol Air Mixtures. **Energy & Fuels**, American Chemical Society, v. 24, n. 5, p. 2830–2840, mai. 2010. ISSN 0887-0624. DOI: 10.1021/ef100076w.

17 CANCINO, L.R. et al. A Six-Compound, High Performance Gasoline Surrogate for Internal Combustion Engines: Experimental and Numerical Study of Autoignition Using High-Pressure Shock Tubes. **Fuel**, v. 261, p. 116439, fev. 2020. ISSN 00162361. DOI: 10.1016/j.fuel.2019.116439.

18 CARBURETOR. **Wikipedia**, out. 2022.

19 CHENG, Song et al. Autoignition and Preliminary Heat Release of Gasoline Surrogates and Their Blends with Ethanol at Engine-Relevant Conditions: Experiments and Comprehensive Kinetic Modeling. **Combustion and Flame**, v. 228, p. 57–77, jun. 2021. ISSN 0010-2180. DOI: 10.1016/j.combustflame.2021.01.033.

20 CHO, Seokwon et al. Prediction Modeling and Analysis of Knocking Combustion Using an Improved 0D RGF Model and Supervised Deep Learning. **Energies**, Multidisciplinary Digital Publishing Institute, v. 12, n. 5, p. 844, jan. 2019. ISSN 1996-1073. DOI: 10.3390/en12050844.

21 COLIN, O.; BENKENIDA, A. The 3-Zones Extended Coherent Flame Model (Ecfm3z) for Computing Premixed/Diffusion Combustion. **Oil & Gas Science and Technology**, EDP Sciences, v. 59, n. 6, p. 593–609, nov. 2004. ISSN 1294-4475. DOI: 10.2516/ogst:2004043.

22 COLIN, O.; BENKENIDA, A.; ANGELBERGER, C. 3d Modeling of Mixing, Ignition and Combustion Phenomena in Highly Stratified Gasoline Engines. **Oil & Gas Science and Technology**, EDP Sciences, v. 58, n. 1, p. 47–62, jan. 2003. ISSN 1294-4475. DOI: 10.2516/ogst:2003004.

23 COOPER, Sean P. et al. High-Pressure Ignition Delay Time Measurements of a Four-Component Gasoline Surrogate and Its High-Level Blends with Ethanol and Methyl Acetate. **Fuel**, v. 275, p. 118016, set. 2020. ISSN 0016-2361. DOI: 10.1016/j.fuel.2020.118016.

24 CURRAN, H. J. et al. A Comprehensive Modeling Study of Iso-Octane Oxidation. **Combustion and Flame**, v. 129, n. 3, p. 253–280, mai. 2002. ISSN 0010-2180. DOI: 10.1016/S0010-2180(01)00373-X.

25 DAVIDSON, D. F.; GAUTHIER, B. M.; HANSON, R. K. Shock Tube Ignition Measurements of Iso-Octane/Air and Toluene/Air at High Pressures. **Proceedings of the Combustion Institute**, v. 30, n. 1, p. 1175–1182, jan. 2005. ISSN 1540-7489. DOI: 10.1016/j.proci.2004.08.004.

26 DAVIDSON, D. F.; HANSON, R. K. Interpreting Shock Tube Ignition Data. **International Journal of Chemical Kinetics**, v. 36, n. 9, p. 510–523, 2004. ISSN 1097-4601. DOI: 10.1002/kin.20024.

27 DOUAUD, A. M.; EYZAT, P. Four-Octane-Number Method for Predicting the Anti-Knock Behavior of Fuels and Engines. **SAE Transactions**, SAE International, v. 87, p. 294–308, 1978. ISSN 0096-736X.

28 DU, Weixin et al. Auto-Ignition and Deflagration Characteristics of Ethanol-Gasoline/Air at High Temperature. **Fuel**, v. 255, p. 115768, nov. 2019. ISSN 0016-2361. DOI: 10.1016/j.fuel.2019.115768.

29 DUCLOS, J. M.; BRUNEAUX, G.; BARITAUD, T. A. **3D Modelling of Combustion and Pollutants in a 4-Valve SI Engine; Effect of Fuel and Residuals Distribution and Spark Location**. Warrendale, PA, out. 1996. DOI: 10.4271/961964.

30 DUCLOS, J. M.; ZOLVER, M. 3D Modeling of Intake, Injection and Combustion in a DI-SI Engine under Homogeneous and Stratified Operating Conditions. **COMODIA**, p. 335–340, 1998.

31 DUKOWICZ, J.K. **Quasi-Steady Droplet Phase Change in the Presence of Convection**. United States, 1979. P. 22.

32 DUKOWICZ, John K. A Particle-Fluid Numerical Model for Liquid Sprays. **Journal of Computational Physics**, v. 35, n. 2, p. 229–253, abr. 1980. ISSN 0021-9991. DOI: 10.1016/0021-9991(80)90087-X.

33 DUNPHY, Mary P.; SIMMIE, John M. High-Temperature Oxidation of Ethanol. Part 1.—Ignition Delays in Shock Waves. **J. Chem. Soc., Faraday Trans.**, v. 87, n. 11, p. 1691–1696, 1991. ISSN 0956-5000, 1364-5455. DOI: 10.1039/FT9918701691.

34 DURBIN, P. A. Near-Wall Turbulence Closure Modeling without "Damping Functions". **Theoretical and Computational Fluid Dynamics**, v. 3, n. 1, p. 1–13, set. 1991. ISSN 1432-2250. DOI: 10.1007/BF00271513.

35 FANG, Ruozhou et al. Effect of Nitric Oxide and Exhaust Gases on Gasoline Surrogate Autoignition: Iso-Octane Experiments and Modeling. **Combustion and Flame**, v. 236, p. 111807, fev. 2022. ISSN 0010-2180. DOI: 10.1016/j.combustflame.2021.111807.

36 FIEWEGER, K.; BLUMENTHAL, R.; ADOMEIT, G. Self-Ignition of S.I. Engine Model Fuels: A Shock Tube Investigation at High Pressure. **Combustion and Flame**, v. 109, n. 4, p. 599–619, jun. 1997. ISSN 0010-2180. DOI: 10.1016/S0010-2180(97)00049-7.

37 FROST, Jim. **How To Interpret R-squared in Regression Analysis**. [S.l.: s.n.], abr. 2017.

38 GAIL, Sandro et al. Evaluating a Novel Gasoline Surrogate Containing Isopentane Using a Rapid Compression Machine and an Engine. **Proceedings of the Combustion Institute**, v. 38, n. 4, p. 5643–5653, jan. 2021. ISSN 1540-7489. DOI: 10.1016/j.proci.2020.07.103.

39 GALPIN, Paul. CFD Best Practices for Industrial Flows and Turbomachinery. In: SIMULATION World 2020. [S.l.: s.n.], 2020.

40 GAUTAM, M; MARTIN, D W; CARDER, D. Emissions Characteristics of Higher Alcohol/Gasoline Blends. **Proceedings of the Institution of Mechanical Engineers, Part A: Journal of Power and Energy**, IMECHE, v. 214, n. 2, p. 165–182, mar. 2000. ISSN 0957-6509. DOI: 10.1243/0957650001538263.

41 GAUTHIER, B. M.; DAVIDSON, D. F.; HANSON, R. K. Shock Tube Determination of Ignition Delay Times in Full-Blend and Surrogate Fuel Mixtures. **Combustion and Flame**, v. 139, n. 4, p. 300–311, dez. 2004. ISSN 0010-2180. DOI: 10.1016/j.combustflame.2004.08.015.

42 GMBH, AVL List. **BOOST User Manual 2021 R1**. [S.l.: s.n.], 2021.

43 _____. **CRUISE M User Manual 2021 R1**. [S.l.: s.n.], 2021.

44 _____. **FIRE CFD Solver User Manual 2021 R1**. [S.l.: s.n.], 2021.

45 GMBH, AVL List. **FIRE Combustion 2021 R1**. [S.l.: s.n.], 2021.

46 _____. **FIRE Emission 2021 R1**. [S.l.: s.n.], 2021.

47 _____. **FIRE Example Documentation 2021 R1 - Description and Data - FIRE 990 Gasoline Direct Injected Engine**. [S.l.: s.n.], 2021.

48 _____. **FIRE Spray 2021 R1**. [S.l.: s.n.], 2021.

49 GMBH, Robert Bosch. **Gasoline Direct Injection**. [S.l.: s.n.], 2022. https://www.bosch-mobility-solutions.com/en/solutions/powertrain/gasoline/gasoline-direct-injection/.

50 _____. **Gasoline Port Fuel Injection**. [S.l.: s.n.], 2022. https://www.bosch-mobility-solutions.com/en/solutions/powertrain/gasoline/gasoline-port-fuel-injection/.

51 GOODWIN, David G et al. **Cantera: An Object-oriented Software Toolkit for Chemical Kinetics, Thermodynamics, and Transport Processes**. [S.l.: s.n.], fev. 2021. Zenodo. DOI: 10.5281/ZENODO.4527812.

52 HALSTEAD, M. P.; KIRSCH, L. J.; QUINN, C. P. The Autoignition of Hydrocarbon Fuels at High Temperatures and Pressures—Fitting of a Mathematical Model. **Combustion and Flame**, v. 30, p. 45–60, jan. 1977. ISSN 0010-2180. DOI: 10.1016/0010-2180(77)90050-5.

53 HANJALIĆ, K.; POPOVAC, M.; HADŽIABDIĆ, M. A Robust Near-Wall Elliptic-Relaxation Eddy-Viscosity Turbulence Model for CFD. **International Journal of Heat and Fluid Flow**, v. 25, n. 6, p. 1047–1051, dez. 2004. ISSN 0142-727X. DOI: 10.1016/j.ijheatfluidflow.2004.07.005.

54 HARTMANN, M. et al. Auto-Ignition of Toluene-Doped n-Heptane and Iso-Octane/Air Mixtures: High-pressure Shock-Tube Experiments and Kinetics Modeling. **Combustion and Flame**, v. 158, n. 1, p. 172–178, jan. 2011. ISSN 0010-2180. DOI: 10.1016/j.combustflame.2010.08.005.

55 HE, X. et al. An Experimental and Modeling Study of Iso-Octane Ignition Delay Times under Homogeneous Charge Compression Ignition Conditions. **Combustion and Flame**, v. 142, n. 3, p. 266–275, ago. 2005. ISSN 0010-2180. DOI: 10.1016/j.combustflame.2005.02.014.

56 HEALY, D. et al. Oxidation of C1-C5 Alkane Quinternary Natural Gas Mixtures at High Pressures. **Energy & Fuels**, American Chemical Society, v. 24, n. 3, p. 1521–1528, mar. 2010. ISSN 0887-0624. DOI: 10.1021/ef9011005.

57 HERZLER, J. et al. Shock-Tube Study of the Autoignition of n-Heptane/Toluene/Air Mixtures at Intermediate Temperatures and High Pressures. **Combustion and Flame**, v. 149, n. 1, p. 25–31, abr. 2007. ISSN 0010-2180. DOI: 10.1016/j.combustflame.2006.12.015.

58 HEUFER, K. Alexander et al. Detailed Kinetic Modeling Study of N-Pentanol Oxidation. **Energy & Fuels**, American Chemical Society, v. 26, n. 11, p. 6678–6685, nov. 2012. ISSN 0887-0624. DOI: 10.1021/ef3012596.

59 HUANG, Y.; SUNG, C. J.; ENG, J. A. Laminar Flame Speeds of Primary Reference Fuels and Reformer Gas Mixtures. **Combustion and Flame**, v. 139, n. 3, p. 239–251, nov. 2004. ISSN 0010-2180. DOI: 10.1016/j.combustflame.2004.08.011.

60 HUNWARTZEN, I. Modification of CFR Test Engine Unit to Determine Octane Numbers of Pure Alcohols and Gasoline-Alcohol Blends. In: SAE INTERNATIONAL CONGRESS and Exposition. [S.l.: s.n.], fev. 1982. P. 820002. DOI: 10.4271/820002.

61 JERZEMBECK, S. et al. Laminar Burning Velocities at High Pressure for Primary Reference Fuels and Gasoline: Experimental and Numerical Investigation. **Combustion and Flame**, v. 156, n. 2, p. 292–301, fev. 2009. ISSN 0010-2180. DOI: 10.1016/j.combustflame.2008.11.009.

62 JOHNSON, Michael V. et al. A Shock Tube Study of n- and Iso-Propanol Ignition. **Energy & Fuels**, American Chemical Society, v. 23, n. 12, p. 5886–5898, dez. 2009. ISSN 0887-0624. DOI: 10.1021/ef900726j.

63 KALGHATGI, Gautam; BABIKER, Hassan; BADRA, Jihad. A Simple Method to Predict Knock Using Toluene, N-Heptane and Iso-Octane Blends (TPRF) as Gasoline Surrogates. **SAE International Journal of Engines**, v. 8, n. 2, p. 505–519, abr. 2015. ISSN 1946-3944. DOI: 10.4271/2015-01-0757.

64 KANG, Dongil et al. Auto-Ignition Study of FACE Gasoline and Its Surrogates at Advanced IC Engine Conditions. **Proceedings of the Combustion Institute**, v. 37, n. 4, p. 4699–4707, jan. 2019. ISSN 1540-7489. DOI: 10.1016/j.proci.2018.08.053.

65 KEE, R et al. PREMIX: A Fortran Program for Modeling Steady Laminar One-Dimensional Premixed Flames. **Sandia Rep**, v. 143, jan. 1985.

66 KÉROMNÈS, Alan et al. An Experimental and Detailed Chemical Kinetic Modeling Study of Hydrogen and Syngas Mixture Oxidation at Elevated Pressures. **Combustion and Flame**, v. 160, n. 6, p. 995–1011, jun. 2013. ISSN 0010-2180. DOI: 10.1016/j.combustflame.2013.01.001.

67 KHALED, Fethi; BADRA, Jihad; FAROOQ, Aamir. Ignition Delay Time Correlation of Fuel Blends Based on Livengood-Wu Description. **Fuel**, v. 209, p. 776–786, dez. 2017. ISSN 0016-2361. DOI: 10.1016/j.fuel.2017.07.095.

68 KHALED, Fethi; FAROOQ, Aamir. On the Universality of Ignition Delay Times of Distillate Fuels at High Temperatures: A Statistical Approach. **Combustion and Flame**, v. 210, p. 145–158, dez. 2019. ISSN 0010-2180. DOI: 10.1016/j.combustflame.2019.08.026.

69 KOZARAC, Darko et al. A Model for Prediction of Knock in the Cycle Simulation by Detail Characterization of Fuel and Temperature Stratification. **SAE International Journal of Engines**, v. 8, n. 4, p. 1520–1534, abr. 2015. ISSN 1946-3944. DOI: 10.4271/2015-01-1245.

70 KUBIC, William L. et al. Artificial Neural Network Based Group Contribution Method for Estimating Cetane and Octane Numbers of Hydrocarbons and Oxygenated Organic Compounds. **Industrial & Engineering Chemistry Research**, American Chemical Society, v. 56, n. 42, p. 12236–12245, out. 2017. ISSN 0888-5885. DOI: 10.1021/acs.iecr.7b02753.

71 KUKKADAPU, Goutham et al. Autoignition of Gasoline Surrogates at Low Temperature Combustion Conditions. **Combustion and Flame**, v. 162, n. 5, p. 2272–2285, mai. 2015. ISSN 0010-2180. DOI: 10.1016/j.combustflame.2015.01.025.

72 LEE, Changyoul et al. Autoignition Characteristics of Oxygenated Gasolines. **Combustion and Flame**, v. 186, p. 114–128, dez. 2017. ISSN 0010-2180. DOI: 10.1016/j.combustflame.2017.07.034.

73 LI, Hua et al. Autoignition of Ternary Blends for Gasoline Surrogate at Wide Temperature Ranges and at Elevated Pressure: Shock Tube Measurements and Detailed Kinetic Modeling. **Fuel**, v. 181, p. 916–925, out. 2016. ISSN 0016-2361. DOI: 10.1016/j.fuel.2016.05.030.

74 LI, Juan et al. A Comprehensive Kinetic Mechanism for CO, CH2O, and CH3OH Combustion. **International Journal of Chemical Kinetics**, v. 39, n. 3, p. 109–136, 2007. ISSN 1097-4601. DOI: 10.1002/kin.20218.

75 LI, Yang et al. Development of a Reduced Four-Component (Toluene/n-Heptane/Iso-Octane/Ethanol) Gasoline Surrogate Model. **Fuel**, v. 247, p. 164–178, jul. 2019. ISSN 0016-2361. DOI: 10.1016/j.fuel.2019.03.052.

76 LINSE, Dirk; KLEEMANN, Andreas; HASSE, Christian. Probability Density Function Approach Coupled with Detailed Chemical Kinetics for the Prediction of Knock in Turbocharged Direct Injection Spark Ignition Engines. **Combustion and Flame**, v. 161, n. 4, p. 997–1014, abr. 2014. ISSN 00102180. DOI: 10.1016/j.combustflame.2013.10.025.

77 LIU, Yao-Dong et al. Development of a New Skeletal Chemical Kinetic Model of Toluene Reference Fuel with Application to Gasoline Surrogate Fuels for Computational Fluid Dynamics Engine Simulation. **Energy & Fuels**, American Chemical Society, v. 27, n. 8, p. 4899–4909, ago. 2013. ISSN 0887-0624. DOI: 10.1021/ef4009955.

78 LIVENGOOD, J. C.; WU, P. C. Correlation of Autoignition Phenomena in Internal Combustion Engines and Rapid Compression Machines. **Symposium (International) on Combustion**, v. 5, n. 1, p. 347–356, jan. 1955. ISSN 0082-0784. DOI: 10.1016/S0082-0784(55)80047-1.

79 MA, Zhihao et al. Shock Tube Studies on Ignition Delay and Combustion Characteristics of Oxygenated Fuels under High Temperature. **International Journal of Energy Research**, v. 44, n. 13, p. 10101–10111, out. 2020. ISSN 0363-907X, 1099-114X. DOI: 10.1002/er.5624.

80 MAN, Xingjia et al. An Experimental and Kinetic Modeling Study of N-Propanol and i-Propanol Ignition at High Temperatures. **Combustion and Flame**, v. 161, n. 3, p. 644–656, mar. 2014. ISSN 0010-2180. DOI: 10.1016/j.combustflame.2013.08.003.

81 MANSFIELD, A. B. et al. Low-Temperature Ignition Behavior of Iso-Octane. **Fuel**, v. 139, p. 79–86, jan. 2015. ISSN 0016-2361. DOI: 10.1016/j.fuel.2014.08.019.

82 MATHIEU, Olivier et al. Experimental Study of Ethanol Oxidation behind Reflected Shock Waves: Ignition Delay Time and H2O Laser-Absorption Measurements. **Combustion and Flame**, v. 208, p. 313–326, out. 2019. ISSN 0010-2180. DOI: 10.1016/j.combustflame.2019.07.005.

83 MERKER, Günter P; SCHWARZ, Christian; TEICHMANN, Rüdiger. **Combustion Engines Development - Mixture Formation, Combustion, Emissions and Simulation**. [S.l.]: Springer, 2012. ISBN 978-3-642-02951-6.

84 METCALFE, Wayne K. et al. A Hierarchical and Comparative Kinetic Modeling Study of C1 - C2 Hydrocarbon and Oxygenated Fuels. **International Journal of Chemical Kinetics**, v. 45, n. 10, p. 638–675, 2013. ISSN 1097-4601. DOI: 10.1002/kin.20802.

85 METGHALCHI, Mohamad; KECK, James C. Burning Velocities of Mixtures of Air with Methanol, Isooctane, and Indolene at High Pressure and Temperature. **Combustion and Flame**, v. 48, p. 191–210, jan. 1982. ISSN 0010-2180. DOI: 10.1016/0010-2180(82)90127-4.

86 MINTEER, S. D. 11 - Biochemical Production of Other Bioalcohols: Biomethanol, Biopropanol, Bioglycerol, and Bioethylene Glycol. In: LUQUE, Rafael; CAMPELO, Juan; CLARK, James (Ed.). **Handbook of Biofuels Production**. [S.l.]: Woodhead Publishing, jan. 2011. (Woodhead Publishing Series in Energy). P. 258–265. ISBN 978-1-84569-679-5. DOI: 10.1533/9780857090492.2.258.

87 MITTAL, Gaurav et al. Autoignition of Ethanol in a Rapid Compression Machine. **Combustion and Flame**, v. 161, n. 5, p. 1164–1171, mai. 2014. ISSN 0010-2180. DOI: 10.1016/j.combustflame.2013.11.005.

88 MODELS with Tensor Variables. In: STATISTICAL Theory and Modeling for Turbulent Flows. Chichester, UK: John Wiley & Sons, Ltd, ago. 2010. P. 155–215. ISBN 978-0-470-97207-6 978-0-470-68931-8. DOI: 10.1002/9780470972076.ch7.

89 MOSES, Eduard; YARIN, Alexander L.; BAR-YOSEPH, Pinhas. On Knocking Prediction in Spark Ignition Engines. **Combustion and Flame**, v. 101, n. 3, p. 239–261, mai. 1995. ISSN 0010-2180. DOI: 10.1016/0010-2180(94)00202-4.

90 NASER, Nimal; SARATHY, S. Mani; CHUNG, Suk Ho. Estimating Fuel Octane Numbers from Homogeneous Gas-Phase Ignition Delay Times. **Combustion and Flame**, v. 188, p. 307–323, fev. 2018. ISSN 0010-2180. DOI: 10.1016/j.combustflame.2017.09.037.

91 NATIVEL, Damien et al. Ethanol Ignition in a High-Pressure Shock Tube: Ignition Delay Time and High-Repetition-Rate Imaging Measurements. **Proceedings of the Combustion Institute**, v. 38, n. 1, p. 901–909, jan. 2021. ISSN 1540-7489. DOI: 10.1016/j.proci.2020.07.021.

92 NOORANI, Khalid Emilio; AKIH-KUMGEH, Benjamin; BERGTHORSON, Jeffrey M. Comparative High Temperature Shock Tube Ignition of C1 C4 Primary Alcohols. **Energy & Fuels**, American Chemical Society, v. 24, n. 11, p. 5834–5843, nov. 2010. ISSN 0887-0624. DOI: 10.1021/ef1009692.

93 ONLINE, CFD. **V2-f Models**. [S.l.: s.n.], fev. 2014. https://www.cfd-online.com/Wiki/V2-f_models.

94 PAYKANI, Amin et al. Progress and Recent Trends in Reactivity-Controlled Compression Ignition Engines. **International Journal of Engine Research**, SAGE Publications, v. 17, n. 5, p. 481–524, jun. 2016. ISSN 1468-0874. DOI: 10.1177/1468087415593013.

95 PEARSON, R. J.; TURNER, J. W. G. 13 - Improving the Use of Liquid Biofuels in Internal Combustion Engines. In: WALDRON, Keith (Ed.). **Advances in Biorefineries**. [S.l.]: Woodhead Publishing, jan. 2014. P. 389–440. ISBN 978-0-85709-521-3. DOI: 10.1533/9780857097385.2.389.

96 PELUCCHI, M. et al. Combustion of N-C3–C6 Linear Alcohols: An Experimental and Kinetic Modeling Study. Part II: Speciation Measurements in a Jet-Stirred Reactor, Ignition Delay Time Measurements in a Rapid Compression Machine, Model Validation, and Kinetic Analysis. **Energy & Fuels**, American Chemical Society, v. 34, n. 11, p. 14708–14725, nov. 2020. ISSN 0887-0624. DOI: 10.1021/acs.energyfuels.0c02252.

97 PELUCCHI, Matteo et al. Alkyl Radicals Rule the Low Temperature Oxidation of Long Chain Aldehydes. **Proceedings of the Combustion Institute**, v. 36, n. 1, p. 393–401, jan. 2017. ISSN 1540-7489. DOI: 10.1016/j.proci.2016.05.051.

98 PINZÓN, L. T. et al. Ignition Delay Time and H2O Measurements during Methanol Oxidation behind Reflected Shock Waves. **Combustion and Flame**, v. 203, p. 143–156, mai. 2019. ISSN 0010-2180. DOI: 10.1016/j.combustflame.2019.01.036.

99 PITZ, JW; WESTBROOK, CK. Combustion Chemistry, 2011.

100 RANZI, E. et al. Hierarchical and Comparative Kinetic Modeling of Laminar Flame Speeds of Hydrocarbon and Oxygenated Fuels. **Progress in Energy and Combustion Science**, v. 38, n. 4, p. 468–501, ago. 2012. ISSN 0360-1285. DOI: 10.1016/j.pecs.2012.03.004.

101 RANZI, Eliseo et al. Prediction of Kinetic Parameters for Hydrogen Abstraction Reactions. **Combustion Science and Technology**, Taylor & Francis, v. 95, n. 1-6, p. 1–50, dez. 1993. ISSN 0010-2202. DOI: 10.1080/00102209408935325.

102 RANZI, Eliseo et al. Reduced Kinetic Schemes of Complex Reaction Systems: Fossil and Biomass-Derived Transportation Fuels: REDUCED KINETIC SCHEMES OF COMPLEX REACTION SYSTEMS. **International Journal of Chemical Kinetics**, v. 46, n. 9, p. 512–542, set. 2014. ISSN 05388066. DOI: 10.1002/kin.20867.

103 RATCLIFF, Matthew A. et al. Impact of Higher Alcohols Blended in Gasoline on Light-Duty Vehicle Exhaust Emissions. **Environmental Science & Technology**, American Chemical Society, v. 47, n. 23, p. 13865–13872, dez. 2013. ISSN 0013-936X. DOI: 10.1021/es402793p.

104 RUSCIC, Branko et al. Active Thermochemical Tables: Thermochemistry for the 21st Century. **Journal of Physics: Conference Series**, IOP Publishing, v. 16, p. 561–570, jan. 2005. ISSN 1742-6596. DOI: 10.1088/1742-6596/16/1/078.

105 SANTANA, Claudio Marcio et al. Measuring and Comparing the Ignition Delay Time of the Reference Diesel, Convectional Diesel, Additive Ethanol and Biodiesel from Soybean Oil Using a Shock Tube. **Journal of the Brazilian Society of Mechanical Sciences and Engineering**, v. 42, n. 2, p. 102, jan. 2020. ISSN 1806-3691. DOI: 10.1007/s40430-020-2183-z.

106 SARATHY, MS. et al. A Comprehensive Experimental and Modeling Study of Iso-Pentanol Combustion. **Combustion and Flame**, v. 160, n. 12, p. 2712–2728, dez. 2013. ISSN 0010-2180. DOI: 10.1016/j.combustflame.2013.06.022.

107 SARATHY, S. Mani et al. A Comprehensive Chemical Kinetic Combustion Model for the Four Butanol Isomers. **Combustion and Flame**, v. 159, n. 6, p. 2028–2055, jun. 2012. ISSN 0010-2180. DOI: 10.1016/j.combustflame.2011.12.017.

108 SARATHY, S. Mani et al. Alcohol Combustion Chemistry. **Progress in Energy and Combustion Science**, v. 44, p. 40–102, out. 2014. ISSN 0360-1285. DOI: 10.1016/j.pecs.2014.04.003.

109 SARATHY, S. Mani et al. Ignition of Alkane-Rich FACE Gasoline Fuels and Their Surrogate Mixtures. **Proceedings of the Combustion Institute**, v. 35, n. 1, p. 249–257, jan. 2015. ISSN 1540-7489. DOI: 10.1016/j.proci.2014.05.122.

110 SCHILLER, L.; NAUMANN, A. A Drag Coefficient Correlation. **Zeitschrift des Vereins Deutscher Ingenieure**, n. 77, p. 318–320, 1935.

111 SCULLY, Sean Michael; ORLYGSSON, Johann. Chapter 5 - Biological Production of Alcohols. In: HOSSEINI, Majid (Ed.). **Advanced Bioprocessing for Alternative Fuels, Biobased Chemicals, and Bioproducts**. [S.l.]: Woodhead Publishing, jan. 2019. (Woodhead Publishing Series in Energy). P. 83–108. ISBN 978-0-12-817941-3. DOI: 10.1016/B978-0-12-817941-3.00005-X.

112 SEABOLD, SKIPPER; PERKTOLD, Josef. Statsmodels: Econometric and Statistical Modeling with Python. **9th Python in Science Conference**, 2010.

113 SHAO, Jiankun et al. A Shock Tube Study of N-Heptane, Iso-Octane, n-Dodecane and Iso-Octane/n-Dodecane Blends Oxidation at Elevated Pressures and Intermediate Temperatures. **Fuel**, v. 243, p. 541–553, mai. 2019. ISSN 0016-2361. DOI: 10.1016/j.fuel.2019.01.152.

114 SHARIATMADAR, F S; PAKDEHI, S Ghanbari; ZAREI, M A. An Empirical Correlation to Predict the Ignition Delay Time for Some Hydrocarbon Fuels. **Iranian Journal of Chemical Engineering**, v. 13, n. 1, p. 14, 2016.

115 SHARMA, Manjul. **Different Types of Fuel Injection System and How Do They Work? - Spinny**. [S.l.: s.n.], mar. 2022. TECHNOLOGY.

116 SHARMA, Nishchay. Knock Model Evaluation – Gas Engine, p. 59.

117 STRANIC, Ivo et al. Shock Tube Measurements of Ignition Delay Times for the Butanol Isomers. **Combustion and Flame**, v. 159, n. 2, p. 516–527, fev. 2012. ISSN 0010-2180. DOI: 10.1016/j.combustflame.2011.08.014.

118 SUNDBERG, Rolf. Statistical Aspects on Fitting the Arrhenius Equation. **Chemometrics and Intelligent Laboratory Systems**, v. 41, n. 2, p. 249–252, jul. 1998. ISSN 0169-7439. DOI: 10.1016/S0169-7439(98)00052-5.

119 TAO, Mingyuan; HAN, Dong; ZHAO, Peng. An Alternative Approach to Accommodate Detailed Ignition Chemistry in Combustion Simulation. **Combustion and Flame**, v. 176, p. 400–408, fev. 2017. ISSN 0010-2180. DOI: 10.1016/j.combustflame.2016.11.009.

120 TSURUSHIMA, T. A New Skeletal PRF Kinetic Model for HCCI Combustion. **Proceedings of the Combustion Institute**, v. 32, n. 2, p. 2835–2841, jan. 2009. ISSN 1540-7489. DOI: 10.1016/j.proci.2008.06.018.

121 VAN REE, R. et al. 21 - Biofuel-driven Biorefineries for the Co-Production of Transportation Fuels and Added-Value Products. In: LUQUE, Rafael; CAMPELO, Juan; CLARK, James (Ed.). **Handbook of Biofuels Production**. [S.l.]: Woodhead Publishing, jan. 2011. (Woodhead Publishing Series in Energy). P. 559–580. ISBN 978-1-84569-679-5. DOI: 10.1533/9780857090492.4.559.

122 VANCOILLIE, J. et al. Temperature Dependence of the Laminar Burning Velocity of Methanol Flames. **Energy & Fuels**, American Chemical Society, v. 26, n. 3, p. 1557–1564, mar. 2012. ISSN 0887-0624. DOI: 10.1021/ef2016683.

123 VANCOILLIE, J. et al. The Potential of Methanol as a Fuel for Flex-Fuel and Dedicated Spark-Ignition Engines. **Applied Energy**, v. 102, p. 140–149, fev. 2013. ISSN 0306-2619. DOI: 10.1016/j.apenergy.2012.05.065.

124 VELOO, Peter S.; EGOLFOPOULOS, Fokion N. Studies of N-Propanol, Iso-Propanol, and Propane Flames. **Combustion and Flame**, v. 158, n. 3, p. 501–510, mar. 2011. ISSN 0010-2180. DOI: 10.1016/j.combustflame.2010.10.001.

125 VELOO, Peter S. et al. A Comparative Experimental and Computational Study of Methanol, Ethanol, and n-Butanol Flames. **Combustion and Flame**, v. 157, n. 10, p. 1989–2004, out. 2010. ISSN 0010-2180. DOI: 10.1016/j.combustflame.2010.04.001.

126 VERMEER, D. J.; MEYER, J. W.; OPPENHEIM, A. K. Auto-Ignition of Hydrocarbons behind Reflected Shock Waves. **Combustion and Flame**, v. 18, n. 3, p. 327–336, jun. 1972. ISSN 0010-2180. DOI: 10.1016/S0010-2180(72)80183-4.

127 VERSTEEG, Henk Kaarle; MALALASEKERA, Weeratunge. **An Introduction to Computational Fluid Dynamics: The Finite Volume Method**. [S.l.: s.n.], 2007.

128 WORK, How Car Parts. **How Car Parts Work: Combustion Chambers for Diesel Engines**. [S.l.: s.n.], jan. 2021.

129 XU, Quanhong et al. Influence of Blending N-Butanol with Isooctane and n-Heptane on Ignition Delay Times in a Fuel Ignition Tester. **Energy & Fuels**, American Chemical Society, v. 32, n. 5, p. 6239–6251, mai. 2018. ISSN 0887-0624. DOI: 10.1021/acs.energyfuels.7b02127.

130 YUE, Zongyu; SOM, Sibendu. Fuel Property Effects on Knock Propensity and Thermal Efficiency in a Direct-Injection Spark-Ignition Engine. **Applied Energy**, v. 281, p. 114221, jan. 2021. ISSN 0306-2619. DOI: 10.1016/j.apenergy.2019.114221.

131 YUE, Zongyu et al. A Transported Livengood-Wu Integral Model for Knock Prediction in CFD Simulation, p. 18.

132 ZHANG, Yingjia et al. Probing the Low-Temperature Chemistry of Ethanol via the Addition of Dimethyl Ether. **Combustion and Flame**, v. 190, p. 74–86, abr. 2018. ISSN 0010-2180. DOI: 10.1016/j.combustflame.2017.11.011.

133 ZHAO, Zhenwei et al. Thermal decomposition reaction and a comprehensive kinetic model of dimethyl ether. **International Journal of Chemical Kinetics**, v. 40, n. 1, p. 1–18, 2008. ISSN 1097-4601. DOI: 10.1002/kin.20285.

134 ZHOU, Lei et al. Spray–Turbulence–Chemistry Interactions under Engine-like Conditions. **Progress in Energy and Combustion Science**, v. 86, p. 100939, set. 2021. ISSN 0360-1285. DOI: 10.1016/j.pecs.2021.100939.

APPENDIX A – CORRELATIONS FOR INDIVIDUAL FUELS

Table 26 shows the ignition delay time (IDT) correlations obtained via ordinary least squares (OLS) multiple linear regression (MLR) for each fuel considered individually. Since there is only one fuel per regression, the anti-knock index (AKI) exponent is meaningless (i.e. zero). Note also that other exponents set to zero mean that there is only one value for the regarded exponent (e.g. only stoichiometric equivalence ratio). As a reminder, the IDT correlation has the following form.

$$IDT = 10^{a} \exp\left(\frac{E_a}{RT}\right) AKI^{b}\, p^{c}\, \phi^{d} \tag{68}$$

where 10^{a} is the pre-exponential factor (A) in base-10, E_a the activation energy in kJ/mol, R the universal gas constant (8.314×10^{-3} kJ/(mol.K)), p the pressure in bar, and ϕ the equivalence ratio.

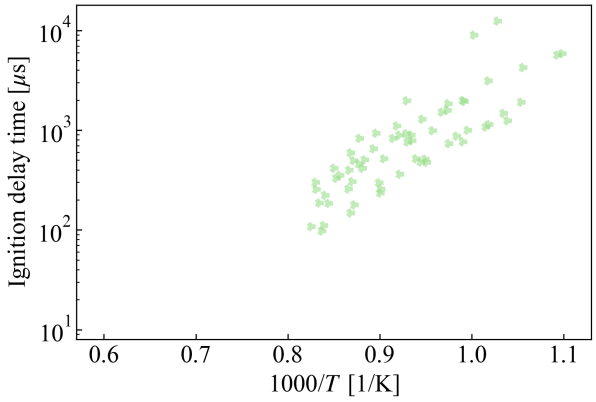

(a) BR1.

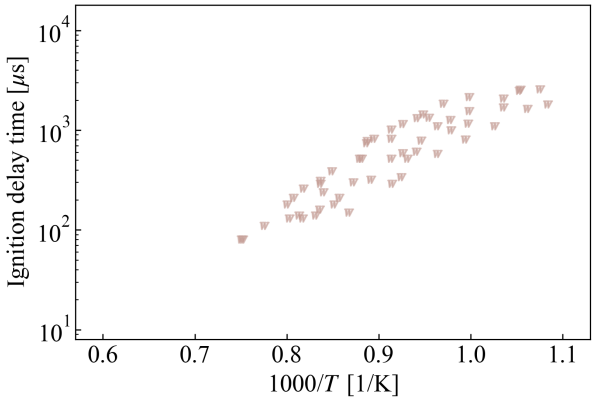

(b) Coryton.

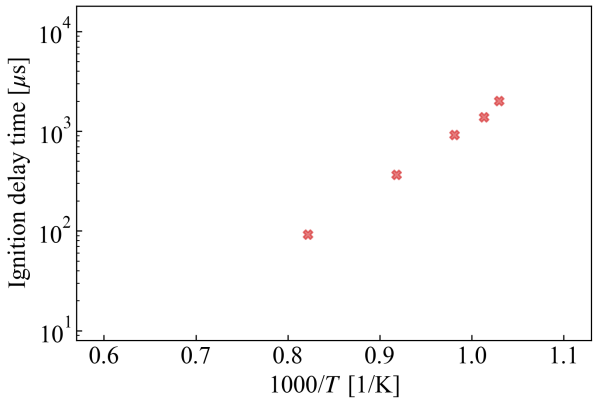

(c) E85.

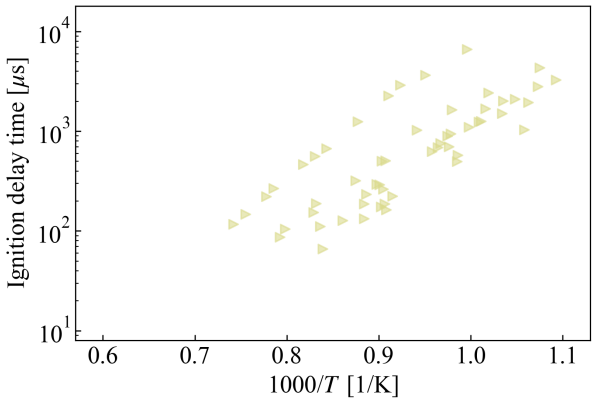

(d) FACE A.

Table 26 – Summary results for all correlations

Regression	a	E_a	b	c	d	R^2	AAE	Max. oversh.	Max. undersh.
BR1	-1.75±0.15	113.1±2.9	-	-0.79±0.04	-0.59±0.05	0.968	12.6%	53.2%	-49.6%
Coryton	-1.43±0.09	109.4±2.2	-	-0.85±0.05	-0.38±0.05	0.979	11.8%	41.0%	-22.3%
E85	-0.27±0.01	121.0±2.6	-	-2.02±0.08	0.44±0.02	0.999	3.2%	6.3%	-6.6%
Ethanol	-1.69±0.12	109.3±3.1	-	-0.78±0.04	-0.35±0.07	0.842	39.4%	238.7%	-71.6%
Ethanol/isoctane (25/75% vol.)	-0.33±0.05	132.6±12.1	-	-2.57±0.36	0.00±0.00	0.952	22.0%	57.4%	-36.5%
FACE A	-1.41±0.14	116.2±3.0	-	-1.20±0.06	-0.86±0.09	0.969	17.3%	50.5%	-38.0%
FACE C	-0.08±0.23	106.9±6.1	-	-1.64±0.11	0.13±0.16	0.853	36.4%	147.1%	-52.3%
Gasoline surrogate	-1.91±0.14	119.9±3.4	-	-0.85±0.04	-0.22±0.08	0.964	14.9%	50.5%	-32.8%
Haltermann	-1.35±0.08	105.7±1.8	-	-0.82±0.05	-0.37±0.04	0.988	9.3%	36.1%	-18.7%
PRF 80	-1.71±0.15	114.3±3.0	-	-0.90±0.05	-0.34±0.08	0.977	13.2%	43.3%	-32.4%
PRF 84	0.21±0.22	95.2±5.1	-	-1.48±0.10	-0.05±0.15	0.870	32.7%	164.6%	-59.2%
PRF 90	-0.12±0.01	87.6±4.3	-	-1.00±0.12	0.00±0.00	0.998	2.2%	2.4%	-3.2%
PRF 91	-2.35±0.16	126.2±3.2	-	-0.81±0.06	-0.14±0.09	0.974	16.8%	64.3%	-36.0%
PRF 95	-1.46±0.21	113.0±3.8	-	-0.96±0.07	-0.18±0.10	0.962	18.3%	114.4%	-31.0%
PRF 100	-1.46±0.07	105.4±2.1	-	-0.74±0.03	-0.77±0.08	0.968	14.7%	79.0%	-29.8%
Quinary mixture [2]	-2.04±0.67	113.6±11.9	-	-0.77±0.21	0.00±0.00	0.912	34.6%	155.6%	-33.3%
RD387	-1.19±0.29	110.1±7.0	-	-1.04±0.11	-0.54±0.13	0.895	20.3%	140.5%	-33.4%
Surrogate A	-1.52±0.44	116.0±8.5	-	-1.17±0.13	0.00±0.00	0.946	27.0%	78.9%	-39.4%
Surrogate A TPRF	-1.53±0.35	116.5±8.5	-	-1.00±0.11	-0.52±0.11	0.893	17.5%	58.8%	-36.2%
Surrogate B TPRF	-0.57±0.34	92.8±7.3	-	-0.90±0.17	0.00±0.00	0.948	12.4%	44.0%	-15.1%
Toluene	-0.76±0.31	90.6±5.9	-	-0.53±0.11	-0.94±0.16	0.881	24.0%	118.8%	-43.2%
TPRF 87 [3]	-1.86±0.11	133.1±2.6	-	-1.08±0.06	-0.26±0.04	0.983	8.6%	28.4%	-23.1%
TPRF toluene/isoctane (10/90% vol.)	-0.26±0.03	126.9±7.5	-	-2.22±0.22	-1.23±0.20	0.981	15.8%	36.9%	-16.9%

[a] atm

[b] Isoctane/toluene/*n*-heptane/di-iso-butylene/ethanol (30/25/22/13/10% in volume)

[c] 56% isoctane, 17% *n*-heptane, 27% toluene in mole

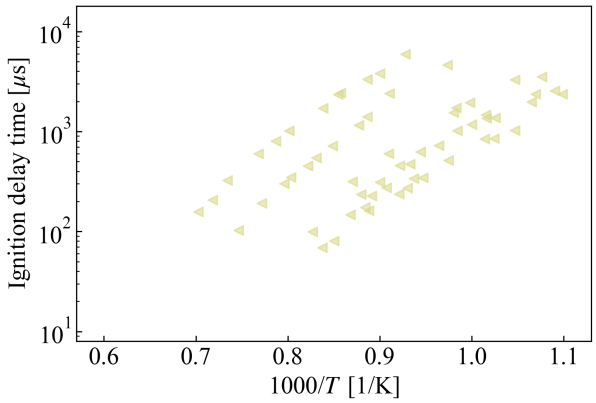

(e) FACE C.

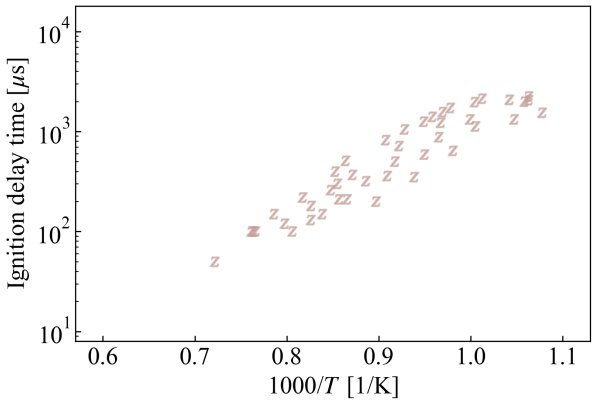

(f) Haltermann.

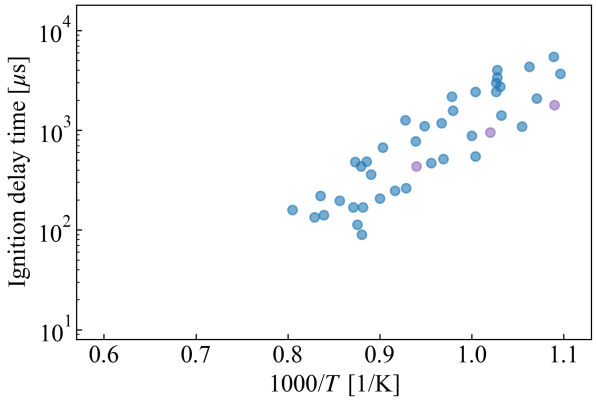

(g) PRF 80

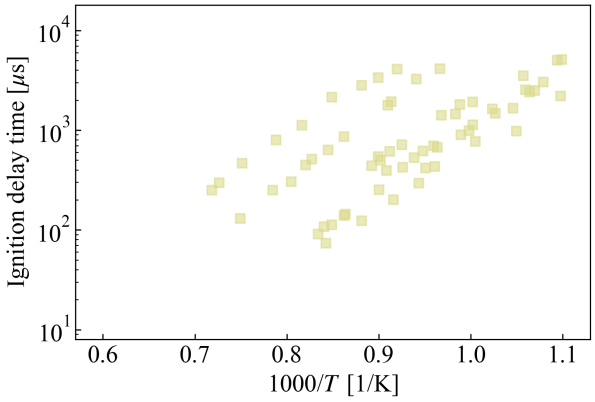

(h) PRF 84

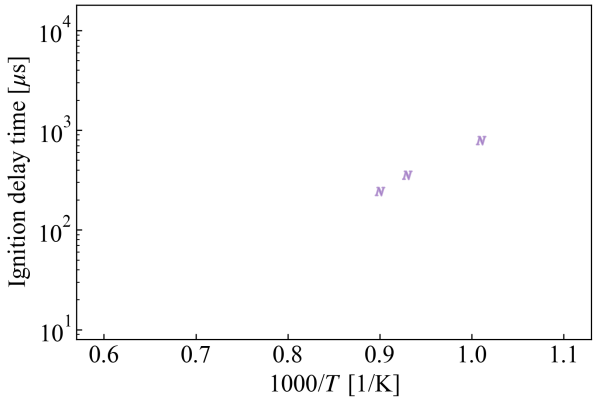

(i) PRF 90

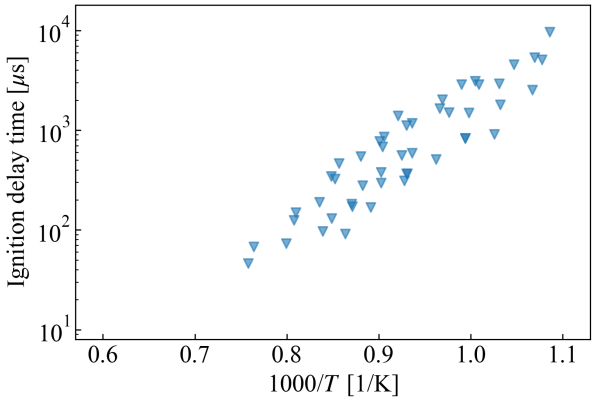

(j) PRF 91

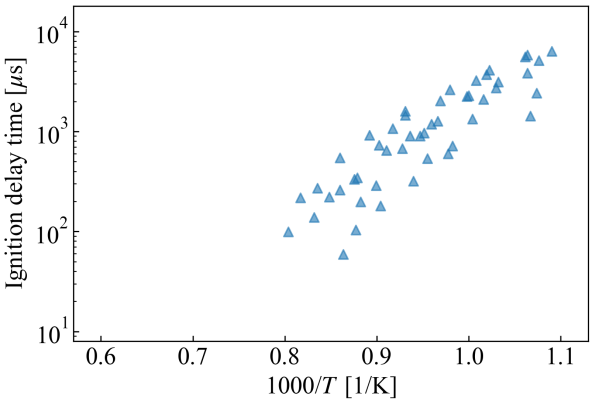

(k) PRF 95

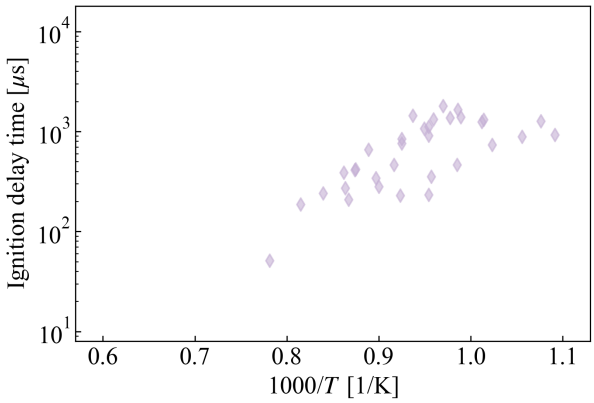

(l) RD387

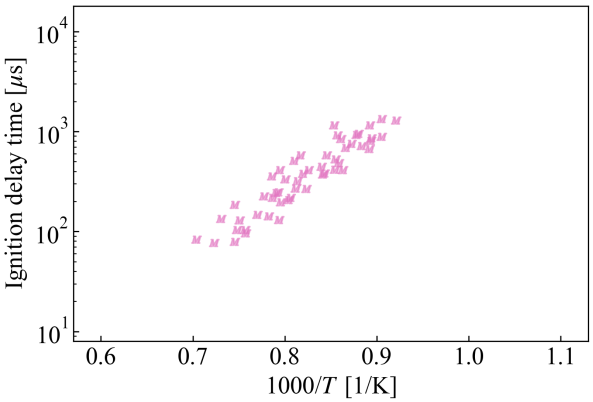

(m) TPRF 87 (56% isoc; 17% nhept; 27% tolu in mole).

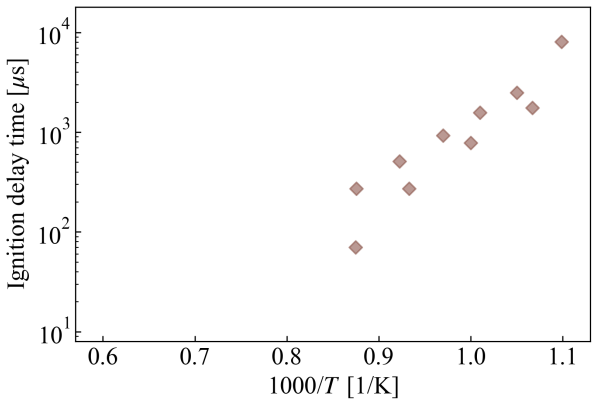

(n) TPRF toluene isoctane 10-90 volume

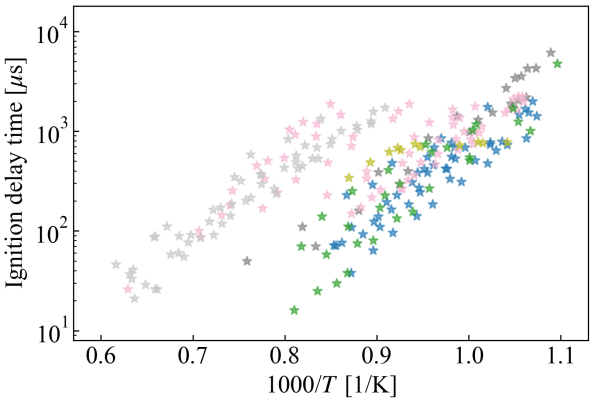

(o) Ethanol

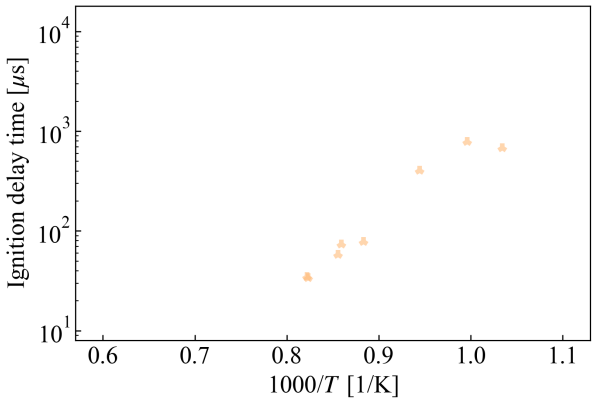

(p) Ethanol/isoctane 25-75 volume.

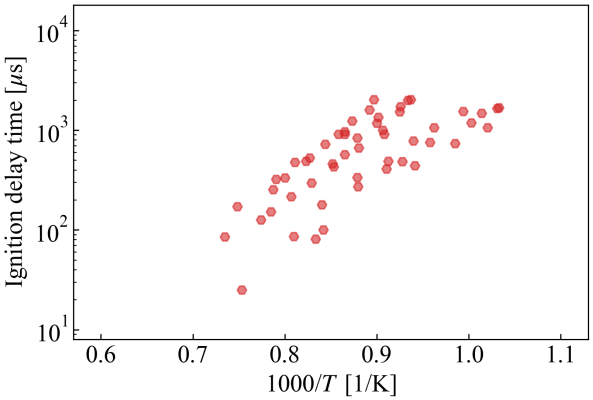

(q) Gasoline surrogate.

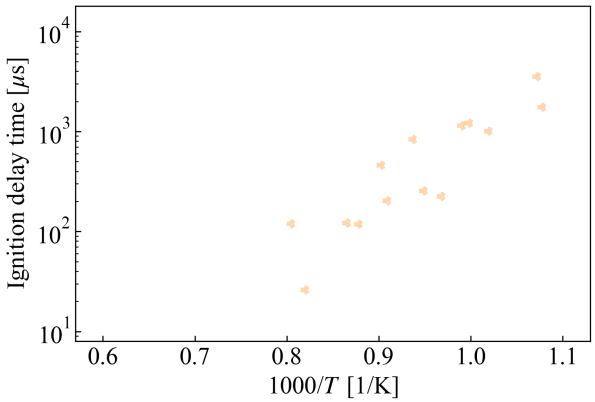

(r) isoctane, toluene, n-heptane, di-iso-butylene, ethanol 30-25-22-13-10.

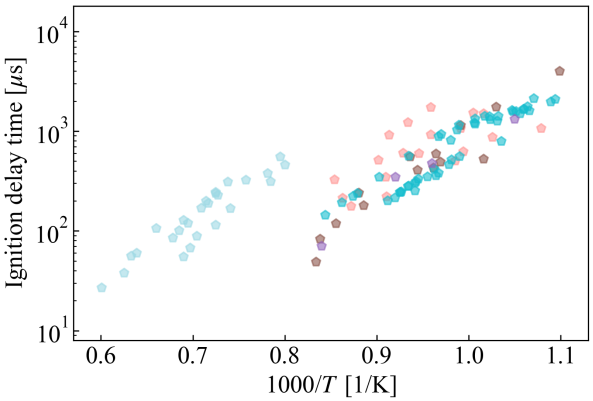

(s) Isoctane.

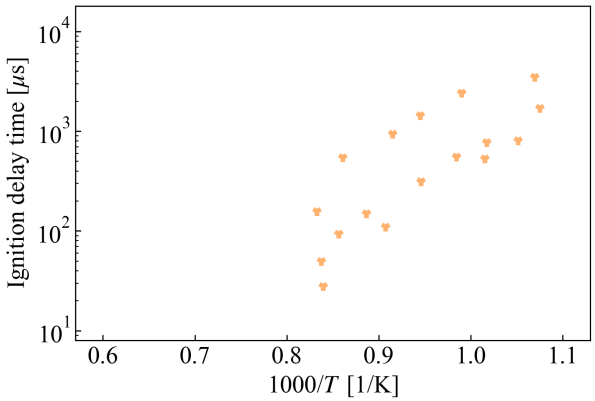

(t) Surrogate A.

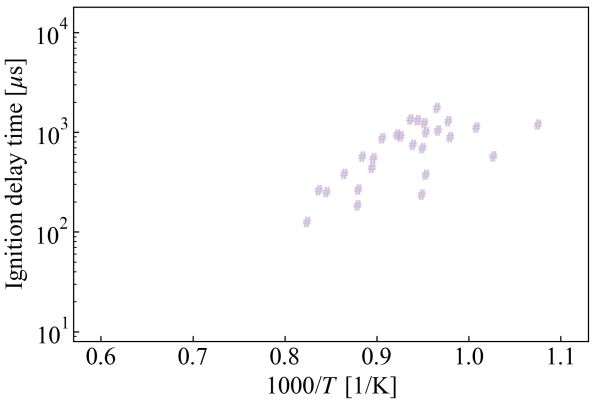

(u) Surrogate A TPRF.

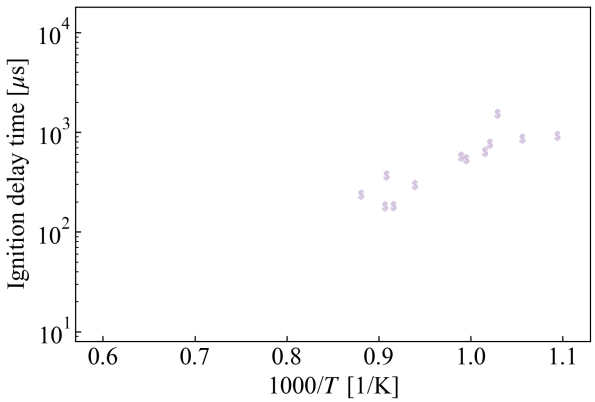

(v) Surrogate B TPRF.

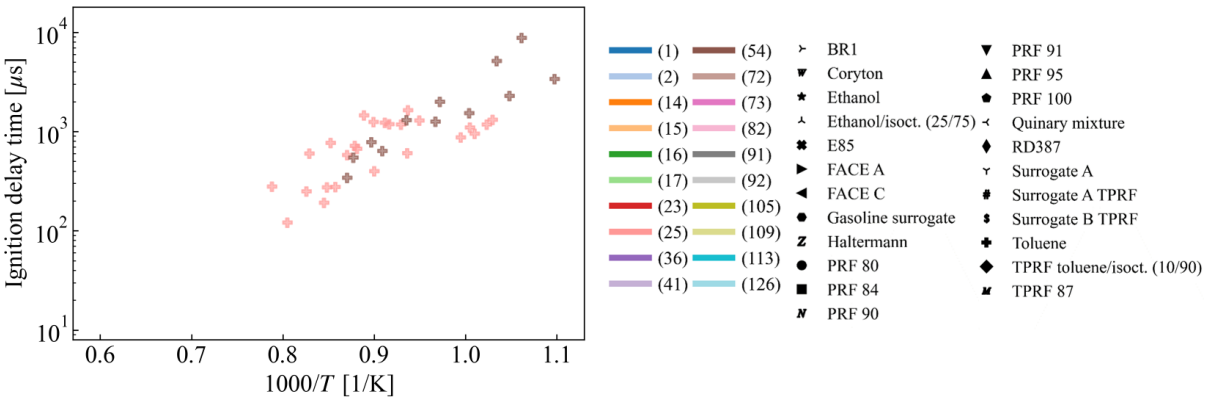

(w) Toluene.

Figure 40 – Mean in-cylinder quantities along crank angle.

APPENDIX B – IGNITION DELAY TIME AND LAMINAR FLAME SPEED ASSESSMENT FOR PRF CHEMICAL KINETICS MECHANISMS

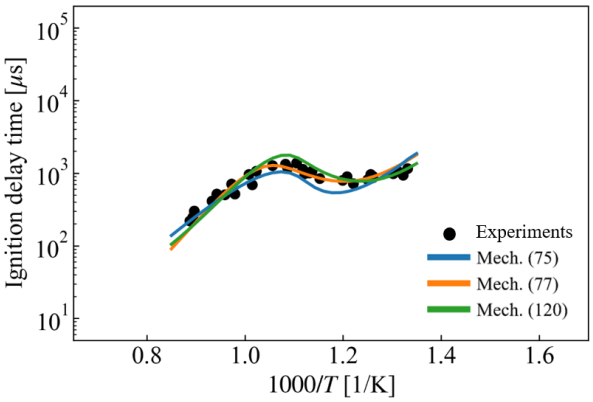

(a) PRF 0 at 28 bar and $\phi = 1.0$ (1).

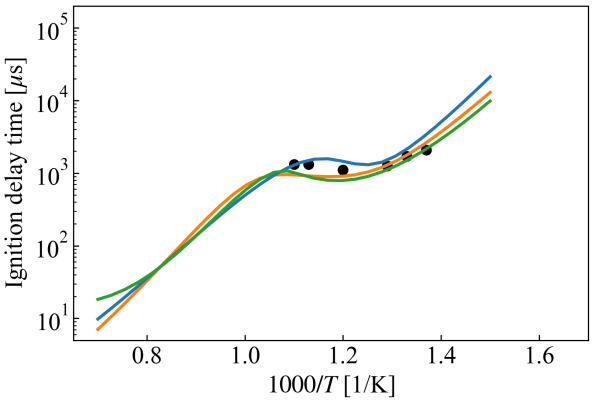

(b) PRF 60 at 40 bar and $\phi = 1.0$ (36)

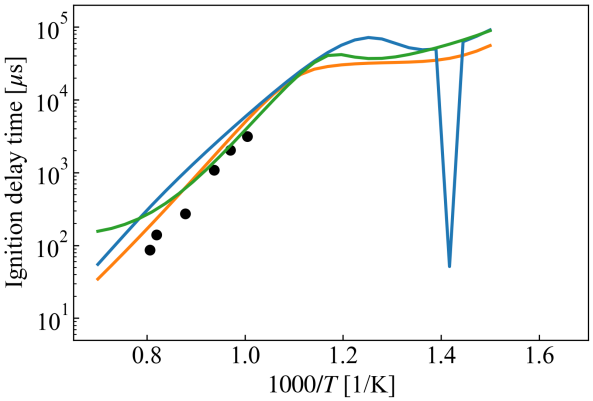

(c) PRF 70 at 10 bar and $\phi = 0.5$ (1)

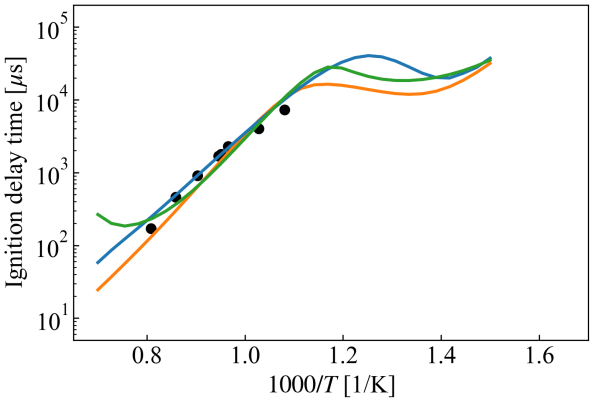

(d) PRF 70 at 10 bar and $\phi = 1.0$ (1)

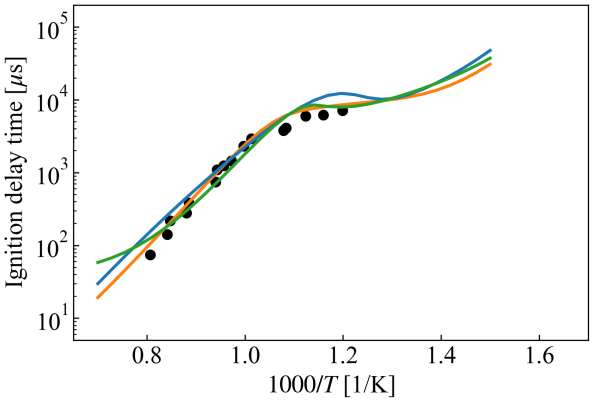

(e) PRF 70 at 20 bar and $\phi = 0.5$ (1)

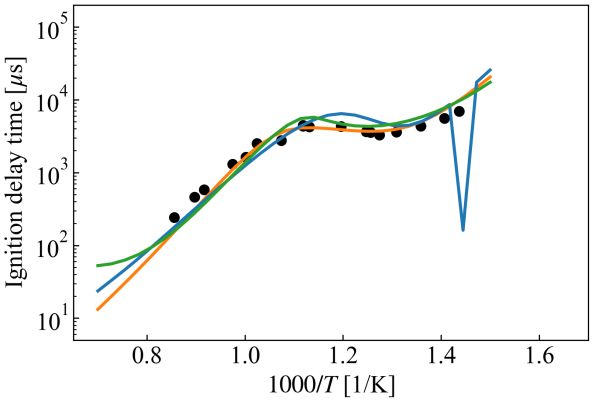

(f) PRF 70 at 20 bar and $\phi = 1.0$ (1)

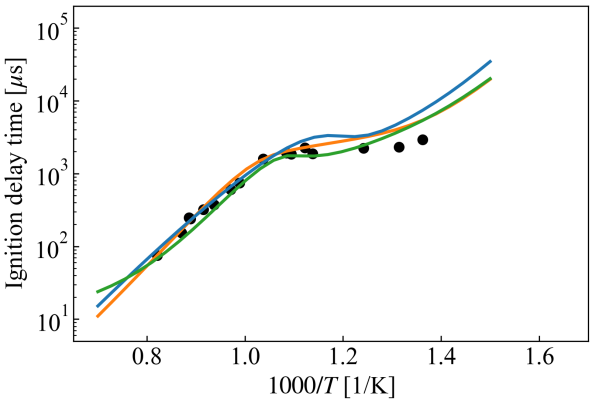

(a) PRF 70 at 40 bar and $\phi = 0.5$ (1)

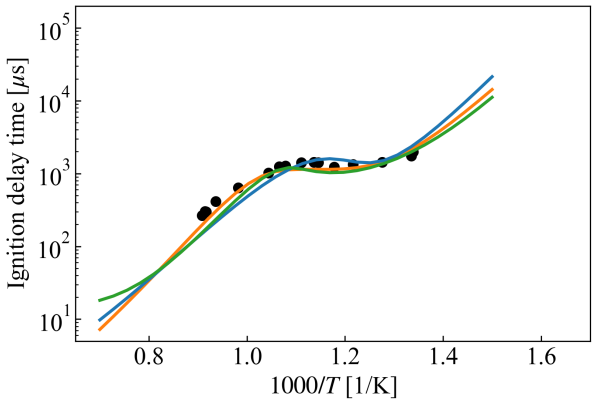

(b) PRF 70 at 40 bar and $\phi = 1.0$ (1)

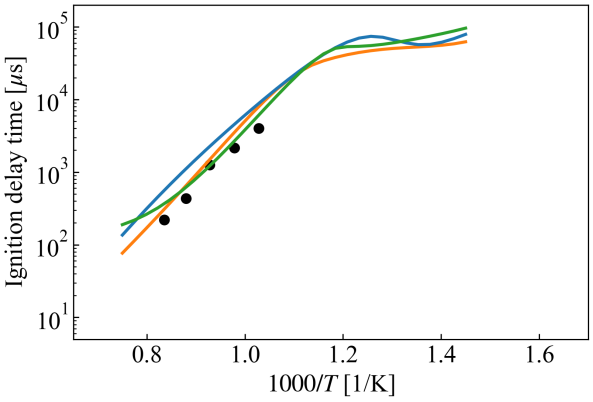

(c) PRF 80 at 10 bar and $\phi = 0.5$ (1)

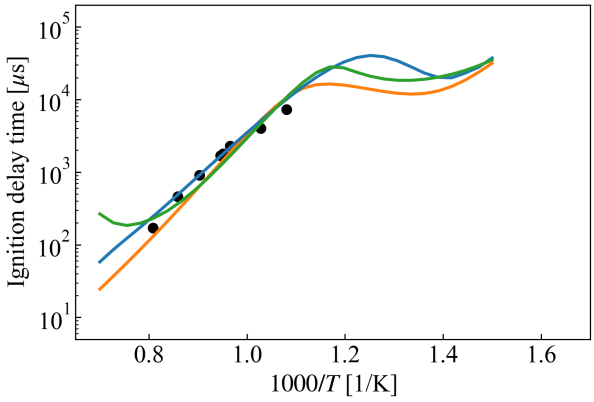

(d) PRF 80 at 10 bar and $\phi = 1.0$ (1)

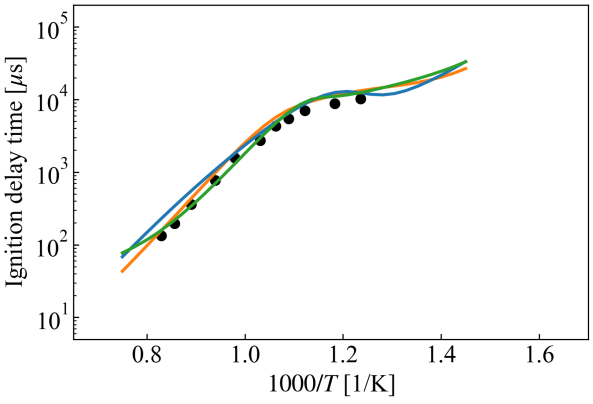

(e) PRF 80 at 20 bar and $\phi = 0.5$ (1)

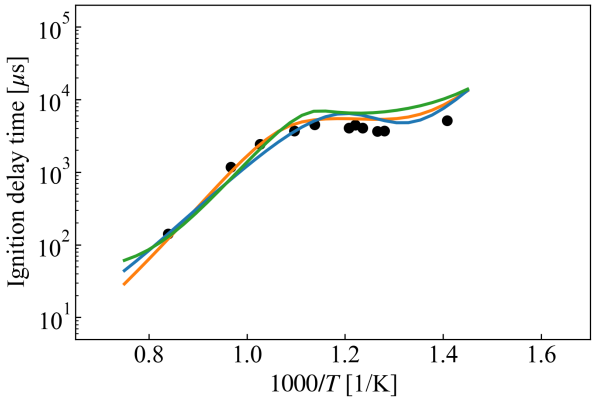

(f) PRF 80 at 20 bar and $\phi = 1.0$ (1)

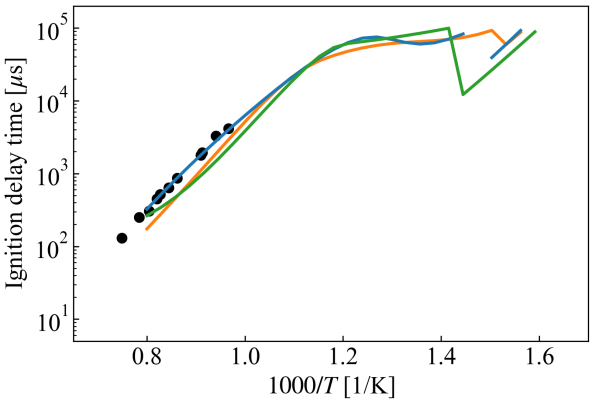

(a) PRF84 at 10 bar and $\phi = 0.5$ (109)

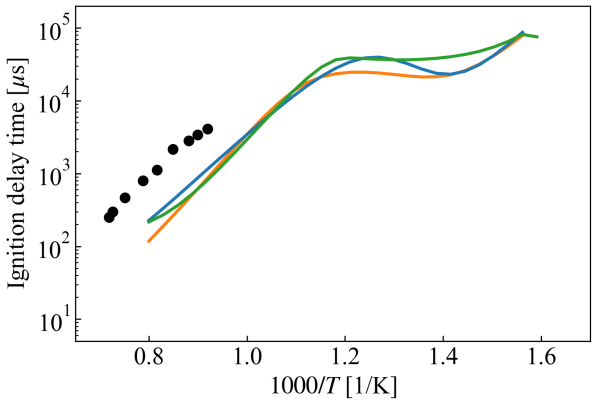

(b) PRF84 at 10 bar and $\phi = 1.0$ (109)

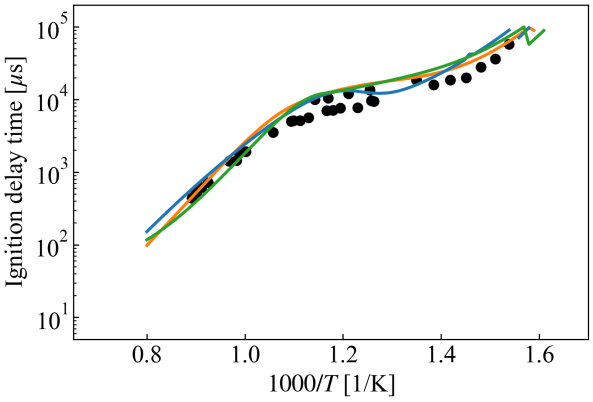

(c) PRF84 at 20 bar and $\phi = 0.5$ (109)

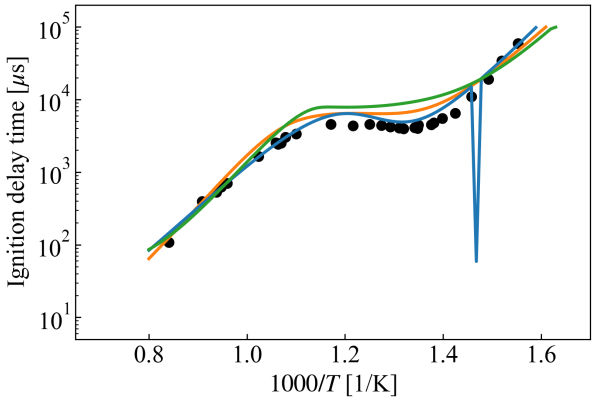

(d) PRF84 at 20 bar and $\phi = 1.0$ (109)

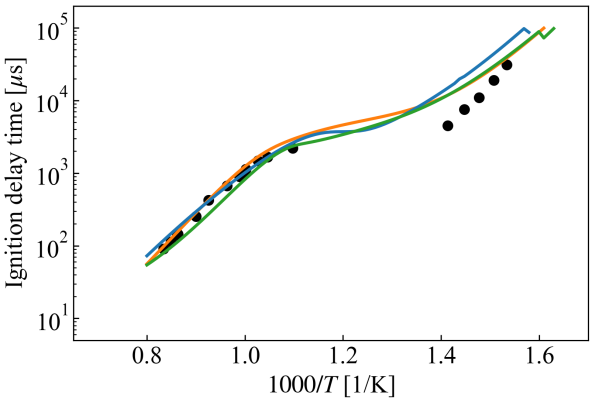

(e) PRF84 at 40 bar and $\phi = 0.5$ (109)

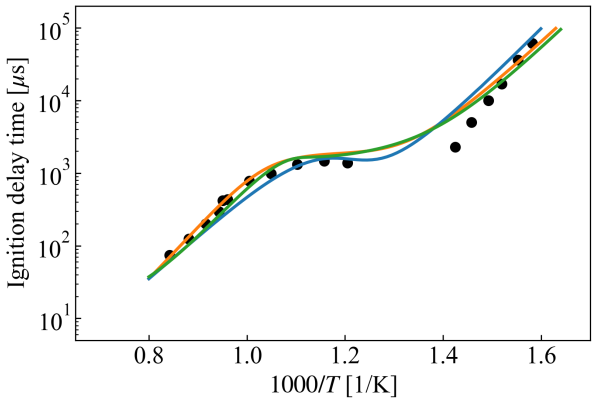

(f) PRF84 at 40 bar and $\phi = 1.0$ (109)

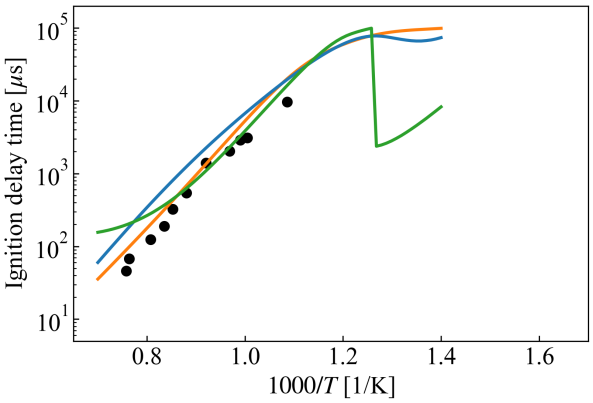

(a) PRF 91 at 10 bar and $\phi = 0.5$ (1)

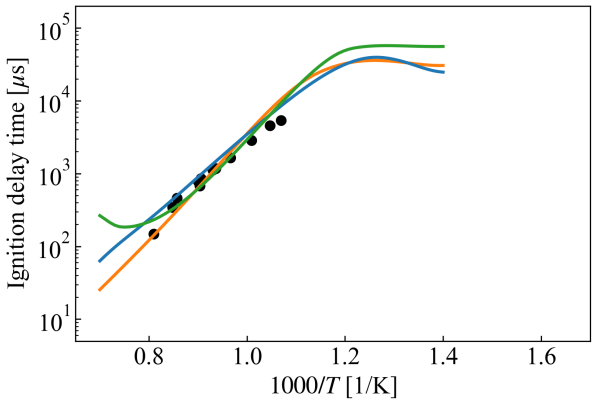

(b) PRF 91 at 10 bar and $\phi = 1.0$ (1)

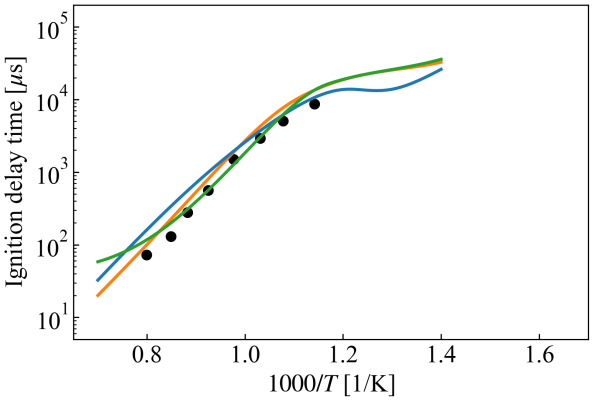

(c) PRF 91 at 20 bar and $\phi = 0.5$ (1)

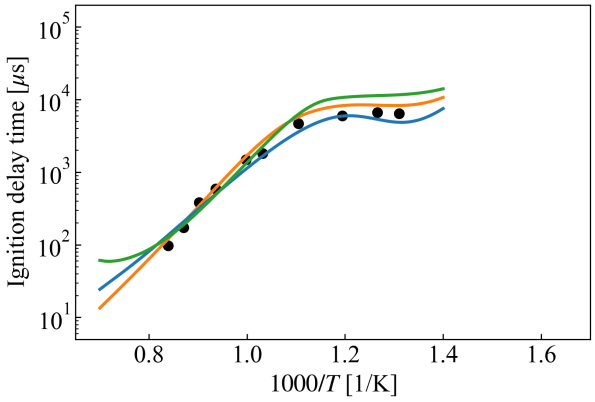

(d) PRF 91 at 20 bar and $\phi = 1.08$ (1)

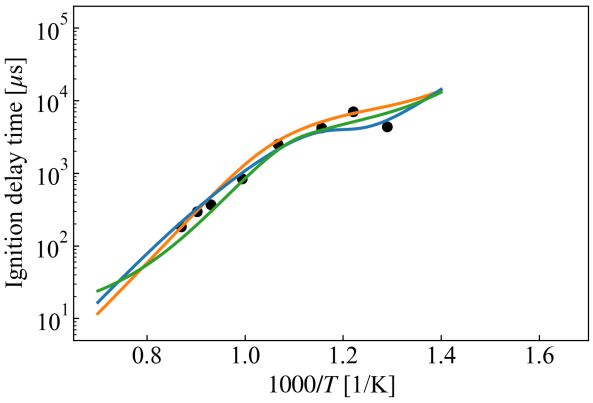

(e) PRF 91 at 40 bar and $\phi = 0.5$ (1)

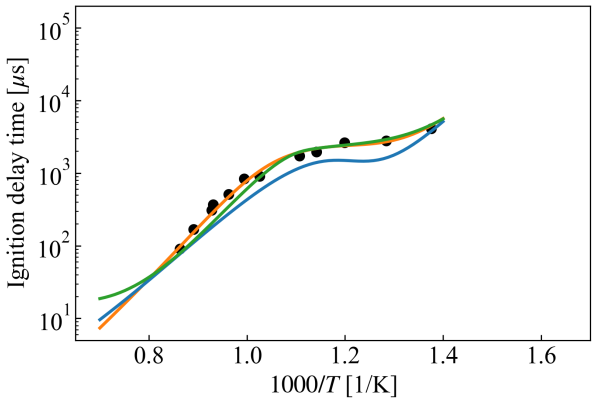

(f) PRF 91 at 40 bar and $\phi = 1.08$ (1)

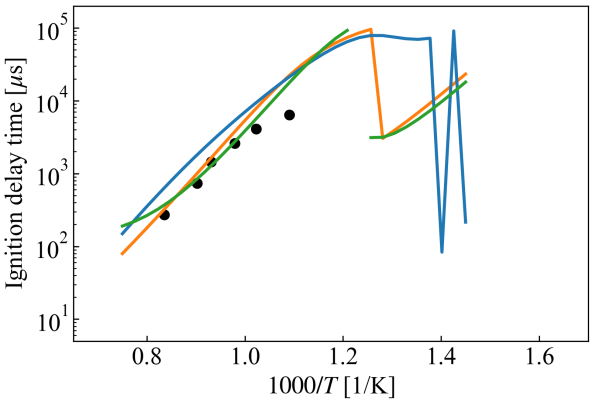

(a) PRF 95 at 10 bar and $\phi = 0.5$ (1)

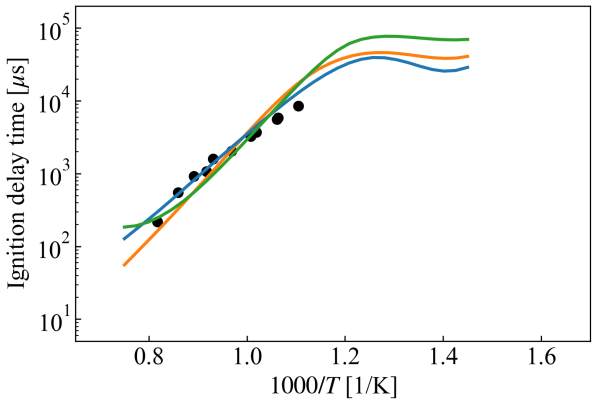

(b) PRF 95 at 10 bar and $\phi = 1.0$ (1)

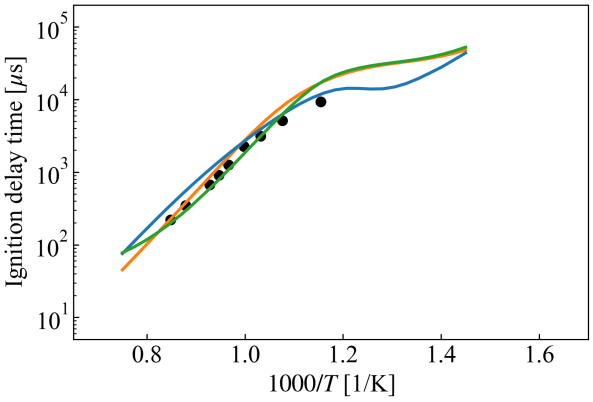

(c) PRF 95 at 20 bar and $\phi = 0.5$ (1)

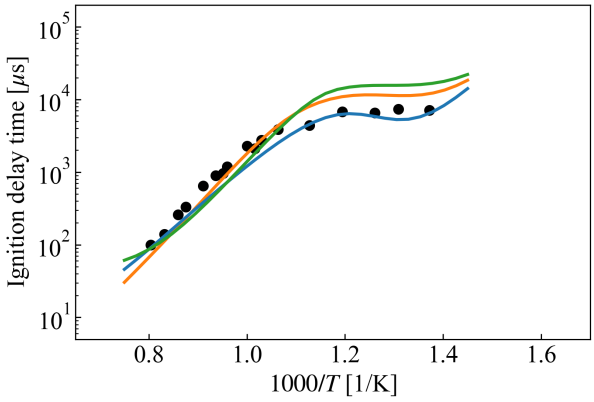

(d) PRF 95 at 20 bar and $\phi = 1.0$ (1)

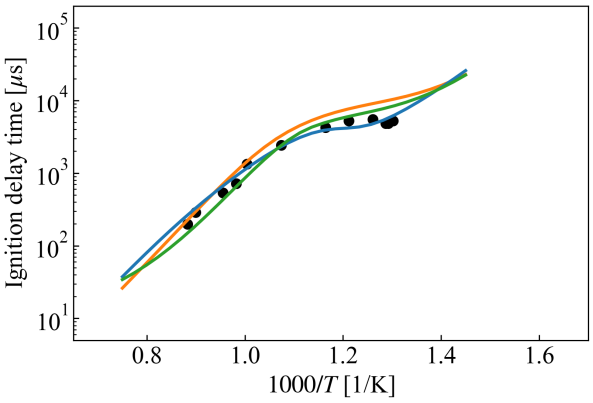

(e) PRF 95 at 40 bar and $\phi = 0.5$ (1)

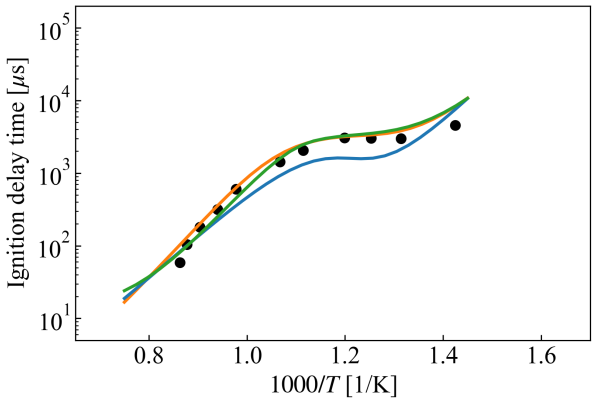

(f) PRF 91 at 40 bar and $\phi = 1.0$ (1)

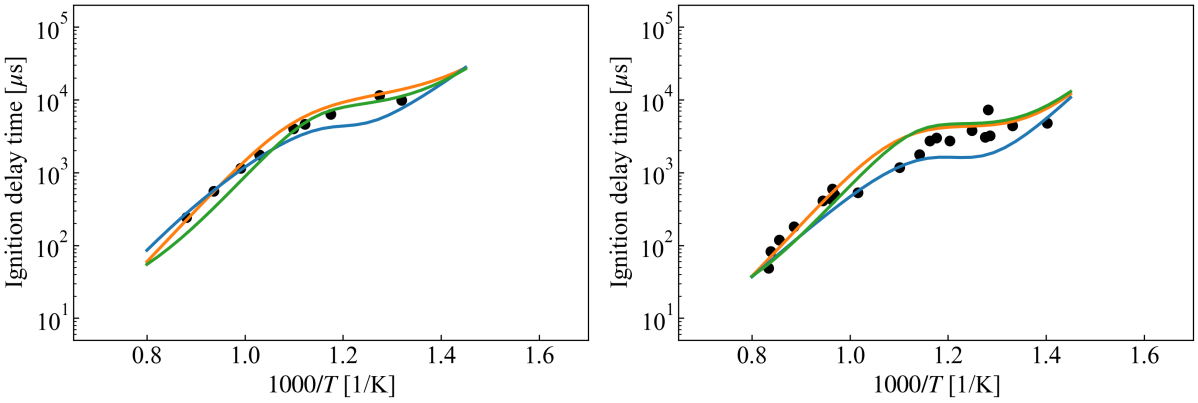

(a) PRF 100 at 40 bar and $\phi = 0.5$ (54)

(b) PRF 100 at 40 bar and $\phi = 1.0$ (54)

Figure 46 – IDT assessment for each PRF mechanism considered.

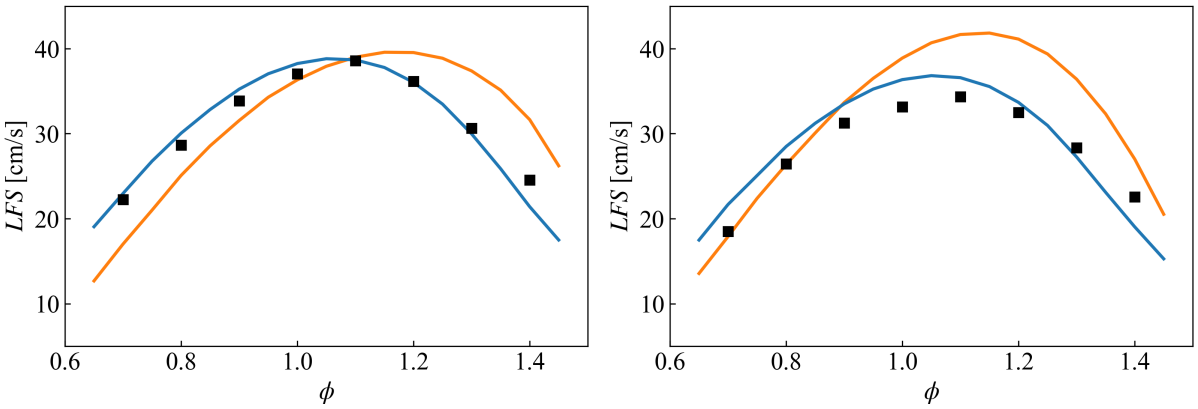

(a) PRF 0 at 298 K and 1 atm (59).

(b) PRF 85 at 298 K and 1 atm (59).

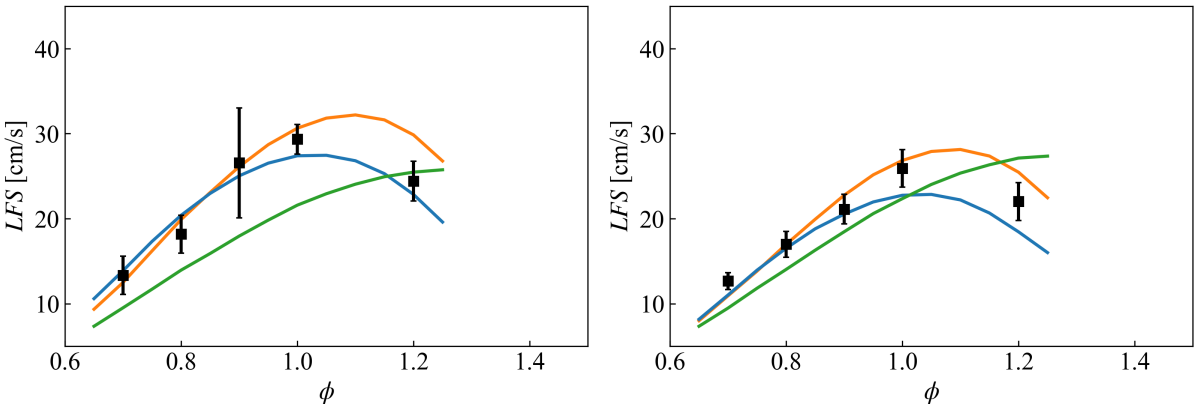

(c) PRF 87 at 373 K and 10 bar (61).

(d) PRF 87 at 373 K and 15 bar (61).

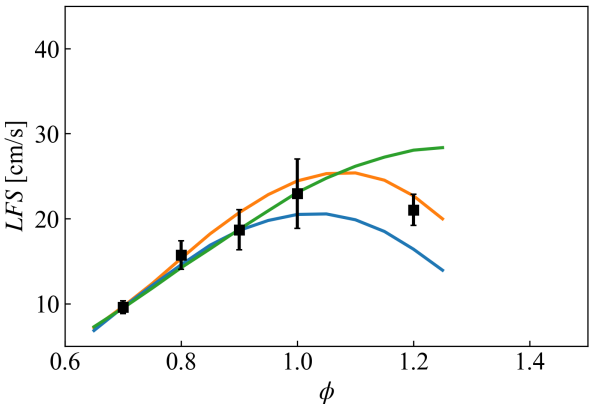

(a) PRF 87 at 373 K and 20 bar (61).

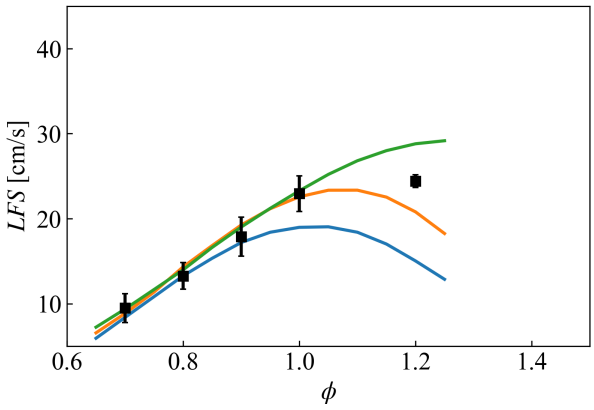

(b) PRF 87 at 373 K and 25 bar (61).

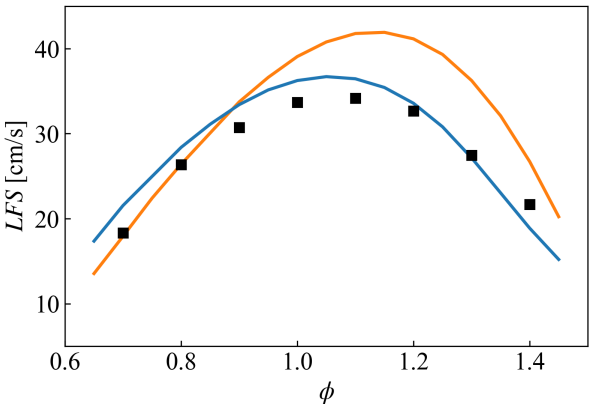

(c) PRF 90 at 298 K and 1 atm (59).

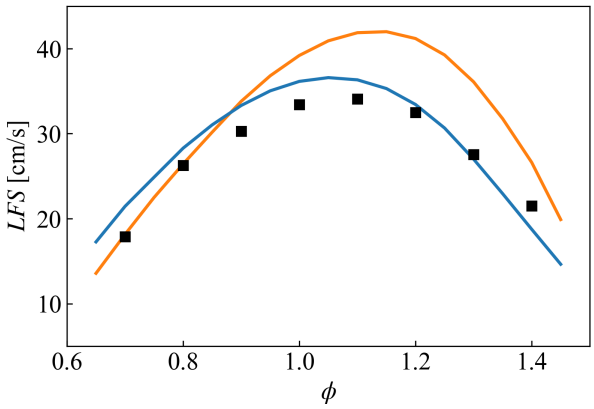

(d) PRF 95 at 298 K and 1 atm (59).

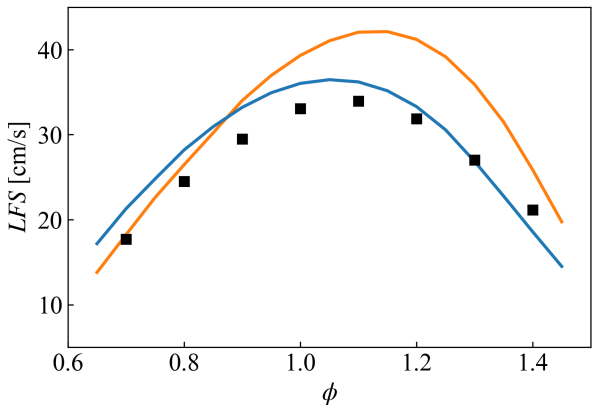

(e) PRF 100 at 298 K and 1 atm (59).

Figure 48 – LFS assessment for the PRF mechanisms considered.

APPENDIX C – KEY PERFORMANCE INDICATORS AND OTHER FLOW QUANTITIES OF INTEREST

Table 27 – Key performance indicators (KPI) calculated for a single four-stroke cycle.

KPI	4000 RPM 100% fuel	2000 RPM 175% fuel	1000 RPM 400% fuel	500 RPM 600% fuel
MFB_2 [CA]	720.6	715.5	713.1	713.1
MFB_{10} [CA]	725.8	719.5	716.6	717.1
MFB_{50} [CA]	733.4	724.9	723.1	729.8
MFB_{90} [CA]	742.8	730.1	734.6	756.2
CBD_{2-90} [CA]	22.3	14.6	21.5	43.1
CBD_{10-50} [CA]	7.6	5.5	6.5	12.8
CBD_{10-90} [CA]	17.1	10.6	17.9	39.1
IMEP [bar]	11.1	22.5	41.6	66.0
Torque [Nm]	40.7	82.1	152.2	241.3
Power [kW]	17.0	17.2	15.9	12.6
BSFC [g/kWh]	226.7	196.6	242.5	229.3

APPENDIX D – KNOCK ONSET PREDICTION ACCORDING TO VARIOUS METHODS

Table 28 – Knock onset prediction according to the various methods at 500 RPM in crank-angle degrees.

Spheres	0°	22.5°	45°	67.5°	90°	112.5°	135°	157.5°	180°	202.5°	225°	247.5°	270°	292.5°	315°	337.5°	Abs. mean	Std. dev
Mech. Y. Li et al. (75)	705.8	705.2	706.1	708.8	707.7	709.0	704.2	704.8	704.9	704.1	705.4	710.8	708.4	709.2	707.6	704.5	706.7	2.1
Mech. Liu et al. (77)	704.7	704.2	704.7	706.7	705.9	706.3	703.2	703.8	703.8	703.1	704.3	708.9	707.1	707.7	706.3	703.4	705.2	1.8
Mech. Tsurushima (120)	703.6	703.2	703.5	705.5	704.9	704.4	702.2	702.6	702.8	702.5	703.2	707.3	705.6	706.3	705.1	702.8	704.1	1.5
Corr. Douaud; Eyzat (27)	688.5	688.3	687.1	687.8	687.4	686.6	687.5	688.3	688.5	688.7	689.6	689.8	689.8	690.2	690.2	688.8	688.6	1.1
Corr. L. Cancino et al. (17)	727.3	727.1	726.9	739.0	737.9	736.3	725.2	725.2	727.1	733.1	732.8	764.3	738.8	738.1	734.3	732.6	734.1	9.5
Corr. from this research	720.8	720.4	720.7	723.8	723.3	723.4	719.7	719.7	720.6	723.0	722.2	728.7	725.1	725.5	723.3	722.4	722.7	2.4
OH 5% peak	740.7	737.5	737.4	739.3	774.0	737.5	735.0	731.5	733.7	736.6	734.9	733.5	735.3	732.6	739.3	735.1	738.4	9.9
OH peak	764.5	764.5	770.5	770.5	866.0	878.0	882.0	759.5	758.0	756.5	749.5	775.0	749.5	751.0	755.5	745.5	781.0	47.6
CO peak	882.0	892.0	892.0	882.0	811.0	818.0	879.0	883.0	882.0	892.0	742.0	877.0	765.5	859.0	744.5	883.0	849.0	54.6
T peak	770.0	775.0	798.5	728.0	878.5	878.5	892.0	773.0	763.0	767.0	748.5	788.5	755.0	759.0	752.0	767.0	787.1	50.3
p peak	729.6	729.6	729.6	729.6	729.6	729.6	729.6	729.6	729.6	729.6	729.6	729.6	729.6	729.6	729.6	729.6	729.6	0.0
$T = 1000$K	745.7	744.9	755.2	-	838.1	876.0	751.3	734.8	736.6	739.2	733.5	771.1	739.2	738.6	734.4	738.0	758.4	41.8
PV=10%	746.0	745.5	751.3	788.0	709.1	790.6	749.1	738.4	738.9	741.4	734.0	756.2	712.4	737.7	735.0	739.3	744.6	21.4
PV=85%	765.5	772.5	-	-	714.7	-	-	765.3	759.3	762.7	772.7	-	716.7	773.2	747.8	764.5	755.9	21.1
KPV peak	723.0	723.0	725.0	736.0	721.0	727.0	722.0	722.0	724.0	725.0	723.0	726.0	720.0	724.0	723.0	725.0	724.3	3.6
I_p peak	724.0	723.0	725.0	738.0	714.0	727.0	723.0	723.0	724.0	726.0	724.0	726.0	715.0	724.0	723.0	726.0	724.1	5.2
$\Omega_{1\%}$	710.0	709.0	710.0	712.0	707.2	707.2	707.2	709.0	709.0	707.2	707.2	751.0	707.2	710.0	707.2	707.2	711.1	10.7
$\Omega_{95\%}$	712.0	712.0	712.0	713.0	707.2	712.0	708.0	711.0	712.0	711.0	708.0	700.0	707.2	717.0	710.0	710.0	710.2	3.7

Table 29 – Knock onset prediction according to the various methods at 100 RPM in crank-angle degrees.

Spheres	0°	22.5°	45°	67.5°	90°	112.5°	135°	157.5°	180°	202.5°	225°	247.5°	270°	292.5°	315°	337.5°	Abs. mean	Std. dev
Mech. Y. Li et al. (75)	716.8	715.9	714.2	698.8	718.8	715.9	713.2	714.8	716.9	695.2	716.6	719.4	718.5	706.1	716.2	717.7	713.4	7.1
Mech. Liu et al. (77)	717.5	716.5	715.3	719.3	719.4	716.5	714.8	715.5	717.8	719.4	716.9	719.4	718.5	718.5	717.0	718.3	717.5	1.5
Mech. Tsurushima (120)	716.5	715.2	713.7	717.6	716.9	715.2	712.7	714.7	716.4	717.5	716.0	718.7	717.8	717.9	715.5	717.0	716.2	1.6
Corr. Douaud; Eyzat (27)	706.6	708.5	707.3	707.4	705.3	706.7	707.1	706.7	706.1	706.5	709.7	711.7	710.9	711.0	709.2	707.9	708.0	1.9
Corr. L. Cancino et al. (17)	725.7	725.7	728.3	734.0	729.1	733.0	726.3	725.3	726.1	728.3	727.5	732.8	730.5	727.9	727.6	727.7	728.5	2.7
Corr. from this research	724.3	724.4	724.1	725.6	724.5	725.3	723.7	723.6	724.0	724.3	724.6	728.7	727.4	726.3	724.6	724.7	725.0	1.4
OH 5% peak	724.8	724.9	728.1	742.1	732.5	733.2	725.7	724.5	725.5	728.7	726.7	730.7	729.0	727.0	726.8	727.2	728.6	4.4
OH peak	733.0	731.4	737.8	758.5	892.0	746.0	735.6	734.6	735.2	744.0	739.0	738.4	737.0	737.0	737.6	741.0	748.6	38.8
CO peak	858.5	796.0	892.0	882.0	892.0	892.0	736.2	878.5	892.0	892.0	737.0	755.0	775.0	739.2	892.0	892.0	837.6	67.0
T peak	735.4	734.0	739.8	766.5	727.6	751.0	738.6	737.6	736.6	747.5	739.2	745.0	740.5	738.2	738.2	742.0	741.1	8.7
p peak	730.2	730.2	730.2	730.2	730.2	730.2	730.2	730.2	730.2	730.2	730.2	730.2	730.2	730.2	730.2	730.2	730.2	0.0
$T = 1000$K	724.7	724.7	727.4	750.1	-	733.2	725.1	724.1	724.9	727.5	726.3	731.6	729.4	726.7	726.4	726.4	728.6	6.5
PV=10%	725.9	726.1	731.3	780.5	709.1	735.2	726.8	725.5	726.7	730.1	727.8	732.3	712.3	727.7	727.9	729.1	729.6	15.1
PV=85%	732.9	732.5	739.2	-	713.8	-	734.2	732.6	734.3	743.6	735.4	-	716.0	737.5	735.7	740.3	732.9	8.7
KPV peak	723.0	723.0	725.0	736.0	721.0	727.0	722.0	722.0	724.0	725.0	723.0	726.0	720.0	724.0	723.0	725.0	724.3	3.6
I_p peak	724.0	723.0	725.0	738.0	714.0	727.0	723.0	723.0	724.0	726.0	724.0	726.0	715.0	724.0	723.0	726.0	724.1	5.2
$\Omega_{1\%}$	721.2	720.8	722.2	727.2	720.0	723.2	720.4	720.8	722.2	723.0	720.4	721.8	720.0	721.8	720.6	722.6	721.8	1.8
$\Omega_{95\%}$	722.8	722.4	723.2	729.0	720.0	723.8	721.2	722.0	723.4	724.8	721.8	723.0	720.0	722.8	721.8	724.4	722.9	2.1

Table 30 – Knock onset prediction according to the various methods at 2000 RPM in crank-angle degrees.

Spheres	0°	22.5°	45°	67.5°	90°	112.5°	135°	157.5°	180°	202.5°	225°	247.5°	270°	292.5°	315°	337.5°	Abs. mean	Std. dev
Mech. Y. Li et al. (75)	722.8	698.6	722.4	724.6	724.2	724.3	722.6	722.4	722.7	723.0	723.0	724.0	723.7	723.9	723.2	723.2	721.8	6.2
Mech. Liu et al. (77)	-	725.3	724.4	725.8	726.6	726.8	724.2	724.3	724.5	724.7	724.6	725.5	726.0	725.6	724.7	725.0	725.2	0.8
Mech. Tsurushima (120)	724.2	724.0	723.9	725.3	725.4	725.5	723.8	723.8	724.1	724.2	724.2	725.0	724.9	725.0	724.2	724.4	724.5	0.6
Corr. Douaud; Eyzat (27)	724.1	723.7	723.7	725.1	724.7	724.6	724.1	723.9	724.2	724.4	724.4	724.7	724.1	724.4	724.5	724.5	724.3	0.4
Corr. L. Cancino et al. (17)	727.3	727.7	728.4	731.9	734.6	734.7	728.7	727.7	727.4	726.8	727.9	729.9	732.8	729.6	727.9	727.0	729.4	2.7
Corr. from this research	726.8	727.1	727.7	731.1	733.2	733.3	728.2	727.1	726.9	726.4	727.3	729.2	731.2	728.9	727.3	726.6	728.6	2.3
OH 5% peak	726.3	726.7	727.4	731.2	732.6	732.7	728.0	726.8	726.5	726.0	726.9	728.9	731.1	728.3	726.8	726.2	728.3	2.3
OH peak	732.4	732.6	733.8	738.0	743.5	741.5	733.6	733.0	733.8	731.6	732.8	734.0	741.0	733.2	732.6	731.4	734.9	3.8
CO peak	799.0	733.0	733.4	738.0	839.0	829.0	734.2	732.2	732.0	732.4	734.8	741.0	878.5	745.0	734.8	781.0	763.6	47.3
T peak	733.6	734.0	735.0	738.0	743.5	751.0	735.0	733.8	733.8	732.8	734.4	738.5	742.5	737.0	734.2	733.4	736.9	4.9
p peak	730.4	730.4	730.4	730.4	730.4	730.4	730.4	730.4	730.4	730.4	730.4	730.4	730.4	730.4	730.4	730.4	730.4	0.0
$T = 1000$K	726.1	726.4	727.0	730.5	732.6	732.9	727.5	726.5	726.2	725.7	726.7	728.6	730.9	728.2	726.6	725.9	728.0	2.4
PV=10%	726.8	727.2	728.0	732.0	600.4	735.4	728.3	727.3	726.8	726.1	727.2	729.1	695.4	729.0	727.2	726.4	718.3	32.6
PV=85%	730.9	731.2	732.5	-	701.2	-	732.2	731.0	730.6	729.7	731.3	735.5	717.5	735.7	731.1	730.1	728.6	8.9
KPV peak	726.0	726.0	727.0	730.0	720.0	732.0	727.0	726.0	726.0	725.0	726.0	728.0	720.0	728.0	726.0	726.0	726.2	3.0
I_p peak	730.0	730.0	731.0	733.0	720.0	737.0	731.0	730.0	730.0	729.0	728.0	731.0	720.0	730.0	728.0	729.0	729.2	4.2
$\Omega_{1\%}$	728.4	728.0	729.2	732.2	720.0	736.6	729.0	728.0	728.2	726.8	728.0	729.8	720.0	730.2	728.0	728.0	728.2	3.9
$\Omega_{95\%}$	722.8	722.4	723.2	729.0	720.0	723.8	721.2	722.0	723.4	724.8	721.8	723.0	720.0	722.8	721.8	724.4	722.9	2.1

Table 31 – Knock onset prediction according to the various methods at 4000 RPM in crank-angle degrees.

Spheres	0°	22.5°	45°	67.5°	90°	112.5°	135°	157.5°	180°	202.5°	225°	247.5°	270°	292.5°	315°	337.5°	Abs. mean	Std. dev
Mech. Y. Li et al. (75)	735.6	735.1	736.6	740.8	731.2	740.8	737.2	735.3	734.7	734.4	738.5	742.5	745.1	740.1	738.0	734.7	737.5	3.6
Mech. Liu et al. (77)	736.0	735.5	737.2	741.7	753.4	741.6	737.8	735.7	735.5	734.7	739.0	744.2	746.9	742.9	739.2	735.4	739.8	5.1
Mech. Tsurushima (120)	735.2	734.7	736.5	741.3	752.7	741.0	737.4	734.8	734.6	734.1	738.3	743.4	745.5	741.9	738.0	734.5	739.0	5.1
Corr. Douaud; Eyzat (27)	738.0	737.5	738.9	743.1	754.1	742.8	739.3	737.7	737.5	736.7	740.7	744.8	745.6	743.5	741.0	737.4	741.2	4.5
Corr. L. Cancino et al. (17)	736.5	735.9	737.7	742.3	754.2	742.3	738.3	736.2	735.9	735.1	739.4	745.1	747.5	743.5	739.8	735.8	740.3	5.3
Corr. from this research	736.2	735.6	737.3	742.0	754.1	741.8	737.9	735.9	735.6	734.8	739.1	744.6	747.0	743.0	739.4	735.5	740.0	5.2
OH 5% peak	734.9	734.4	736.0	739.8	746.3	738.6	736.0	734.5	734.1	733.7	738.2	739.4	739.5	736.8	737.8	734.2	737.1	3.2
OH peak	741.5	741.0	742.5	749.0	762.5	751.0	743.5	741.0	741.5	740.5	744.5	758.5	755.0	751.0	745.5	741.0	746.8	6.9
CO peak	744.0	743.0	747.0	798.5	892.0	851.0	766.0	743.5	743.5	745.5	748.5	892.0	890.0	892.0	751.5	745.0	793.3	64.9
T peak	743.5	742.5	745.0	754.5	768.0	755.0	746.0	744.0	742.5	740.5	746.5	762.0	764.0	759.0	748.5	743.0	750.3	8.8
p peak	738.2	738.2	738.2	738.0	738.2	738.2	738.2	738.4	738.4	738.4	738.2	738.4	738.2	738.2	738.2	738.2	738.2	0.1
$T = 1000$K	734.7	734.2	735.9	740.0	751.0	739.3	736.3	734.4	734.1	733.5	737.9	741.4	743.0	739.4	737.7	734.0	737.9	4.5
PV=10%	734.7	734.4	736.1	742.0	713.9	741.8	736.8	734.5	734.3	733.5	738.0	742.9	715.4	740.3	737.8	734.0	734.4	8.3
PV=85%	740.1	739.4	741.9	-	726.9	-	743.5	739.9	739.7	738.4	743.6	-	725.3	-	744.9	739.6	738.6	6.2
KPV peak	723.0	723.0	725.0	736.0	721.0	727.0	722.0	722.0	724.0	725.0	723.0	726.0	720.0	724.0	723.0	725.0	724.3	3.6
I_p peak	724.0	723.0	725.0	738.0	714.0	727.0	723.0	723.0	724.0	726.0	724.0	726.0	715.0	724.0	723.0	726.0	724.1	5.2
$\Omega_{1\%}$	728.0	728.0	729.0	732.0	725.6	735.0	729.0	728.0	728.0	727.0	728.0	730.0	725.6	730.0	728.0	728.0	728.7	2.3
$\Omega_{95\%}$	722.8	722.4	723.2	729.0	720.0	723.8	721.2	722.0	723.4	724.8	721.8	723.0	720.0	722.8	721.8	724.4	722.9	2.1

APPENDIX E – IGNITION DELAY TIME RESULTS FOR ALL CRFD SIMULATIONS

This section brings all ignition delay time (IDT) results for all regions of interest of each CRFD simulation. They regard the three simulated CV-PSR Cantera setups, with the reduced mechanisms from (75, 77, 120) and the three IDT correlations, from (27) and (17) and the one proposed in this work (Eq. 67).

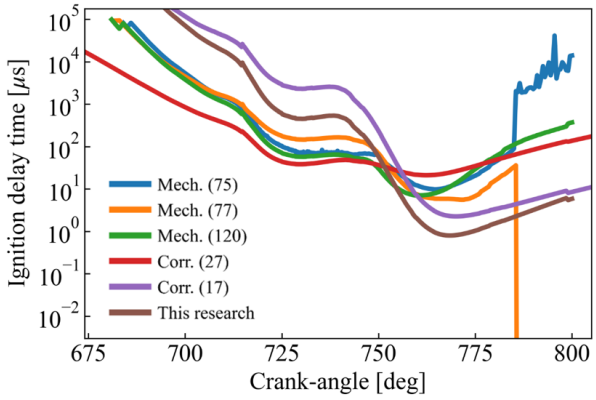

(a) Sphere 0°.

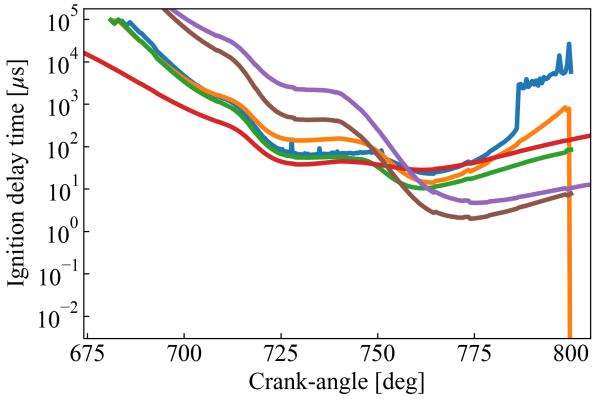

(b) Sphere 22.5°.

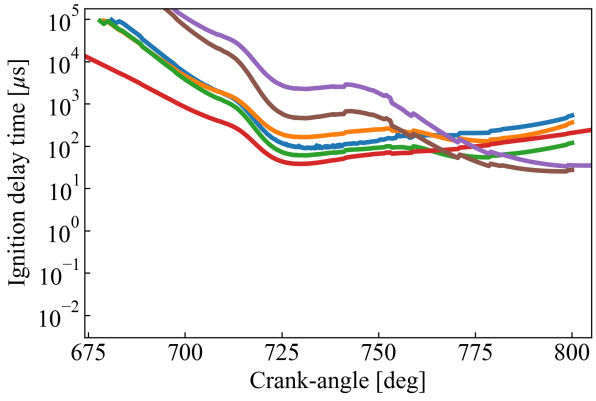

(c) Sphere 45°.

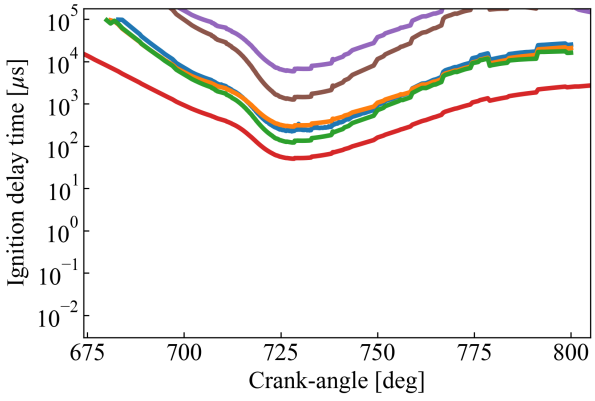

(d) Sphere 67.5°.

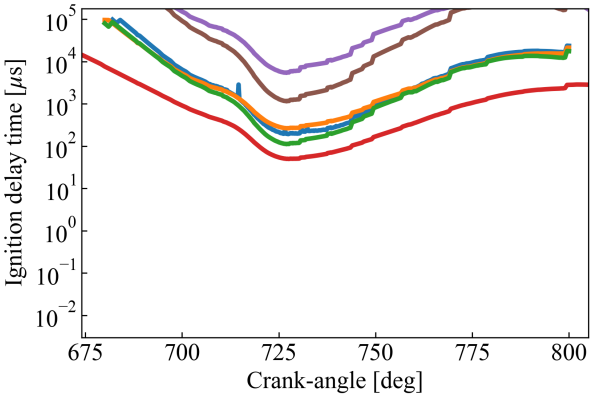

(e) Sphere 90°.

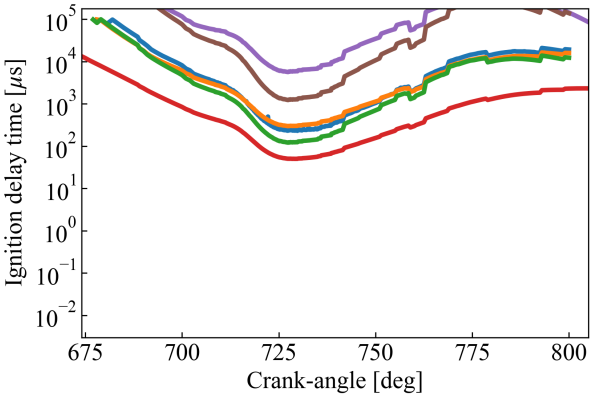

(f) Sphere 112.5°.

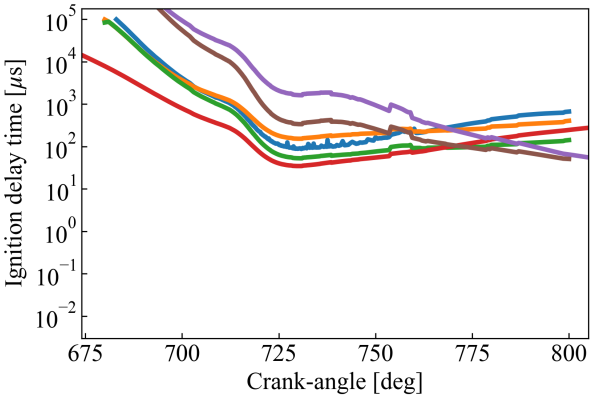

(g) Sphere 135°.

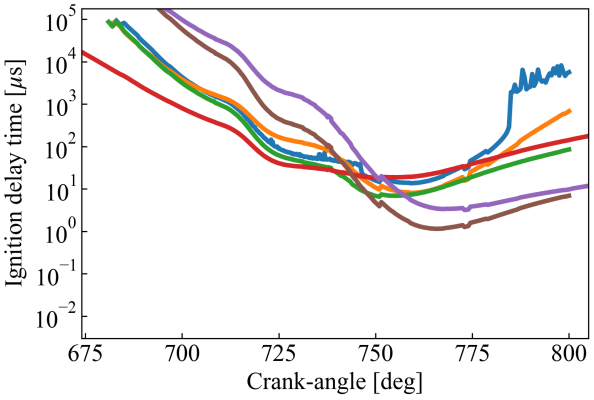

(h) Sphere 157.5°.

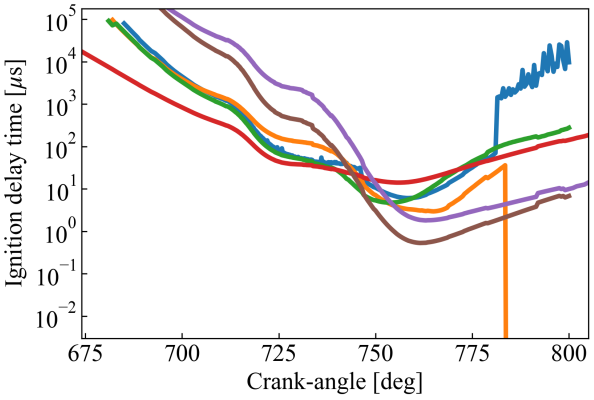

(i) Sphere 180°.

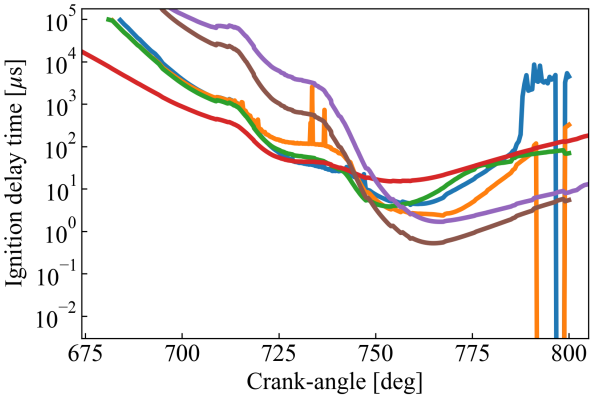

(j) Sphere 202.5°.

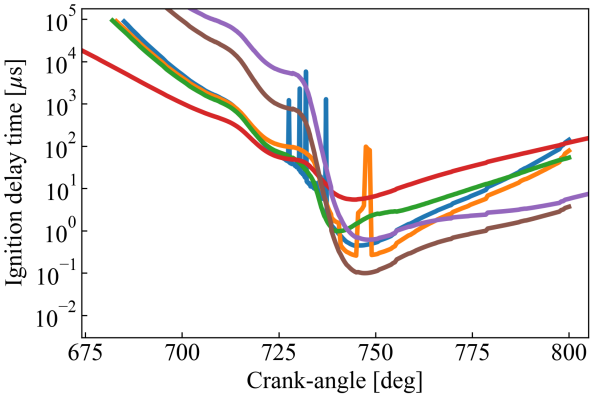

(k) Sphere 225°.

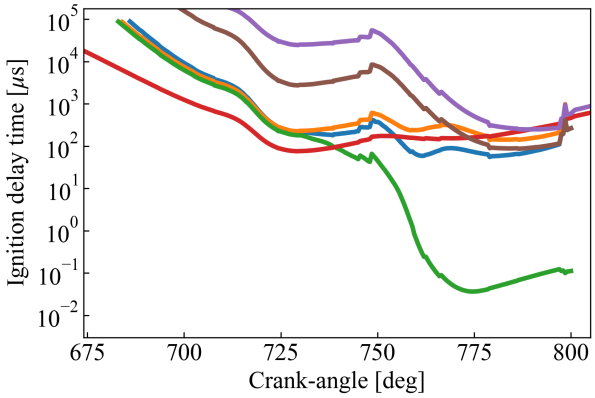

(l) Sphere 247.5°.

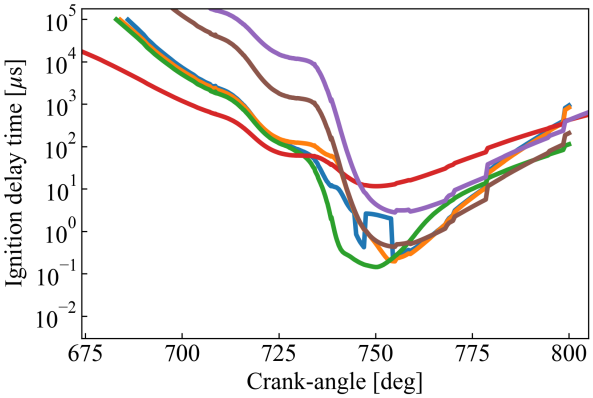

(m) Sphere 270°.

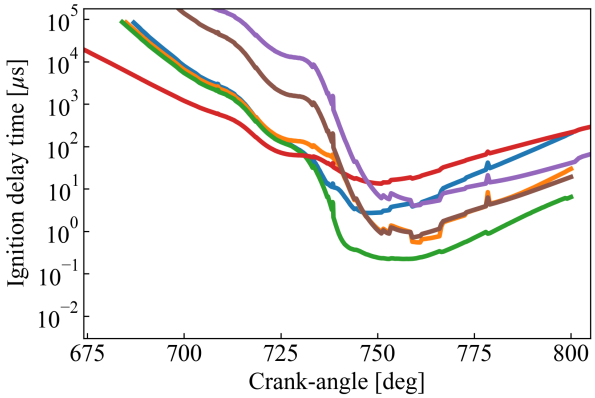

(n) Sphere 292.5°.

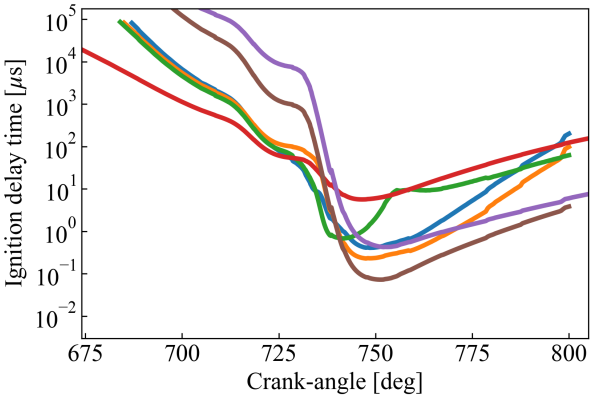

(o) Sphere 315°.

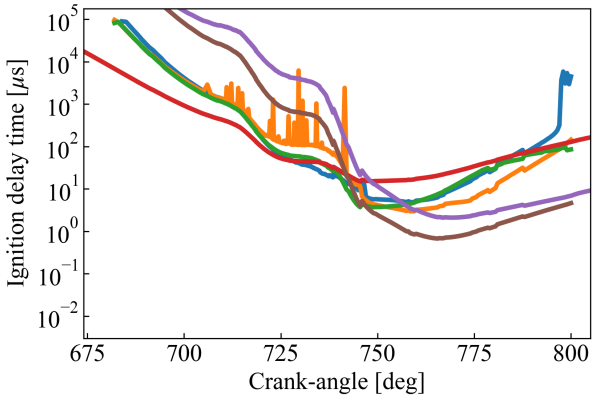

(p) Sphere 337.5°.

Figure 49 – IDT for each AVL FIRE region of interest at 500 RPM.

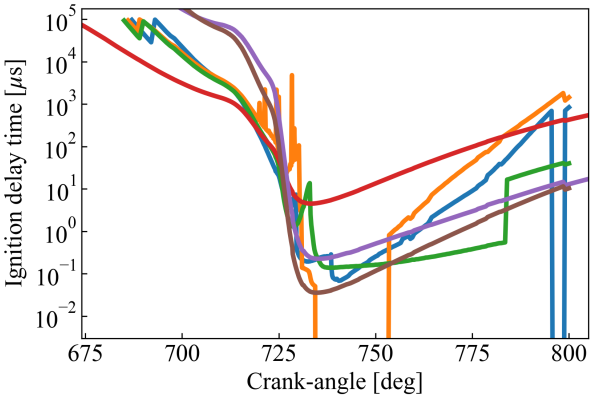

(a) Sphere 0°.

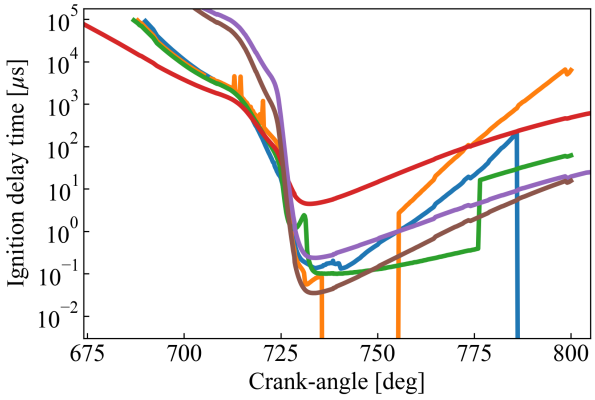

(b) Sphere 22.5°.

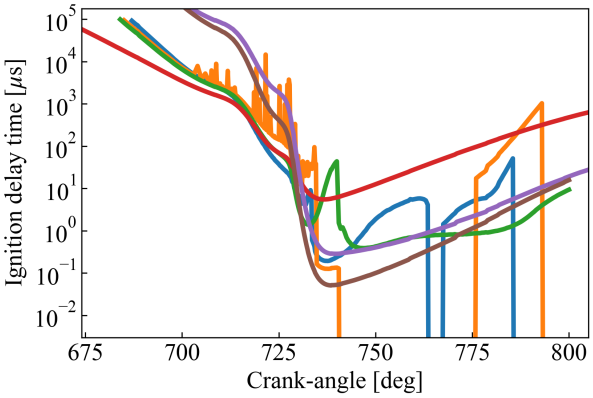

(c) Sphere 45°.

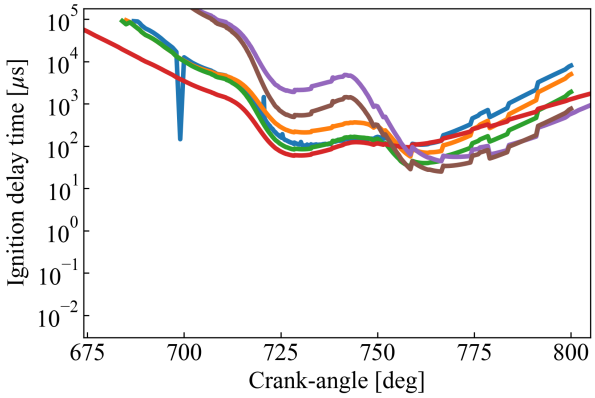

(d) Sphere 67.5°.

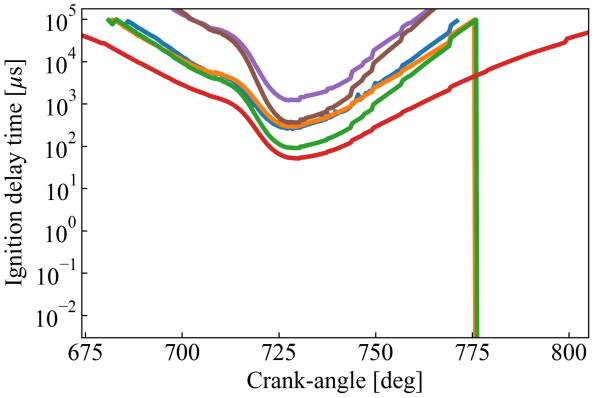

(e) Sphere 90°.

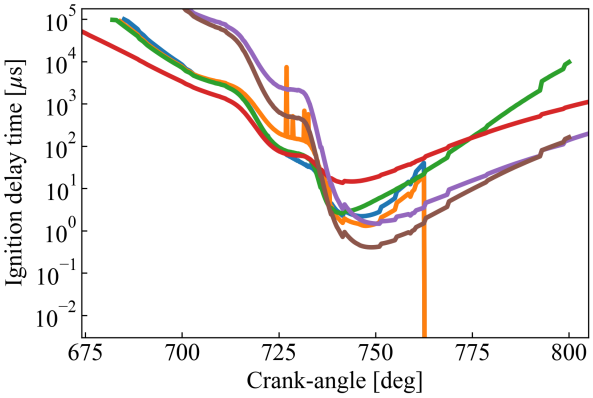

(f) Sphere 112.5°.

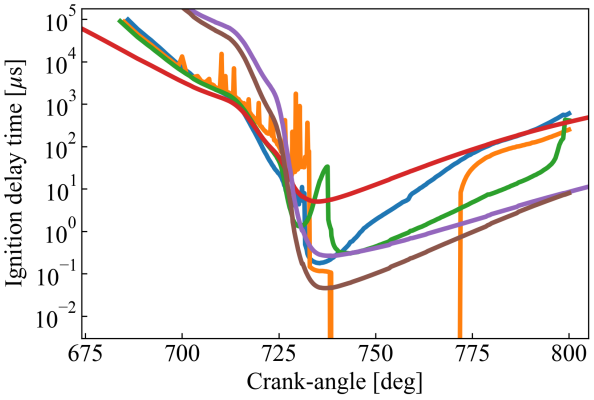

(g) Sphere 135°.

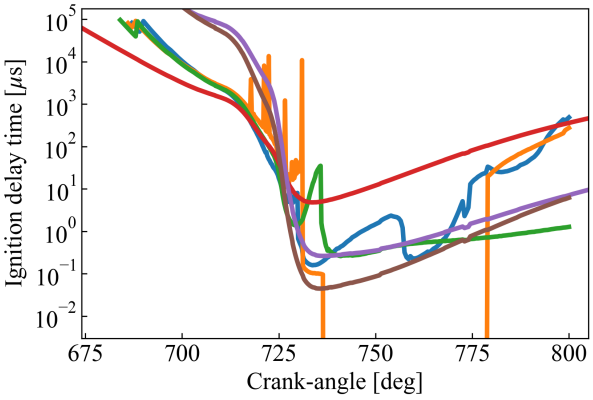

(h) Sphere 157.5°.

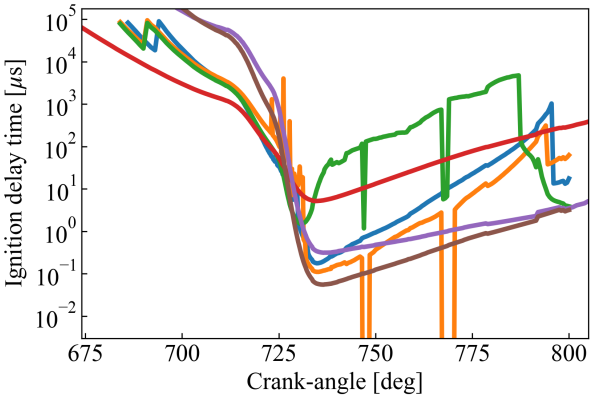

(i) Sphere 180°.

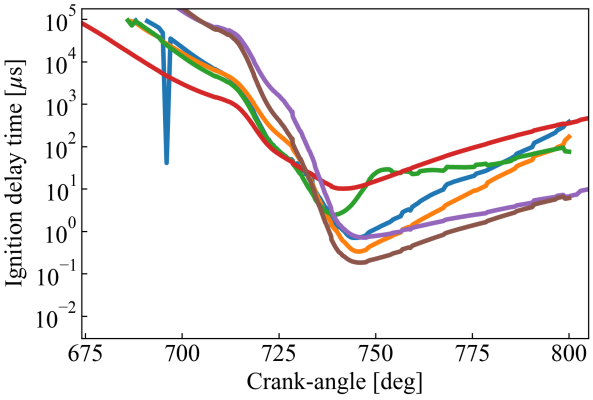

(j) Sphere 202.5°.

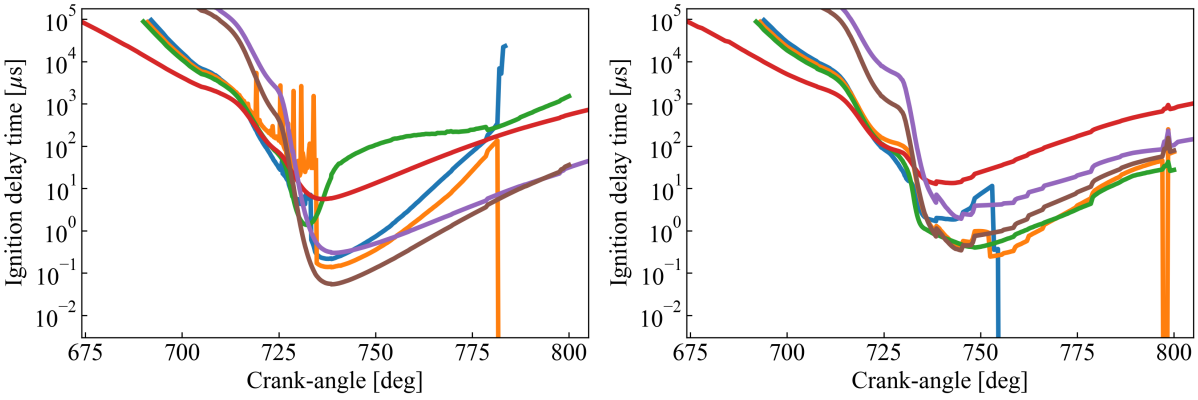

(k) Sphere 225°.

(l) Sphere 247.5°.

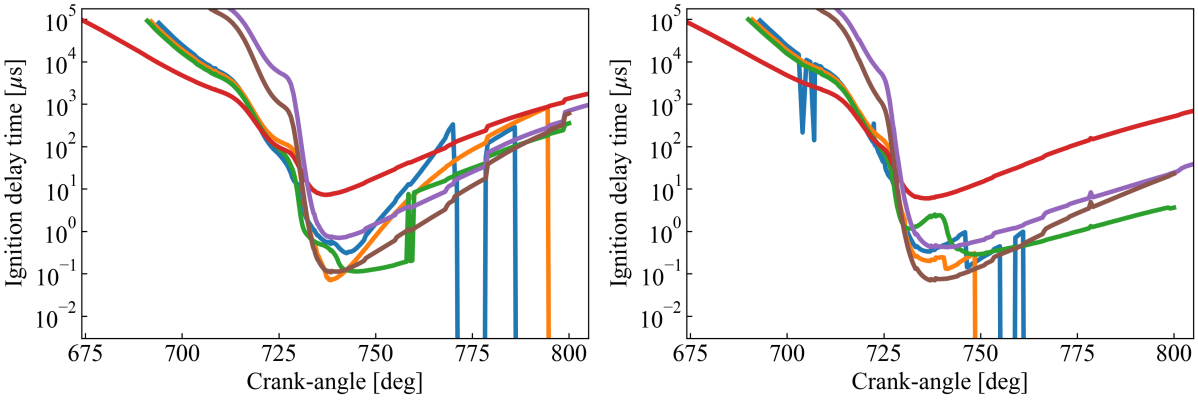

(m) Sphere 270°.

(n) Sphere 292.5°.

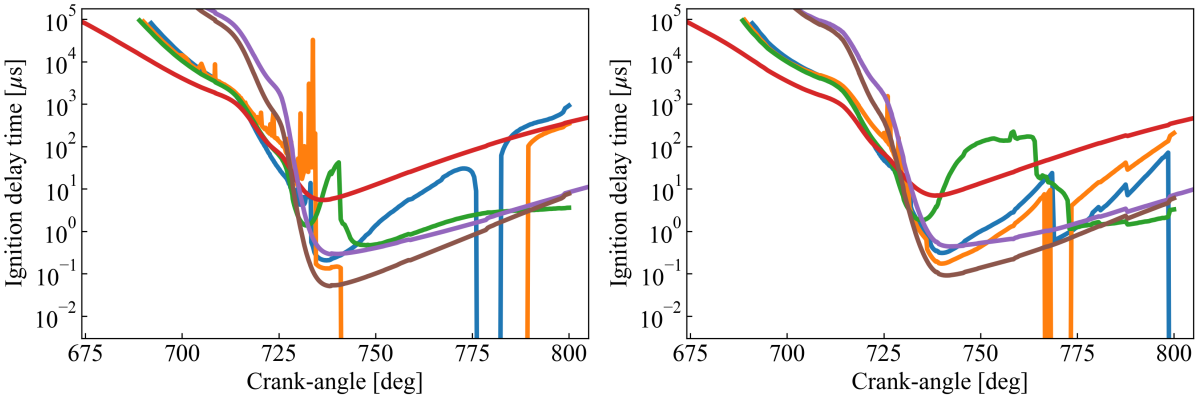

(o) Sphere 315°.

(p) Sphere 337.5°.

Figure 50 – IDT for each AVL FIRE region of interest at 1000 RPM.

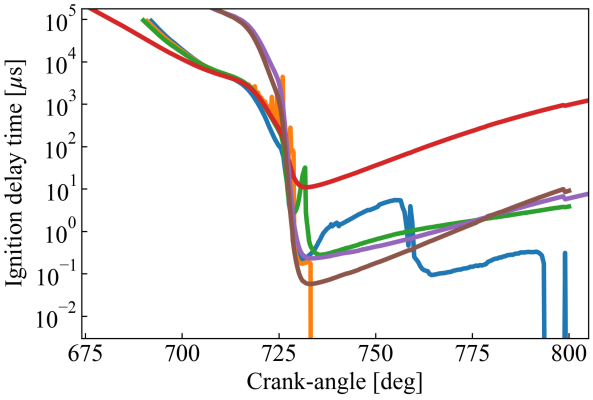

(a) Sphere 0°.

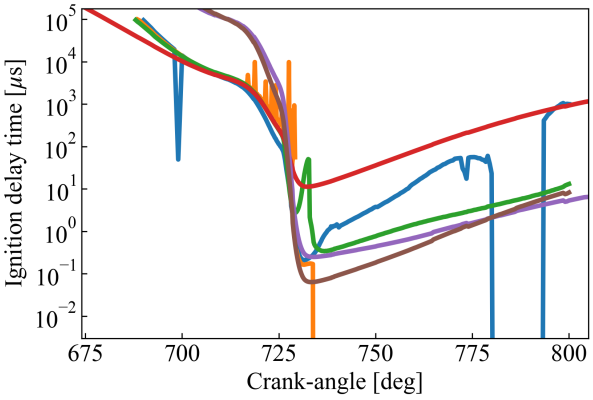

(b) Sphere 22.5°.

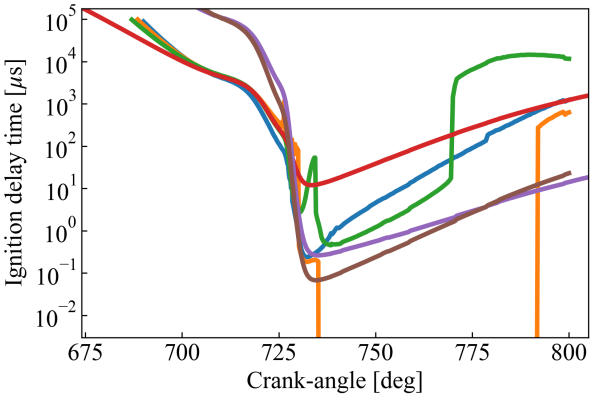

(c) Sphere 45°.

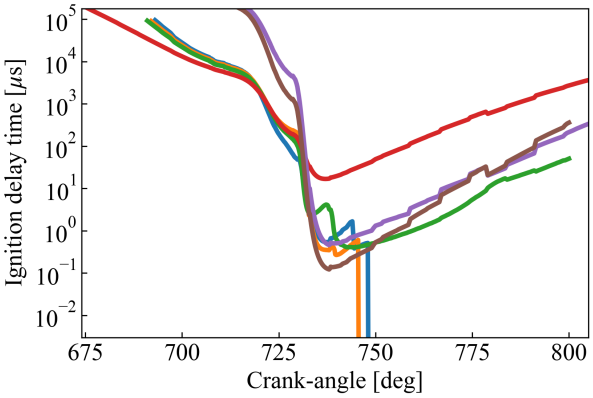

(d) Sphere 67.5°.

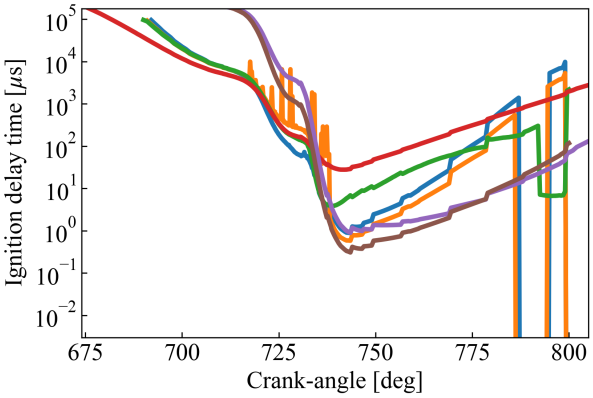

(e) Sphere 90°.

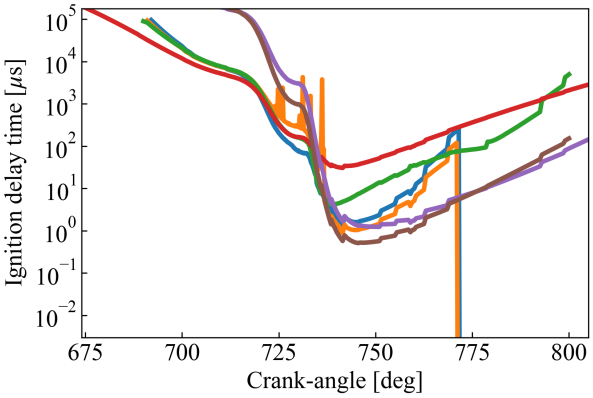

(f) Sphere 112.5°.

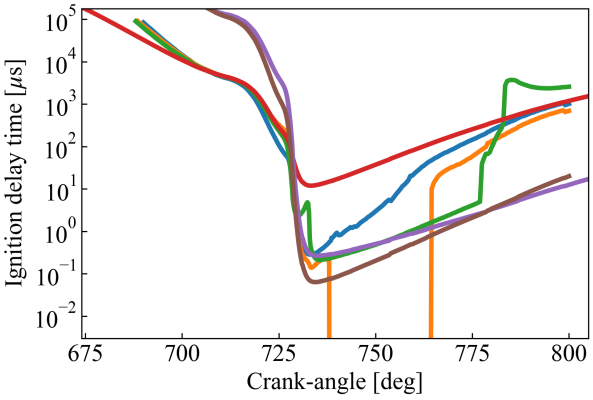

(g) Sphere 135°.

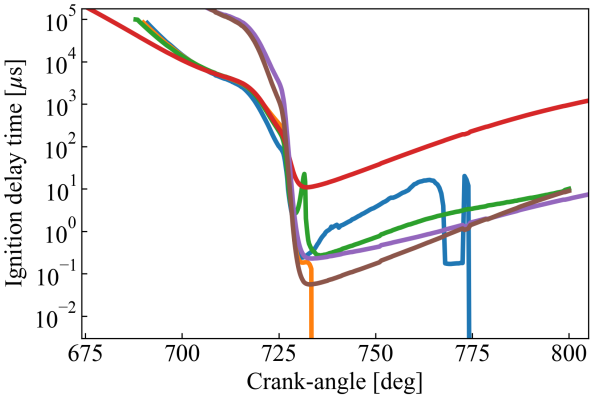

(h) Sphere 157.5°.

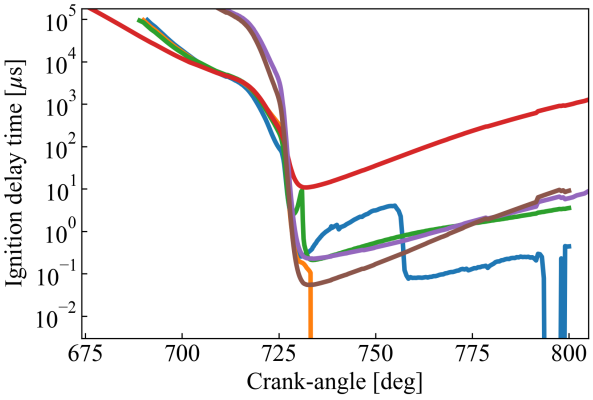

(i) Sphere 180°.

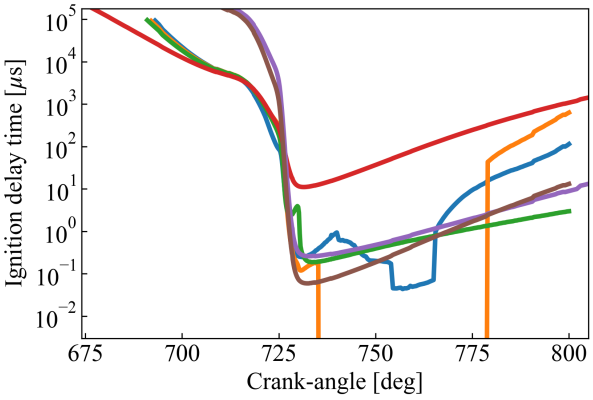

(j) Sphere 202.5°.

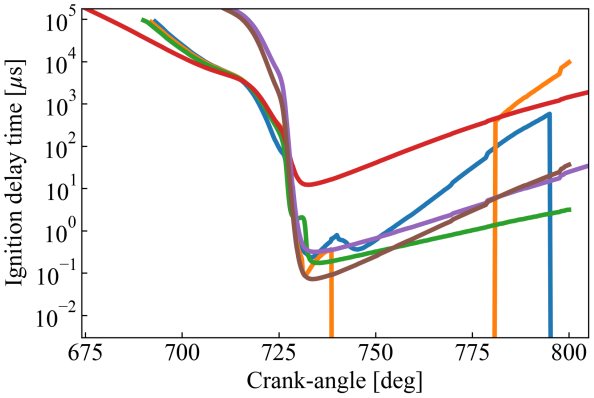

(k) Sphere 225°.

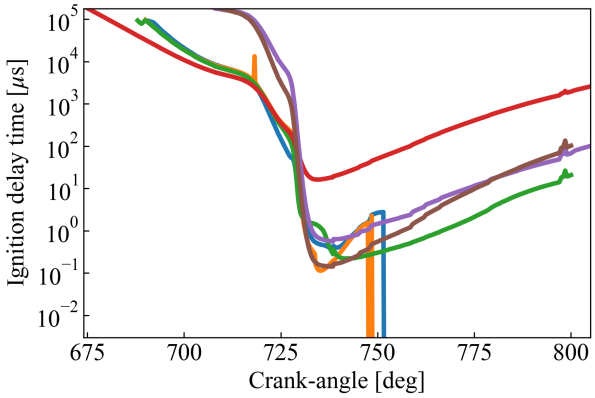

(l) Sphere 247.5°.

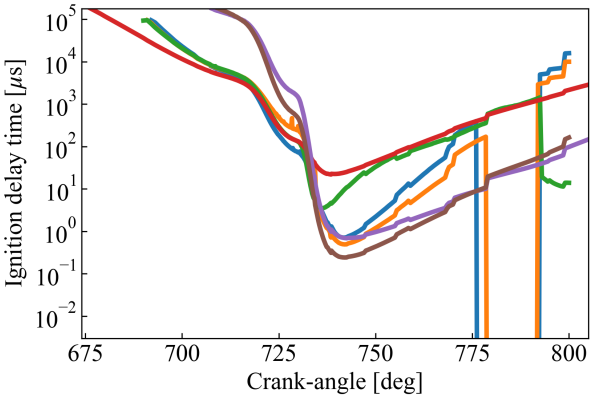

(m) Sphere 270°.

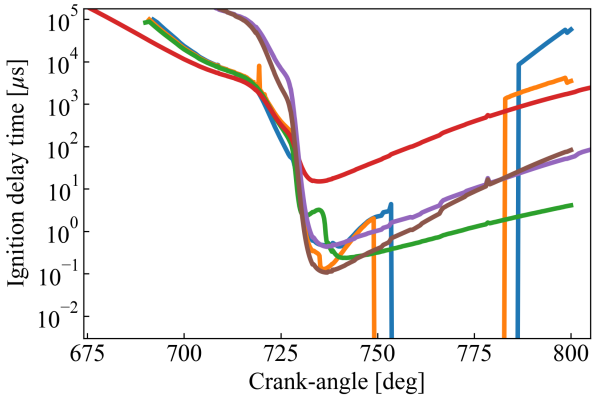

(n) Sphere 292.5°.

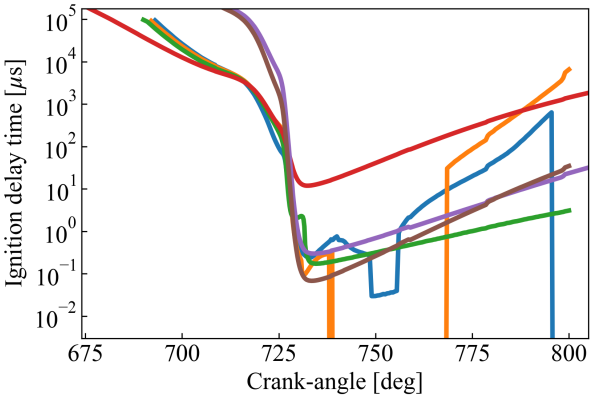

(o) Sphere 315°.

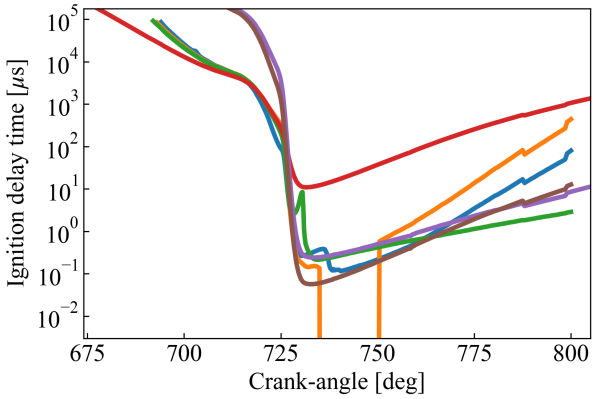

(p) Sphere 337.5°.

Figure 51 – IDT for each AVL FIRE region of interest at 2000 RPM.

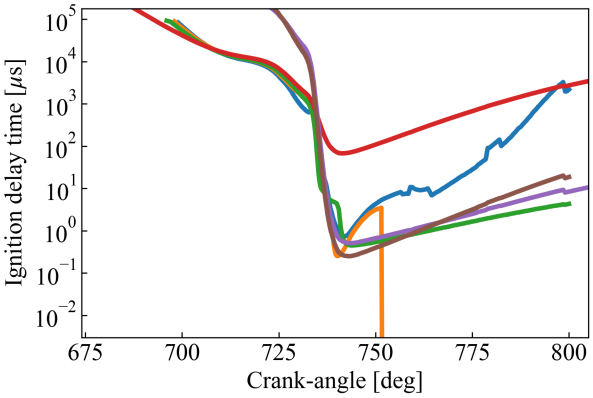

(a) Sphere 0°.

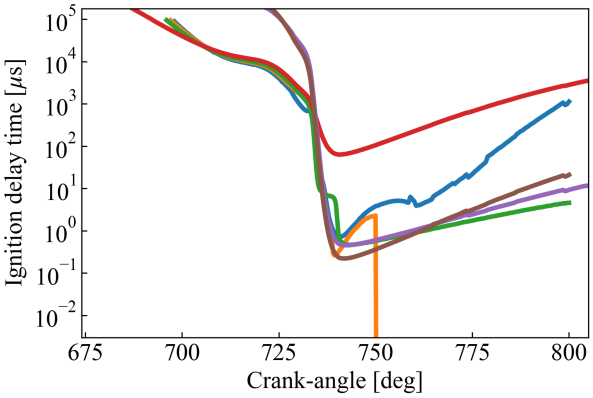

(b) Sphere 22.5°.

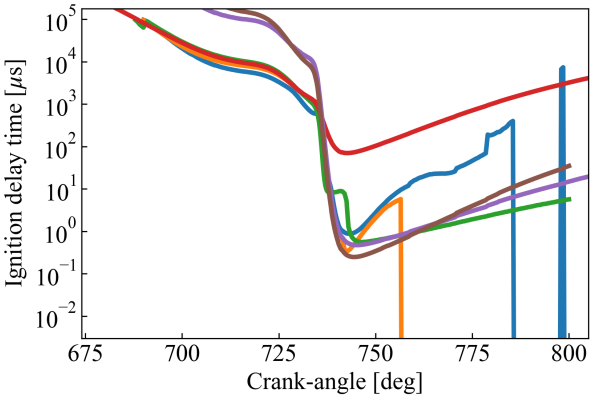

(c) Sphere 45°.

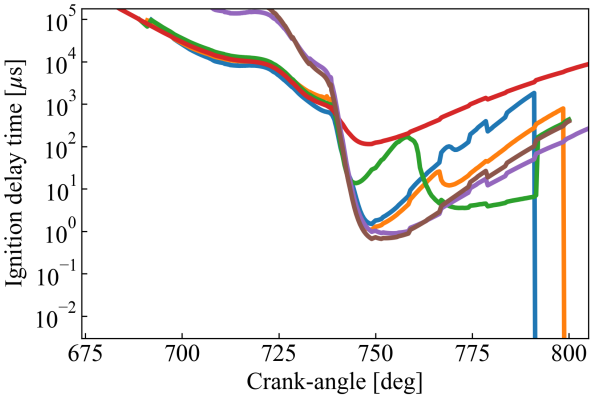

(d) Sphere 67.5°.

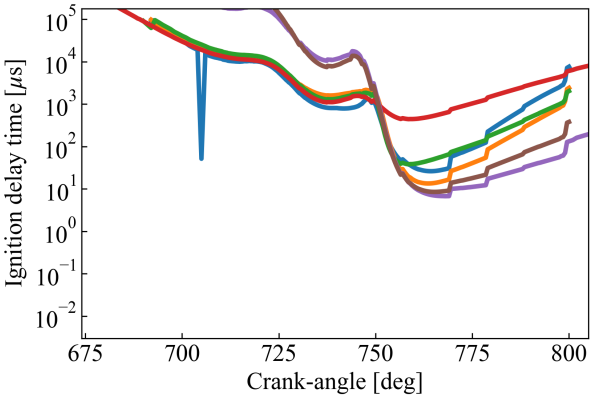

(e) Sphere 90°.

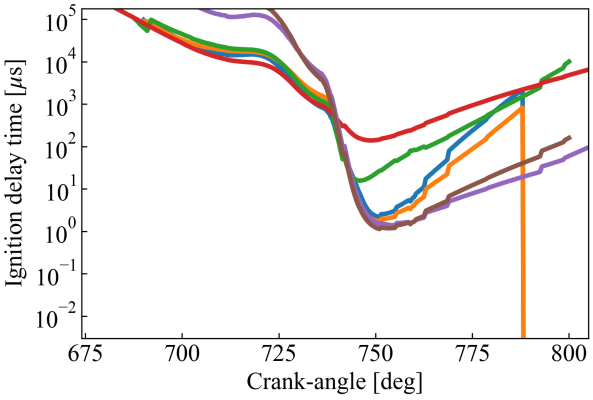

(f) Sphere 112.5°.

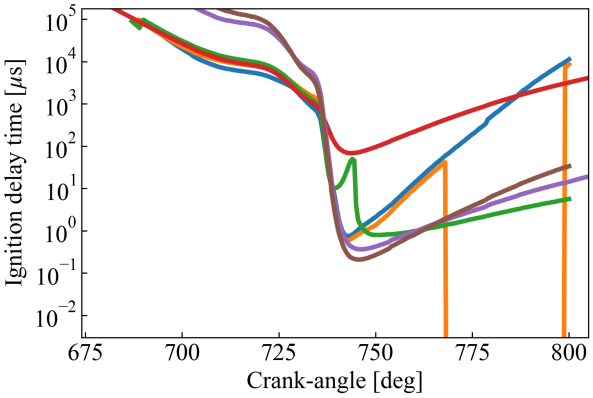

(g) Sphere 135°.

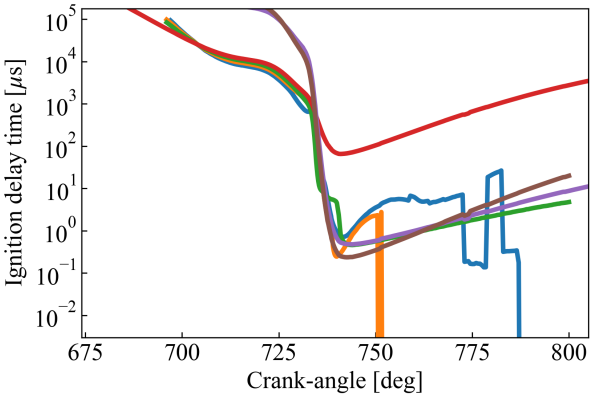

(h) Sphere 157.5°.

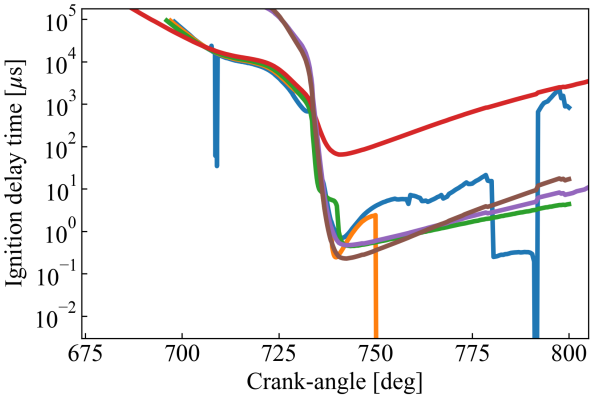

(i) Sphere 180°.

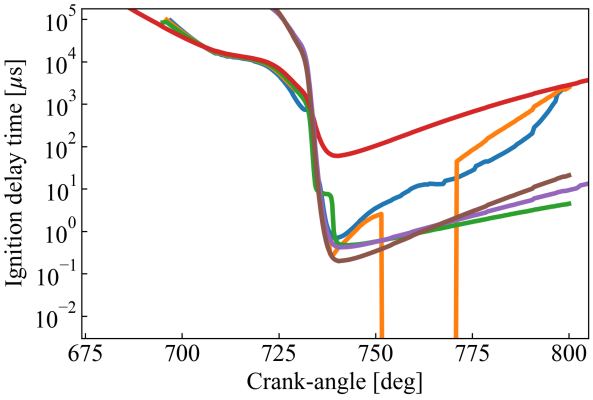

(j) Sphere 202.5°.

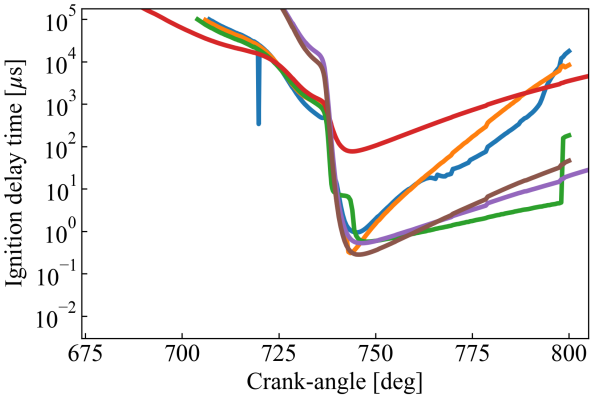

(k) Sphere 225°.

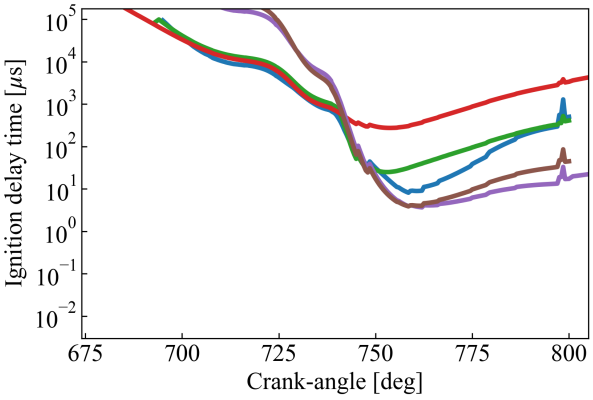

(l) Sphere 247.5°.

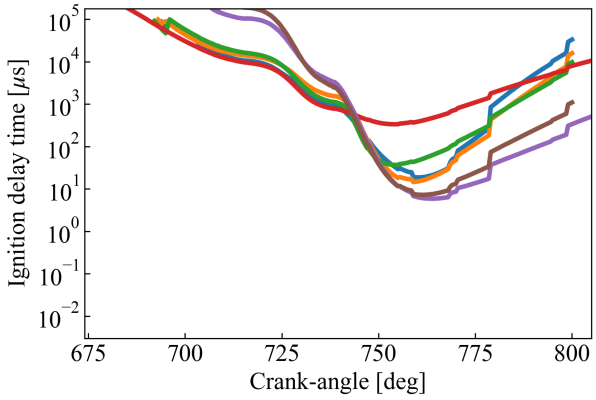

(m) Sphere 270°.

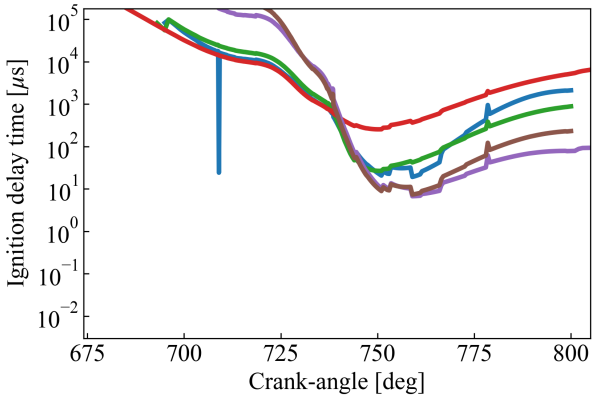

(n) Sphere 292.5°.

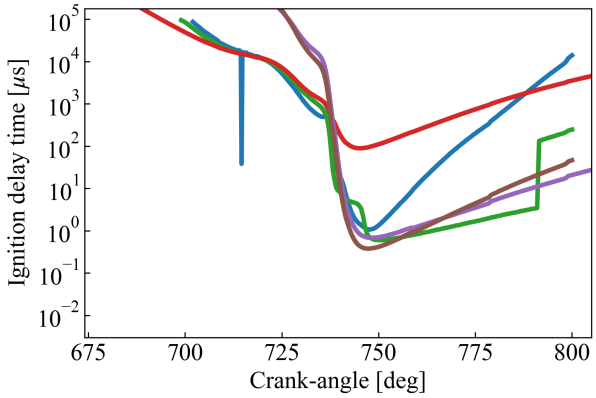

(o) Sphere 315°.

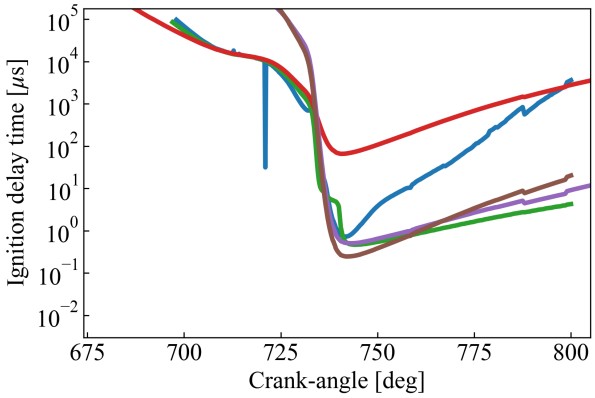

(p) Sphere 337.5°.

Figure 52 – IDT for each AVL FIRE region of interest at 4000 RPM.

APPENDIX F – LIVENGOOD-WU INTEGRAL FOR ALL CRFD SIMULATIONS

This section brings all Livengood-Wu integrals for all regions of interest of each CRFD simulation. They regard the IDT obtained by the three simulated CV-PSR Cantera setups, with the reduced mechanisms from (75, 77, 120) and the three IDT correlations, from (27) and (17) and the one proposed in this work (Eq. 67). Since most Cantera simulations started to ignite around 680 CAD, the L-W integrals are shown beyond this point.

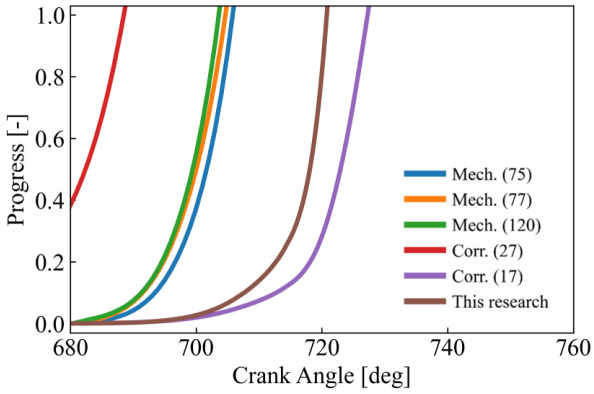

(a) Sphere 0°.

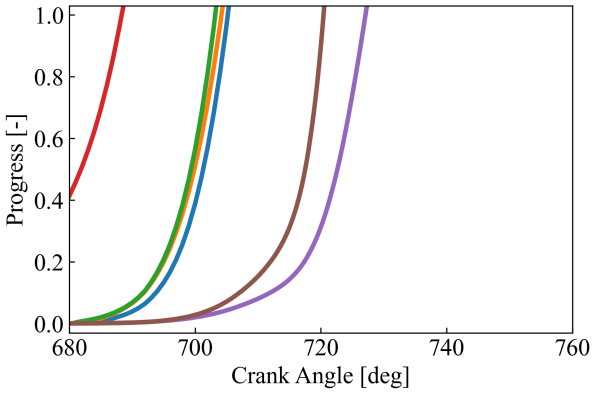

(b) Sphere 22.5°.

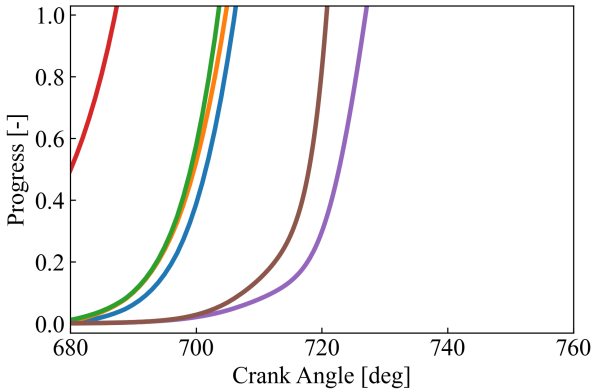

(c) Sphere 45°.

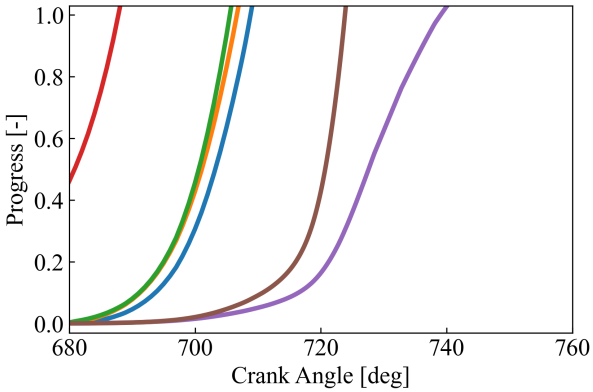

(d) Sphere 67.5°.

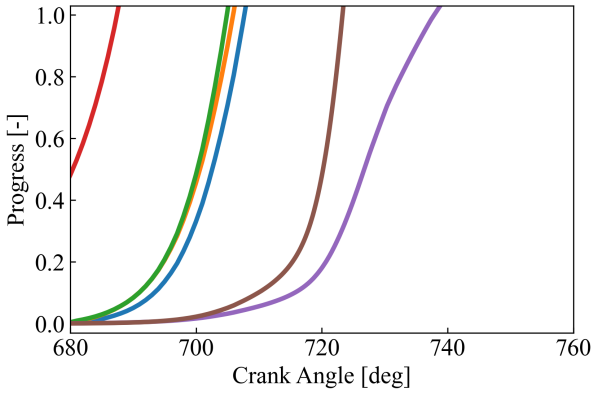

(e) Sphere 90°.

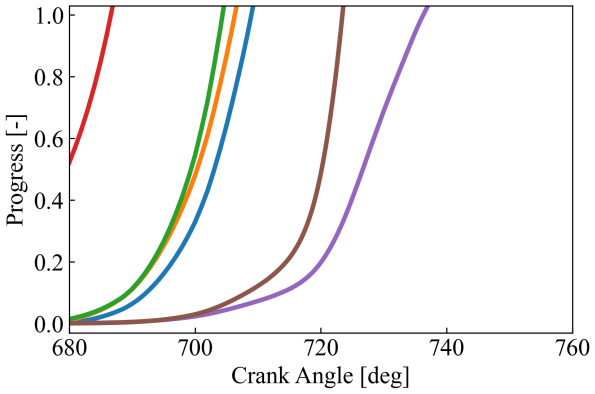

(f) Sphere 112.5°.

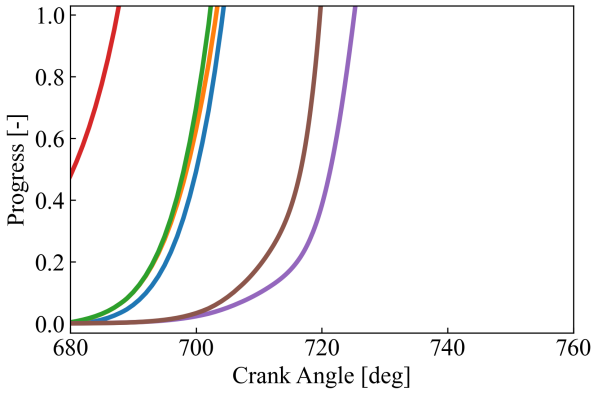

(g) Sphere 135°.

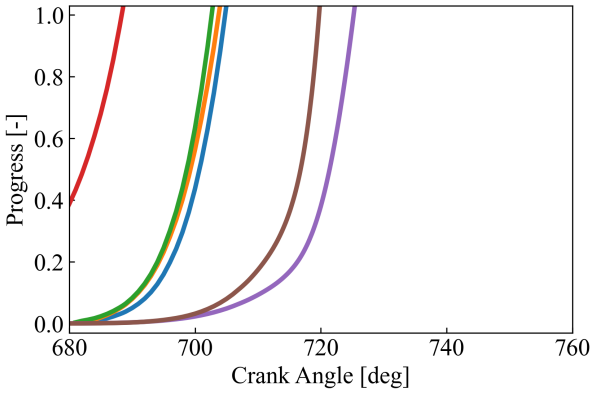

(h) Sphere 157.5°.

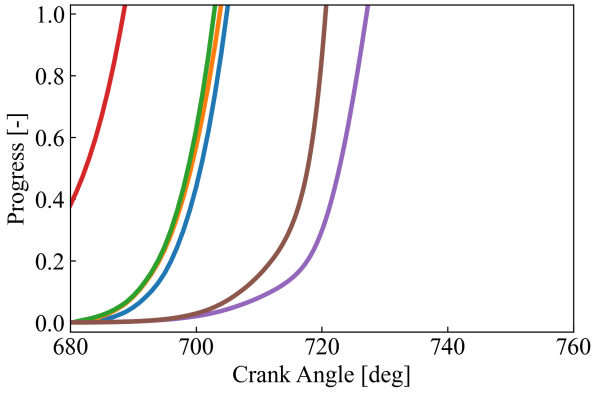

(i) Sphere 180°.

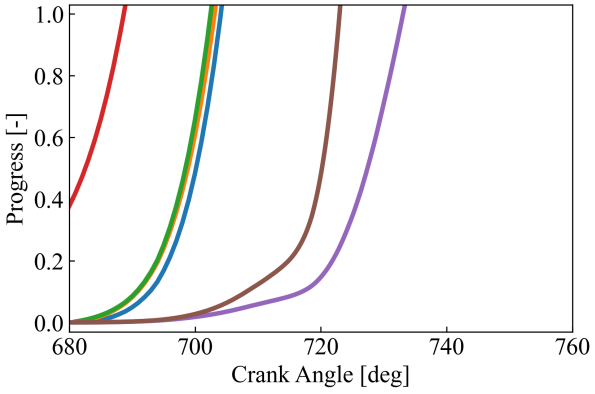

(j) Sphere 202.5°.

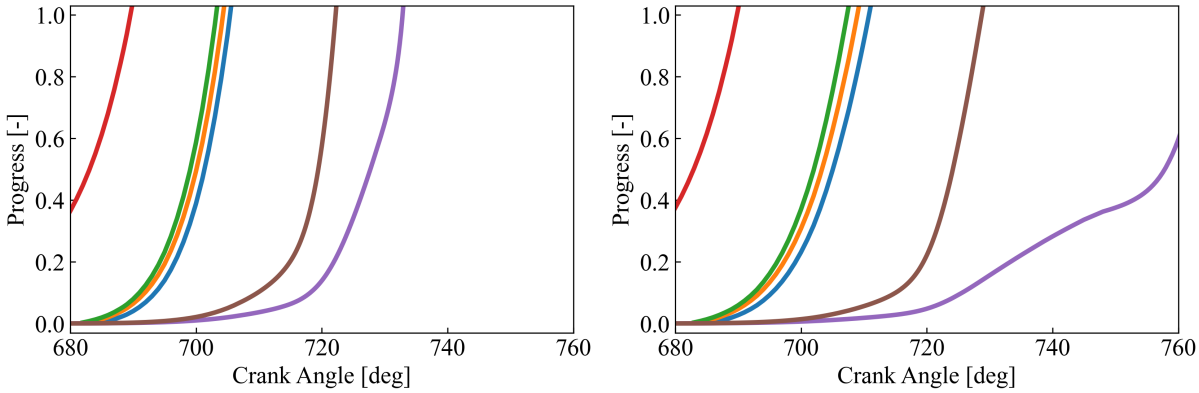

(k) Sphere 225°.

(l) Sphere 247.5°.

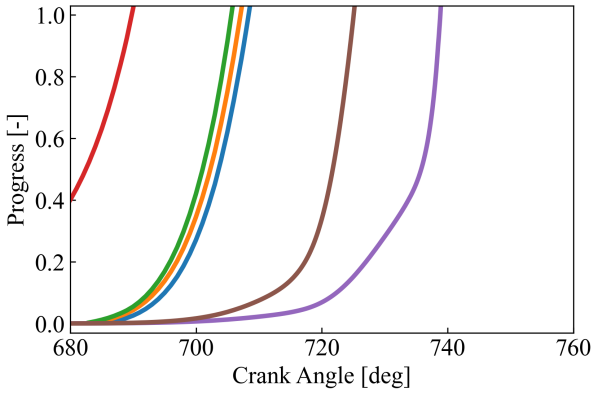

(m) Sphere 270°.

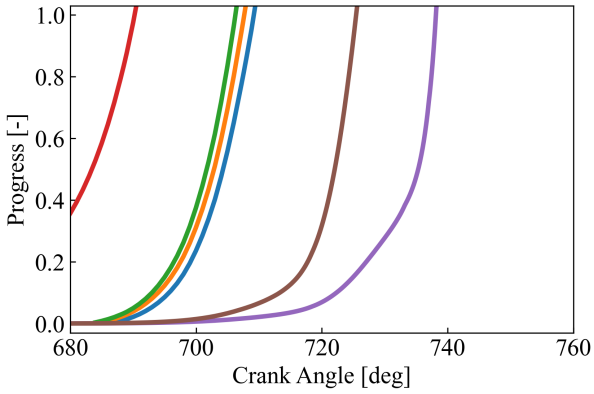

(n) Sphere 292.5°.

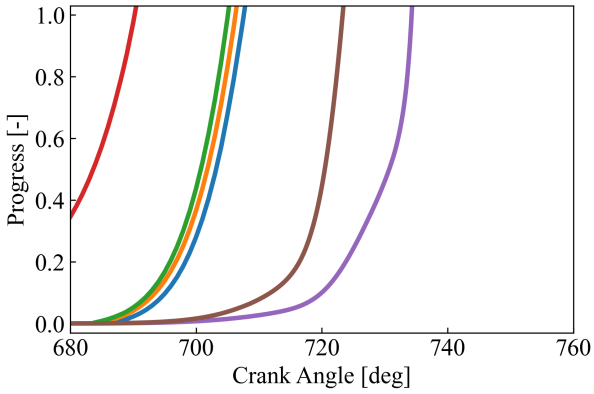

(o) Sphere 315°.

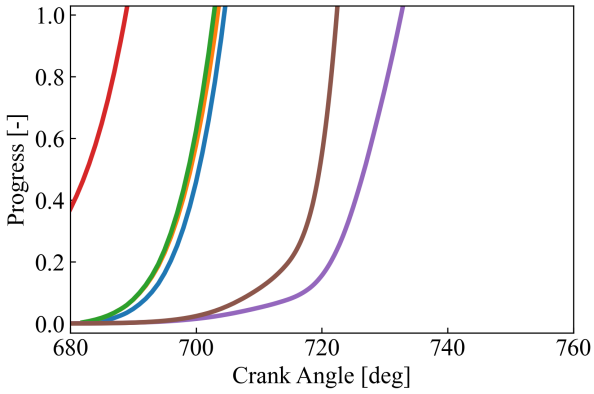

(p) Sphere 337.5°.

Figure 53 – Livengood-Wu integral for each AVL FIRE region of interest at 500 RPM.

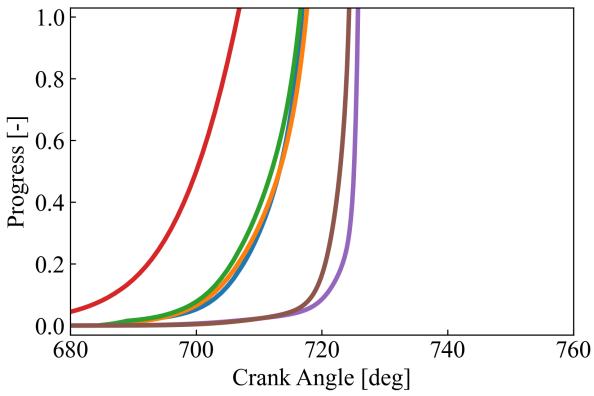

(a) Sphere 0°.

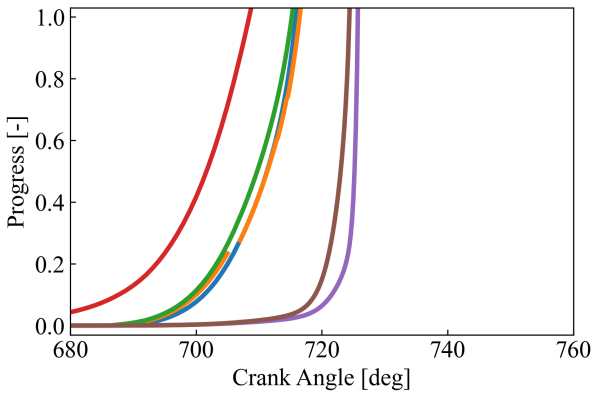

(b) Sphere 22.5°.

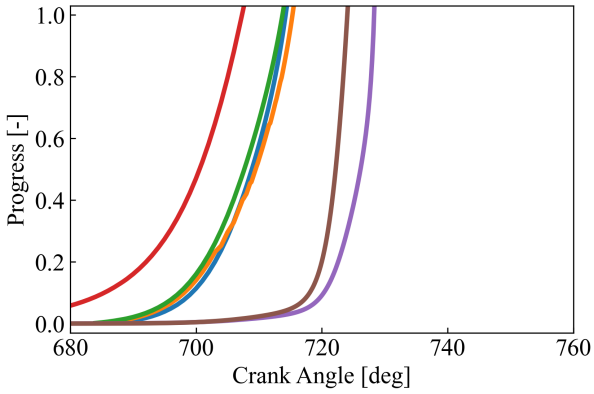

(c) Sphere 45°.

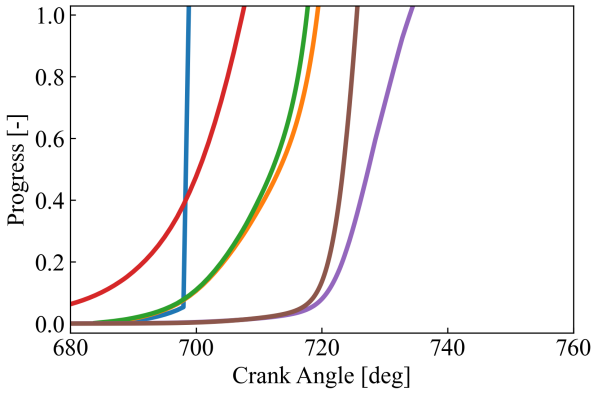

(d) Sphere 67.5°.

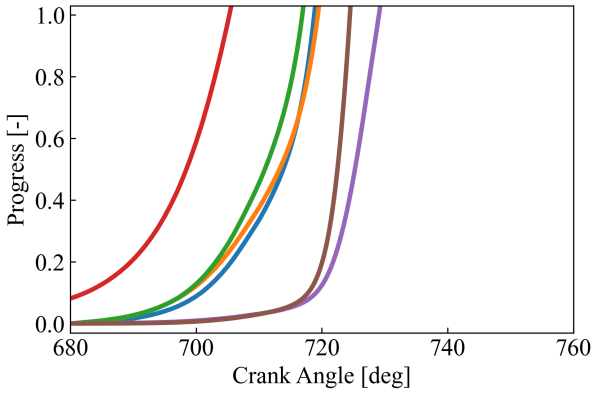

(e) Sphere 90°.

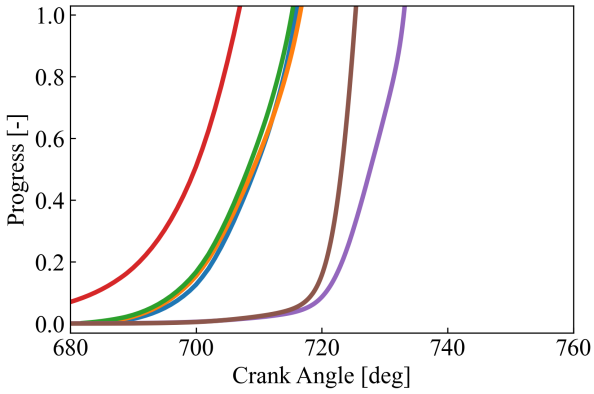

(f) Sphere 112.5°.

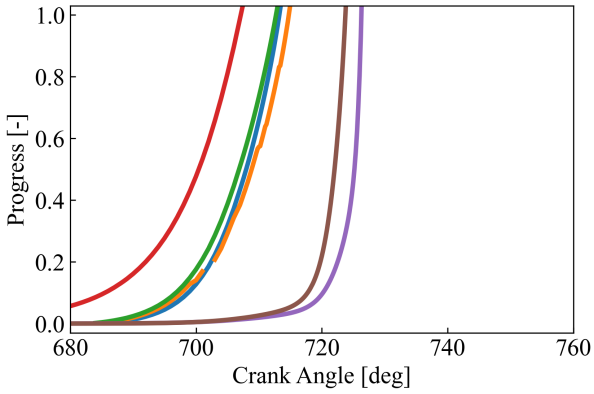

(g) Sphere 135°.

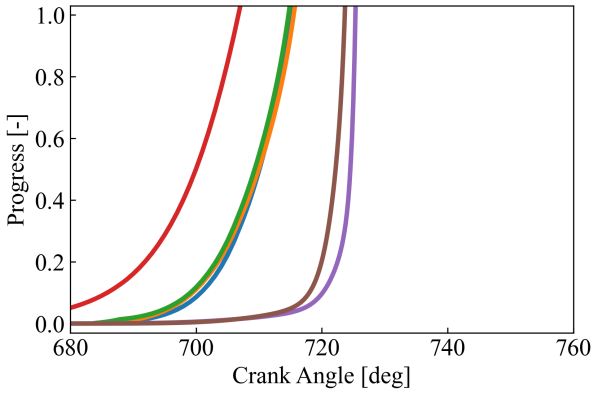

(h) Sphere 157.5°.

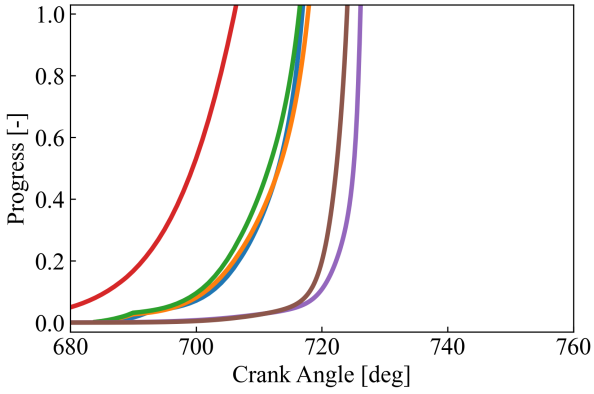

(i) Sphere 180°.

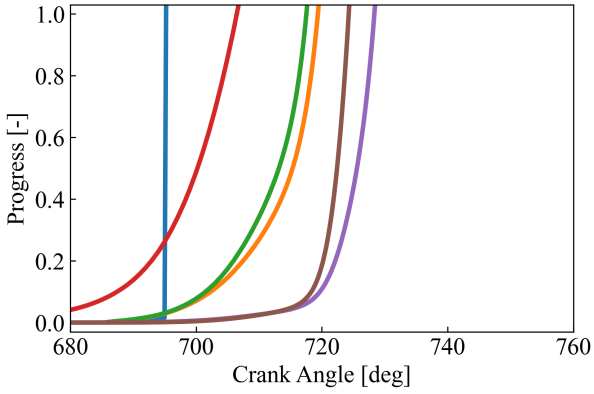

(j) Sphere 202.5°.

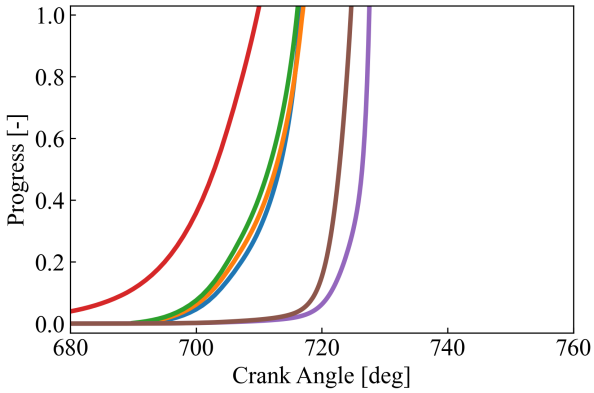

(k) Sphere 225°.

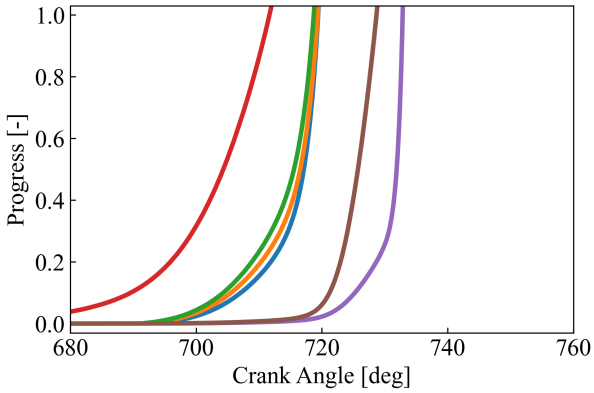

(l) Sphere 247.5°.

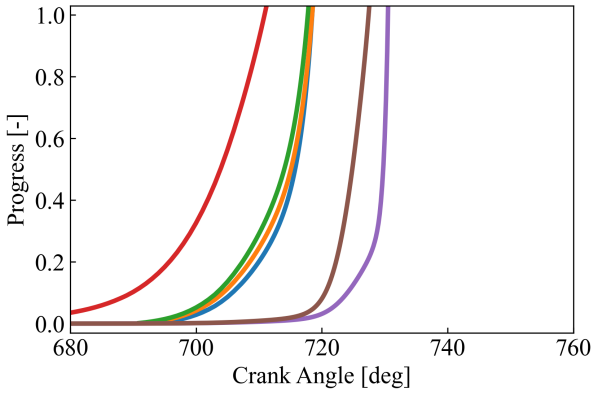

(m) Sphere 270°.

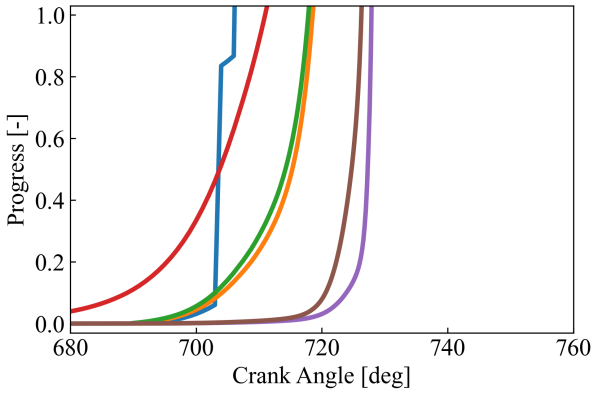

(n) Sphere 292.5°.

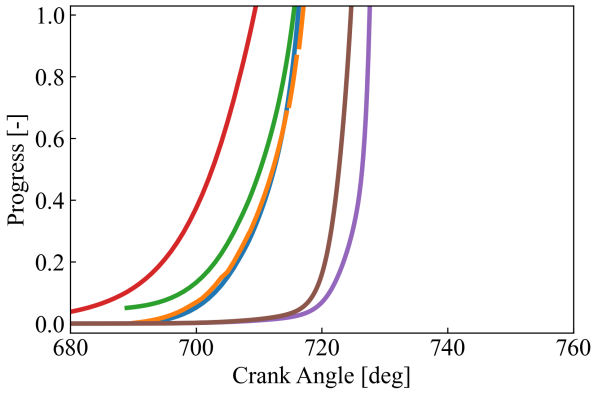

(o) Sphere 315°.

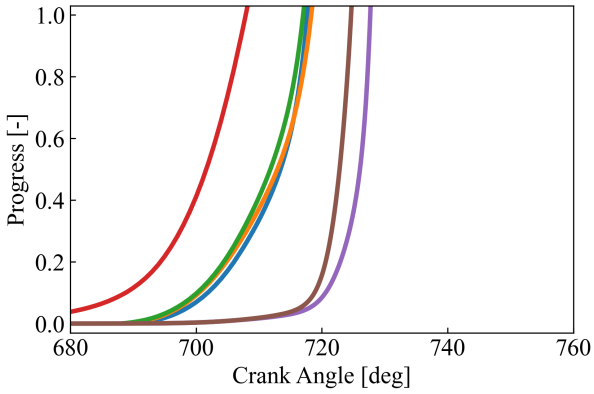

(p) Sphere 337.5°.

Figure 54 – Livengood-Wu integral for each AVL FIRE region of interest at 1000 RPM.

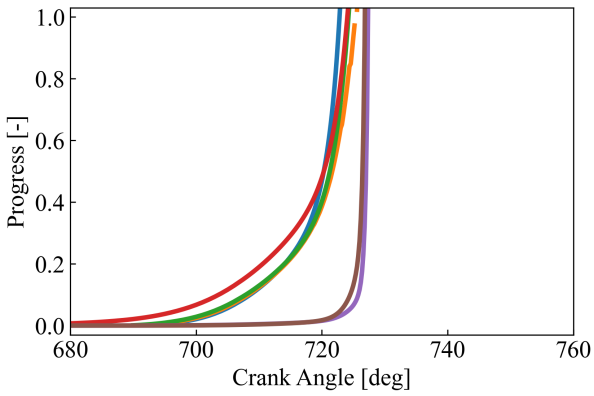

(a) Sphere 0°.

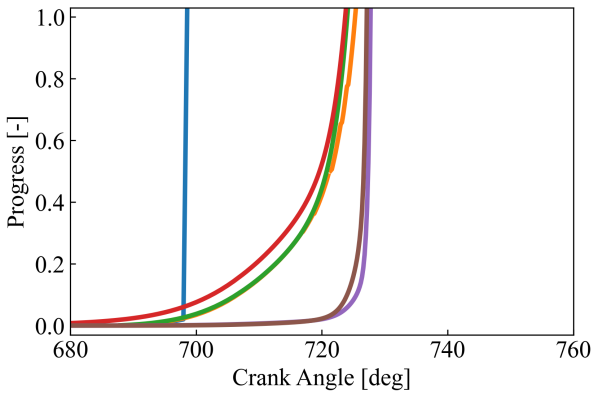

(b) Sphere 22.5°.

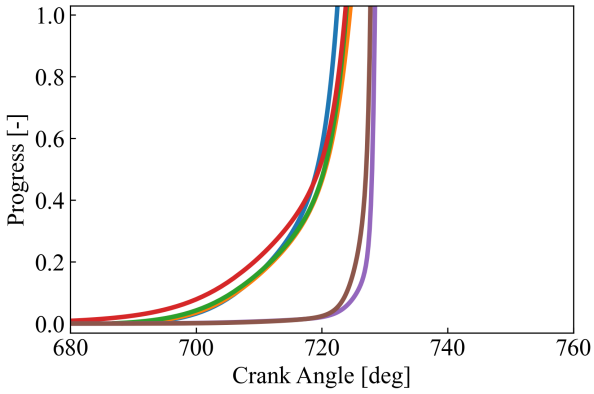

(c) Sphere 45°.

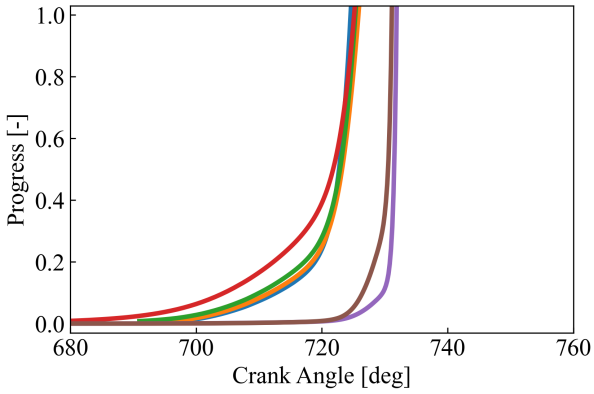

(d) Sphere 67.5°.

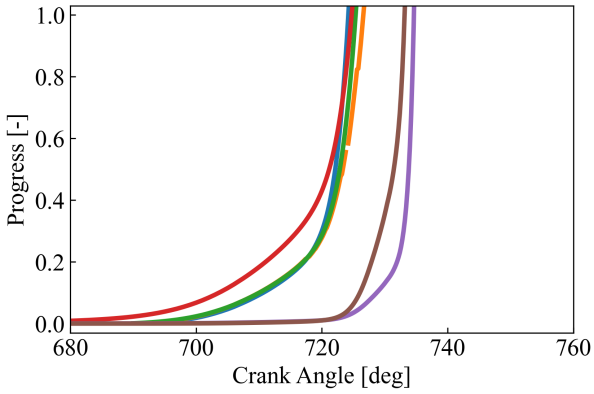

(e) Sphere 90°.

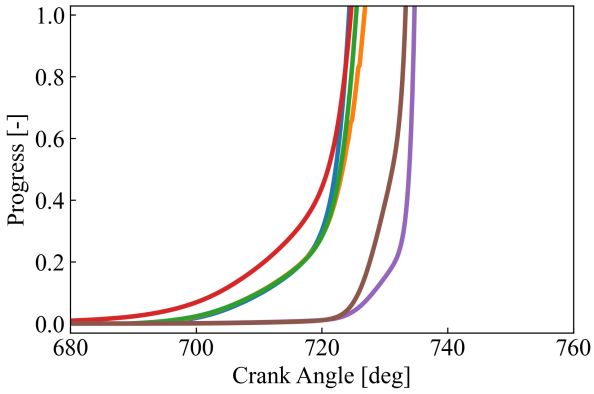

(f) Sphere 112.5°.

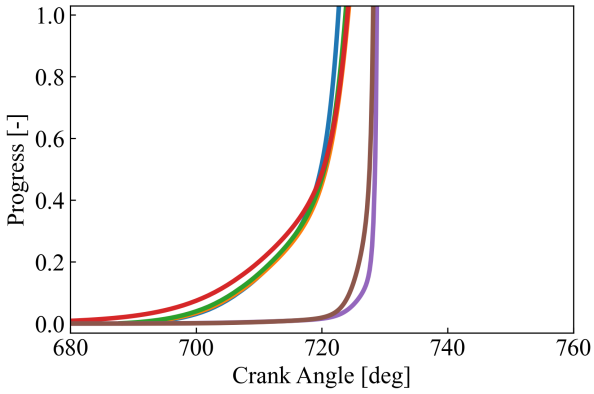

(g) Sphere 135°.

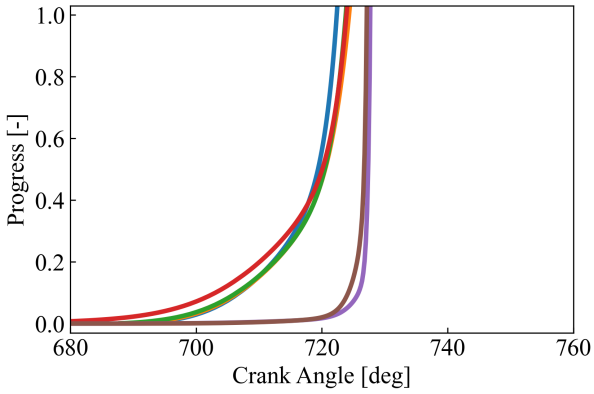

(h) Sphere 157.5°.

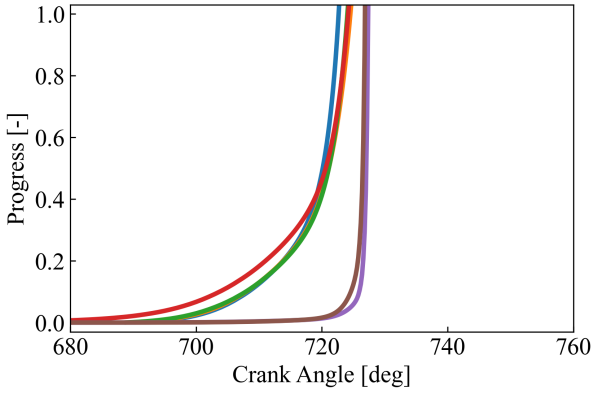

(i) Sphere 180°.

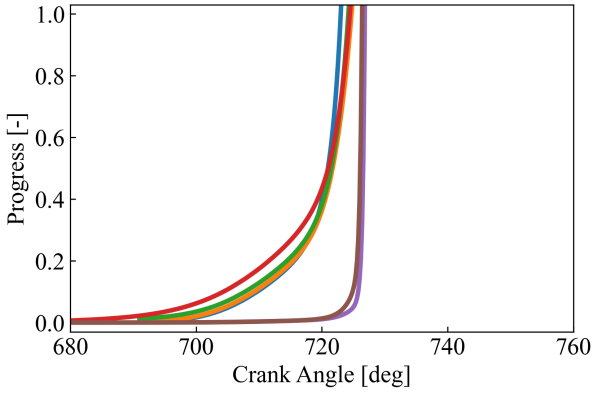

(j) Sphere 202.5°.

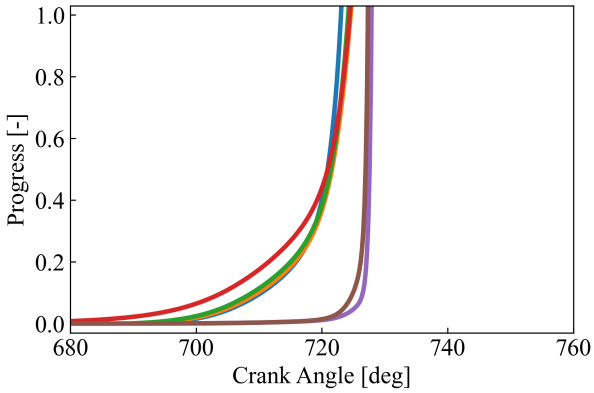

(k) Sphere 225°.

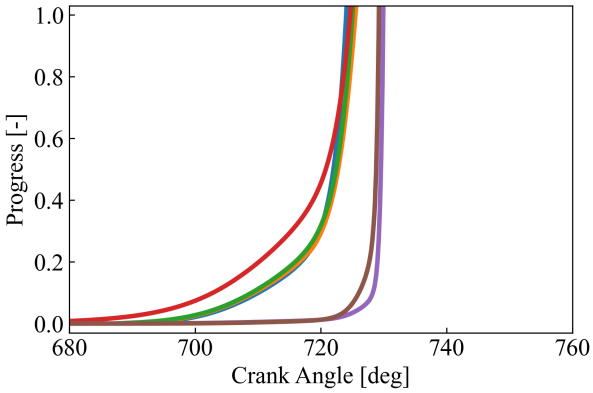

(l) Sphere 247.5°.

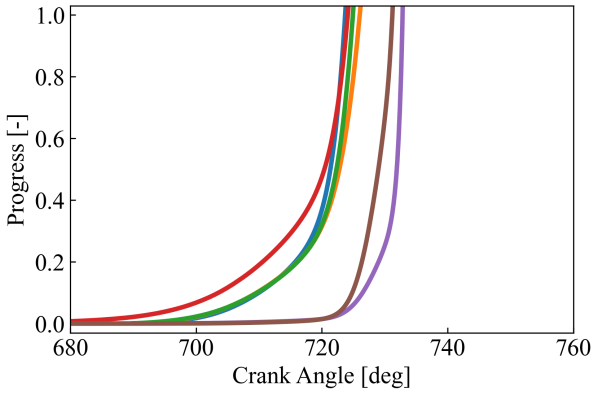

(m) Sphere 270°.

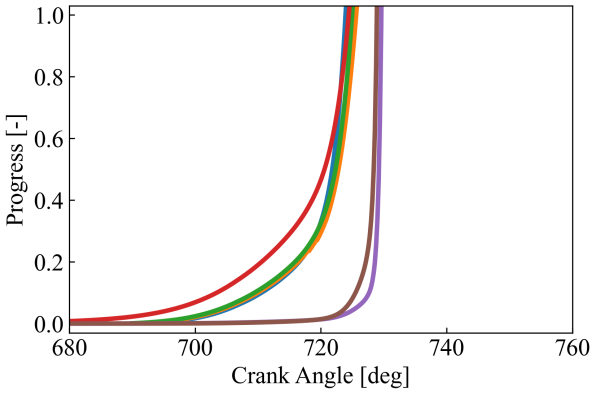

(n) Sphere 292.5°.

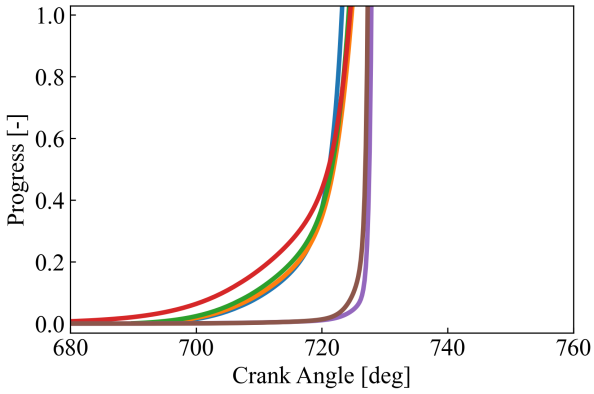

(o) Sphere 315°.

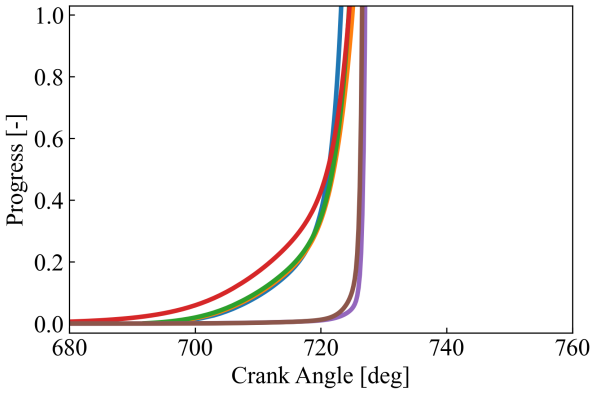

(p) Sphere 337.5°.

Figure 55 – Livengood-Wu integral for each AVL FIRE region of interest at 2000 RPM.

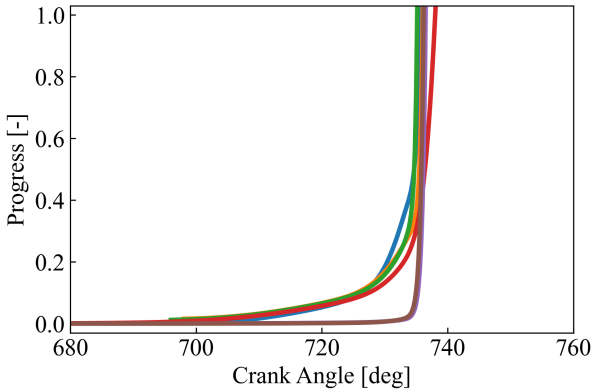

(a) Sphere 0°.

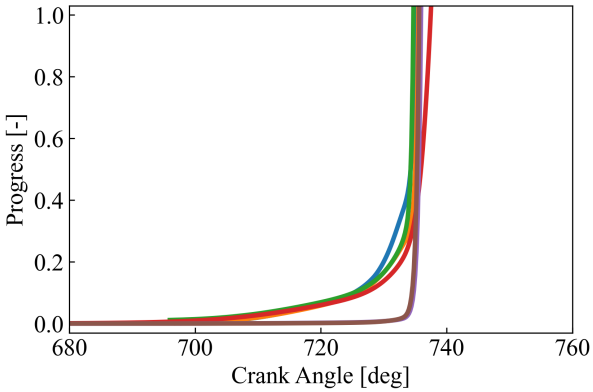

(b) Sphere 22.5°.

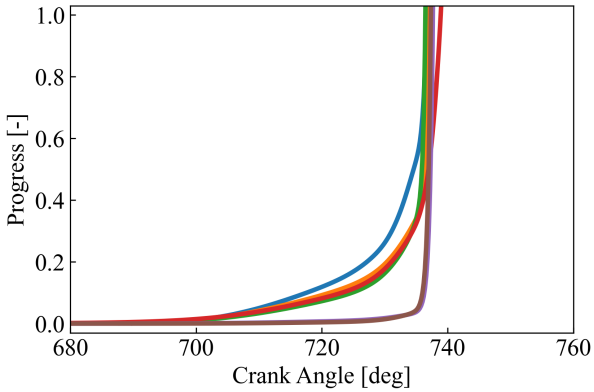

(c) Sphere 45°.

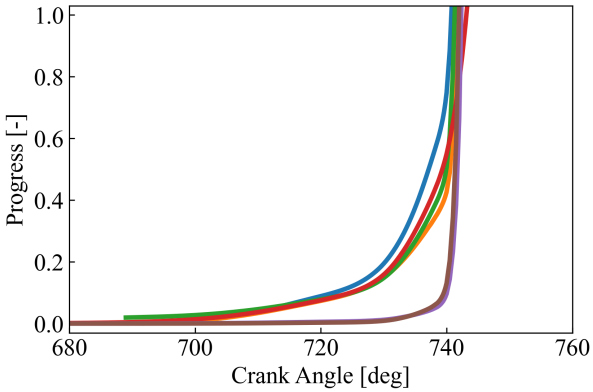

(d) Sphere 67.5°.

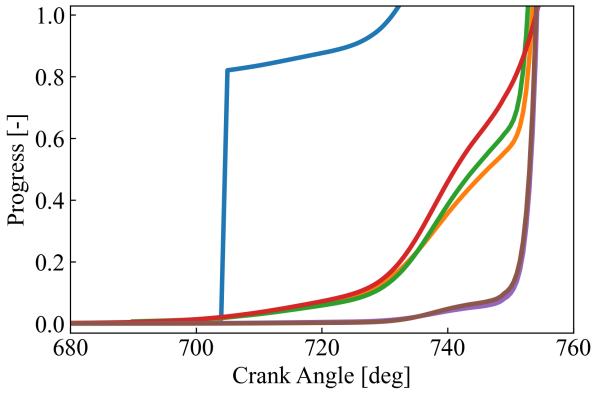

(e) Sphere 90°.

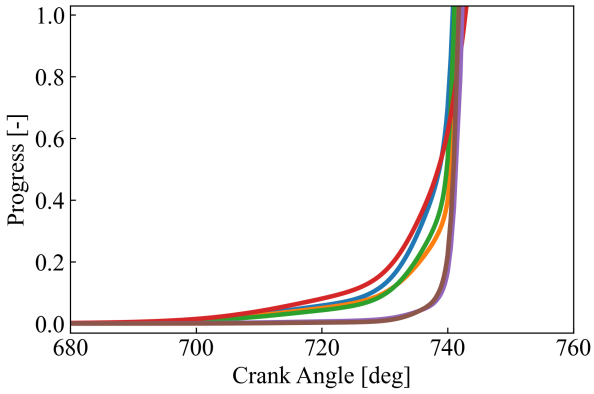

(f) Sphere 112.5°.

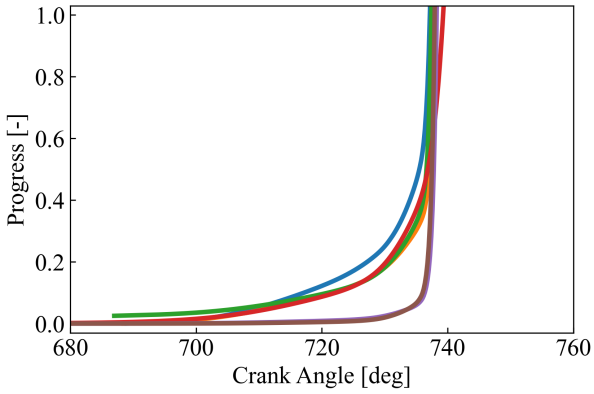

(g) Sphere 135°.

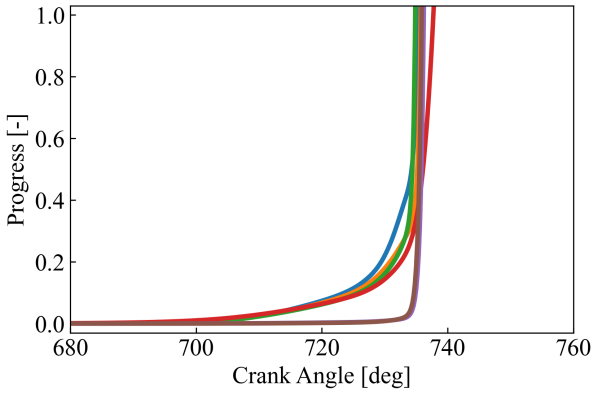

(h) Sphere 157.5°.

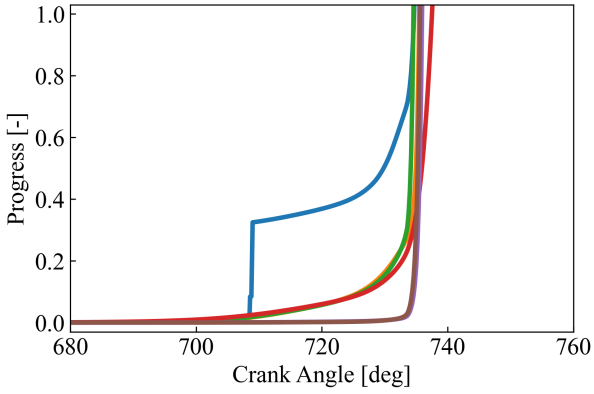

(i) Sphere 180°.

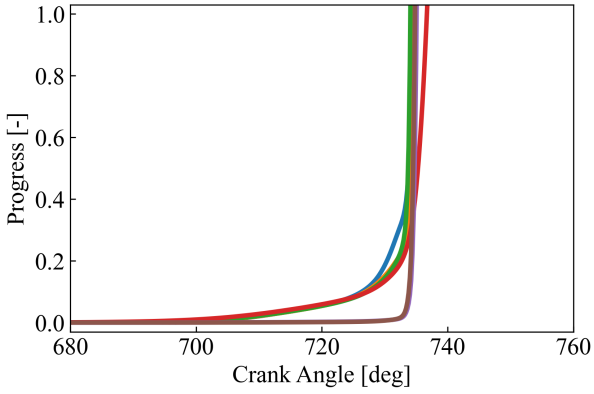

(j) Sphere 202.5°.

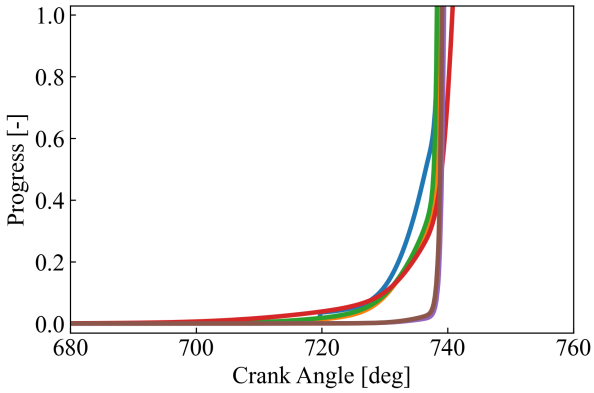

(k) Sphere 225°.

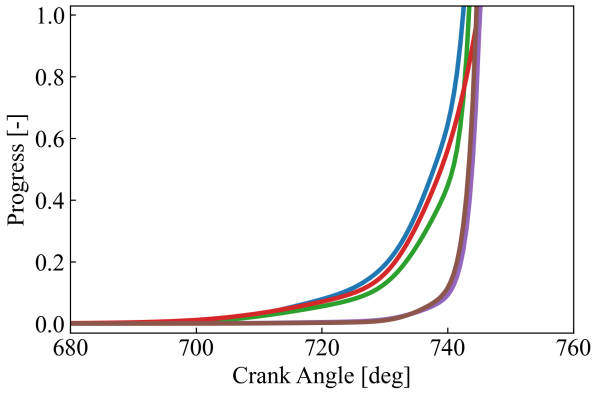

(l) Sphere 247.5°.

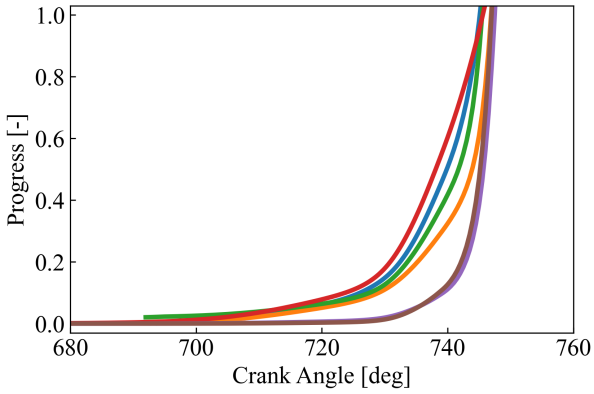

(m) Sphere 270°.

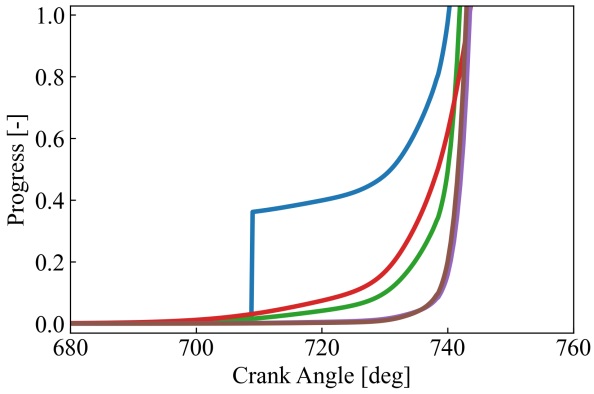

(n) Sphere 292.5°.

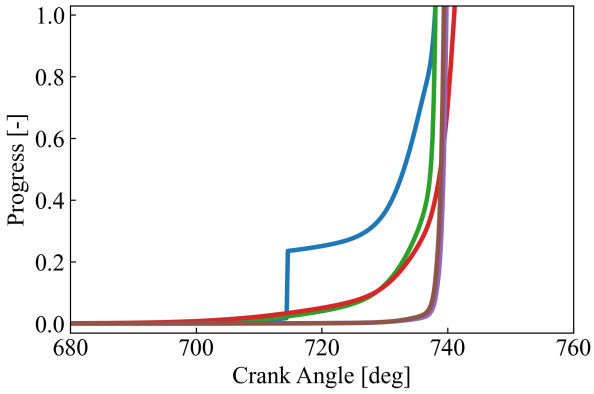

(o) Sphere 315°.

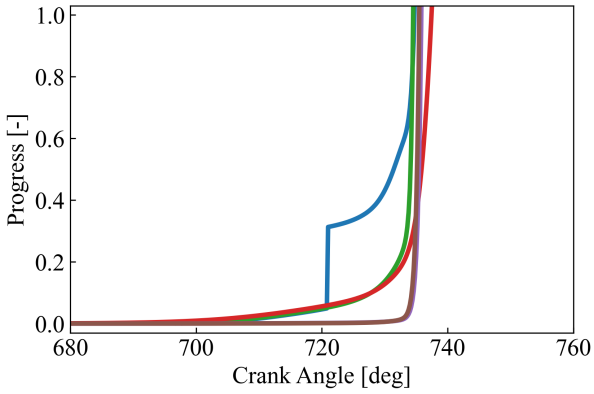

(p) Sphere 337.5°.

Figure 56 – Livengood-Wu integral for each AVL FIRE region of interest at 4000 RPM.

APPENDIX G – LIVENGOOD-WU INTEGRALS COMPARED TO THE REFERENCE KNOCK CRITERIA

Table 32 – Livengood-Wu integrals knock onset prediction compared to the 1000 K criterion at 500 RPM in crank-angle degrees.

Spheres	0°	22.5°	45°	67.5°	90°	112.5°	135°	157.5°	180°	202.5°	225°	247.5°	270°	292.5°	315°	337.5°	Abs. mean	Std. dev
Mech. Y. Li et al. (75)	-39.8	-39.7	-49.0	-	-130.5	-167.0	-47.1	-30.0	-31.7	-35.1	-28.1	-60.3	-30.9	-29.4	-26.8	-33.5	51.9	40.9
Mech. Liu et al. (77)	-41.0	-40.7	-50.5	-	-132.3	-169.6	-48.1	-31.1	-32.8	-36.1	-29.2	-62.2	-32.2	-30.9	-28.2	-34.5	53.3	41.3
Mech. Tsurushima (120)	-42.0	-41.7	-51.7	-	-133.2	-171.6	-49.1	-32.2	-33.8	-36.7	-30.3	-63.8	-33.6	-32.3	-29.4	-35.1	54.4	41.5
Corr. Douaud; Eyzat (27)	-57.1	-56.5	-68.1	-	-150.7	-189.4	-63.9	-46.5	-48.2	-50.5	-44.0	-81.3	-49.5	-48.3	-44.2	-49.2	69.8	42.6
Corr. L. Cancino et al. (17)	-18.4	-17.8	-28.2	-	-100.3	-139.7	-26.2	-9.6	-9.5	-6.1	-0.7	-6.8	-0.4	-0.4	-0.2	-5.4	24.6	40.4
Corr. from this research	-24.9	-24.4	-34.4	-	-114.9	-152.5	-31.6	-15.1	-16.0	-16.2	-11.3	-42.4	-14.2	-13.1	-11.1	-15.6	35.9	41.4
Abs. mean	37.2	36.8	47.0	-	127.0	165.0	44.3	27.4	28.7	30.1	24.0	52.8	26.8	25.8	23.3	28.9	48.3	41.4
Std. dev.	13.8	13.8	14.1	-	17.3	17.1	13.6	13.2	13.9	16.1	15.4	25.7	17.1	16.7	15.5	15.7	15.8	0.7

Table 33 – Livengood-Wu integrals knock onset prediction compared to the 1000 K criterion at 1000 RPM in crank-angle degrees.

Spheres	0°	22.5°	45°	67.5°	90°	112.5°	135°	157.5°	180°	202.5°	225°	247.5°	270°	292.5°	315°	337.5°	Abs. mean	Std. dev
Mech. Y. Li et al. (75)	-7.9	-8.8	-13.2	-51.3	-	-17.4	-11.8	-9.3	-8.0	-32.2	-9.7	-12.2	-10.9	-20.6	-10.2	-8.7	15.5	11.8
Mech. Liu et al. (77)	-7.1	-8.2	-12.1	-30.8	-	-16.7	-10.3	-8.6	-7.1	-8.1	-9.4	-12.3	-10.9	-8.2	-9.4	-8.1	11.2	6.0
Mech. Tsurushima (120)	-8.2	-9.5	-13.7	-32.5	-	-18.0	-12.3	-9.4	-8.5	-9.9	-10.3	-12.9	-11.6	-8.9	-10.9	-9.4	12.4	6.1
Corr. Douaud; Eyzat (27)	-18.1	-16.2	-20.1	-42.7	-	-26.5	-18.0	-17.4	-18.8	-21.0	-16.6	-20.0	-18.5	-15.8	-17.2	-18.5	20.4	6.7
Corr. L. Cancino et al. (17)	1.1	1.0	0.9	-16.1	-	-0.2	1.2	1.2	1.2	0.9	1.2	1.2	1.1	1.1	1.2	1.3	2.1	4.4
Corr. from this research	-0.4	-0.3	-3.4	-24.5	-	-7.9	-1.3	-0.5	-0.9	-3.2	-1.7	-3.0	-1.9	-0.5	-1.8	-1.8	3.5	6.1
Abs. mean	7.1	7.3	10.6	33.0	-	14.4	9.2	7.7	7.4	12.6	8.2	10.3	9.2	9.2	8.4	8.0	10.8	6.9
Std. dev.	6.8	6.4	7.6	12.6	-	9.2	7.3	6.8	7.0	12.3	6.4	7.7	7.2	8.5	6.7	6.9	7.0	2.5

Table 34 – Livengood-Wu integrals knock onset prediction compared to the 1000 K criterion at 2000 RPM in crank-angle degrees.

Spheres	0°	22.5°	45°	67.5°	90°	112.5°	135°	157.5°	180°	202.5°	225°	247.5°	270°	292.5°	315°	337.5°	Abs. mean	Std. dev
Mech. Y. Li et al. (75)	-3.3	-27.8	-4.6	-6.0	-8.4	-8.5	-4.9	-4.1	-3.5	-2.7	-3.6	-4.6	-7.2	-4.3	-3.4	-2.7	6.2	6.0
Mech. Liu et al. (77)	-	-1.1	-2.5	-4.7	-6.0	-6.1	-3.4	-2.2	-1.6	-1.0	-2.1	-3.1	-4.9	-2.6	-1.9	-0.9	2.9	1.7
Mech. Tsurushima (120)	-1.9	-2.4	-3.1	-5.2	-7.3	-7.4	-3.8	-2.7	-2.1	-1.5	-2.5	-3.6	-6.0	-3.3	-2.4	-1.4	3.5	1.9
Corr. Douaud; Eyzat (27)	-2.0	-2.7	-3.3	-5.4	-7.9	-8.3	-3.5	-2.6	-2.0	-1.3	-2.2	-3.9	-6.8	-3.8	-2.1	-1.4	3.7	2.2
Corr. L. Cancino et al. (17)	1.2	1.4	1.5	1.3	2.0	1.9	1.2	1.2	1.2	1.1	1.2	1.3	1.9	1.4	1.2	1.1	1.4	0.3
Corr. from this research	0.7	0.8	0.7	0.6	0.5	0.4	0.6	0.7	0.7	0.7	0.6	0.6	0.3	0.7	0.7	0.7	0.6	0.1
Abs. mean	1.8	6.0	2.6	3.9	5.4	5.4	2.9	2.2	1.8	1.4	2.1	2.9	4.5	2.7	2.0	1.4	3.1	2.1
Std. dev.	1.9	11.1	2.4	3.3	4.6	4.6	2.5	2.1	1.8	1.4	1.9	2.5	3.9	2.4	1.8	1.4	2.0	2.1

Table 35 – Livengood-Wu integrals knock onset prediction compared to the 1000 K criterion at 4000 RPM in crank-angle degrees.

Spheres	0°	22.5°	45°	67.5°	90°	112.5°	135°	157.5°	180°	202.5°	225°	247.5°	270°	292.5°	315°	337.5°	Abs. mean	Std. dev
Mech. Y. Li et al. (75)	0.9	0.9	0.8	0.8	-19.8	1.5	0.9	0.8	0.6	0.9	0.7	1.1	2.1	0.7	0.3	0.7	2.1	5.2
Mech. Liu et al. (77)	1.3	1.3	1.3	1.7	2.4	2.3	1.5	1.3	1.4	1.2	1.1	2.8	3.9	3.5	1.5	1.4	1.9	0.9
Mech. Tsurushima (120)	0.4	0.5	0.6	1.3	1.7	1.7	1.1	0.4	0.5	0.6	0.4	2.0	2.5	2.5	0.3	0.5	1.1	0.8
Corr. Douaud; Eyzat (27)	3.3	3.2	3.0	3.2	3.0	3.5	3.0	3.3	3.4	3.2	2.9	3.4	2.6	4.0	3.3	3.4	3.2	0.3
Corr. L. Cancino et al. (17)	1.8	1.7	1.8	2.4	3.2	3.0	2.0	1.8	1.8	1.5	1.5	3.8	4.5	4.1	2.1	1.8	2.4	1.0
Corr. from this research	1.4	1.4	1.4	2.0	3.0	2.5	1.7	1.4	1.5	1.3	1.2	3.2	4.0	3.5	1.7	1.5	2.0	0.9
Abs. mean	1.5	1.5	1.5	1.9	5.5	2.4	1.7	1.5	1.5	1.4	1.3	2.7	3.3	3.1	1.5	1.5	2.1	1.5
Std. dev.	1.0	0.9	0.9	0.8	9.2	0.8	0.7	1.0	1.1	0.9	0.9	1.0	1.0	1.3	1.1	1.0	0.7	1.8

Table 36 – $\Omega_{1\%}$ knock onset criterion compared to the 1000 K criterion in crank-angle degrees.

RPM	0°	22.5°	45°	67.5°	90°	112.5°	135°	157.5°	180°	202.5°	225°	247.5°	270°	292.5°	315°	337.5°	Abs. mean	Std. dev
500	-35.7	-35.9	-45.2	-	-130.9	-168.8	-44.1	-25.8	-27.6	-32.0	-26.3	-20.1	-32.0	-28.6	-27.2	-30.8	-	-
1000	-3.5	-3.9	-5.2	-22.9	-	-10.0	-4.7	-3.3	-2.7	-4.5	-5.9	-9.8	-9.4	-4.9	-5.8	-3.8	-	-
2000	2.3	1.6	2.2	1.7	-12.6	3.7	1.5	1.5	2.0	1.1	1.3	1.2	-10.9	2.0	1.4	2.1	-	-
4000	-6.7	-6.2	-6.9	-8.0	-25.4	-4.3	-7.3	-6.4	-6.1	-6.5	-9.9	-11.4	-17.4	-9.4	-9.7	-6.0	-	-

Table 37 – Livengood-Wu integrals knock onset prediction compared to $\Omega_{1\%}$ criterion at 500 RPM in crank-angle degrees.

Spheres	0°	22.5°	45°	67.5°	90°	112.5°	135°	157.5°	180°	202.5°	225°	247.5°	270°	292.5°	315°	337.5°	Abs. mean	Std. dev
Mech. Y. Li et al. (75)	-4.2	-3.8	-3.9	-3.2	0.5	1.8	-3.0	-4.2	-4.1	-3.1	-1.8	-40.2	1.2	-0.8	0.4	-2.7	4.9	9.7
Mech. Liu et al. (77)	-5.3	-4.8	-5.3	-5.3	-1.3	-0.9	-4.0	-5.2	-5.2	-4.1	-2.9	-42.1	-0.1	-2.3	-0.9	-3.8	5.9	9.8
Mech. Tsurushima (120)	-6.4	-5.8	-6.5	-6.5	-2.3	-2.8	-5.0	-6.4	-6.2	-4.7	-4.0	-43.7	-1.6	-3.7	-2.1	-4.4	7.0	9.9
Corr. Douaud; Eyzat (27)	-21.5	-20.7	-22.9	-24.2	-19.8	-20.6	-19.7	-20.7	-20.5	-18.5	-17.6	-61.2	-17.4	-19.8	-17.0	-18.4	22.5	10.5
Corr. L. Cancino et al. (17)	17.3	18.1	16.9	27.0	30.7	29.1	18.0	16.2	18.1	25.9	25.6	13.3	31.6	28.1	27.1	25.4	23.0	6.0
Corr. from this research	10.8	11.4	10.7	11.8	16.1	16.2	12.5	10.7	11.6	15.8	15.0	-22.3	17.9	15.5	16.1	15.2	14.3	9.3
Abs. mean	10.9	10.8	11.0	13.0	11.8	11.9	10.4	10.6	11.0	12.0	11.2	37.1	11.6	11.7	10.6	11.6	12.9	9.2
Std. dev.	13.8	13.8	14.1	17.5	17.3	17.1	13.6	13.2	13.9	16.1	15.4	25.7	17.1	16.7	15.5	15.7	8.3	1.6

Table 38 – Livengood-Wu integrals knock onset prediction compared to $\Omega_{1\%}$ criterion at 1000 RPM in crank-angle degrees.

Spheres	0°	22.5°	45°	67.5°	90°	112.5°	135°	157.5°	180°	202.5°	225°	247.5°	270°	292.5°	315°	337.5°	Abs. mean	Std. dev
Mech. Y. Li et al. (75)	-4.4	-4.9	-8.0	-28.4	-1.2	-7.3	-7.2	-6.0	-5.3	-27.8	-3.8	-2.4	-1.5	-15.7	-4.4	-4.9	8.3	8.4
Mech. Liu et al. (77)	-3.7	-4.3	-6.9	-7.9	-0.6	-6.7	-5.6	-5.3	-4.4	-3.6	-3.5	-2.4	-1.5	-3.3	-3.6	-4.3	4.2	1.9
Mech. Tsurushima (120)	-4.7	-5.6	-8.5	-9.6	-3.1	-8.0	-7.7	-6.1	-5.8	-5.5	-4.4	-3.1	-2.2	-3.9	-5.1	-5.6	5.5	2.1
Corr. Douaud; Eyzat (27)	-14.6	-12.3	-14.9	-19.8	-14.7	-16.5	-13.3	-14.1	-16.1	-16.5	-10.7	-10.1	-9.1	-10.8	-11.4	-14.7	13.7	2.9
Corr. L. Cancino et al. (17)	4.5	4.9	6.1	6.8	9.1	9.8	5.9	4.5	3.9	5.3	7.1	11.0	10.5	6.1	7.0	5.1	6.7	2.2
Corr. from this research	3.1	3.6	1.9	-1.6	4.5	2.1	3.3	2.8	1.8	1.3	4.2	6.9	7.4	4.5	4.0	2.1	3.4	2.2
Abs. mean	5.8	5.9	7.7	12.4	5.5	8.4	7.2	6.5	6.2	10.0	5.6	6.0	5.4	7.4	5.9	6.1	7.0	3.3
Std. dev.	6.8	6.4	7.6	12.6	8.0	9.2	7.3	6.8	7.0	12.3	6.4	7.7	7.2	8.5	6.7	6.9	3.7	2.5

Table 39 – Livengood-Wu integrals knock onset prediction compared to $\Omega_{1\%}$ criterion at 2000 RPM in crank-angle degrees.

Spheres	0°	22.5°	45°	67.5°	90°	112.5°	135°	157.5°	180°	202.5°	225°	247.5°	270°	292.5°	315°	337.5°	Abs. mean	Std. dev
Mech. Y. Li et al. (75)	-5.6	-29.4	-6.8	-7.6	4.2	-12.3	-6.4	-5.6	-5.5	-3.8	-5.0	-5.8	3.7	-6.3	-4.8	-4.8	7.4	7.3
Mech. Liu et al. (77)	-	-2.7	-4.8	-6.4	6.6	-9.8	-4.8	-3.7	-3.7	-2.1	-3.4	-4.3	6.0	-4.6	-3.3	-3.0	4.6	4.2
Mech. Tsurushima (120)	-4.2	-4.0	-5.3	-6.9	5.4	-11.1	-5.2	-4.2	-4.1	-2.6	-3.8	-4.8	4.9	-5.2	-3.8	-3.6	4.9	3.9
Corr. Douaud; Eyzat (27)	-4.3	-4.3	-5.5	-7.1	4.7	-12.0	-4.9	-4.1	-4.0	-2.4	-3.6	-5.1	4.1	-5.8	-3.5	-3.5	4.9	3.9
Corr. L. Cancino et al. (17)	-1.1	-0.3	-0.8	-0.3	14.6	-1.9	-0.3	-0.3	-0.8	0.0	-0.1	0.1	12.8	-0.6	-0.1	-1.0	2.2	4.9
Corr. from this research	-1.6	-0.9	-1.5	-1.1	13.2	-3.3	-0.8	-0.9	-1.3	-0.4	-0.7	-0.6	11.2	-1.3	-0.7	-1.4	2.6	4.6
Abs. mean	3.3	6.9	4.1	4.9	8.1	8.4	3.7	3.1	3.2	1.9	2.8	3.4	7.1	4.0	2.7	2.9	4.4	4.8
Std. dev.	1.9	11.1	2.4	3.3	4.6	4.6	2.5	2.1	1.8	1.4	1.9	2.5	3.9	2.4	1.8	1.4	1.9	1.3

Table 40 – Livengood-Wu integrals knock onset prediction compared to $\Omega_{1\%}$ criterion at 4000 RPM in crank-angle degrees.

Spheres	0°	22.5°	45°	67.5°	90°	112.5°	135°	157.5°	180°	202.5°	225°	247.5°	270°	292.5°	315°	337.5°	Abs. mean	Std. dev.
Mech. Y. Li et al. (75)	7.6	7.1	7.6	8.8	5.6	5.8	8.2	7.3	6.7	7.4	10.5	12.5	19.5	10.1	10.0	6.7	8.8	3.4
Mech. Liu et al. (77)	8.0	7.5	8.2	9.7	27.8	6.6	8.8	7.7	7.5	7.7	11.0	14.2	21.3	12.9	11.2	7.4	11.1	5.8
Mech. Tsurushima (120)	7.2	6.7	7.5	9.3	27.1	6.0	8.4	6.8	6.6	7.1	10.3	13.4	19.9	11.9	10.0	6.5	10.3	5.7
Corr. Douaud; Eyzat (27)	10.0	9.5	9.9	11.1	28.5	7.8	10.3	9.7	9.5	9.7	12.7	14.8	20.0	13.5	13.0	9.4	12.5	5.2
Corr. L. Cancino et al. (17)	8.5	7.9	8.7	10.3	28.6	7.3	9.3	8.2	7.9	8.1	11.4	15.1	21.9	13.5	11.8	7.8	11.6	5.9
Corr. from this research	8.2	7.6	8.3	10.0	28.5	6.8	8.9	7.9	7.6	7.8	11.1	14.6	21.4	13.0	11.4	7.5	11.3	5.9
Abs. mean	8.3	7.7	8.4	9.9	24.3	6.7	9.0	7.9	7.6	8.0	11.2	14.1	20.7	12.5	11.2	7.6	10.9	5.3
Std. dev.	1.0	0.9	0.9	0.8	9.2	0.8	0.7	1.0	1.1	0.9	0.9	1.0	1.0	1.3	1.1	1.0	1.2	1.0

ANNEX A – AVL FIRE SPRAY SETUP SPREADSHEET

This section shows the main tabs of the Macroed Excel spreadsheet provided by AVL for AVL FIRE GDI fuel injection and spray. The figures bring the details for the baseline simulation, at 4000 RPM. The variations in these tabs are mentioned in the main text, with the variations of injection duration and injected mass.

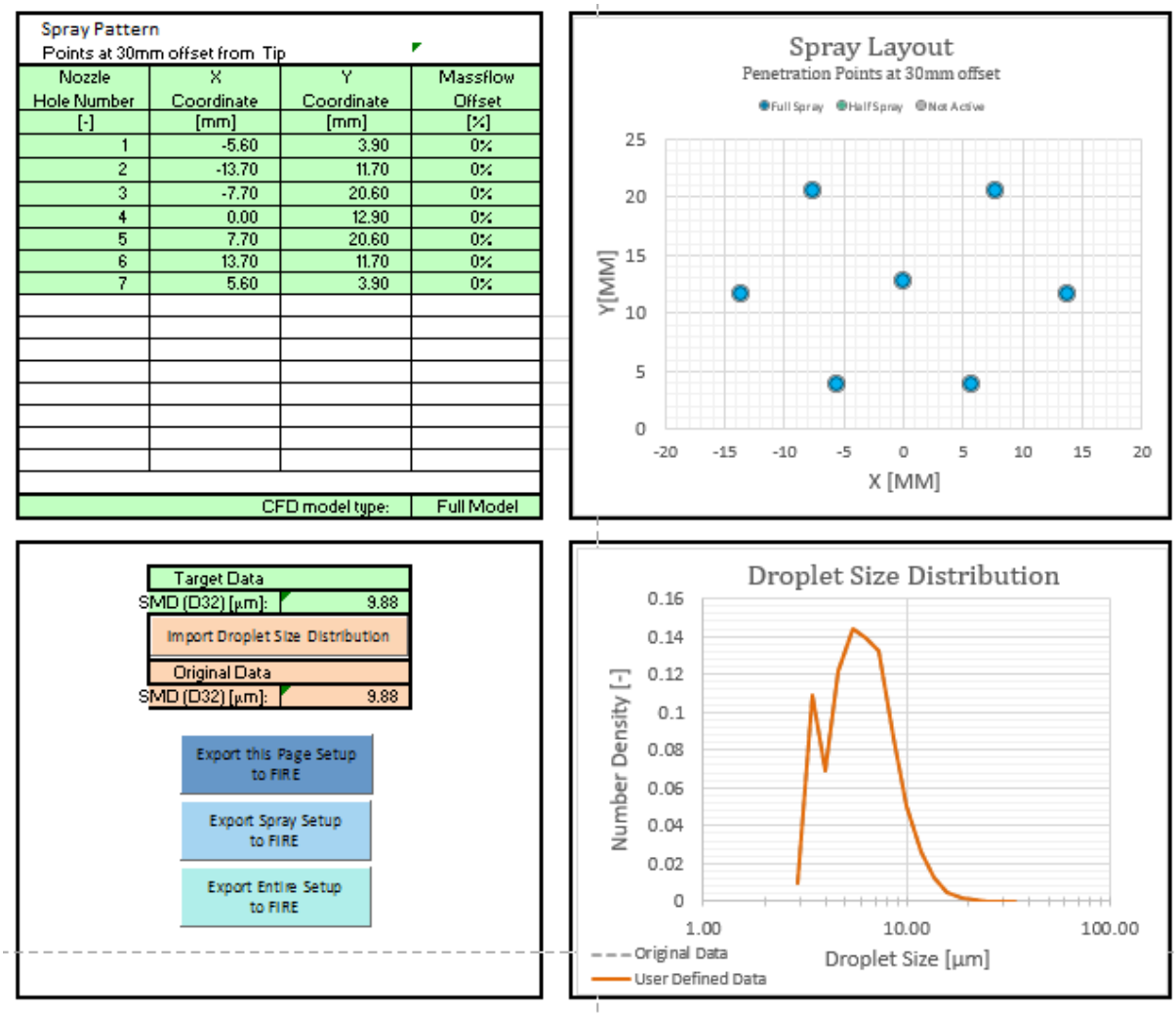

Figure 57 – AVL FIRE spray pattern, layout, and droplet size distribution.

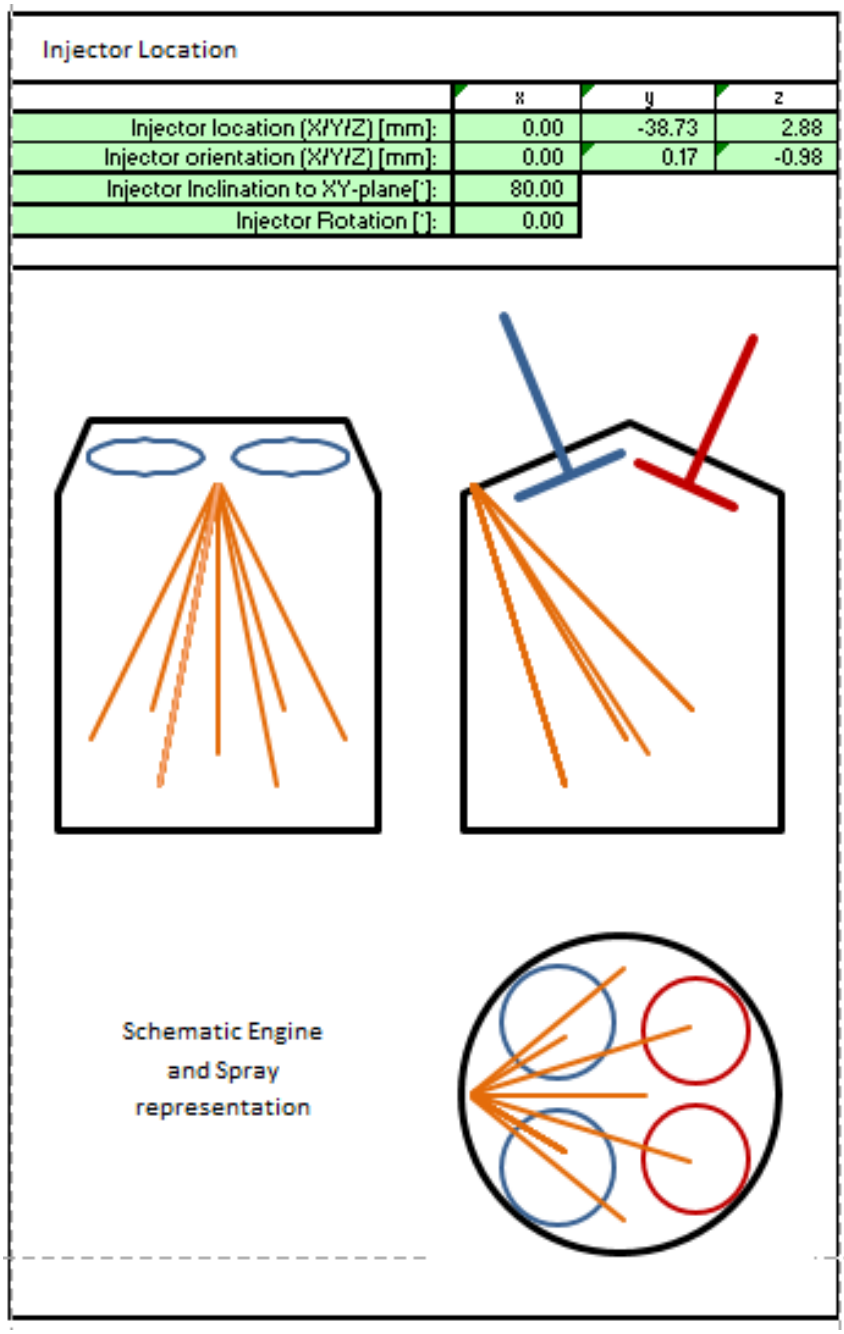

Figure 58 – AVL FIRE spray injector location.

Input Injector Measurement Conditions		
Rail pressure:	**80.0**	[bar]
Chamber pressure:	**1.0**	[bar]
Fluid Temperature:	**20**	[°C]
Fluid used for testing (G=Gasoline, H=N-Heptane, D=Diesel, E=Ethanol):	**G**	[-]
Maximum flow rate of injector:	**16.26**	[ccm/s @ 80 bar]
Fluid density during measurement conditions:	**736**	[kg/m³]

Engine Specific Parameters		
Engine Speed:	**4000.00**	[rpm]
Number of injector holes:	**7**	[-]
Number of injection events (max 5):	**1**	[-]
Rail pressure:	**150**	[bar]
Injected fuel mass:	**32.20**	[mg]
Droplet Start Velocity:	**110.0**	[m/s]
Fluid Temperature:	**50**	[°C]
Absolute mean cylinder pressure during injection:	**1**	[bar]
Fuel (G=Gasoline, H=N-Heptane, D=Diesel, E=Ethanol):	**G**	[-]

Output Engine Operation		
Fuel density:	**710**	[kg/m³]
Resulting maximum flow rate of injector:	**21.88**	[ccm/s @ 150 bar]
Theoretical droplet start velocity, based on Bernoulli's equation (@ 150bar):	**205**	[m/s]
Duration of single injection with rectangular shape:	**5.00**	[°CA]
Duration of single injection with user-defined shape:	**2.00**	[°CA]
Shortest possible injection duration (based on user-defined shape):	**2.80**	[°CA]

Additional FIRE input		
Half outer cone angle (typical 7.5):	**6.5**	[°]
Radial Pertubation (as factor of velocity):	**0**	[-]
Minimum Droplet Start Velocity (set to "-" if not used):	-	[m/s]
Maximum Droplet Start Velocity (set to "-" if not used):	-	[m/s]
Outer diameter:	**190.21**	[µm]

Figure 59 – AVL FIRE spray injection and engine parameters.

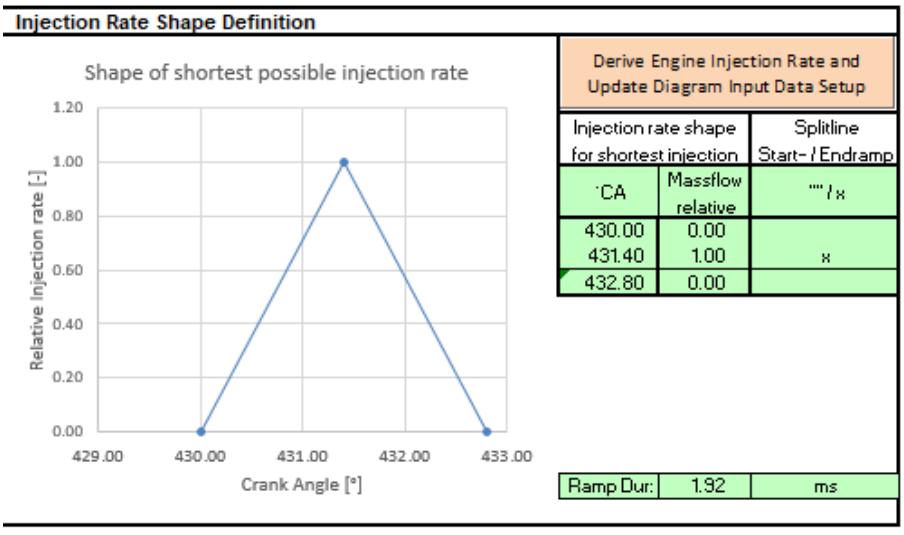

Figure 60 – AVL FIRE spray injection rate shape.

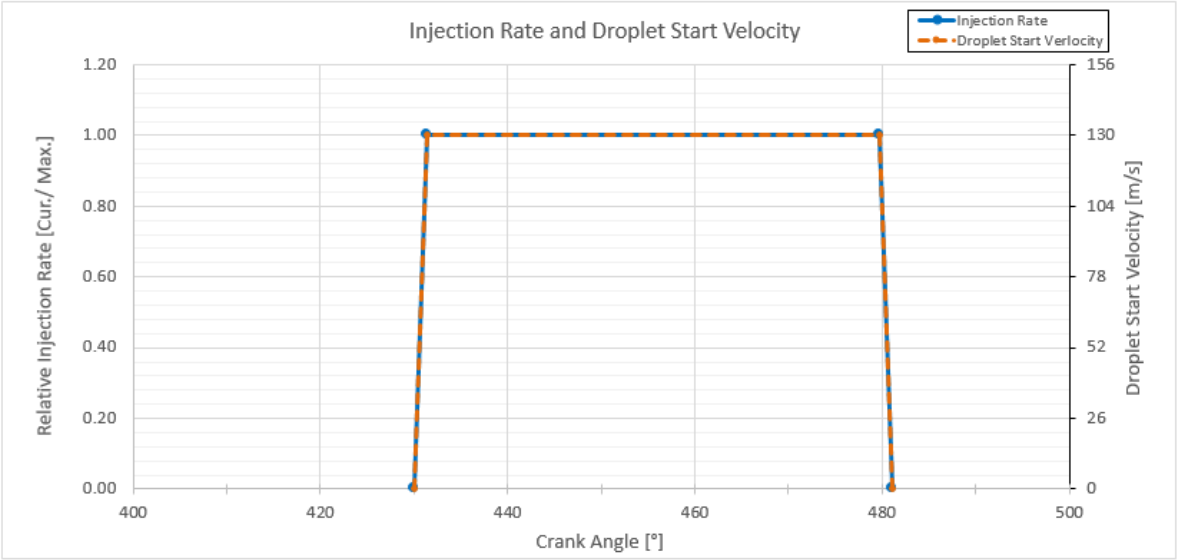

Figure 61 – AVL FIRE spray injection rate and initial droplet velocity.